UNIVERSITY OF HULL

Focusing and Delivery of Laser Radiation for Nano - and Microfabrication.

being a thesis submitted in partial fulfilment of the requirements for the degree of

Doctor of

Mathematics and Physical Sciences

in the University of Hull

by

Qassim Ahmed Al-Jarwany

BSc and MSc

December 2020

Dedication

This PhD research thesis is dedicated to my mother who passed away before I defended; I also dedicate this work to my wife for her endless support and encouragement to chase my dreams and to my three lovely sons Ahmed, Anas and Adam. I love you to the moon and back.

Acknowledgements

This thesis has been the result of hard work for close to four years. Despite setbacks, delays and sometimes even frustration, the work continued, and I was finally able to complete the work of which I feel very happy about, and deeply proud of.

This work could not have been completed without the assistance of many people around me, including my family, friends, colleagues and the University of Hull.

I feel absolutely obliged to extend my gratitude to my supervisors, **Dr. Chris Walton** and **Professor Nicole Pamme** for their continuous support, guidance, motivation and knowledge, without which this work could not have been accomplished.

Dr. Walton was an inspiration and guide all along. His feedback, encouragement, support and supervision during this PhD journey is truly appreciated.

I am also deeply thankful to to all faculty members, technical officers and administrative staff at the University of Hull. In particular, I would like to thank **Mr. T. Sinclair** and **Mr. Timothy S Dunstan** for their assistance with SEM measurements.

This work is dedicated to my wife, **Hala**, who gave me so much love, support and care during my work and was able to put up with so much pressure for so long. It is also dedicated to my three lovely sons, **Ahmed**, **Anas** and **Adam**, who gave me so much love, and the opportunity to give them love back.

Other people also supported me during this journey. I am grateful to my brother in law, **Duraid Okasha**, who helped me frequently, my family who gave their love and support all along, and my friends and colleagues who were equally supportive.

I would also like to thank the Iraqi cultural attaché in London for their support.

Finally, I would like to express my sincere gratitude to the Ministry of Higher Education and Scientific Research in Iraq and the University of Babylon for their financial support in the form of the PhD scholarship to undertake this study at the University of Hull.

Above all, I am most grateful to Allah for the countless blessings He bestowed on me.

Publications and Conferences

1 Q.A. Al-Jarwany, A.F. Mohammed, A.O. Hamza, J-S G. Bouillard, A. Adawi, N. Pamme1, and C.D. Walton." Realisation of a sub-wavelength dimpleusing a 193 nm wavelength photonic nano jet". Chemical Physics Letters, DOI: 10.1016/j.cplett. Volume 750, July 2020, 137400.

2 A.F. Mohammed, Q.A. Al-Jarwany, A.J. Clarke, T.M. Amaral, J. Lawrence, N. Kemp, C.D. Walton. Ablation Threshold Measurements and Surface Modifications of 193 nm Laser Irradiated 4H-SiC. Chemical Physics Letters, DOI.org/10.1016/j.cplett.2018.09.057. Volume 713, December 2018, Pages 194-202

3 Q.A. Al-Jarwany, A.F. Mohammed, A.O. Hamza[1,5], A. Adawi, N. Pamme[1], and C.D. Walton "Excimer laser nano-structuring of SU-8 using silica micro-spheres". Poster presented a at international conferences (Photon 2018), Aston University, Birmingham, UK , September 2018.

Abstract

The recent advances in nanotechnology and nanofabrication motivate the drive to achieve a tighter focusing of light; this requires a high numerical aperture (NA) optical system. The need for high optical resolution has led scientists to discover the use of optical microlens for improving the performance of high numerical aperture (NA) optical systems. By focusing the laser beam through a microlens, the width of the beam can be reduced according to the needs of the application. In this work, the laser beam was focused by a microspherical lens (NA=0.7) into 150 nm or by tapered fibre into 4 μm diameter spots. The measurements indicate the strong influence of tightly focused beams. This thesis comprises of three parts; the first results chapter investigates the choice of material by considering the material properties and feasibility of fabrication (chapter 2). It has been shown in previous studies that the glass transition temperature of the polymer is an important factor in determining the laser ablation rate. High glass transition temperatures make it a good material candidate for optical waveguides. Polycarbonate (PC), polymethylmethacrylate (PMMA), negative photoresist SU-8, and chitosan have been characterised to choose suitable material as a substrate for soft nanolithography (chapter 3). The choice of material due to the glass transition temperature of the material (from literature), material optical properties are investigated experimentally at the range of wavelength from 190 nm to 1000 nm. Laser ablation experiments on PC, PMMA, SU-8 and chitosan using a 193 nm ArF laser over a fluence range of 10 $mJcm^{-2}$ –1000 $mJcm^{-2}$. The ablation threshold at 193nm was found to be 24, 110, 40, and 95 $mJ.cm^{-2}$ for PC, PMMA, SU-8, and chitosan respectively. The photoresist SU-8 and chitosan were chosen as both materials are biocompatible, and have a high glass transition temperature. Optical properties measured for these materials found that both materials have much higher absorption coefficients ($\alpha_{SU-8} \sim 4.2\times10^{5}m^{-1}$ and $\alpha_{chitosan} \sim 3.3\times10^{5}m^{-1}$) compared with PC and PMMA ($\alpha_{PC} = 1\times10^{5}m^{-1}$ and $\alpha_{PMMA} = 2\times105m^{-1}$)at 193 nm.

The second part of this thesis reports experimental and computational results of an irradiated laser microsphere supported on biocompatible materials; SU-8 photoresist and chitosan (chapter 3). An ArF excimer laser (193 nm wavelength) was used with 11.5 ns pulse width to modify the underlying substrate, producing a single concave dimple. Atomic force microscopy and scanning electron microscope measurements have been used to quantify the shape and size of laser inscribed dimple. The dimple has a diameter of 150 ± 10 nm FWHM and a depth of 190 ± 10nm on SU-8 compared to 180 ± 10 nm FWHM and a depth of 350 ± 10nm on chitosan due to the optical properties of the

materials. Finite-difference time-domain (FDTD) simulations were carried out to simulate the propagation of 193 nm laser radiation, focussed by a 1 μm diameter silica sphere. Finite Element Method (FEM) simulations were carried out to calculate laser-induced temperature rise of the both SU-8 and Chitosan layer beneath the microsphere. The SiO_2 microsphere acts as a small ball lens tightly focussing the laser radiation. Delivery of the focussed laser radiation locally heats the substrate beneath the microsphere. As a consequence, mass transport takes place, forming a nano dimple.

The third part of this thesis presents the use of a CO_2 laser (10.6 μm wavelength) for producing microlenses at the end of silica optical fibre (chapter 4). By focused CO_2 laser beam, silica optical fiber is irradiated and heated to the softening points (1800 K) of the silica material. Surface tension and the parameters of the fabrication system shape the melted material into a spherical micro-lens or tapered fiber that remains joined to the optical fiber. Different core diameters (125, 400, 600, 1000, and 1500 μm) of multimode fibres have been used for this fabrication. The roughness of the microlens was reduced to less than 20 ± 1 nm roughness by polishing the surface with a CO_2 laser at low power (1-2 W). Throughout this work, different microlenses (ball/parabolic) and tapered fibres were fabricated at the end of silica optical fibre. The minimum spot diameter at FWHM was close to 160 μm and 110 μm for microball and parabolic lenses, respectively. While the tapers had the minimum waist diameters down to 4 μm and maximum taper length of ~ 3.5 mm using silica multi-mode fibre. Finally, the knife-edge technique and He-Ne laser beam (632.8 nm wavelength) were coupled into a fibre to investigate the properties of the microlenses which produced a minimum spot size of 5 ±1 μm at FWHM in the focal region of the tapered fibre lenses of 125, 400 and 600 μm core diameter of the fibre.

As a result, Chitosan and SU-8 have been used as substrate materials for recording tightly focussed focal regions, 193nm ArF laser has been used to realise extremely small, 150nm diameter, Photonic Nano Jets (PNJ's). FDTD optical simulations accurately predict the spatial properties of microsphere PNJ's emitting at 193. CO_2 laser (10.6 μm) radiation has been used to form tapers and spherical lenses on the distal end of optical fibres. Finally, tight focusing using microspheres and lensed optical fibres could be integrated on lab-on-chip platforms for applications such as optical trapping and cell membrane modifications. An important application related to the results of this study is that focusing laser light produces a force that can be used to remove or trap selected cells or large tissue areas from living cell culture down to a resolution of individual single cells and subcellular components similar to organelles or chromosomes, respectively.

The nanostructures fabricated in this chapter can be refined to achieve specific dimensions in; diameter, depth, shape, and periodicity so they can be used as antireflective surfaces for solar-cell applications [1].or could be used in drug delivery [2]. While laser microbeams are frequently used for measurement or imaging of biological parameters as well as using the optical tweezer system for trapping or moving of cells, the future medical applications will be focused on micromanipulation or microdissection methods for delivering molecules or nano drugs into a cell [3]. Delivering such nano-drugs into cancer cells requires overcoming the cell membrane by focusing the laser. This phenomenon is named photoporation which is based on the generation of localized transient pores in the cell membrane using the photonic nano jet [4].

Contents

List of Figures

List of Tables

Symboles

Term	Definition	Units
NA	Numerical aperture	dimensionless
α_{eff}	Coefficient of the absorption effectiveness	m^{-1}
d(f)	Ablation depth per laser pulse	$\mu m.pulse^{-1}$
f_{th}	Ablation threshold	$\mu m.pulse^{-1}$
f	Fluence of irradiation	$mJ.cm^{-2}$
EFL	Effective focal length	nm
BFL	Back focal length	nm
λ	laser wavelength	nm
V	Velocities of removed materials	$m.s^{-1}$
DOF	Depth-of-focus	nm
AA	Astigmatic aberration	nm
SA	Spherical aberration	nm
CA	Coma aberration	nm
H	Particle displacement	nm
C	Specific heat of the fibre	$J.kg^{-1}.K^{-1}$
d	The diameter of the fibre	µm
H	Surface conductance or convection heat-transfer coefficient	$W .m^{-2} .K^{-1}$
I	The intensity of laser	$W. m^{-2}$
k	Extinction coefficient	Dimensionless
K	Thermal conductivity	$W m^{-1} K^{-1}$
n	Refractive index	Dimensionless
P_0	Minimum required laser power	W
P	Quantity of heat liberated per unit time	W
P_t	Total output laser power	W
q(z)	Rate of heat generation from the laser	$W.m^{-3}$
Q_{abs}	The efficiency factor of absorption	Dimensionless
r	The radius of the fibre	µm
w	Beam waist of the laser	µm
T_{air}	Initial temperature	K
T_m	The melting point	K
ρ	The density	$kg m^{-3}$
R	Reflectivity	Dimensionless

Chapter 1 Introduction

1.1 Thesis overview

This thesis is primarily concerned with tightly focusing laser radiation in laser processing. Tightly focused laser beams are attractive targets for applications in alignment, measurement, super-resolution imaging, laser machining precise delivery of energy, and optical communications. Firstly, we investigate the ablation characteristics of polymeric materials, namely, SU-8, Polycarbonate (PC), Chitosan, and PMMA and the work is discussed in Chapter 2. In Chapter 3, we carry out computer simulations to complement the experimental work. The Finite Element Method (FEM) was used to simulate the temperature rise in the substrate and the results used to investigate the interaction process. Similarly, Finite Difference Time Domain (FDTD) simulations were effectively carried out to calculate the electric field and intensity of laser radiation focused by a microsphere.

The second experimental study is discussed in Chapter 3, where we investigate the focal properties of silica spherical microspheres irradiated at 193 nm. Small sub-wavelength features were realised in SU-8 photoresist and chitosan. The last experimental chapter (Chapter 4) presents the laser processing of optical fibres using a pulsed RF CO_2 laser. Infrared laser radiation was delivered to heat the distal end of optical fibres to form tapers and ball-type lenses. The knife-edge scanning method and surface roughness measurements were used to characterise the focusing properties. Finally, focusing of light could provide important applications in nano-optics using a nanohole array or microlensed fibre. For example, these results can be used for drug delivery, which is explained clearly at the end of this chapter.

1.2 Introduction

The area of ‘nanotechnology and materials in physics’ is based upon basic sciences for example material science, optics, life science, information technology, and mathematics. Nanoscience deals with phenomena occurring at the nanoscale (1 nm = 1 $\times 10^{-9}$m) [5]. Many basic technologies, for the modification and improvement of various devices and components applications, measurements, manufacturing details, and simulations based structured nanoscience are used [6], [7]. The resulting devices also play vital roles in other fields such as environmental, energy, and its renewable formation, medical and health care, social infrastructures, information communication, and electronics [7], [8]. Due to the unique and different properties of nanostructures and their fabrication methods, this

field took a highly active part in the research field for both industry and academia, which cannot be done on a macroscopic scale [9]. The rapid progress in nanoelectronics, nanophotonics, and biomedical devices has been characterised by combining material composition and structure geometry, which has led to novel applications in nanostructured materials [6,10]. Over the last few decades, much attention has been paid to the production, characterisation, and application of nanomaterials. For example, in the present day, laser applications are important in daily life, especially in the material processing industry [11,12].

Lasers are useful tools for patterning the surface and near-surface of a material [7,13], [14] It is possible, with the correct choice of optical components, to pattern material with high precision. Lasers are particularly useful and offer many advantages over other processing systems: high spatial resolution and localisation of energy that shows control of the heat-affected zone (HAZ). Pulsed lasers are a unique and novel tool for nanofabrication [15]. Absorption of pulsed laser energy, where the pulse duration is typically nanoseconds and shorter, results in huge peak powers delivered to the sample or component. Laser energy can be delivered to the sample by focusing, sometimes referred to as a direct-write process, or imaging an object aperture and moving the workpiece relative to the laser beam. The latter is referred to as mask dragging. In the former, when light is focused on the surface of solid material, pulsed laser radiation causes different effects, including heating, melting, sublimation, and vaporisation and finally leading to ablation of the target [16]. These effects depend on the specific application and can be selected by choosing the relevant parameter reference [17] for examples of various applications.

Temporal and spatial coherent energy is provided by a laser. The correlation between waves at different points in space, either lateral or longitudinal is described by the spatial coherence, the correlation between waves observed at different moments in time is described by temporal coherence [18]. Understanding these features is required to process materials at the micro and nanoscale [19]. Significant variation can occur to the photon generation emission wavelengths depending on the mechanism used.

The types of lasers that usually work at the UV wavelengths are metal vapour lasers (e.g., HeCd lasers) and excimer lasers (e.g., F_2, ArF, KrF, KrCl, and XeF lasers) [20]. However,

there are various types of lasers, mainly categorised as solid-state lasers like Nd: YAG laser [21], function and operate differently, ranging from UV to infrared. A good example to illustrate this is CO_2 lasers, which operate at infrared wavelengths [22].

Lasers can be operated in either continuous wave or pulsed modes [23]. In continuous wave mode, the energy output is constant over time (the average and peak power are the same). In a pulsed laser beam, for a certain rectangle pulsed energy, a shorter duration gives out higher peak power, and the ratio between average and peak output is called the duty cycle. The laser energy specifically points to the output of a pulsed laser and is related to the power output, where the energy (E) is the laser's peak power multiplied by the laser pulse duration [24].

The application of lasers for material processing dates back to the birth of the laser itself [17]. This application led to the discovery of various other laser types, which subsequently led to other novel applications. To enhance laser-material interaction studies and to optimise many laser-material processing applications, homogenisation techniques and laser beam shaping have attracted substantial focus. The provision of the process-adapted laser beam shaping involves diffractive optical elements which have an important role in this respect [25].

Lasers and laser-based processes are preferred for applications that need precise structures and surface functionalisation. This is due to these processes having a low heat input, high flexibility, and high lateral resolution, such that they can be focused down to a few nanometres [26]. The laser is arguably the most important optical device developed in the last 60 years. Since its arrival, it has made optics one of the most rapidly growing fields in science and technology to date [27]. Processing materials with a laser have benefited various applications such as cutting and welding of materials, drilling/ micromachining, repairing expensive components, joining plastics, surface modification, etc [28]. In many cases, the feature size and the resolution of machining are above 1 μm because of an optical system resolution reaches a fundamental maximum due to the diffraction limit of laser in the far-field [7].

The fabrication resolution can be improved when different approaches in series have been considered with the use of high numerical aperture optics and shorter wavelength of light

sources, deep ultra-violet (DUV) laser source an example of a short wavelength that includes the Krf (248 nm) the ArF (193 nm) and Hg (198nm) [29]. The short wavelength, the resultant high resolution [30], and the higher spatial resolution of materials processing are all unique benefits offered by the UV lasers for processing a wide range of materials [31]. Having said that, the spatial resolution represents half of the laser spot diameter. For a smaller spot size, a shorter wavelength, and a higher numerical aperture NA objective are used [32]. NA is defined as the ability of a lens to collect light and resolve image details at a fixed object distance The requirement of conventional photolithography is an expensive unchangeable photomask, high vacuum facility, corrosive chemicals, and complicated over-lay steps to create nanostructures [33]. In recent years, researchers have been fabricating micro/ nano-scale metallic structures without a harsh vacuum environment, triggered by the development of alternative maskless, high resolution, and direct writing technique [11].

Using of nano/microspheres for optical nanolithography is a consolidated method for realizing subwavelength structures using a cost-effective approach; this method exploits the capability of the beads to focus electromagnetic waves into subwavelength beams called photonic nanojets, [34]. Photonics studies the behaviour of light on the nanometre scale and the interaction of nanometre-scale objects accompanied by highly intensive electromagnetic beams that are light and narrow. The latter spread either in the free-space or in material from the bottom surface of a lossless dielectric microsphere. Another characteristic is illumination on the top side of the microsphere by a plane wave [35]. Photonic nanojet is the near-field optical focusing of light when the illuminating wavelength similar to or larger than the sphere [36]. Photonic nanojets is a branch of electrical engineering and nanotechnology, optics, and optical engineering. The nano jet width defines at the full width at half maximum (FWHM) of the intensity profile at the focal plane [36].

1.3 Theory of focusing

This section introduces functions that will be used throughout this thesis. Lasers have become the primary energy source for an ever-growing number of applications in science, medicine, and various industries. This is because they deliver light energy in an exceedingly useful range of ways. Characterization and analysis of both the laser and laser systems are much more than the measurement of output power and pulse energy.

Other aspects to consider are spatial intensity profile, the beam spot size in the focal region and the surface temperature rise during/after laser irradiation [37].

Often, a specific criterion is crucial, and the parameters used can define success or failure. Therefore, the control, sensitivity, and optimisation of the system are critical. Classical light confinement techniques are limited due to the limit of the focus of the laser beam. Reducing the diameter of a focal spot means that high spatial resolution fluorescent microscopy can be achieved [38]. One of the potential elements is apodizing apertures; these make the divergence of the output near to the diffraction limit [39].

An apodization function (also called a tapering function or window function), in optics, the initial stage is used to remove Airy disks which are caused by diffraction around an intensity peak, improving the focus. The efficiency of the aperture under the influence of defocusing and the primary spherical wave aberrations greatly depend on the values of the numerical aperture of width and the shading parameter [40]. Patterns of theoretical diffraction for light passing through an apodizing aperture are an easy method to analyses the apodizing capability of the aperture [39]. Due to the applications mentioned previously, several techniques have been developed to characterise the structure of focal regions. These include knife-edge measurements, the Z-scan method, translation of small slits and pinhole, and single molecular fluorescent measurements [41– 45].

The first part of this chapter concentrates on focusing the laser beam by high NA then introduces important basic functions (Debye & Richards-Wolf Integrals) for describing the propagation of light through the focusing system that will be used throughout this thesis. The next section describes the theory of laser ablation by using an excimer laser (ArF) and light-matter interaction. Finally, the theory of melting silica optical fibre (OF) by laser irradiation to fabricate a microlens on the end of an OF is explained.

1.3.1 Focusing light by using high numerical aperture lenses.

Many processes depend on tightly focusing light for which the shape and size of the spot must be known to achieve the desired outcome [46,47]. The minimal spot of light that can be focused by a lens with a circular aperture is the Airy disc, which is described as the diffraction limit. The focal pattern may have a deviation from the circular shape of the Airy disc with tightly focused conditions due to the paraxial approximation, which is no longer accurate under tight focusing [48]. To achieve a nano-scale resolution by

indirect laser fabrication of surface structures, several approaches have been considered, including shorter wavelength light sources and high NA optics. For example, deep ultra-violet (DUV, ArF 193 nm) laser sources have been used in producing nanoholes of sub-micron lithography [29, 49]. One of the probabilities to achieve an even good sense of the singular beam microscopy process is by increasing the NA of the optical system, which causes tighter focusing of a scanning singular beam [50]. It is derived by a mathematical formula,

$$NA = n\sin\theta \tag{1.1}$$

Where n is the refractive index of the medium and θo is the half-angle subtended by the exit pupil at the focal point (see Figure 1-1). From this figure, the higher NA objective has a much larger light cone, larger internal lens elements, and light gathering ability from the specimen for more than the objective having a lower NA [51]. Figure 1-1 shows the influence of the refractive index of the medium and the material of the ball lens is critical in getting high NA. It can be seen that the lens focal length and angle θ_o increase because of the reduction of light scattering brought about by the air-to-cover-glass interface when an immersion medium is used (see Figure 1-1.A). Furthermore, by using a highly refractive index lens material, the focal length decreases and the optical cone extends (angle θ_o increases) (see Figure 1-1.B).

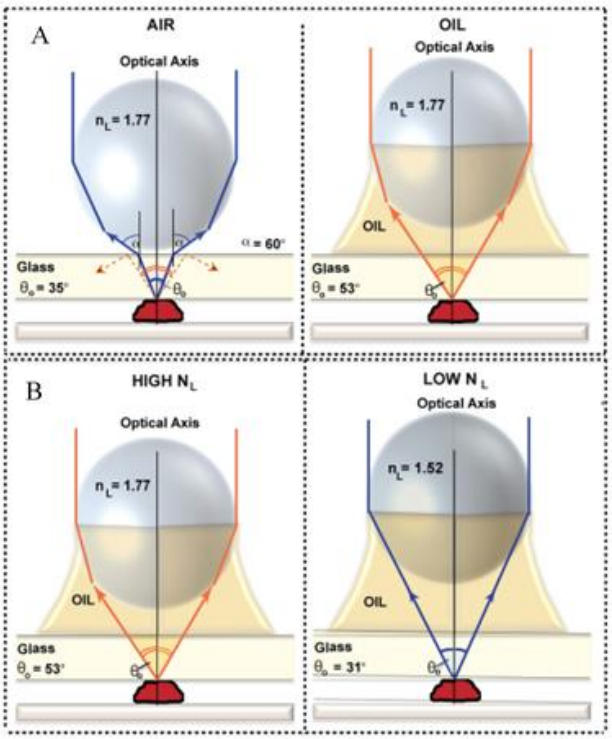

Figure 1-1 The refractive index effect of the medium (A) and the material of ball lens (B) on the ray collection angle θo [51].

Research in the field of laser science was pioneered by a series of individuals; this began with V. S. Ignatowsky who investigated the diffraction properties of light passing through an arbitrary aperture [52, 53]. The diffraction problem was later rederived by Richards and Wolf [54] and later extended by Wolf [55], the latter work involved the integral equations referred to as the Debye Kirchoff integrals [56].

In present-day applied optics, tightly focused light is regulated by the availability of high NA objective lenses (OL). When combined with different laser beam modes and optical masks, the spot size can be reduced to the nanoscale [56]. Focused spots with small size are used in a great many applications, laser scanning optical micro and nanoscopy, material processing, photolithography, and super-resolved imaging, as well as numerous other applications mentioned previously [57]. The continuous development of these techniques has given rise to the need for controlling not only the approximate size of the focal spot but also finer details, such as control of the amplitude, phase, polarization, orbital momentum, absorption, reflectance, and emissivity of light with high spatial resolution. This has led research groups to reconsider various traditional applications in optics with a different perspective [58].

1.3.2 Debye and Richards-Wolf Integrals

Current developments in nanotechnology and nanofabrication drive the requisite for tighter focusing of specially structured wavefronts with optical systems of high [59] . Wolf [60] and Wolf' and Richards [54] theoretically settled a vectorial diffraction theory for systems with high numerical aperture. An integral representation has been shown for the electromagnetic field in the image space of an optical system, which made it possible to find the complete structure of the image in systems of low as well as high angular aperture [60]. They successfully found that the focus of a linearly polarized beam is asymmetrically deformed. This asymmetry is an effect of the vector character of the electric field and was explained in detail by Stamnes [61].

The structure of the electromagnetic field near the focus of an aplanatic system which images a point source is investigated. Initially, expressions are derived for the electric after magnetic vectors in the image space and the case of a linearly polarized incident field is examined [54]. Then, the Seidel aberrations at the exit pupil at the focusing optical

system were realized after related expressions were derived for Gaussian beam amplitude distribution at the entrance pupil [62]. The term, Seidel aberrations," is the generic name of the third-order aberrations, the Seidel aberrations of a system in monochromatic light are called spherical aberration, coma, astigmatism, Petzval curvature, and distortion. It occurs for a monochromatic but non-paraxial electron beam [55]. Smaller two-dimensional focal spot sizes for many applications have been used to improve the performance of an optical system. The major part is to know the third dimension of the focal field distribution in the case of confocal microscopy [63].

1.3.3 Depolarisation

Annular illumination influences both focal intensity distribution and the structure of the electric field in focus. From electromagnetic focusing theory [54], [61], when focusing linearly (x-polarized) light at high apertures, there exhibits significant perpendicular and longitudinal components Ey and Ez in the focal field. The depolarization is because of the curvature of the spherical wavefront of the focused field which is predicted to be stronger for higher apertures [64], in agreement with the intuitive expectation that larger focusing angles of the marginal rays produce a stronger bending of the field vector.

Depolarization can be made more pronounced with annular apertures as they generate only marginal rays. This is clear by the fact that annular illumination or detection is used for resolution increase where high apertures are required [64]. Differential transmission and phase shift bring to spatial polarization changes in the exit pupil plane called ‘‘polarization aberrations’’ [65]. The polarization aberrations are the differences of amplitude, phase, polarization, and retardance related to light transmission through an optical system. It causes undesirable polarization components, “depolarization”, that reduce the extinction in the image plane [66].

1.3.4 Vector diffraction theory –Debye approximation

According to the Debye approximation, the electromagnetic field is symmetrical about the focal plane for a fixed focal distance [37]. In the scalar case, it was noted that for a fixed focal distance, the Debye approximation gets better as the angular aperture increases, and for a fixed angular aperture, it gets better as the focal distance increases [67]. However, the Debye theory is valid when the focal point is located many

wavelengths away from the aperture along with a sufficiently large angular aperture [68]. The requirement for a high numerical aperture system is the vector diffraction theory, which affects because of the vector character of the electric field which becomes important. A plane wave incident on a focusing system is transformed into a converging spherical wave. This approach initiates with expanding the spherical wave into an angular spectrum of plane waves [60, 63].

The incident optical wave when entering the pupil of a focusing aplanatic optical system is represented with rays parallel to the optical axis, required by the Richards-Wolf method. Phase variations in the plane of the entrance pupil are contradicted by this requirement when entering the plane of pupil [62]. Furthermore, the assumption is made that only a small fraction of the energy in the incident field is contained in regions where non-negligible phase variations happen, especially at the boundaries between neighboring segments. The use of the principle of superposition to determine the field in the focal region as a linear superposition of the contributions which are obtained from each constant-phase segment of the incident field under these conditions is possible. There is no assumption for the incident optical field amplitude or polarization[69]. In many applications, high NA lenses are used for tight focusing. Focusing across an interface that has different refractive indices causes a change in polarization. Tight focusing results in electric field components being transformed. We can represent the beam propagation using a converging wave. By using the Richards–Wolf vectorial diffraction method, the focusing property of highly focused polarized beams can be analysed numerically.

B. Richards and E. Wolf's study was undertaken of the electromagnetic field structure close to the focus of a high numerical aperture system which imaged a point source [54]. An incident field (linearly polarized) is examined, and the equations below are used to calculate the electric vector in the image space. These equations are not suitable for systems of low numerical aperture. The results cover values that are specific for the angular semi aperture α on the image side, in the whole range $0 < \alpha < 90°$. The condition α reaches to zero is examined in detail, the field is then completely characterized by a single, generally complex, scalar function. This is identical to the classical scalar theory of Airy [70], Lommel, and Struve, who investigated aberration-free focusing by a uniformly illuminated ideal lens and approached the problem using the theory of paraxial scalar diffraction [71]. The equations below represent the analytic solution for the component's vectors of the field at a point *P* in the image region. It is reported that the

field at any point P (spherical polar coordinates (R_P, θ_p, ϕ_p) in terms of the three integrals I_o, 1_1 and I_2 [54]:

$$E_x\left(r_p,\theta_p,\phi_p\right)=-iA\left(I_0+I_2\cos 2\phi_p\right) \tag{1.2}$$

$$E_y\left(r_p,\theta_p,\phi_p\right)=-iAI_2\sin 2\phi_p \tag{1.3}$$

$$E_z\left(r_p,\theta_p,\phi_p\right)=-iAI1\cos\phi_p \tag{1.4}$$

Where

$$\left.\begin{aligned} I_0=I_0\left(kr_p,\theta_p,\alpha\right)&=\int_0^\alpha\cos^{\frac{1}{2}}\theta\sin\theta\left(1+\cos\theta\right)J_0\left(kr_p\sin\theta\sin\theta_p\right)e^{ikr_p\cos\theta\cos\theta_p}d\theta\\ I_1=I_1\left(kr_p,\theta_p,\alpha\right)&=\int_0^\alpha\cos^{\frac{1}{2}}\theta\sin^2\theta J_1\left(kr_p\sin\theta\sin\theta_p\right)e^{ikr_p\cos\theta\cos\theta_p}d\theta\\ I_2=I_2\left(kr_p,\theta_p,\alpha\right)&=\int_0^\alpha\cos^{\frac{1}{2}}\theta\sin\theta\left(1-\cos\theta\right)J_2\left(kr_p\sin\theta\sin\theta_p\right)e^{ikr_p\cos\theta\cos\theta_p}d\theta \end{aligned}\right\} \tag{1.5}$$

and J_0, J_1 and J_2 are the Bessel functions, α is the angular semi-aperture on the image side, for example, 2α is the angle which the diameter of the exit pupil subtends at the geometrical focus, and A is the constant:

$$A=\frac{kfl_0}{2}=\frac{\pi\, fl_0}{\lambda} \tag{1.6}$$

where the peak amplitude at the pupil plane is l_0. These equations are widely known as "Richards-Wolf equations" for the investigation of an electric field of focusing regions. A cylindrical vector (CV) beam with a planar wavefront is generalized over the pupil by the illumination. Aspherical wave converging to the focal point is produced by an aplanatic objective lens [72]. E_r, E_z, and E_ϕ are the amplitudes of the three orthogonal components, which can be derived as:

$$E_r\left(r,\phi,z\right)=2A\cos\varphi_0\int_0^{\theta_{\max}}P\left(\theta\right)\sin\theta\cos\theta J_1\left(kr\sin\theta\right)e^{ikz\cos\theta}d\theta \tag{1.7}$$

$$E_z\left(r,\phi,z\right)=2iA\cos\varphi_0\int_0^{\theta_{\max}}P\left(\theta\right)\sin^2\theta J_0\left(kr\sin\theta\right)e^{ikz\cos\theta}d\theta \tag{1.8}$$

$$E_\phi\left(r,\phi,z\right)=2A\sin\varphi_0\int_0^{\theta_{\max}}P\left(\theta\right)\sin\theta J_1\left(kr\sin\theta\right)e^{ikz\cos\theta}d\theta \tag{1.9}$$

where θ_{max} is the maximal angle corresponding to the NA of the objective lens, $P(\theta)$ is the pupil apodization function that strongly depends on the objective lens design as shown below: $P(\theta) = P(f \sin\theta)$, $J_n(x)$ is the Bessel function of the first kind with order n, and wavenumber, k.

1.4 Light-matter interaction

Absorption is one type of laser light-matter interaction. In metals, free electrons are excited to electronic or vibrational states, thereby reducing energy from the optical field [73]. To fully understand the effect the laser beam has on the irradiated material, the electronic and lattice dynamics must be considered. To induce an effect of sufficient magnitude on the material, the incident laser light must be coupled into the material via absorption. It also becomes apparent that, although driven by the incident light beam, the source can be time-varying depending on the electrons and lattice responses within the material [18]. The two systems must be considered as separate entities for small pulse duration $\approx 10^{-14}$ s. For pulse durations longer than the electronic relaxation time, a single temperature model can be used. This is because, on timescales of the order of the electron relaxation time, it can be assumed that the electronic and the lattice temperature are in equilibrium. In general, the interactions between laser light and condensed matter include, but are not limited to the following processes: (i) radiation coupling and absorption within the target material. (ii) Following this, there will be heat transfer in the target due to thermal diffusion within the sample. (iii) For sufficiently high fluence there will be evaporation, vaporisation and condensation located on the surface of the material; (iv) and finally, the behaviour of the vapor and the ambient gas (if present) [74].

Many complex processes need to be accounted for when dealing with pulsed laser irradiation of materials. All the parameters should be optimised to prevent maximum localized damage. When designing a fabrication method utilising a laser, it is prudent to start the design by selecting the wavelength of the laser, because each material has its unique refractive index and extinction coefficient. Both of these terms are strong functions of wavelength. One should aim to minimise the reflection of the beam and maximise the absorption coefficient. Thereby coupling the laser radiation into the material much more efficiently. Other key parameters include the spot size of the incident beam, the pulse duration of the laser pulse, its spatial and temporal pulse shapes, the repetition rate, and duty cycle. These are all laser parameters that influence the choice of

laser to be used to optimise efficiency [75]. These optimal factors depend on the material and laser type. Absorption leads to the conversion of the energy into heat, which is a photothermal mechanism, whereas a chemical reaction which is induced after excitation is known as a photochemical mechanism. When material is removed from the bulk, the term "laser ablation" is utilised, regardless of the process which causes the material to be removed [76].

It has been proven that for fluences below the breakdown threshold of a material, that heat deposition can potentially cause changes of state in materials. One example is the photocoagulation of tissue in retinal surgery, where the laser-induced denaturation of tissue is due to the structural transitions of the proteins within the ocular region. Another example is the laser deposition of heat, causing vaporisation. This is utilised as explosive vaporization [73]. The laser ablation process is a thermal process if the irradiated time is much longer than the thermal relaxation time of a material (τ) [77]. The heating caused by these thermal processes causes the material to evaporate after the first melting if the level of temperature reaches a sufficiently high level to drive the transition. In addition, if the chemical structure is sufficiently heated, that results in the breaking of weak bonds. In polymers, it is observed that evaporation can occur without reaching the solid-liquid transition point. The processes of photothermal laser ablation have been investigated for various polymers [78]. A key result was that the breadth of the ablated layer (Δh) per pulse is strongly dependent on thermal penetration and optical penetration. The relationship between the parameters above of the thickness is defined as [24]:

$$\Delta h \approx Max\left(I_T, I_\alpha\right) \tag{1.10}$$

where l_α is the value of optical penetration of the material, that is; the reciprocal of the absorption coefficient; $L_T=2(D\tau)^{1/2}$ is the thermal penetration depth where D *is* the thermal diffusivity and τ is the thermal relaxation time. It is also of high importance to describe the distribution of the velocities of removed materials; this can be determined as [24]:

$$V = V_0 e^{\left(-\frac{\Delta E}{T_s}\right)} \tag{1.11}$$

Here, ΔE, is the energy required to break the chemical bonds within the material, and T_s is the surface temperature of the material, respectively.

The light intensity when incident on the material is explained by the Lambert-Beer equation [79].

$$I_0 = Ie^{(-\alpha d)} \tag{1.12}$$

The absorption coefficient can be find by function below [168]:

$$\alpha = \frac{1}{d}\ln\left(\frac{(1-R)^2 + \sqrt{(1-R)^4 + (2RT)^2}}{2T}\right) \tag{1.13}$$

Where R is the reflectivity of the material surface, T is the material transmittance and d is the material thickness. In general terms, the absorption coefficient of materials is determined by the wavelength and material of the absorbed light. The absorbance of the material increases proportionally with increasing film thickness, as per Beer's law [80]. The absorption coefficient of a thin film is calculated from the formula [81],

$$\alpha = \frac{2.303A}{d} \tag{1.14}$$

where α, A and d, represent the absorption coefficient, the absorbance and the film thickness, respectively. α for all the biocompatible materials in this study was calculated by using the last equation.

1.5 Theory of laser ablation

Laser ablation, as the process of removing material from the substrate surface by focusing the high-powered laser beam onto a targeted workpiece, melting and vaporizing the materials to clean a surface, texturing, and manufacturing enhancement [12]. The fabrication of microstructures by pulsed excimer lasers has attracted significant interest over the past 30 years [73– 77]. The laser ablation of polymers has been studied using specifically designed materials to evaluate both the ablation mechanism and the role of

photochemical active groups in the ablation process. Hence the possible applications of laser ablation and designed polymers can be evaluated [87]. The fundamental parameters within laser processing are wavelength, pulse duration, fluence (i.e., the laser energy delivered per unit surface area of the irradiated material), repetition rate (i.e., the time interval elapsing between subsequent pulses), and several deposition pulses [59]. The fundamental parameter which describes the process of ablation is referred to as the ablation rate, *d (F).* The ablation rate describes the rate of removal of material from the bulk per pulse. There are several other key elemental factors within this parameter, such as the ablation threshold fluence (F_{th}). The threshold fluence is defined as the minimum amount of energy (optical energy per area per pulse) required to observe the ablative process [88]. Another important parameter is the coefficient of effective absorption, α_{eff}, which yields information on how strongly the incident radiation field is being coupled into the material. It is an important parameter because the effective absorption coefficient often becomes larger than the linear absorption coefficient at high irradiances [89] because of linear absorption coefficient is constant and depends on the laser wavelength and the extinction coefficient while the effective absorption coefficient is proportional to laser fluence. The effective absorption coefficient can be determined as the slope of the semi-logarithmic plots of averaged ablation rates vs maximal fluence. An important parameter for laser ablation is the pulse duration. A long pulse duration (nanosecond) can generate a heat-affected zone around the irradiation site extending hundreds of nanometres, depending on the thermal diffusivity. Therefore using a laser with a nanosecond pulse duration is suitable for removing materials via ablation [90]. When dealing with nanosecond duration laser pulses, it is typically assumed that most of the absorption is due to single-photon interactions. [91]. Excimer laser gained attraction because most polymers exhibit a high absorption coefficient at excimer wavelengths and the ease of making a small portion of laser to attack into the work surface using an aperture[76, 83, 84].

Laser pulse ablation processing is defined by three mechanisms: thermal, photophysical, and photochemical mechanisms [18, 85]. Biopolymer materials can also have a fourth photoacoustic mechanism. For thermal processing, the main function is the absorption of light by the electrons of the material itself, causing local melting and evaporation of the material, as the energy is transferred to the atomic lattice [91]. In the non-thermal process, photochemical ablation results due to the electronic excitation during the process of direct bond breakage [95]. Figure 1-2 shows that interaction processes between a material and

a laser beam are accompanied by thermal effects [96]. These effects range from processes directly due to irradiation by the laser such as photo-thermal, melting, and gasification, to other effects such as the generation of plasma, chemical reactions in the condensed phase and gaseous phase, laser-supported detonation (LSD) and laser supported combustion (LSC). The observation of these phenomena depends directly on incident irradiance and material characteristics.

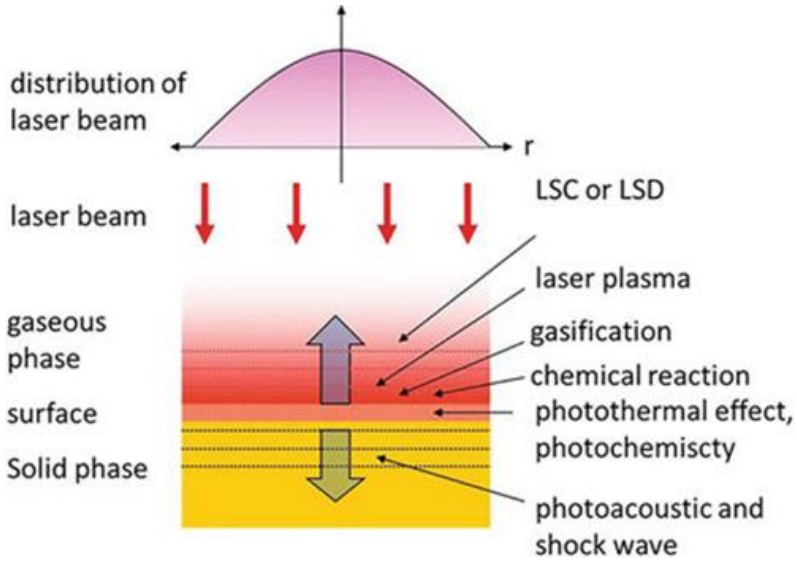

Figure 1-2.The interaction of ablation mechanisms, including photoacoustic, photothermal and photochemical mechanisms [96].

1.5.1 Nanosecond laser ablation mechanisms

There are various models to analyse Nanosecond laser ablation. It depends on initial activation, we can recognize the difference of photo-thermal ablation, photochemical ablation and a combination of both processes (Photo-physical) [59]. There is always a single dominant mechanism for the description of ablation for all these models. Due to this reason, each of these models allows the analyses of experimental results for particular material only within a limited range of parameters. Several types of research have focused on explaining the mechanisms present at the laser-material interaction area by assuming one mechanism dominates and then simulating the dominant process [97]. In this work, the photo-thermal effect is the most dominant in laser-material interactions. For a more general description, simultaneous consideration of different interaction mechanisms and coupling between them is required [13]. Using the block diagram shown in Figure 1-3, further discussion in detail is as follows:

These processes, which are involved in photo-thermal ablation, are started with single or multi-photon excitation of the irradiated material surface. If instantly excitation energy is

transformed into heat, it causes a rise in temperature at the surface that increases the surface temperature [98]. This coupling among thermal field and optical properties as shown in the figure above is indicated by a double-headed arrow (see Figure 1-3). The rise in temperature results in (thermal) material ablation (vaporization) with or without melting of the surface. Another possibility is that the raised temperature induces stress which can results in explosive-type ablation, also with thin films on a thick substrate, material pop-off has been observed [99].

These stresses can bring changes to the optical properties as well as can influence the temperature rising. Another feedback can be observed with the relation of thermally induced defects. Irrespective of the importance of thermally induced stresses or defects, we can refer to this overall process as thermal ablation [12]. With the shorter excitation time as compared to the required time to heat the material, to bring the temperature to its boiling point, non-thermal, photochemical ablation can appear. In photochemical ablation, the sufficiently high amount of photon energy laser excitation can lead to direct bond breaking [88]. Consequently, single atoms, molecules, clusters or fragments absorb from the surface. Besides this direct channel, there is again an indirect channel (dashed arrows). Mechanical ablation can be produced when light-induced defects, for example, photo-chemically dissociated bonds, build up stresses. Both the ways mentioned above, applicable in principle without changing the temperature in the surface. Due to this, we name this process as photochemical ablation [90].

In the photo-physical ablation case, process, thermal and non-thermal mechanisms contribute to rate ablation [59]. An example would be like a system, in which the lifetime of electronically excited species or broken bonds kept for a long time that species desorbs from the surface before the total excitation energy is dissipated into heat. The process of desorption is enhanced when the temperature increases. The overall process of photo-physical ablation is being influenced by thermal or non-thermal defects, stress, and volume change. Thermal ablation and photochemical ablation can be considered as limiting cases of photo-physical mechanism [95]. Above mentioned possible mechanisms are not completed, due to additional development of plasma emission, especially electrons and ions. Due to these processes, additional electric fields can cause, it may change the activation energy for thermal desorption or direct bond breaking [1].

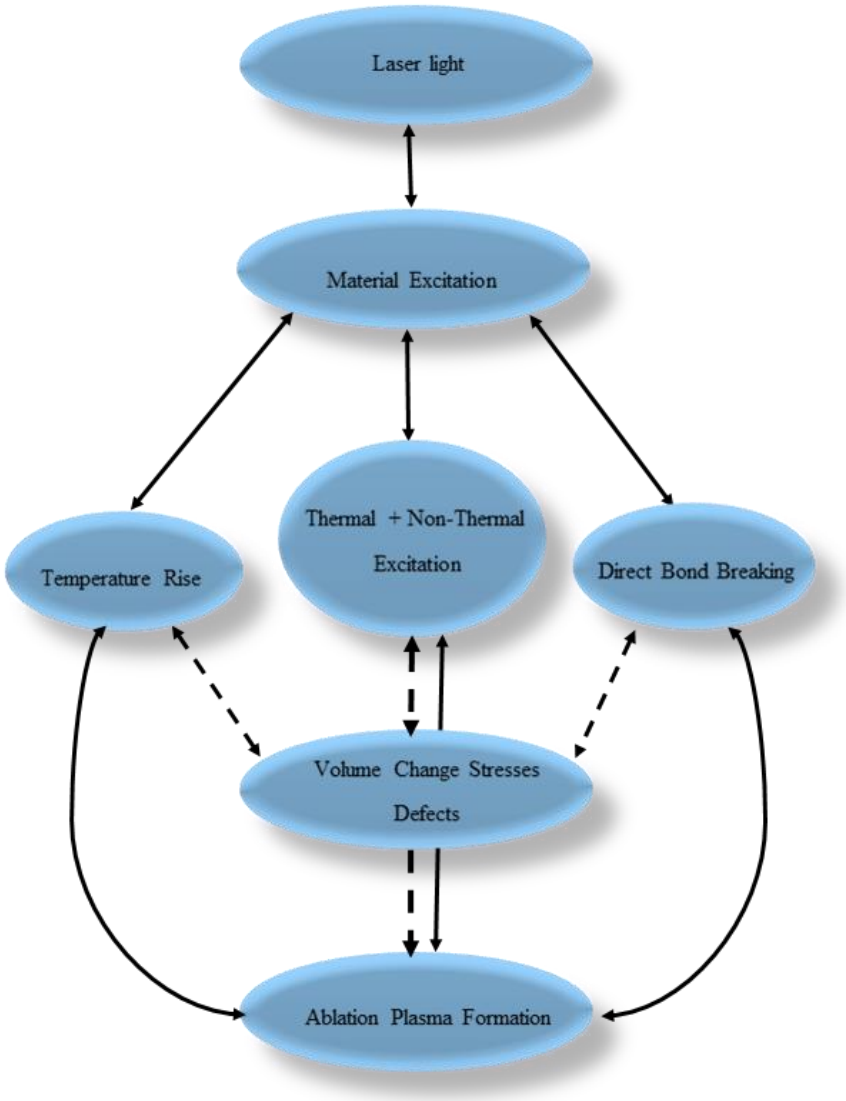

Figure 1-3 Reflects various interaction and feedback mechanisms in pulsed laser ablation. Ablation can be based on thermal mechanism only (left path), on processes that break chemical bonds in the molecule (photochemical ablation; right path), or on a combination of both (photophysical ablation; intermediate regime)[13].

1.5.2 Ablation threshold

The ablation threshold is the minimum incident fluence required to generate material ablation [59]. There are various mechanisms by which ablative effects can occur, such as ablation via photolytic or pyrolytic processes. In studies of laser interactions with various materials, it is found that the magnitude of the ablation processes becomes substantially above the ablation threshold range. The threshold varies awarding to the type of polymer depending on various material-dependent factors [100]. Some of them include molecular properties, such as how strong the intermolecular forces are in the given polymer and the

strength of the bond between each monomer. Other factors depend on the laser wavelength as each polymer possesses different complex refractive indices and respond differently, dependent on the incident wavelength. The ablation rate is described by the equation below [101].

$$d(f) = \frac{1}{\alpha_{eff}} \ln\left(\frac{f}{f_{th}}\right) \tag{1.15}$$

where $d(f)$ is the ablation rate (ablation depth per laser pulse), α_{eff} is the coefficient of the absorption effectiveness, f is the fluence of irradiation, and f_{th} is the threshold fluence laser evaporation by nanosecond laser pulses. The ablation rate is described as the mass removed per pulse from the radiated sample [59], [88][102]. For thermal ablation mechanisms such as melting, with the increase in absorption coefficient α, the ablation threshold decreases [77]. This is due to the small material volume which is excited with the laser energy. This is because the material is strongly absorbing at that wavelength, and so has a small optical penetration depth. Various methods of measurement can yield different ablation rates. The ablation process does not always begin with the first pulse [59]. This could be due to the fact the depth of the ablation crater being too small to measure, or because the ablation process starts after successive pulses. This regime is referred to as the incubation effect, as the chemical or physical material is modified by successive pulses of the laser, rather than each pulse being considered as an individual event [98].

1.6 Micro and nanosphere laser lithography

Nanostructures fabrication by laser micro/nanosphere lithography for both micro and nanoscale devices is used for super-high-resolution imaging and the microchip industry [11]. Lithography is currently the most widely used microfabrication technology [103]. Lithography refers to the fabrication of one- and two-dimensional structures in which at least one of the lateral dimensions is in the nanometer range. Lithography replicates patterns (positive and negative masks) into underlying substrates (see Figure 1-4) [104]–[106]. Photolithography can be further subdivided into near-UV (350-450 nm), mid-UV

(300-350 nm), and deep-UV (< 300 nm) technologies, depending on the wavelength of the exposure [107]. The resolution is proportional to the exposing wavelength and inversely proportional to the numerical aperture (NA) of the lens [57]. Advantages and disadvantages of each process depending on what it is you want to fabricate. Some lithography techniques have the disadvantage of being much slower than photolithography. The photolithography technique uses a single beam of UV light and does not require any additional materials [6], [108]. UV light has a wavelength < 450 nm, giving a limiting feature size, set by diffraction effects ($\lambda/2NA$) [17], [109]. These make photolithography to less expensive and highly efficient in fabricating extremely small incisions on a substrate. The fabrication of exact shape and size of any substrate can be controlled by using photolithography [106]. Along with the advantages, Photolithography has several disadvantages, it requires a completely flat substrate in order to produce effective patterns, it is not efficient at producing objects that are not flat and the process of photolithography requires extremely clean conditions that are void of all contaminants, liquids, and environmental hazards. Photolithography has many applications to fabricate integrated circuits, microcircuits, MEMs, NEMs, organic memory devices, medical devices, etc [6, 31, 108, 110]. Consequently, some other microfabrication ways are being explored as alternatives. Laser processing has also been explored as a microfabrication method for the self-assembly of structures as well as for the micro/nano machining of materials [111]. The fabrication process is schematically shown in Figure 1-4.

The need for manufacturing at the nanoscale indicates not only from the need for increasingly sophisticated devices and structures with novel properties but also with the rapid decrease in component sizes, material usages, and the energy consumption of end products [32]. To meet the requirements for product miniaturization and novel functionalities, there has been an achievement of nano-precision and resolution through the development and implementation of nanofabrication technologies. Lithography is based upon to provide higher resolution with large process latitudes. In order to meet supply and demand quotas, the lithography industry, on the whole, has decreased its exposure and the wavelength used and increased the size of projection optics [71].

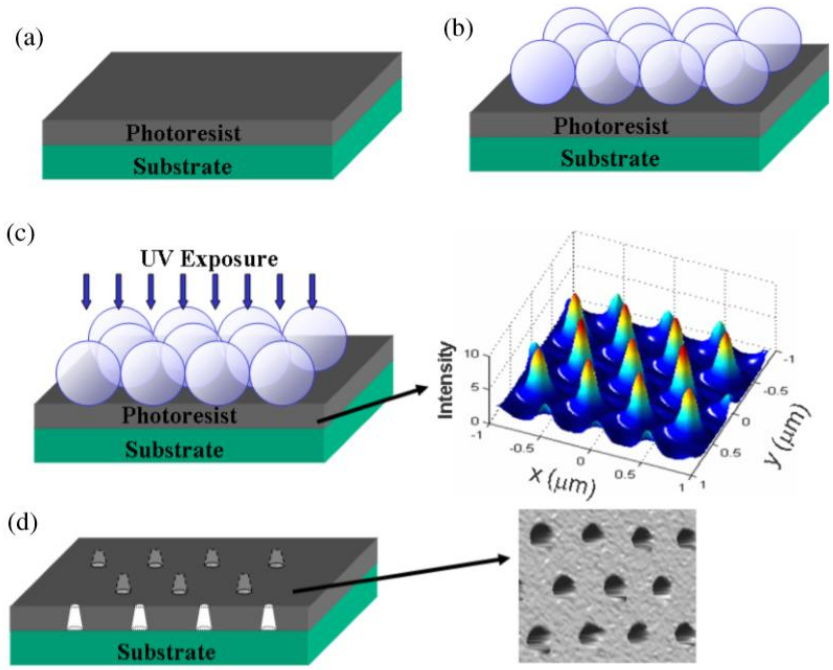

Figure 1-4 A schematic diagram of the fabrication process of periodic nanostructures: (a) photoresist spin-coated on a substrate, (b) microspheres silica or polystyrene coated on top of the photoresist film, (c) UV light exposure the monolayer of hexagonal-close-packed microspheres which covered the photoresist. Three-Dimensional FDTD simulated the two-dimensional intensity of the UV light in the photoresist plane (right-middle), (d) nanoholes patterns have gotten on photoresist film after cleaning the sample. On the right-bottom, an AFM image of a developed photoresist is presented [104].

Nanolithography, nanoimprinting, and micro/nano printing are some frequently used patterning techniques. Nanolithography uses lights, charged ions, or electron beams. To chemically etch the transferred pattern onto the target material, a series of post-treatments is used via the technique [8]. Laser nanolithography shows the potential for improving nanomaterials for optoelectronic components. The advantages of these techniques are that large quantities of the one-dimensional nanostructure can be prepared, using varied materials, which are available [112].

Some groups refer to Interferometric Lithography (IL) as both Interference Lithography and Holographic Lithography. Various techniques and self-assembly approaches (such as surface plasmon lithography and nanosphere lithography) are encapsulated by IL, e.g., advanced optical lithography and nano-printing. Chou *et al* [113] in 1995 were the first to introduce a simpler, low-cost, and high throughput Nanoimprint Lithography (NIL) as an alternative to micro and nano-fabrication. NIL has been successfully viable in fabricating nanoscale photodetectors, silicon quantum dots, quantum wire, and ring transistors. As far as the inherent features of various two- and three-dimensional

structures are concerned, their sizes range from several micrometers to below 50 nm [114]. High throughput and parallel nanofabrication techniques are under increasing demand.

To produce highly uniform arrays of nano-pillars and nanoholes, there is a demand for a low-cost efficient process. These patterns cover a wide range of applications in many devices such as solar cells, fuel cells, memory devices, photodetectors, surface plasmonic, photonic crystals, nanofiltration, and artificial kidneys [115]. As for manufacturing, there are commercially available and widely implemented conventional techniques for nanofabrication. Some drawbacks and limitations to these conventional approaches are high cost and the difficulty in accessing the facilities to use them. The two dominant methods for photolithography are ion beam and conventional lithography [116]. The desired resolution can be obtained using novel techniques like x-ray, electron-beam, focused ion beam, and NIL. However, these are considered slow and no cost-effective for fabrication for large areas.

A demanding technique to produce a periodic structure array, that initially used as a tool for nanopatterning have the term “natural lithography”, which is the self-assembly of monodispersed micro/nanospheres on a planar surface [17], It is reported that 500 nm polystyrene (PS) nanospheres are spin-coated on a silicon wafer forming a hexagonal array. After that, a lift-off mask for metal evaporation is made using the assembled nanospheres. The term nanosphere lithography (NSL) was adopted [3].

NSL uses planar ordered arrays of micro-nanospheres as a lithography mask to generate ordered arrays on a substrate [117]. Various nanostructures and well-ordered two-dimensional nanoparticle assemblies are yielded using NSL which is a simple, effective, and relatively inexpensive parallel nanofabrication technique [17]. A variety of materials are suitable for NSL. The investigation of their size-dependent optical, magnetic, electrochemical, thermodynamic, catalytic, and other properties is used in the production of nanoparticles and nanostructures involved in such investigation [18].

Noticeably, the fabrication of nanoparticles and nanostructures from refractory materials is largely obtained using lasers in this method. However, there are drawbacks to this method. Firstly, the layer called monolayer in spheres always contains defects resulting in agglomerations of clusters/particles after metallic evaporation and prevents successful lift-off. Secondly, the coupling of size and spacing of the holes; which cannot be controlled independently [5].

Finally, NSL requires spheres to be formed and deposited directly on to the surface of the substrate, not the bulk, though this is not possible for many materials. Based on the particle size and wavelength of the laser source, an enhancement in the optical field can be produced which is due to a lens focusing effect or Mie scattering by the spherical dielectric particles [118]. A considerable amount of research has been made on the 'photonic nanojet' (PNJ) effect due to its multiple potential applications, including detecting and manipulating nanoscale objective, cavitation assisted drug delivery, nanolithography, super-resolution white-light nanoscope, Raman spectroscopy, optical nanopatterning, etc.[119, 120]. A brief review of early research in photonic nanojets can be found in Zhu *et al*. [121]. Light nanojets by microsphere focusing can perform a low-cost and offers high subwavelength resolution technique [34]. Photonic nanojet gave the motivation to research in many related fields including optical waveguide, microscopy, sensing…etc [35,120].

Many researchers have used different wavelengths and microlens for nanostructuring surfaces, some of them related to the present work and explained in the following paragraphs. In 2001, Mosbacher *et al.* [122] reported electric field enhancement produced as the light was focused by polystyrene 1.7 μm diameter microspheres. Light at wavelengths of 800 nm and 400 nm produced holes in a Si substrate. Interference of light between the microsphere (n = 1.51) and substrate (n=3.69) causes a complex focal region and the concomitant asymmetric hole in the substrate. In 2015, the possibility to create arrays of nanostructures with hole diameter close to 169 ± 23 nm and the depth 11.5 ± 2.8nm was demonstrated by Afanasiev et al. [123], using the same wavelength but with small microsphere polyester (D=0.45 μm) on a PMMA substrate.

Simple and efficient techniques to fabricate micro/nano-structures on a glass surface by a femtosecond (FS) laser were investigated by Wang et al. in 2008 [124]. They fabricated a two μm diameter hole on a glass surface (fused silica) by using an FS laser (800 nm wavelength) that was focused by using a 5 μm silica sphere. The possibility of surface patterning by contact microsphere lens arrays, using a focused laser beam at an incident angle normal to the substrate surface was explored by Sedao and co-workers [15]. A picosecond laser system (wavelength of 515 nm) was used to irradiate silica particles, 1.3 μm diameter, producing nanoholes 380-400 nm diameter and depths of about 140 nm.

A Schwarzschild objective was demonstrated by Karstens and others in the method of the parallel fabrication of periodic hole arrays with a sub-micron pitch and holes with

diameters below 300 nm by using a 193 nm-ablation by phase mask imaging [125]. A weak function of sphere size can be presented by a pattern of this size, which means that the monodisperse array can be constructed. Pattern formation can be in both conventional negative and positive photoresists. The illumination of spherical particles on the surface of substrates by a laser has been widely investigated using this method of rapid and rigorous nanofabrication[126]. In 2007, Wei *et al.* [127] reported their work using micro-silica spheres (0.97 μm diameter) with a UV source (400 nm wavelength) to make a hole size 250 nm.

In 2010, Ana et al. [128] investigated the direct writing of micro/nano-holes structures (1000 nm diameters) by using a diode-pumped Nd: YVO4 laser (532 nm wavelength) that irradiated a silica microsphere (5 μm diameter) on single-crystalline silicon (Si) substrate. In 2016, Brodoceanu *et al*. [129] reported the fabrication of arrays of silicon nanowires (170-200 nm diameter) by irradiating with a single pulse laser (355 nm wavelength) through a polystyrene microsphere (0.5 μm diameter). In 2003, Denk *et al* [130], used a silica microsphere (3 μm diameter) to focus a UV laser (λ=248 nm) to produce nanoholes on PI substrate; the hole diameter was 400-500 nm and depth between 75 and 250 nm.

Furthermore, silica (SiO_2) particles with 0.97 μm diameter were imprinted on Si substrate by single pulse laser (λ=248 nm) at fluences ranging from 0.35 to 1.7 $J.cm^{-2}$ to create hemispherical cavities with diameters from 410 to 750 nm. These results were investigated by Li *et al*. [131], reporting the sizes of the cavities as a function of the laser fluence. In 2017, Hidetoshi et al. [132], reported the creation of micro swelling structures size 1.3μm diameter and 1.3μm height were created on a silicon rubber substrate by focusing 193 nm ArF laser through silica particles of 2.6 μm diameter which coated on the substrate before irradiation. Around 300 nm is the smallest diameter of dimple fabricated by using 1 um silica that is illuminated at 193nm wavelength [133]

Finally, in 2019, Cao *et al.* [134], presented that a nanohole-structured dielectric microsphere can be used for deep subwavelength-scale light focusing and strong light confinement, well below the diffraction limit. Table 1-1 below shows the minimum hole diameter that a large array of different research groups has reported for microspherical particles at different laser wavelengths.

Table 1-1 lists some of the fabricated nanoholes related to this work at different wavelengths using both SiO_2 and PS microparticles.

Wavelength (nm)	Material	Sphere diameter (μm)	Hole diameter (nm)	Reference
400	SiO_2	0.97	250	[135]
532	SiO_2	5	1000	[128]
355	PS	0.5	170	[129]
515	SiO_2	1.3	340	[118]
800	SiO_2	5	2000	[124]
515	SiO_2	1.3	400	[15]
248	SiO_2	3	400-500	[130]
800	SiO_2	1.7	400	[136]
248	PS	1	350	[122]
248	SiO_2	0.97	400	[131]
400 800	PS PS	0.3 1.7	200 400	[137] [137]
532	SiO_2	0.8	300	[111]
800	PS	0.45	150-190	[123]
193	SiO_2	4.6	1000	[126]
193	SiO_2	2.5	1300	[132]
193	SiO_2	2.5	1000	[138]
193	SiO_2	1	300	[133]
PS – Polystyrene SiO_2 – Silica				

Two types of an excimer laser, ArF and KrF, are widely used in high-resolution photolithography machines, such as materials surface modification, due to the ability to modify the surface morphology and the electrical conductivity of polymers with spatial resolution on a nanometre scale [80], [139]. The 193 nm and 248 nm excimer lasers are commonly used for these applications. More specifically, Photons for 193 nm ArF and 248 nm KrF excimer lasers have the ability to make the ejection of materials from solid surface viable and transfer their high energy into bulk materials [24].

There are two mechanisms to explain the one-step material removal process; firstly, the occurrence of photochemical ablation at the stage when the laser photon energy is

absorbed, and chemical bonds are broken; leading to the removal of materials without thermal effect. Secondly, photothermal ablation where the material surface is heated and the conversion of the laser energy is reached by having a lattice vibration energy in the form of melting and vaporisation [140].

Ideally, the size of microstructures that can be used with a KrF laser is approximately 0.25 nm. ArF lasers have higher photon energy at 193 nm (6.4 eV) [59], compared to KrF, which has a photon energy of 5 eV at 248 nm [141]. Therefore, smaller structures of 0.20 nm can be used with an ArF laser. Hence, the direct disintegration of the material can occur at the molecular level with minimal thermal effect. Finer structures can be obtained due to the minimal thermal effect generation via this process.

Most importantly, better processing of soft materials such as polymers is made particularly feasible with an ArF excimer laser and a decrease of the wavelength used in lithography improves the resolution [31, 73]. Due to these features, ArF (193 nm wavelength) was chosen in our study. Today, advanced lithography is implemented using excimer lasers, having a wavelength of 193 nm, despite the prediction that extreme ultraviolet lithography will be the lithography source of the future (EUV with a wavelength of 13.5 nm) [17, 142]. EUV is still under development to address the current challenges, therefore, it will be some time before EUV takes over. Since it was first proposed in 1988, EUV lithography has been the subject of numerous intensive studies. Thus far, many technological challenges have been overcome, but many improvements are needed for practical application [143]. There are still three issues to be solved before this technique can be applied in mass production: a light power source resists, and mask infrastructure. Among these issues, to make such a lithography tool, economical production capacity and producing a stable light source are the most difficult issues to be solved [144].

1.7 Laser Structuring of optical fibres

The basic structure of a lensed optical fibre (LOF) for an optical probe is shown in Figure 1-5. It can be seen the input beam from SMF is expanded before being focused by the lens, to provide an effective light-gathering power to the fibre lens.

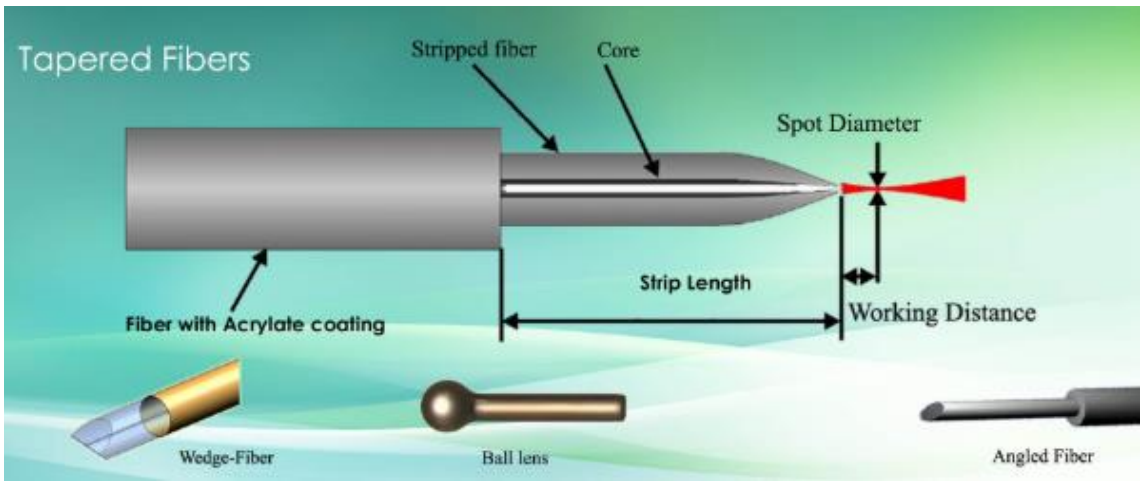

Figure 1-5 Schematic diagram of a lensed optical fibre structure and images of the micro-lensed optical fibre [145].

Optical fibres (OFs) are a waveguide for light, operating on the principle known as total internal reflection [146]. The core is an important component of OFs which is usually prepared from glass and surrounded by another glass or plastic layer, called cladding. Traveling through the core by repeatedly bouncing off the cladding is what distinguishes the light behaviour in a fibre-optic cable [42]. Low loss OFs were first proposed in the 1960s, following a growing demand for fibre in response to the progress in related technologies and calls for great efforts to push forward fibre-based technology [42]. Due to the excellent properties of optical fibre devices, which include compact structure, low loss, wide bandwidth, and immunity to electromagnetic interference, optical fibre devices have been intensively exploited in many fields, for instance, enhancing related technology, such as the sensitivity of optical sensing, the resolution of optical imaging and many others [44]. Typically, a more powerful optical fibre is yielded by having better confinement. [147]. OFs are biocompatible, mechanically resistant, and cheap various strategies have been applied in an attempt to compare and determine the best strategy to achieve efficient coupling of an optical fibre with a light [148]. If the fibre-core area is smaller than the source emitting area, then high efficient coupling can be achieved, this is known as the law of brightness. However, if the fibre-core area larger than the emitting area of the source, low coupling efficiency can be produced [149].

There has been a strong motivation in recent years for the miniaturisation of optical traps. One example is the ability to use lab-on-a-chip setups. Miniaturised optical traps do not feature large microscope objectives; instead, they utilise OFs [150]. Efforts to obtain more

efficient coupling of light from a laser continue for various applications, such as links for optical fibre communication systems. Ball lenses are one of the physically simplest and most economical micro-optic elements to fabricate and mount [151]. These systems utilise lenses, in both single and multielement assemblies. Such devices have been actioned to perform coupling tasks economically, efficiently, compactly, and without alignment complexity.

Micro-lenses grafted to the end of an optical fibre was first envisioned for improving the coupling between light sources and OFs. As the cost of low loss OFs decreases, the potential applications have been ever increasing. In addition to optical communication, other possibilities include power transmission, medical endoscopy, optical fibre sensors and the measurement of the current [152]. For decades, optical fibre processing relied on conventional heating methods such as filaments or electrodes [153]. Laser heating was a known alternative since the first industrial application that used carbon dioxide (CO_2) laser to cut materials in 1971[154]. Since then, carbon dioxide laser (CO_2) laser sources have sparked commercial interest in the optical fibre processing.

A CO_2 is the optimal heating source for fibre lens manufacturing due to its cleanliness, lower maintenance, and long term consistency [155]. Different parameters including laser power, frequency, duty cycle, irradiation time and rotation speed of optical fibre can be chosen for different materials to obtain an optical fibre microlens [156]. Photolithographic techniques have been used to fabricate microlenses onto the end of single fibres. Cohen [157] first reported the idea of using a microlens to significantly improve the efficiency of coupling a laser diode to an optical fibre. Cohen's fabrication process is more precise than Bear's [158] for controlling the size of the lens geometry; however, Bear's is much simpler. Bear has shown that his process can produce a microlens using the light of 632.8 nm or 775-nm wavelengths without going through the development process.

In 1975, the first fabrication of microlensed fibre was reported by Paek and Weaver [159] ; they described the feasibility of using a CO_2 laser to form a hemispherical lens on the end of a fibre. The process includes a novel two-stage fabrication method utilising a CO_2 laser source operating within continuous wave mode. During the first step, the fibre is heated with the laser and subsequently elongated until the fibre splits. In the second

step, the micro-lens (120 μm diameter) is fabricated by melting the fibre (250 μm core diameter) tip with the laser while it is being rotated. Using this CO_2 laser melting method, rod microlenses can be fabricated, as reported by Calixto *et al*. [22]. They used microlenses to form images, not to feed light into the fibre or to focus it.

Grellier et al, in 1998, reported a model of heat transfer within an optical fibre which incorporates the above effect and also the temperature dependence of the several parameters of fibre [160]. In 2015, the technologies for design, fabrication, and application of lensed fibres of many different types were investigated by Zheng [52]. Ball lens (679 μm diameter) was fabricated by heating single mode fibre (80 μm core diameter) which is also referred to as an axicon shaped fibre lens (10 μm diameter) from 125 μm diameter of single mode optical fibre.

In order to increase sensing performance, research based on a combination of fibre taper techniques has been reported in the literature. This involves modifying fibre ends into various forms. Examples of such are spherical [159] or sharp tapering of the fibre end [155, 161]. For the case of the taper optical fibre (TOF), the mechanical alignment must incorporate greater precision as the coupling efficiency becomes more intense as a function of the spatial alignment. Alignment tolerances are higher for other types of lensing systems. During taper fabrication, the heat source used is usually a flame or a carbon dioxide (CO_2) laser, which produces radiation at 10.6 μm [58].

The propagation of light through the OF core can be made to interact with the medium surrounding it, by removing the cladding, using the method of either etching or tapering the fibre. in 2007 Chandani et al.[162] reported a sensor in which the fibre cross-section has been etched to a D-shaped profile. Kieu et al. in 2006 [163] describe a biconical fibre taper sensor. In a biconical fibre taper, the diameter of single-mode fibre (SMF) reduces over a short distance to form a tapered waist then the fibre diameter increases back to its original diameter after the waist. Shabaneh et al. in 2015 investigated the tapered optical multi-mode fibre tip coated with carbon nanotube (CNT), which is drop-casted and annealed at 70 °C to enhance the binding of the nanomaterial to the silica fibre tip [164].

The TOF is created by heating the end of the fibre to its melting point, rather than stretching. There is an advantage of tapering the fibre in comparison to etching because it is easy to manage the interaction of the transmitted light with the surrounding medium. With the propagation of light on the fibre within the non-tapered region, the energy is confined within the fibre core. However, once the light reaches on the diameter taper waist where it is smaller, the evanescent field of the propagating mode extends into the surrounding environment for a distance [52] of approximately 0.5 μm and is no longer confined.

A wide range of applications in telecommunications, medicine, and biochemical sensing [58] have been attributed to the tapered OF properties of small size, low-cost, no interference with electromagnetic radiation, high sensitivity, and ability in designing distributed sensing systems. The feature of sensitivity to the local optical properties outside the fibre, or the tapered section of the optical fibre, forms the basis for the use of a fibre taper as an optical sensor [62], using either a CO_2 laser, which produces radiation at 10.6 μm or a flame as the heat source employed during taper fabrication [63].

Fibre optics has many beneficial applications due to its resistance to electromagnetic fields (electromagnetic interference), and slight and sometimes no power loss. On the one hand, standard optical fibres are primarily used in telecommunications, sensing, imaging, and other fields. Tapered optical fibres, on the other hand, maintain properties that standard fibres may not suit when it comes to some applications [47]. A novel and emerging platform for exploring fibre-optic technology on the micro/nanoscale are the Optical microfibres and nanofibres (MNFs). In recent years [56] active devices such as lasers, optical sensors, passive micro-couplers and resonators have been reported as variable technological applications. Consequently, large evanescent fields for high sensitivity, high Q-factors for low detection limits, and corresponding small resonant bandwidths for good wavelength selectivity are provided by optical fibre tapers [75].

There are several significant properties and opportunities offered by the micro /nano optical fibre (MNF) when compared with conventional optical fibres. Below are some interesting characteristics:

i- MNFs have the potential for compact circuits and devices with smaller footprints, faster response, and lower power consumption as a result of the tight optical confinement, small allowable bending radius, and small mode area [44].

ii- The ability of the MNFs makes them highly favorable for optical sensing due to the strong evanescent field offering strong near-field interaction and surrounding environment [64].

iii- MNF has higher sensitivity to change the momentum of photon guided through mechanical vibration or displacement due to its small mass or weight. Hence, the MNF has the potential for realising compact optomechanical components/devices and for triggering evident photon-photon coupling or conversion in these tiny fibres [65].

Different types of lensed fibre have been fabricated by using CO_2 laser, and a few examples that are related to the present work are investigated and illustrated in the table below (see

Table 1-2).

Table 1-2 shows different types of micro lensed fibre fabricated by micromachining technique

Wavelength (μm)	Fiber Diameter(μm)	Microlens type	Microlens diameter(μm)	Spot diameter(μm)	Reference
10.6	125	Taper	25		[165]
10.6	125	Sphere	116		[166]
10.6	400	Sphere	1000,750		[167]
10.6	400	Taper	20		[167]
10.6	250	Sphere	120		[168]
10.6	330	Taper	5		[169]
10.6	80,125	Sphere, taper	679,8	137, 2.4	[155]
10.6	300	ball	1008	201	[155]
10.6	125	sphere	150	20	[155]
10.6	125	sphere	26	4.4	[170]
10.6	125-200	sphere	150-300		[171]

Several methods have been reported for the fabrication of microstructured fibres. The advantages and disadvantages of each fabrication method can be dependent on the factors including, the type of lens it can fabricate, cost-effectiveness; throughput, reproducibility, and ease of implementation determine the advantages and disadvantages of each fabrication method. None of the single fabrication methods is versatile enough to achieve all the different types of required structures for several applications. It is therefore essential to select the suitable fabrication technique to fabricate the structures that are required for each specific application. A one to one comparison of these techniques would not be reasonable, because the fabrication techniques were developed for a different application. Some of these techniques are shown below:

1.7.1 Arc discharge technique

A widely used technique for fibre splicing is Arc discharge. Microlensed fibres fabricated, on the other end of coreless silica fibre (CSF), use this method in a commercial fibre fusion splicer (see Figure 1-6) [172]. Holistically, the tip of the optical fibre melts during fusion arc discharge as a result of the thermal. The cause of the melted portion to become a rounded hemisphere is surface tension and diameter is determined by the distribution of heat along with the amount of material above the glass melting temperature. The advantage of this technique is that long working distance microlens can be fabricated,

suitable for high-peak-power pulsed laser applications that are easy to use and inexpensive. However, the drawback is that it is unsuitable for batch fabrication, manipulation is more difficult when a smaller silica rod is used and low reproducibility and low fabrication efficiency can be observed as well [17,174].

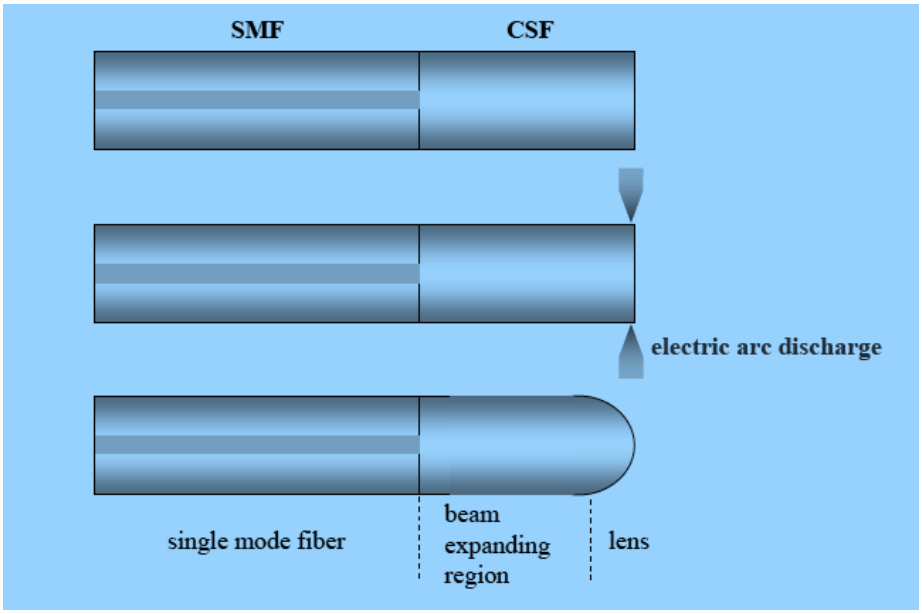

Figure 1-6 Schematic diagram for fabricating lensed fibre. A piece of coreless silica fibre (CSF) is fusion spliced to a single-mode fibre (SMF), and a lens is fabricated on the other end of the CSF using the electric arc discharge of a conventional fusion splicer [172].

1.7.2 Polishing technique

Polishing is another technique to approach and fabricate a microlensed fibre and is usually combined with techniques such as chemical etching and fusing in order to obtain the desired structures [175]. Manual polishing is appropriate for certain micro-structured fibre tips that are characterised with simple shapes, e.g. a wedge. In most cases to achieve fibre tips with complex microstructures, a fibre polisher or beveled is used (Figure 1-7). Having single-step fabrication, axion wedge and polygon pyramid tipped fibre are advantages of this technique. Noticeably, lens fabrication does not depend on the nature of the fibre that is purely a physical process. Other benefits involve smooth surface, fast fabrication speed, and high reproducibility. An observed drawback it's difficulty in fabricating traditional spherical surface and complex-shaped lenses, as they require computer-assisted control and a fibre beveled [173].

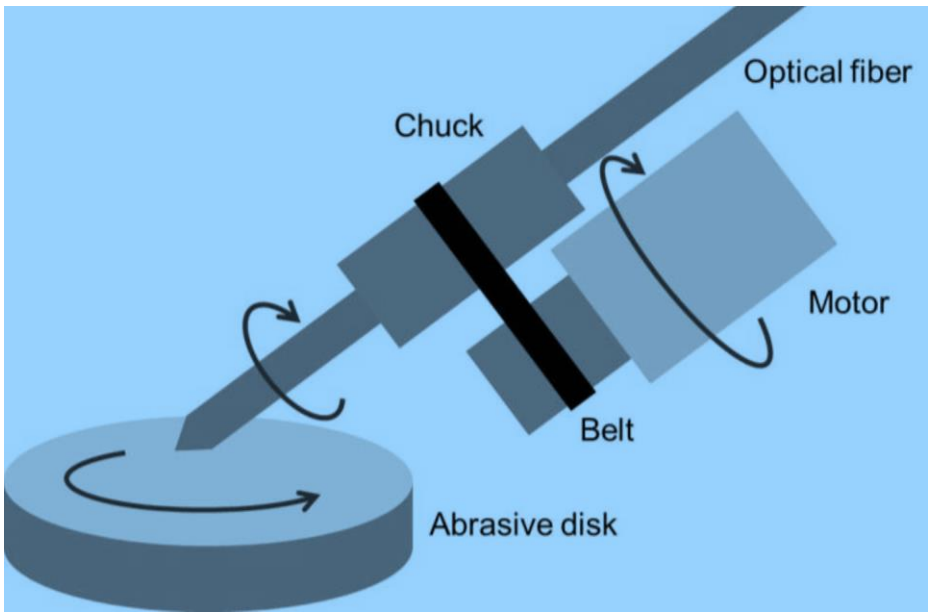

Figure 1-7 Schematic diagram of the polishing technique. Insert, enlargement of the contact zone, the optical fibre tip, fixed onto a motorized beveller was pressed against an abrasive disk to fabricate a microlensed at the end of an OF [173].

1.7.3 Chemical etching technique

For the purpose of processing dielectric materials, chemical etching has been widely used utilising buffered hydrofluoric (HF) acid. This is an easy and low-cost chemical method to produce taper fibres. Cladding is removed by etching with an HF solution and then the fibre core diameter is reduced using a low concentration of HF. The following three categories are the main divisions of the fabrication method: chemical etching selectively, the protection layer method along with tube etching. In chemical etching, as a common and useful method to fabricate such probes, the schematic of the etched fibre includes two parts as shown in Figure 1-8, which illustrates part A, immersed into coverage liquid (oleic acid) and part B immersed in etching solution (HF acid). The vapour of HF acid diffuses into the oleic acid forming a concentration gradient. Here lower concentration gives out a lower etching rate. Therefore, part A is comparatively faster than part B in terms of the etching rate. The result yields that part B is etched to a filament and part A is detached to a trapezoid [176].

Some other merits of this technique are that it is suitable for fabrication in batch along with a process that is self-terminating involving the protection layer, using multi-step etching sharp probes (with nm radius curvature) and properties that can be tailored and fabricated. Multicore fibres can be etched to make multiple microlenses. However, there

are also drawbacks. Though a microlens is self-aligned, flexible, and inexpensive, the etching time and the control of the shape of the fibre during the etching is a difficult task [173]. It is not possible to fabricate a traditional spherical surface due to the involvement of complex etching procedures for multistep etching. The process is sensitive to temperature; rough surface , which is produced by protection layer etching, and the etchant is highly dangerous etchant [176].

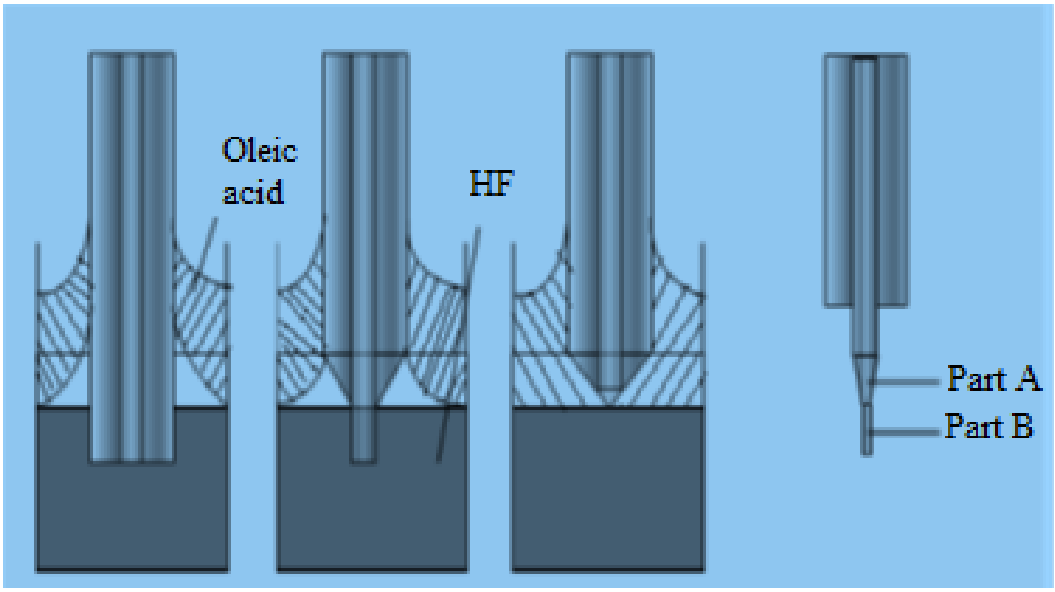

Figure 1-8 Principle of an optical fibre tip formation by chemical etching of. The conical shape is obtained by the regular reduction of the meniscus height related to a decrease of the tip diameter (B) and the reduced fibre (B) [176].

1.7.4 Focused ion beam milling method

Focused ion beam (FIB) milling is purely a physical process in which ions collide with the specimen and effectively become the reason for the removal of the material at the sub-micrometer level (see Figure 1-9). Hence, a micro-structure can be sculptured by effectively scanning FIB with specific energy illuminating a substrate with a pre-designed route using specific dwell time at each point. milling directly on the substrate, therefore no other preparation is required [177]. However there are some drawbacks; it is not suitable for batch fabrication, is an expensive method, and requires complicated non-linear modeling [173,177].

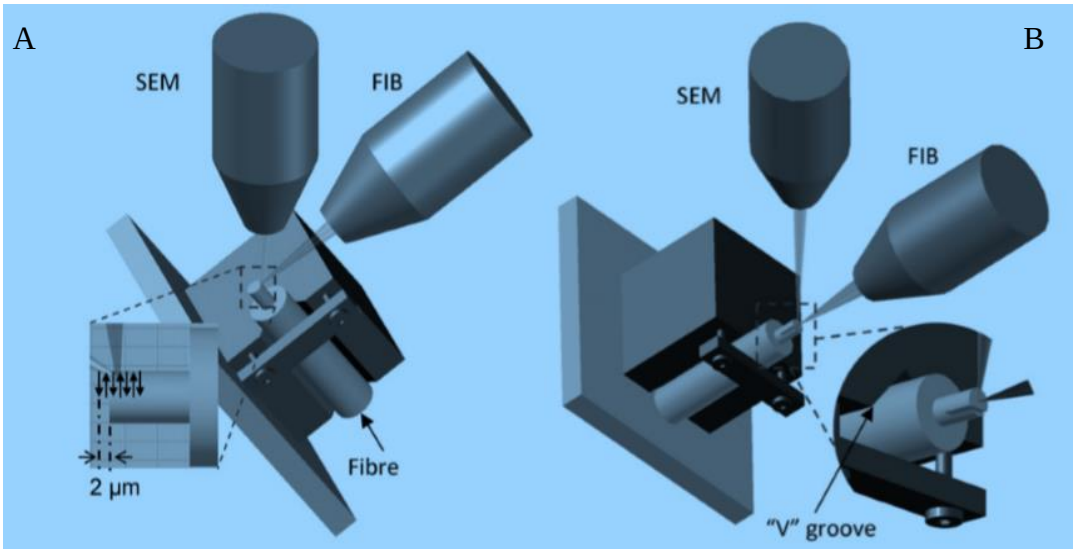

Figure 1-9 Experimental setup of the FIB machining process: (A) the fabrication of the Fabry–Perot cavity by side machining of the fibre; the incident ion beam is perpendicular to the fibre length direction; (B) fabrication of the 45◦ reflective mirror on the fibre end face; the ion beam is incident along the fibre axis [178].

1.7.5 Laser micro-machining technique

Reportedly two types of laser micromachining techniques, in which a CO2 laser is involved are one in which laser is utilised as a source of heating adopting a heating-pulling scheme [173]. Here fibre can be either pulled apart or it is cleaved at a required point prior to melting the tip to form a lens. This method gives sharp tips that are widely used as scanning probes for scanning near-field microscopy [167]. Second in which, a pulsed CO_2 laser is focused on the tip of a spinning fibre (Figure 1-10). The beam ablates the fibre tip by cutting and heating simultaneously. The shape of the lens is controllable by using the relative position and movement of the fibre and focus of laser. Using this type of laser micro-machining has several advantages when compared with the other techniques. It has high repeatability and predictability compared with other techniques [179]. To increase coupling efficiency, hyperbolic shaped micro-lens can effectively be fabricated. It is a long-established industrial application that is commonly used to process several materials because CO_2 laser systems are robust and cost-efficient. However, it is unsuitable for batch fabrication, has low reproducibility and low flexibility [179, 180].

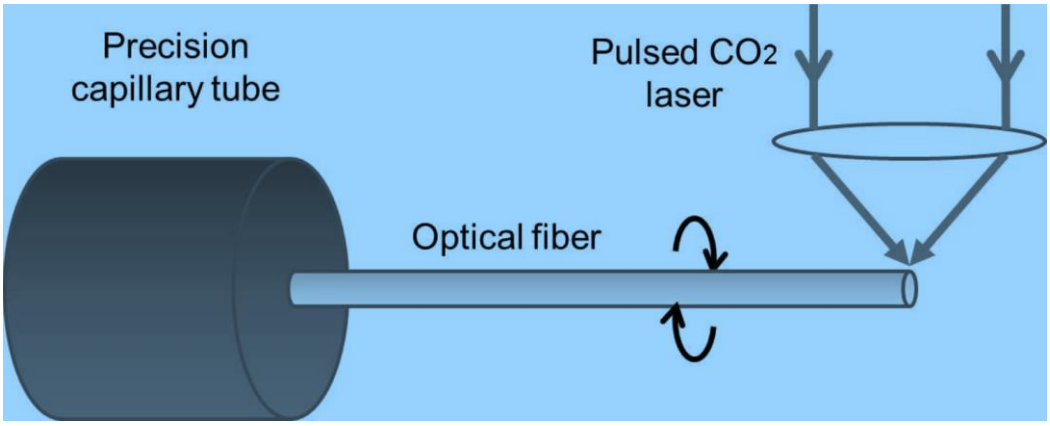

Figure 1-10 Schematic drawing of the fabrication of hyperbolic shape microlens on the tip of an optical fibre using a pulsed CO_2 laser [173].

The details of various microlensed fibre fabrication methods were discussed above. When selecting a suitable and workable method of microlens fabrication for specific applications, several factors should be considered including operating wavelength, output beam profile, optical breakdown threshold, fabrication cost, instrumentation, and throughput. The functionality of the lenses made at the end of a fibre can be characterised by studying the numerical aperture (NA), focus length, spot size, beam diverging angle, and propagation direction [155]. Due to the versatility of microlensed fibres, they can be designed for many different applications.

There is no best fabrication technique as each fabrication method has its own merits. Having said that, some specific requirements of each method depend on the field of application. Even though the field of microlensed fabrication has seen a lot of technological advancements over the past decade, there is still room for optimising these techniques in terms of reproducibility, flexibility, and throughput so that they would be commercially viable for various applications. Such commercially viable techniques would greatly aid fields like bio-medical optics in realising miniaturised fibre-based probes for endoscopic or handheld imaging and microscopy [173].

For laser glass processing, there is a limited choice of laser sources. In the UV regime, F_2 lasers operate at 157 nm and excimer lasers operate at 193 (ArF) and 248 nm (KrF), Through irradiation by these lasers, point lattice are produces and defects in the glass that cause strong absorption bands in UV regions [181]. Coupling energy into the glass via defects or near-band edge states, providing one approach for micro-machining glass or driving refractive index change on nanosecond or longer time scales [61]. In the IR

regime, there is only the CO_2 laser source that is working at 10.6 μm wavelength band. CO_2 lasers can be operated in both continuous and pulsed modes [23]. The use of a CO_2 laser has several advantages over a flame: first, it provides controllable heated-zone properties in a repeatable fashion. Second, it avoids the air turbulence production that is present when using a flame, which can influence the shape and uniform of the diameter of the lensed fibre region [54]. There are three fundamental aspects that one can engineer to develop a specialty fibre: glass composition, waveguide design, and coatings [182]. There are three most important components of optical fibers such as the core which is usually prepared from the glass. The core is surrounded by another glass or plastic layer called cladding which is characterized by a lower refractive index material compared to the core material [183].Glass optical fiber preform can be made from three mechanisms: modified chemical vapor deposition (MCVD), outside vapor deposition(OVD), and vapor axial deposition (VAD) [184].

The laser's interaction with the optical fibre material depends on several parameters related to the laser source (its wavelength and emission regime) and also the characteristics of the material itself [8]. On contact with silica glass, for example, that used in optical fibre fabrication, the 10.6 μm radiation of the CO2 laser is absorbed in the fibre surface [153]. Then two effects occur: (i) glass at the surface is raised above its melting temperature and (ii) heat is conducted into the bulk of the fibre. Pulses of longer duration and lower intensity will simply melt the glass, an effect that has been used to round the end of the fibre or to splice the fibre [185].

In this study, the laser micro-machining technique was chosen to fabricate lensed fibre. The CO_2 laser is chosen as a heat source for the optical fibres to provide a higher degree of flexibility than other methods. Using a CO_2 laser also to avoid probable contamination from the gases present in techniques that use open flames as a heat source [186]. A uniform CO2 laser beam is incident onto the fibre end face for a controlled duration. As soon as the fiber starts to melt, the laser beam is removed. This causes a melting of the fiber surface, which solidifies upon removal of the laser. The exposure energy and duration are key in producing an ideal surface [156]. In CO2 glass processing applications, using fibre which is generally made from fused silica. Fused silica is silica glass having a non-crystalline (amorphous) structure and it is created by melting high purity naturally occurring quartz crystals (silica sand). CO2 laser heating of fibre tips results in more consistent lens curvature over other techniques [185]. All of these optical-fibre-based trapping and manipulation methods provide many new possibilities, as well as new

insights for biomedical applications of biophotonics [187]. Recently, optical fibre tweezers have involved important attention in the optical trapping field because of their flexible manipulation, compact structure, and easy fabrication [188]. Different single and a multiple-cell can be trapped only by optical gradient force which provides a higher trapping efficiency to other methods [189].

1.8 Applications

Fields such as optics, electronics, photocatalysis, chemical sensing, photoelectron-chemistry, conversion of solar energy, biomedical detection and therapy, and environmental protection have seen the emergence of new applications owing to the unique optical and dynamic properties of nanomaterials [13]. For example, nanomedicine is a developing branch of nanotechnology that is mostly used for the targeted delivery of drugs for many types of cancer cells [190]. Fabricating micro/nanostructures by a laser have a wide range of applications in photonics, surface plasmon resonance (SPR), optoelectronics, biochemistry fields, micro/nanofluidics, biomedical applications, and associated fields [6].

The subwavelength focusing of light could provide numerous applications in nano-optics using a nanohole array. For example, by scanning the object under investigation across the focal spot, a single hot spot appropriately isolated by a mask may be used as a light pen for subwavelength imaging [81]. A sub-wavelength and high-intensity focus spot with a long effective length often characterises the generated photonic nanojet. Several optical and photonic applications utilise the photonic nanojet, including super-resolution white-light nanoscopy, low loss waveguides, optical nano-patterning, optical data storage, optical forces, optical tweezers, high-resolution optical microscopy, and laser surgery. As well as the photonic nanojet, there are enhancements of backscattering of light, Raman scattering signals, and photon fluorescence. Other applications include the detection of single nanoparticles and biomolecules.

In future biosensing applications, the employment of biocompatible microspheres can useful. Optoporation has been advanced as a promising alternative method, offering unique benefits over other methods of drug delivery [4]. In its standard form, nano-pores are created in the cell membrane by laser pulses that are focused by microlenses through the cell membrane.

An important application related to the results of this study is that focusing laser light produces a force that can be used to remove or trap selected cells or large tissue areas from living cell culture down to a resolution of individual single cells and subcellular components similar to organelles or chromosomes, respectively [3]. A current treatment issue is that drugs are not specifically targeted to cancer cells, so only a low amount of chemotherapy drugs penetrate tumour tissue and its cancer cells [191]. To reach all viable cells in the tumour, anticancer drugs must be delivered efficiently through the tumour vasculature, cross the cell membrane to kill cancer cells or prevent them from dividing. Therefore, the fabrication of nanojet which creates nanobubbles and nanoholes also lensed optical fibre which produces nanobeam laser opens the door to improve the efficiency of drug delivery systems and treatment of diseases, like cancer [190], [192].

An example of the application of this work in the future, is to use the nanojet that will be fabricated by micro silica particles and excimer laser (Chapter 3) to obtain sufficient laser energy density for the generation of membrane nanopores and thus improve the efficiency of drug delivery to inside cancer cells. Figure 1-11 shows the schematic diagram of controlled drug delivery by using nanojet. Figure 1-11.A and B shows nano-particles produce a nanojet incident on the cancer cell membrane to make nano-holes which enable direct delivery of the drug materials across the cell membrane into the cytoplasm. Figure 1-11.C shows how the nanonjet produces nanobubbles. Strong pressure distributions can be created by nanobubbles on the membrane surface of the cancer cell, pushing the drug into the cell.

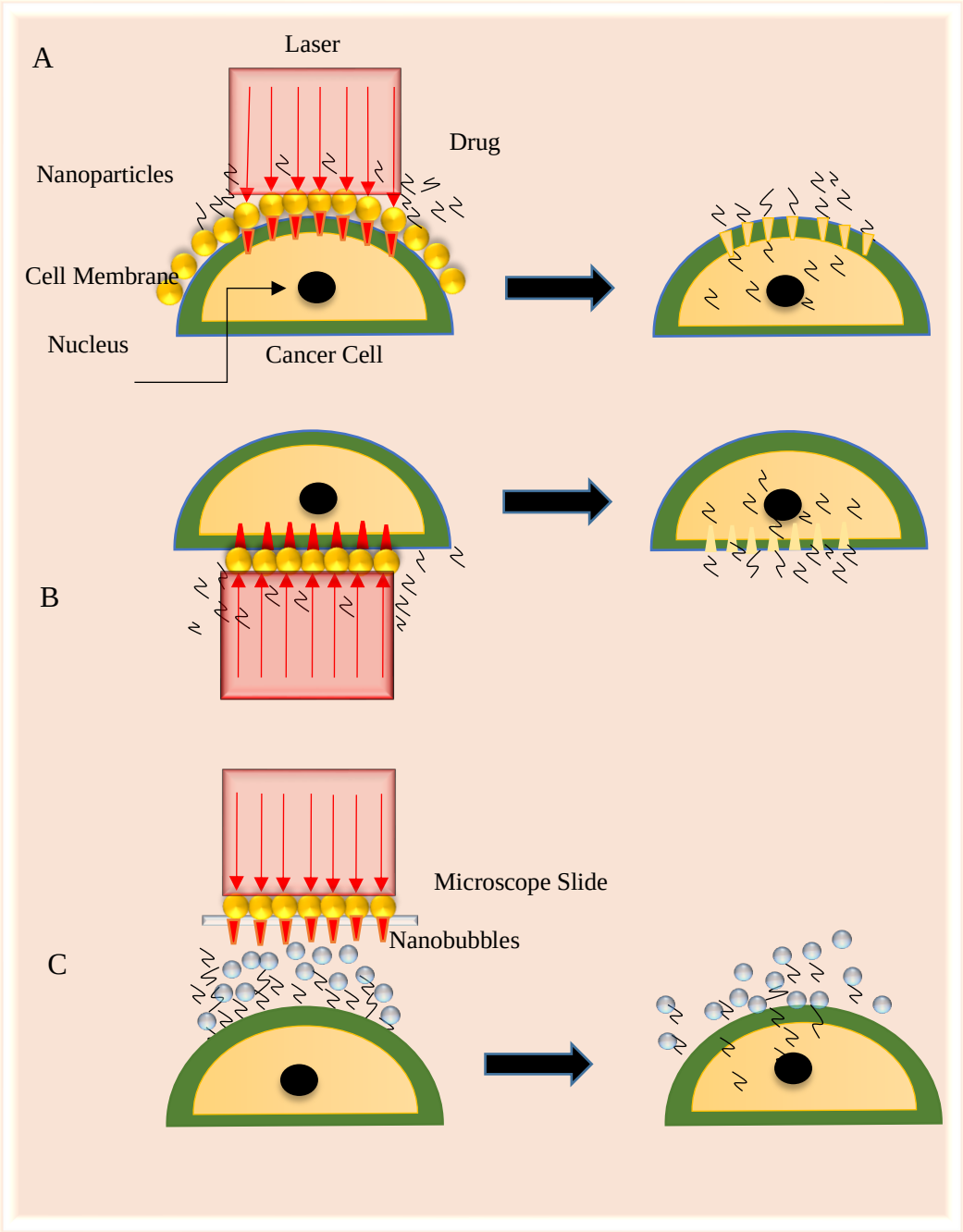

Figure 1-11. Nanojet drug delivery by creating nanoholes on the cancer cell membrane (top and midle). Nanobubbles deliver the drug by generating pressure on the membrane surface of the cancer cell (bottom).

Other applications of micro-lensed an optical fibre include ball and tapered fibre lenses that have been fabricated in this work (Chapter 4) are explained below:

An emergent field follows the concept of “lab-on-fibre.” Some examples of the “lab-on-fibre” achievement is a phase gradient plasmonic metasurface on the fibre tip and the

nanosphere lithography of the optical fibre end facet [77]. Another potential example can be found in works from Cusano and co-workers. A lot of potential of OF in textile fields such as decoration, fashion, and design, safety, therapy, etc. could be developed in terms of microlensed OF applications [53]. Below are some examples:

i- Key components in high-speed optical switches, MEMS system for optical networks, and high-power fibre laser systems for a touchless connection. Photonic resonances produced by Nonconducting materials can effectively be combined in order to design structures at a nanometric scale known as hybrid structures [61].

ii- Widely used in fibre laser systems is a ball-shaped end-cap to reduce the fibre facet damage threshold and the back reflection. End-caps can be of different types [155].

iii- Fibre and Laser Diode Coupling [193].

Many different sensing applications have used tapered optical fibres. Some examples are label-free DNA detection in real-time; Raman spectroscopic sensing; gas sensors magnetic field sensor, etc. [194,195]. To couple light to a microsphere, tapers have also been used, for environmental sensing systems [196]. The optical tapers used in the mentioned systems usually have diameters for the waist that is less than 25 μm and the overall lengths that are used are usually from 2 mm to 25 mm [195]. The biconical nonadiabatic tapered optical fibre has many favorable properties for optical sensing. These can be used in a biological setting for cell, protein, and DNA sensors. These types of biosensors are low cost, highly sensitive, and provide label-free detection [197]. Figure 1-12 A, B, and C show an important application of three types of micro-lens fibre fabricated in this work which can be used in the future as an efficient drug delivery device

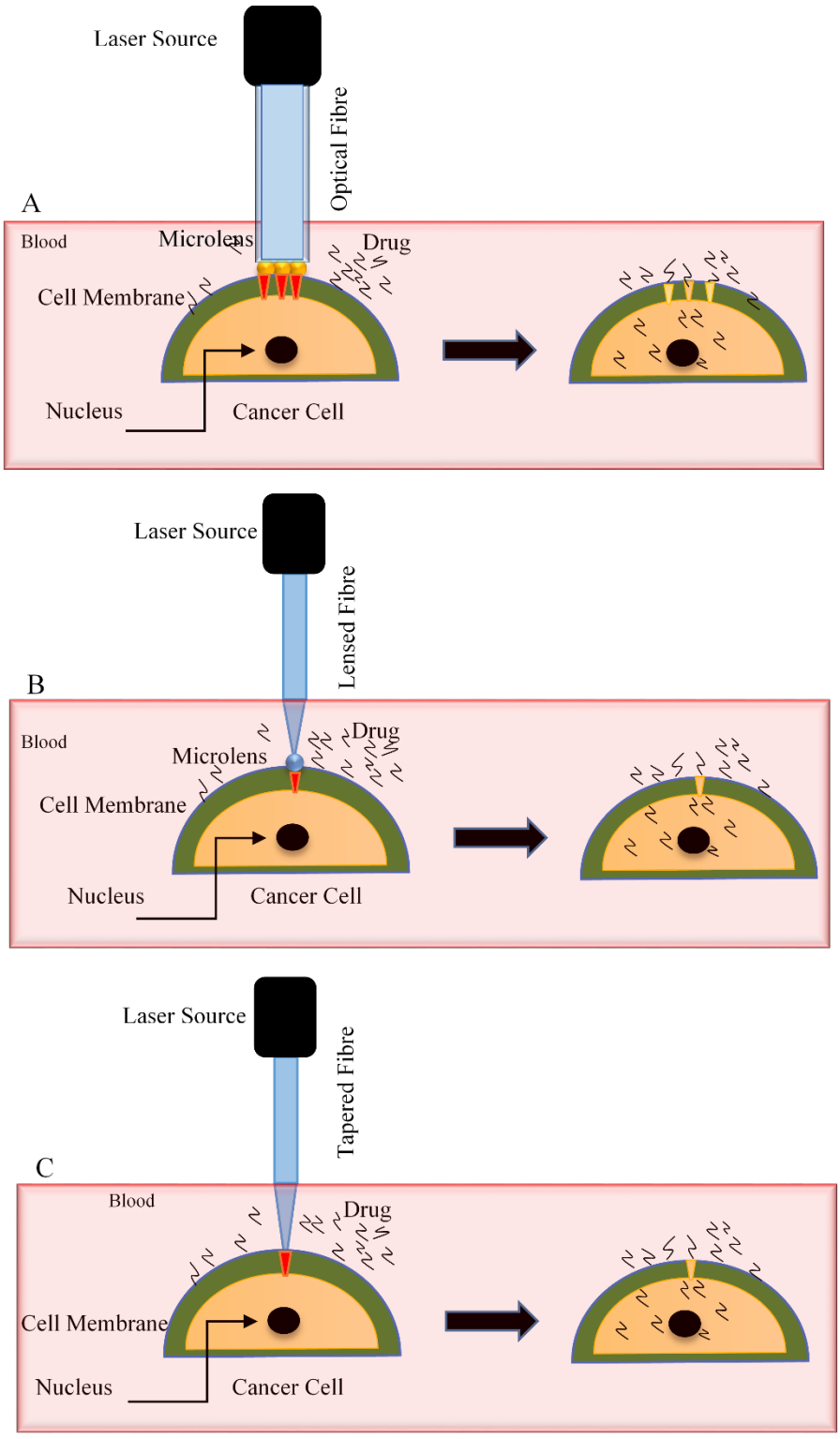

Figure 1-12 Drug delivery through membrane cancer cell by using three types of micro-lens fibre: (A) parallel photonic nanojet array generated by coating microlenses to the end face of an optical fibre, (B) micro ball lensed optical fibre, (C) tapered optical fibre.

Chapter 2 Laser ablation of substrate materials and their thermo-physical properties.

2.1 Introduction

In this chapter, polycarbonate (PC), polymethylmethacrylate (PMMA), negative photoresist SU-8, and chitosan are characterized in order to choose a suitable material as a substrate for soft nanolithography (Chapter 3). Polymers are large molecules, or macromolecules, which occur naturally in living things and can also be produced by chemical processes in the industry. Since a huge number of materials come under the name of polymers, several applications can be seen within the biological industry in which these materials can be used [198]. The choice of material depends on the glass transition temperature of the material (from literature), material optical properties, and ablation threshold with ArF laser (193 nm wavelength), which are investigated experimentally in this chapter.

2.2 Excimer lasers.

The word "excimer" is derived from two words: excited and dimer. In an excimer laser, the lasing medium is formed of diatomic molecules. When a diatomic molecule is in its excited state, it is stable, however, when the molecule resides in the ground state, it is unstable. [199]. This causes only a few dimer molecules to reside in the ground state, and therefore direct excitation from the ground state is not possible. Laser radiation is, therefore, achieved through varied indirect excitations by electrical discharge. A common excimer laser consists of a mix of argon and fluorine. When the mixture of fluorine and argon is excited in electrical discharge, the following happens [23]:

Electron attachment: $e + F_2 \rightarrow F^- + F_2$.

Excited molecule creation: $Ar^+ + F^- \rightarrow (ArF)^*$

Separation of excited molecule: $(ArF)^* \rightarrow Ar + F + Photon\ (193\ nm)$

Due to the electron attachment of the fluorine, $(ArF)^*$ can form through excited molecule creation. The molecule now, resides in the excited state, as the molecule relaxes down to its ground state, a photon is emitted. The molecule is unstable in the ground state, causing

the atoms to repel one another. Since the ground state is inherently unstable, the ground state population remains low therefore, population inversion is easier to achieve. Typical characteristics of excimer lasers include average power in the range of 200 W and pulse energy up to 2 J per pulse. Other types of excimer lasers include *KrF*, and *XeCl* [23]. Figure 2-1**Error! Reference source not found.** illustrates the graph for energy (eV) versus the atomic distance (nm). Here the lower curve displays the ground state and the upper curve displays the excited state.

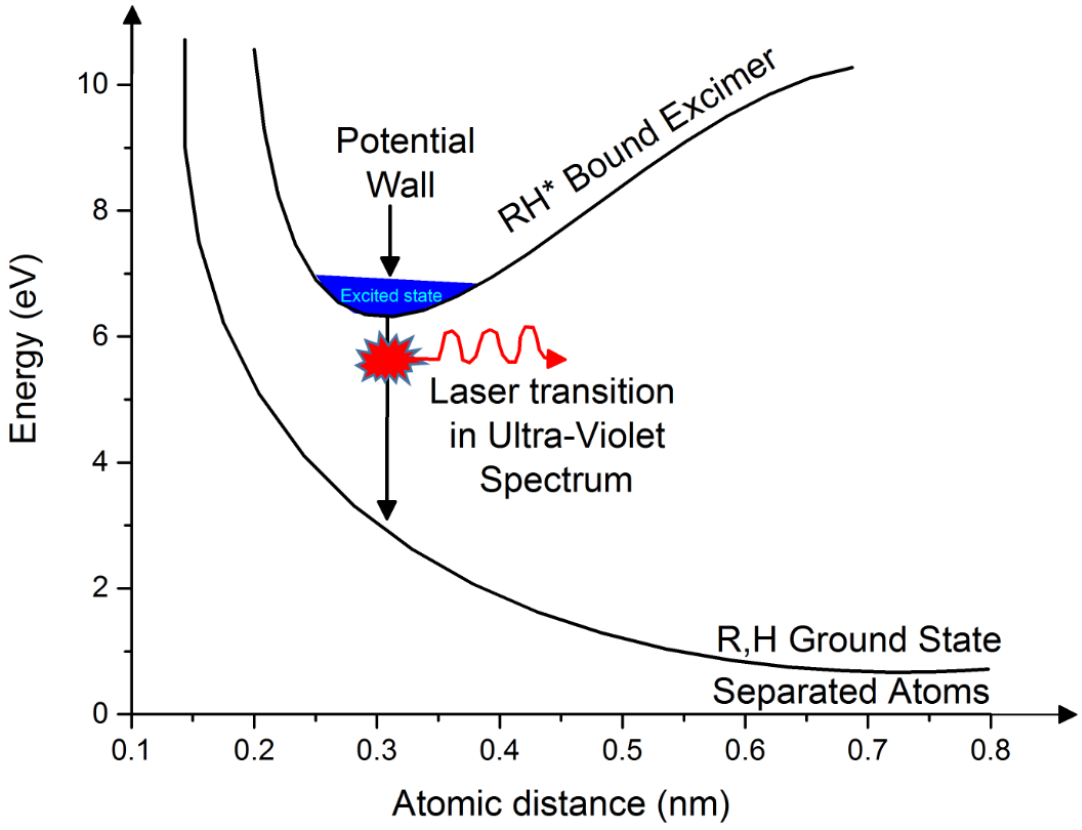

Figure 2-1. Energy scheme of the ground and the excited electronic states in an excimer laser [93].

2.3 Characterisation of ArF laser beam.

There is a growing interest in the importance of excimer laser beams characterisation and beam delivery optics. The ability to have high stability and accurate control over their characteristics allows them to be used in several applications. Figure 2-2 shows the near field for an ArF excimer laser (193 nm Novaline, lambda Physik). The dimensional energy density distribution in the near field can be used efficiently in the evaluation of beam parameters. The profile along the vertically aligned long axis displays a top-hat profile, whereas, at the horizontally aligned short axis, the energy distribution has a near-Gaussian shape [200]. A flat-top beam allows for a very uniform distribution of the energy across a given area.

The temporal pulse shape of 193 nm ArF laser (Lambda Physik LPF 202) is 11.5nm at FWHM as shown in Figure 2-2.

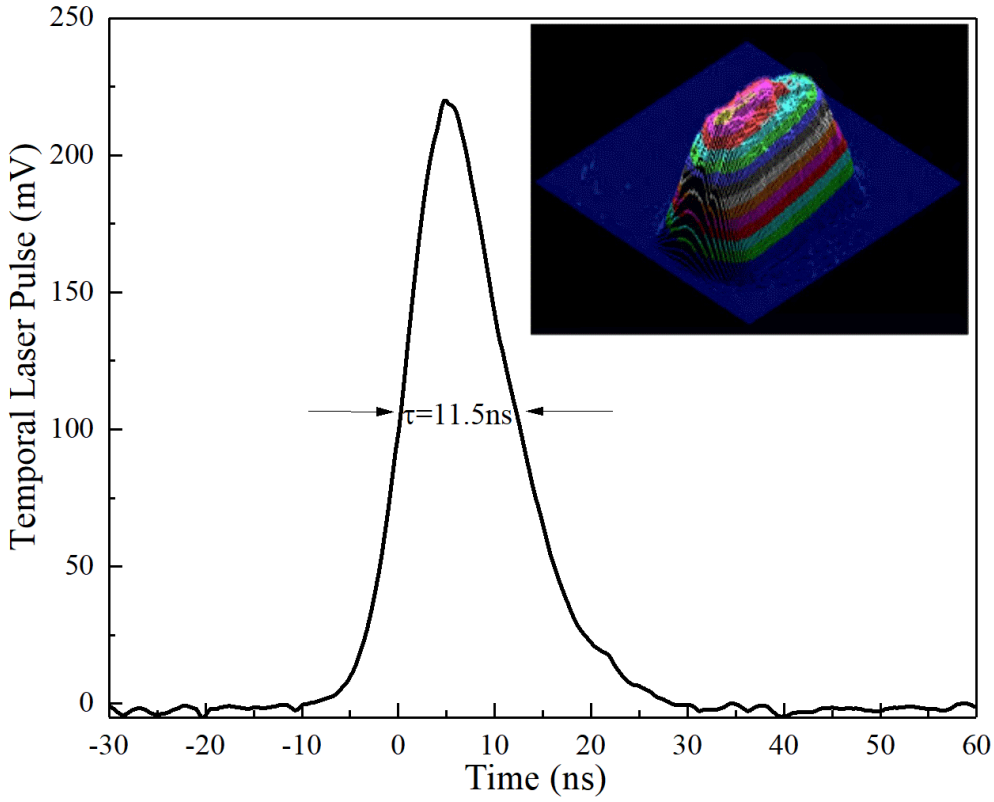

Figure 2-2 Near-field profile of an ArF laser (193 nm) recorded simultaneously with a camera-based measurement system. The evaluated second-moment beam width in horizontal and vertical directions are indicated. The pulse shape of ArF laser (λ=193 nm). A fast photodiode (Hamamatsu, S7911) was used to investigate the data, pulse duration, τ=11.5ns.

2.4 Materials

There are emerging new processes that use polymers as functional and structural materials. Recently, polymers have become more popular as a substrate material in the field of micro/nanostructuring materials because they are low cost and, in general, compatible with chemical and biological applications [24, 201]. A wide range of polymer materials has been evaluated for the fabrication of optical devices. Because of their good plasticity, high optical transmission, and mechanical properties, polymer-based optical materials are commonly used in the fabrication of optical waveguides, polymer fibres, and micro-nano optics [90]. The development of different processes and protocols to control polymer-based MEMS and properties such as mechanical, optical, magnetic, and electrical has been driven by the growing interest in polymer-based MEMS. Also, intense studies have focused on the surface chemistry, the resolution attainable throughout optical lithography,

and the topographic features [202]. Common examples of polymers that are processed by the so-called ‘soft lithography’ fabrication scheme and are the most commonly used polymers include polymethylmethacrylate (PMMA), polycarbonate (PC), a photoresist (SU-8), PI (polyimide) plastic resin, chitosan, and poly dimethyl siloxane (PDMS). The choice of material is guided by the material properties and feasibility of fabrication [203].

2.4.1 Polymethyl methacrylate (PMMA)

PMMA has been used as a polymer host because of its high transparency in the visible region as a favored solid electrolyte in the electrochromic window. The chemical notation for this material is [CH2=C(CH3) COOCH3] as shown in Figure 2-3. It is written in this format, rather than the more common chemical notation [C5H8O2], to show the double bond (=) between the two carbon atoms in the middle. In micro and nanofabrication, PMMA is widely used as a very high resolution electron beam resist,[204] and extensively used for both electron beam lithography and x-ray lithography, however, it is not used as a photoresist due to its insensitivity to incident light of wavelengths of 280 nm and longer [205]. PMMA is inexpensive, non-toxic, widely available, easily processed, and different molecular weights can be obtained [206]. It also has high sensitivity, exceptionally high resolution, and moderate resistance to wet and dry etch environments. Another advantage of PMMA as a resist is that it has high optical transparency (it is somewhat more transparent than even ordinary soda-lime glass) [204].

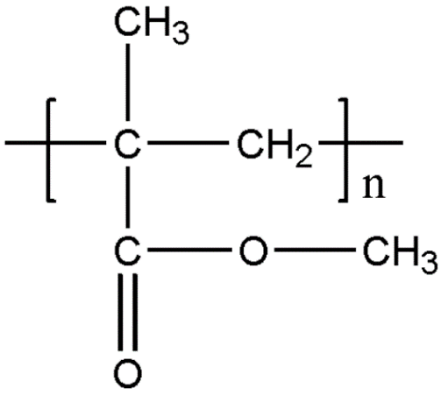

Figure 2-3 Chemical structure of PMMA [207]

2.4.2 Polycarbonate (PC)

The General PC is polymerized from bisphenol-A with carbonyl or diphenyl ether. PC is similar to styrene in terms of its optical properties such as; transmission, refractive index, and dispersion. PC, however, has a much broader operating temperature band of -137°C to 120°C. For this reason, PC is the "flint" material of choice for systems that are required to withstand severe thermal conditions [208]. The chemical structure unit of polycarbonate is illustrated in Figure 2-4. It contains 14 atoms of hydrogen, 16 of carbon, and 3 of oxygen [29]. Due to their unique physical properties, the PC substrates have a variety of applications in industries [30]. PC is often used in the fabrication of microfluidic devices, as it is highly durable, strong, temperature resistant, have low density, and carries good optical properties [32]. Other benefits of PC are its high impact resistance, lightweight, low absorption of moisture, good machining properties, high glass transition temperature (Tg =145 ^{o}C), a high melting temperature of 314 ^{o}C, and excellent optical transparency.

PC is classified as a thermoplastic (as opposite to thermoset), due to the way the plastic responds to heat. Thermoplastic materials become liquid at their melting point (155 ^{o}C for PC) [209]. A major trait of thermoplastics is that they can be melted, cooled, and reheated again without significant degradation in the physicochemical structure. Instead of burning, thermoplastics like PC turn to a liquid, which allows them to be easily injected into moulds and hence recycled [210].

In contrast, thermoset plastics can only be heated once (typically during the injection moulding process). After a thermoset material has been heated, the chemical structure changes, and cannot be reversed. This causes the material to burn when it goes through the heating process a second time. Thermoset materials are, therefore, poor candidates for recycling. When PC is exposed to UV light the material gradually changes from transparent to yellow it, therefore, requires a UV-resistant coating. In contrast, PMMA is inherently stable towards UV light. Another drawback of PC, therefore, its poor resistance to certain organic solvents, which it wash off the UV-resistant coating [211].

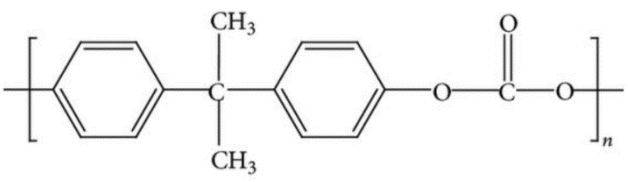

Figure 2-4 Chemical structure unit of polycarbonate [212]

2.4.3 Photoresist SU-8(GM1060, Gersteltec Sarl.)

The photoresist SU-8 was invented by IBM, due to the continuous development in lithography and micromachining [213]. It is high contrast, epoxy-based photoresist. It was designed for micromachining and other microelectronic applications in which a thermally stable image is desired. It has high chemical and thermal stability, as well as good mechanical properties. SU-8 is very well suited for imaging near-vertical sidewalls in very thick films because it has a very high optical transparency above 360 nm [214]. Therefore, it is an ideal candidate for applications where the material will be permanently installed [215]. The first publication using SU-8 as a material for microfabrication was published in 1997 [216], highlighting the potential of the said negative photoresist in respect of the near-UV structures of the thick layers and the production of components of high aspect-ratio. SU-8 quickly became a cheap alternative to X-ray LIGA for applications where there is no requirement of the extreme aspect ratios and precision. The early adoption of SU-8 in the industry was due to its wide range of applications made possible by the possibility to pattern easily multi-level structures of SU8. SU-8 demonstrates a much higher absorption coefficient with shorter wavelengths. Therefore, in lithography, a light source with broad bandwidth tends to result in overexposure at the surface of the resist layer and underexposure at the bottom of the resist layer [106].

In all application areas of micro-technology, a wide range of components have been manufactured using SU-8 and the interest in SU-8 has not decreased in the last 15 years, especially in the MEMS community [216]. The micro-fabrication community has paid a lot of attention to the epoxy-based negative-tone resist SU-8 right from its introduction. This material has been chosen due to several reasons: SU-8 shows stable mechanical, thermal, and chemical characteristics, it can be coated in thicknesses greater than 1 mm, and can be patterned to make tall microstructures with high aspect ratios. In conventional photoresists, these are unprecedented characteristics. Applications including microcantilever in scanning force microscopy, optical waveguide, microfluidic channel, and neural probe [108], to name a few, have used the unique characteristics of cross-linked SU-8 as a sacrificial micro-mould for electroplating as well as final microstructures. It is used in many lithography techniques, including the conventional ultraviolet (UV) lithography. The chemical structure of SU-8 is a single molecule that contains eight epoxy groups in a bisphenol, as is illustrated in Figure 2-5.

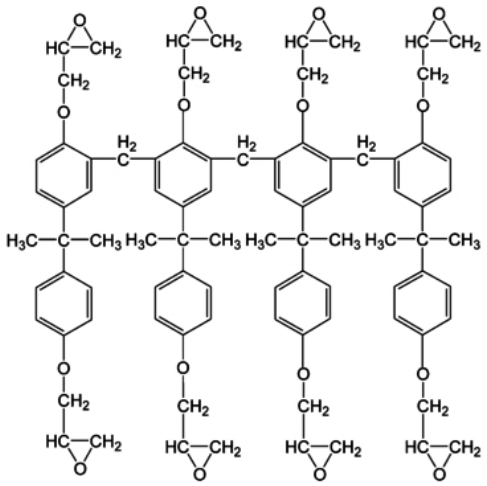

Figure 2-5 SU-8 chemical structure [217]

2.4.4 Chitosan

Chitosan is found in nature as chitin. Several natural products to obtain chitin have varying amounts of chitin for each, for example, the concentration of chitin in bio-creatures are crab 85%, shrimp 58%, mosquito 20%, butterfly 60% [218]. Hoofs and feet of animals also contain chitin. While Chitosan is a derivative of Chitin in the form of Deacetylation Degree (DD) [219], the degree of acetylation varies between users. The molecule is insoluble; however, by moving enough acetyl groups (CH_3-CO), the molecule can be dissolved using the most diluted acids. This process is termed deacetylation, it's this process that transforms chitin to Chitosan, using the deacetylation degree over 60% [220] The degree of deacetylation is calculated as [221]:

$$DD = \frac{100 n_{Gl}}{n_{Gl} + n_{Gn}} \tag{2.7}$$

where n_{Gl} represents the average number of units of D-glucosamine and n_{Gn} gives the average units of N-acetylglucosamine. Chitosan is a copolymer derived from D-glucosamine and N-acetylglucosamine [222]. Therefore, referring to equation (2.7), the DD is a ratio between the units of N-acetylglucosamine and D-glucosamine. Figure 2-6 illustrates the structure of chitosan, showing a semi-crystalline polymer in the solid-state.

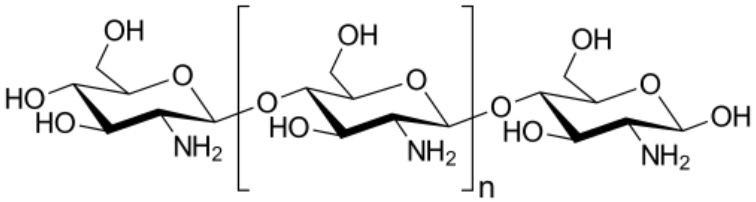

Figure 2-6. Chemical structure of Chitosan [223]

Chitosan contains NH_2 functional groups, which allow it to be used for applications in medicine and pharmaceuticals, as shown in Figure 2-6. Chitosan is suitable for many biomedical applications, as it is biodegradable, biocompatible, and non-toxic [224]. Chitosan also benefits from a linear polyamine, reactive amino groups, and reactive hydroxyl groups available in many transitional metal ions.

Structural degradation has different mechanisms; hydrolytic, oxidative, thermal, and ultrasonic, all of which are receptive to chitosan [225]. Chitosan provides an active surface for photochemical reactions. Chitosan's surface has positive amino groups, which are important for photochemical reactions. The special properties of chitosan films are due to the amino groups allowing chitosan to be suitable for various reactions, which include biological reactions occurring on the chitosan surface [226].

Nanolithography requires excessive heat and a chemical etchant, which could damage sensitive substrates during device fabrication. Soft lithography processes include: i) the process of microfabrication in which a soft polymer is cast onto a mould containing a microfabricated pattern; ii) polymers, i.e. PI, PMMA, PC, etc; iii) materials for Mold; SU-8, thick film positive photoresist. The advantages of soft lithography include: 1. It has the capacity for rapid prototyping; 2. easy fabrication without the need for expensive equipment; 3. tolerant process parameters. Both PC and PMMA have similar advantages. The choice of the material depends on the application, as well as the feasibility of fabrication [206]. SU-8 is one example of polymers that are usually processed by the so-called 'soft lithography' fabrication scheme and is the most used polymer.

When choosing a photoresist, it must meet several demanding requirements: high sensitivity, effective adhesion, high contrast, easy processing, workable etching

resistance (wet or dry etching), effective resolution, high purity index, longer shelf life, minimal use of solvent, cost-effective, and high glass transition temperature, *Tg*.

In general, negative photoresist helps pattern structures with higher aspect ratio whereas positive photoresist gives a good resolution, Zn. However, the use of the correct resist depends on many application-specific factors.

As previously described, laser ablation encompasses both photothermal and photochemical processes that depend on the nature of polymers and the experimental conditions, such as fluence of laser, wavelength, and pulse duration. From previous studies, the glass transition temperature of the polymer is an important factor in determining the rate of laser ablation. High glass transition temperature makes a polymer a good candidate for optical waveguides [227]. The glass transition temperature *Tg* is the temperature where glass transitions from hard and relatively brittle to a soft and rubbery state. Amorphous polymers with high *Tg* can be considered for a range of applications. Polymers at temperatures above and below *Tg*, exhibit very different physical properties. Therefore, the location of this thermal transition is critical to many applications [210]. High glass transition temperature polymers are useful for several high-temperature applications. Due to the significantly higher *Tg,* both SU-8 and chitosan are biocompatible and can be used in imprinting techniques for producing free-standing films comprising of micro and nanostructures. SU-8 can effectively be used as a negative tone photoresist, especially in multiple-photon interference lithography, as the periodic structure scales down to deep sub-micron to photonic crystals. Lithography techniques developed for SU-8 lead to several unprecedented capabilities for the creation of distinctive micro- and nanostructures [108].

Micro- and/or nanostructures can be used for sensing applications in biological components. However, one of the main challenges of using these systems for sensors is the assimilation of biological components [228]. These kinds of microdevices typically and effectively need to be functionalized alongside biomolecules such as DNA, enzymes, or antibodies, in order to operate with sufficient specificity and sensitivity. Chitosan has claimed its importance as one of the most promising candidates for interfacing biology with microdevices, and it is the choice of this chapter because the unique film-forming and chemical properties of chitosan allow coatings to be grown onto the substrate using the thickness of tens to hundreds of nanometres. This makes it attractive for many industrial and biomedical applications, making it possible to functionalize the basis of

their integrated optical functional structures. Owing to the fact that the physicochemical properties of chitosan considerably depend on the ionic form and the degree of deacetylation [229], the characteristics of biopolymer chitosan allow the use of this auspicious material as a resist for submicron electronic lithography and it has contains the ability to produce planar and three-dimensional heterogeneous structures. It also can be co-deposited with other polymers or nanoparticles. The major practical interest is the changing of the mechanical properties of a polymer around Tg. Polymer molecular mobility rises exponentially at a temperature above Tg and its viscosity decreases affecting several physical properties. Table 2-1 presents the important properties of PC, PMMA, SU-8 and chitosan. These properties are taken into account to choose the suitable material that can be used in the next chapter as a substrate for soft lithography.

Table 2-1 Properties of Materials PC, PMMA, SU-8 and chitosan

Material	Coefficient of thermal expansion (CTE), K^{-1}	Tg ^{o}C	Thermal conductivity at 293 K ($W.m^{-1}$ K^{-1})	Refractive index at 193nm	Absorption coefficient m^{-1}
PMMA	55×10^{-6}	65	0.12	1.65	2×10^{5}
PC	70.2×10^{-6}	145	0.2	1.49	1×10^{7}
Chitosan	-2.5×10^{-6}	202	0.39	1.7	3.3×10^{5}
SU-8	$50\text{-}52\times10^{-6}$	>200	0.3	1.8	4.2×10^{5}

2.5 Experimental set-up of ablation.

Figure 2-7 illustrates the experimental setup for the beam delivery system used in this work. It includes a 193 nm ArF laser (Lambda Physik LPF 202) having a maximum output energy of ~285 mJ at a charging voltage of 25 kV. The pulse duration of ll.5 ns full width at half-maximum, and with a power average 5.7 W at the maximum repetition rate of 20 Hz. The charging voltage of the laser may be varied between 19 kV and 25 kV, and this allowed the laser energy and hence, laser fluence at the target to be controlled.
The polymer samples were held on a motorised nano-stage (Aerotech), which was capable of movements in the x-y-z directions that has an electrical resolution ~10nm increments. In these experiments the beam delivery system includes construction rails, by Thorlabs. There are two vertical rails, which are 750 mm long and 95 mm wide, and a 2000 mm

long horizontal rail which is 66 mm wide. There are three high energy excimer, designed to be used at 193 nm. The mirrors with an angle of 45° and a diameter of 25 mm. The two mirrors attached to the horizontal rail were purchased from Edmund co. and the third mirror was purchased from CVI co. A fused silica lens in plano-convex configuration (Newport Co.) was also used with a diameter of 25.4 mm (focal length of 81.8 mm at 193 nm). Photomask was used to select a quasi-uniform section of the beam which is imaged onto the target. The laser fluence can be increased by arranging the imaging system at different magnifications. The output beam of the laser is directed through the attenuator onto the sample, which is positioned on the motion control stage. A long beam path (approximately 2180 mm) facilitates large magnifications. The output energy of the laser was measured by using a Molectron Joule meter and Hewlett Packard oscilloscope (*hp*, HEWLETT PACKARD). Laser fluence was determined by using the energy output measurements obtained by irradiating an area of the sample. For ablation measurements, White light interferometry (WLI, Wyko NT1100) permitted high-resolution 3D surface measurements.

The vertical resolution is ~ 1nm in the verticle direction and typically 500nm in the lateral direction. The interferometer consists of a turret that secures the objective lenses(2.5×, 10×, and 50×). The field-of-view lenses permit further magnification of 0.5x, 1.0x, and 2.0x, Vertical Measurement Range 0.1 nm to 1 mm. The ablation depths were measured using both WLI and Dektak XT (Bruker) instruments. An optical microscope (LEICA DMLM) was also used for optical characterisation. The high-resolution morphology of samples was measured by using SEM (Zeiss, EVO60). The optical properties of the experimental material were measured by using both for Horiba FluoroMax® four spectro-meters and a UV-visible spectrophotometer (EVOLUTION 220).

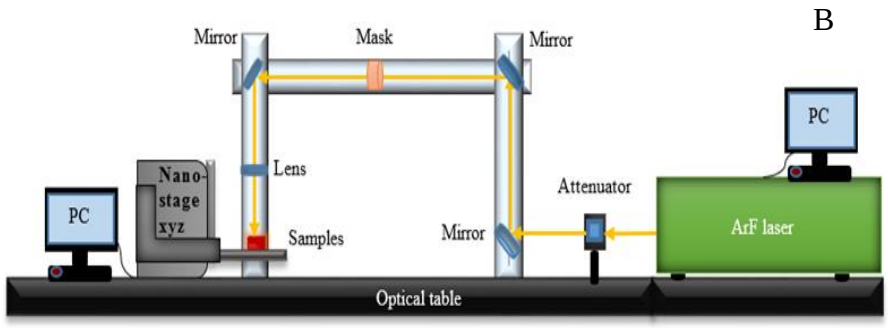

Figure 2-7. Set up of the laser ablation system, B. Schematic diagram of the ArF laser (λ=193nm) nano/micro ablation workstation.

2.5.1 Methodology

There are four identical 15×15 mm samples, first one was cut from 2 mm thick (polycarbonate PC (Sigma-Aldrich) and the second sample was cut from 2mm Polymethylmethacrylate (PMMA, Goodfellow), and the third one was SU-8 film (5 µm thickness) prepared as described below:

A solving cleaning process was used to clean the Soda-lime glass using ionized water, acetone, and isopropanol respectively to eliminate the influence of oxidation on the substrate surface, each of them sonicating for 10 min using an ultrasonic bath (UW ultra-wave mode QS5, ultrasonic cleaner). It removes the adsorbed solvent on the substrate surface. SU-8-negative tone photo-epoxy (GM1060, Gersteltec Sarl.) was spin-coated (SUSS Micro-Tec Lithography, GmbH, Type DELTA 10TT). The time taken for spin coating was 30 seconds at 5000rpm. It produced 5 µm film thickness when cooled down. Below are the steps further for the sample left at room temperature for approximately 40

minutes then placed on a hot plate at 65℃ for 5 minutes then increase the temperature to 95℃ and heat the sample for another 5 minutes. The coated substrate was then cured by exposure to UV lamp of 10mW cm^{-2} intensity at 365nm. The sample was left for 10 minutes at room temperature. Figure 2-8. A shows Film thickness calibration vs spin speed (rpm),

The last sample was a chitosan film, prepared as described below:

The chitosan used in this work was ordered from Sigma-Aldrich (Chitosan-448869, 0.1M acetic acid). 2% concentration of chitosan solution was prepared by mixing chitosan powder as much as 0.2 g in a 10 mL of acetic acid. Chitosan films were prepared by spreading the chitosan solution on soda-lime glass microscope slides (Thermo Scientific) using a spin coating method. A calibration curve was obtained to compare the spin speed for samples with thicknesses ranging 300 nm to 2 μm (see Figure 2-8.B. The samples were allowed to dry at room temperature about 12 hours before irradiating by ArF laser.

For PC, PMMA, Chitosan, and SU-8 films, 5 absorption/ transmission measurements were taken using UV-VIS spectrophotometer (Thermo Scientific, Evolution 220). Figure 2-9 illustrates the features of the spectrophotometer used. The wavelengths which are selected range from 190nm and 1100 nm. The setup includes two plates and cuvette holders. The interval in the data and integration time can be changed as required, with the data interval usually set at 1 nm. The data is exported as a CSV file.

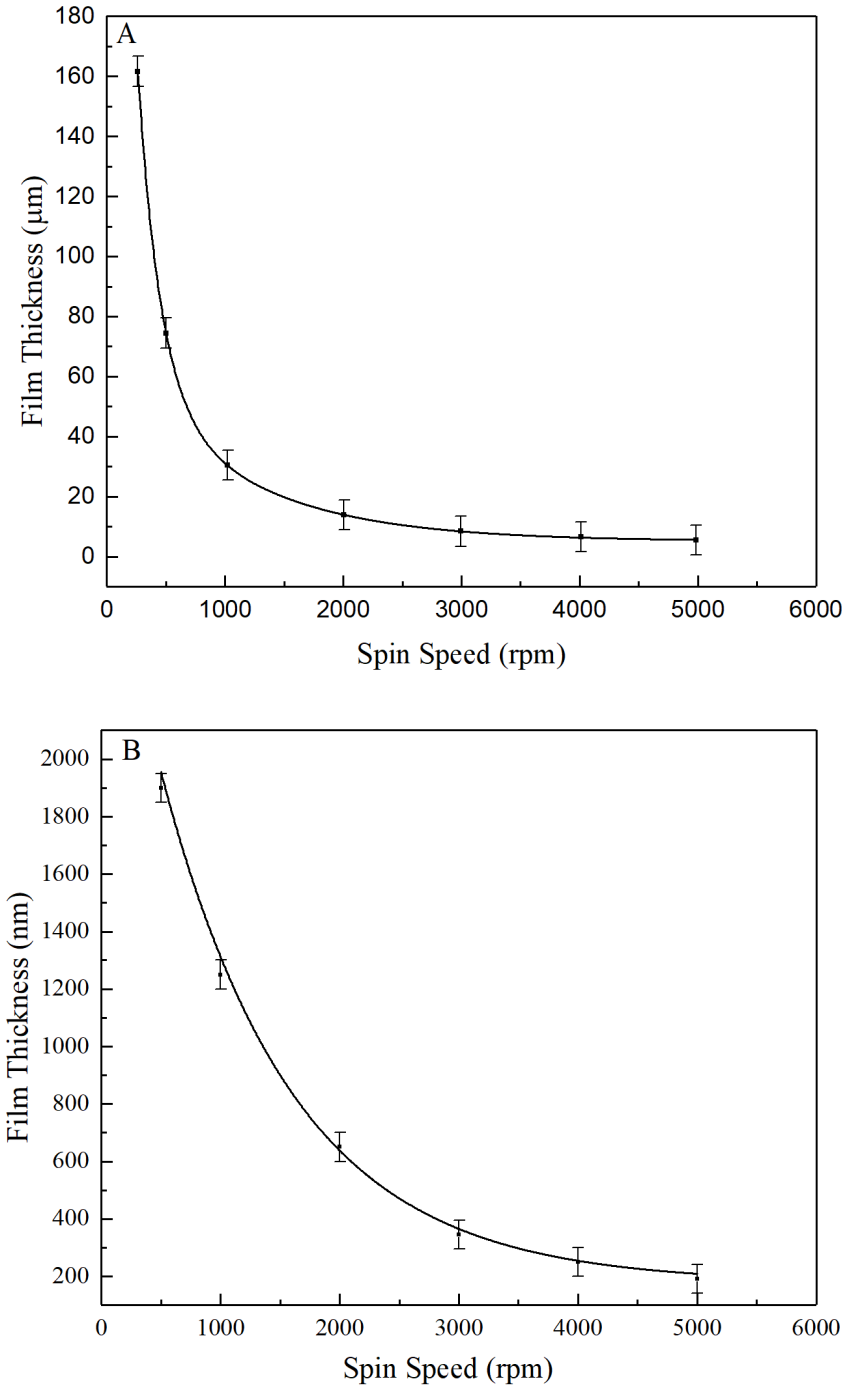

Figure 2-8. Film thickness calibration vs spin speed (rpm), (A) SU-8 film and (B) chitosan film.

Figure 2-9 Evolution™ 201/220 UV-Visible Spectrophotometers UV-VIS spectrophotometer.

2.6 Results and discussion

2.6.1 UV spectrum

Transmission and absorption for PC and PMMA samples were measured with a UV-VIS spectrophotometer at wavelengths between 190 and 1000 nm (see Figure 2-10). Both samples show high transmission beyond the 400 nm wavelength, which is expected as PMMA and PC find wide applications as optically transparent window materials. The high absorption below 400 nm is due to the electronic excitation within the cabony1 chromophores (C=O) present in the chemical structure of PMMA. As can be seen in Figure 2-10. A below, polycarbonate is quite effective in the UV (less than 400nm). It becomes opaque almost exactly where the visible range ends and UV starts. Light transmission is lower for polycarbonate (90%) when compared to PMMA (95%). Otherwise, the absorption of PC is higher than the absorption of PMMA below 400 nm wavelength (see Figure 2-10. B).

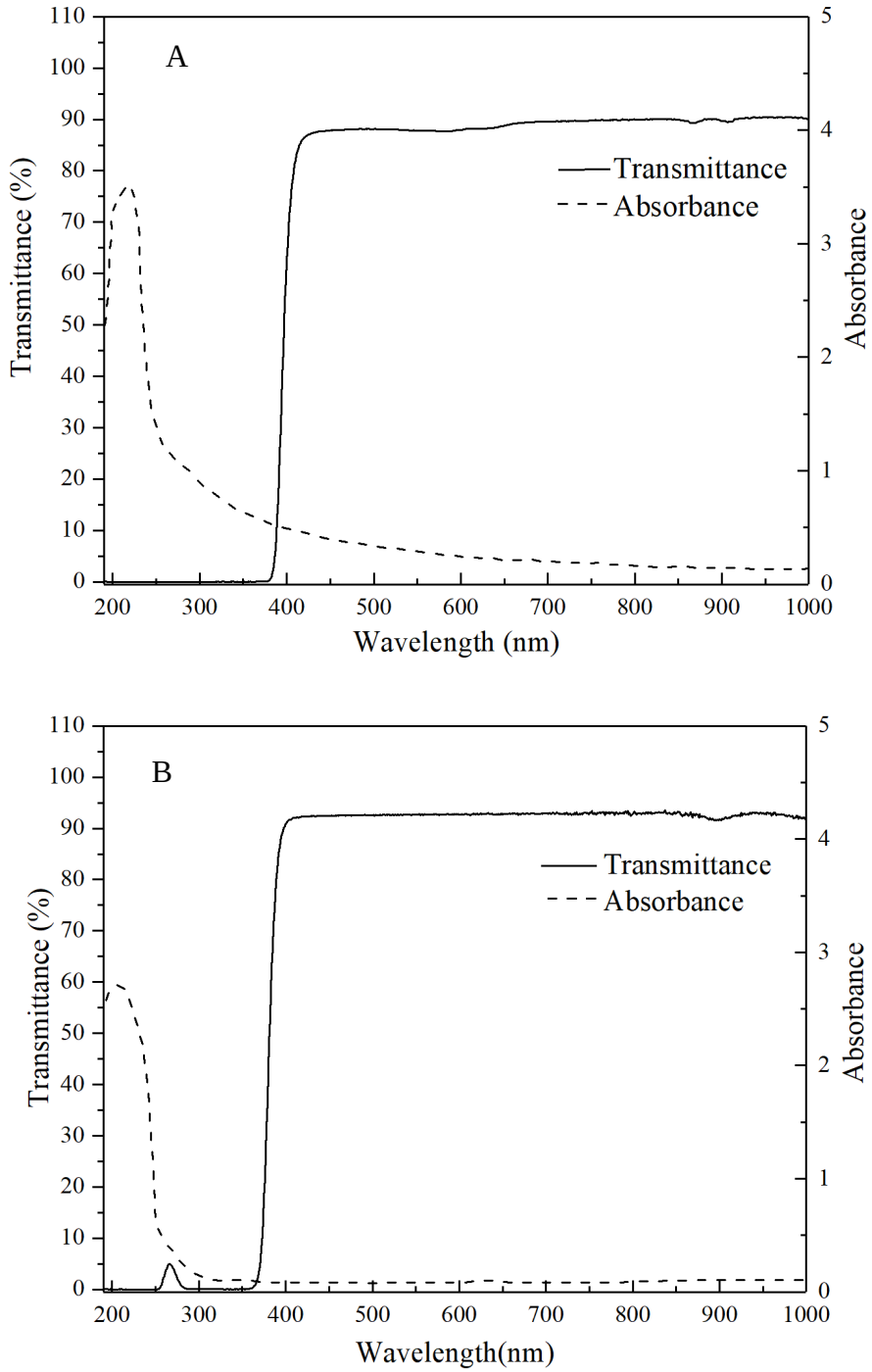

Figure 2-10. The optical spectrum of PC and PMMA in the visible regime. The transmission and absorption spectra of a flat 2 mm thick PC (A) and PMMA (B) were measured with a spectrophotometer. In the visible regime (380−780 nm), the transmission is almost constant, with a value of ~90 %, as indicated by the thin solid line.

Absorption of SU-8 film starts increasing sharply below 400nm, as can be observed from Figure 2-11. A, while Figure 2-11. B shows the optical absorption of chitosan film increases rapidly around 220nm. Absorbance peaks around 200 nm for the chitosan film whereas it peaks around 300nm for the SU-8 film (see Figure 2-11. B). Then the SU-8

film also shows a little lower absorbance than the chitosan film. In the case of the chitosan film, this difference in the absorption peak and enhanced absorption may be attributed to a structural rearrangement most probably the formation of conjugation in the structure because of relatively longer heating of the film at a higher temperature and the removal of dangling bonds. Beyond 400nm, from both spectra, it can be observed that absorption is very low and continues to decrease with higher wavelengths.

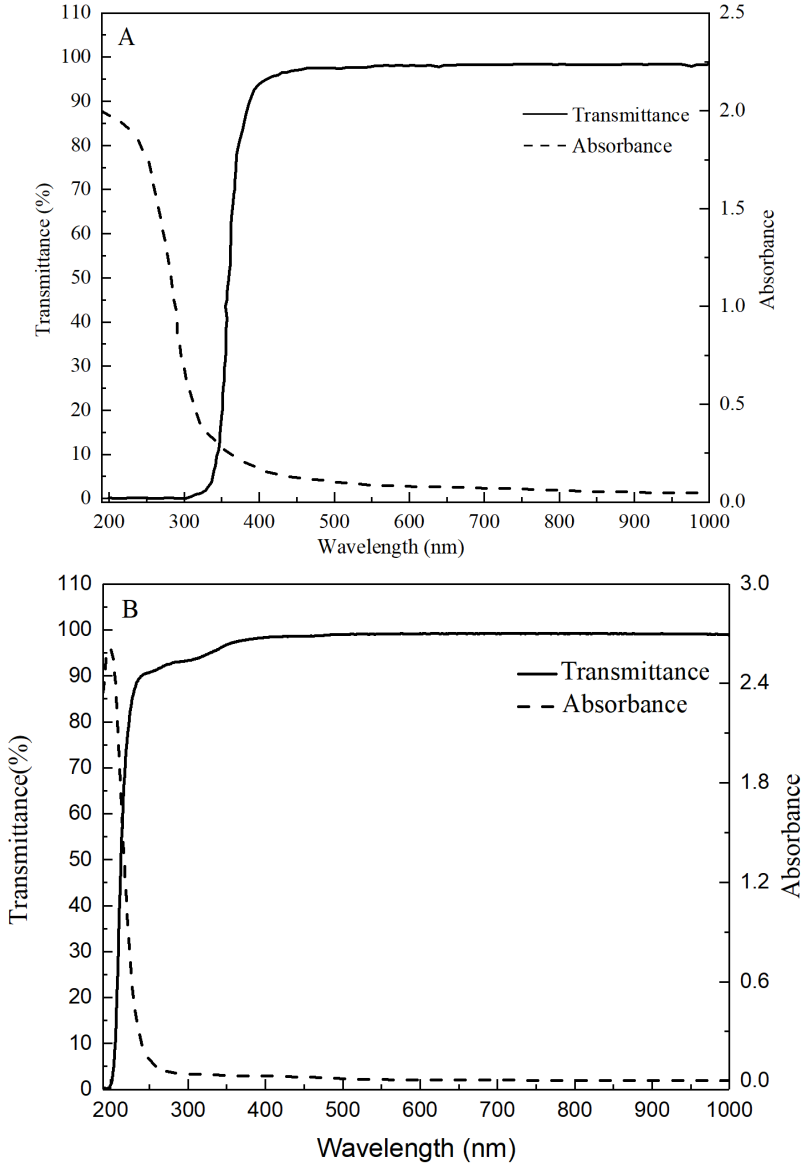

Figure 2-11. The optical spectrum of SU-8 and chitosan in the visible regime. The transmission and absorption spectra of a flat 2 µm film thickness of SU-8 (A) and chitosan(B) were measured with a spectrophotometer. In the visible regime, the transmission is almost constant, with a value of ~95 %, as indicated by the thin solid line.

Over a broad range of the visible spectrum, both SU-8 and chitosan films exhibit excellent optical transparency as indicated by the spectra. This makes both materials an excellent

polymer material for a variety of optical applications. These measurements show the average absorption coefficients of SU-8 and chitosan are 4.2×10^5 m^{-1}, 3.2×10^5 m^{-1} respectively, at film thickness 5μm. The thermal damage must be minimised during laser processing in many applications. This is achieved by using a low laser fluence.

2.6.2 Ablation threshold

The ablation threshold indicates how effective a specific technique is at etching a material. That is because to remove material from a substrate; minimal laser energy is required, as indicated by low threshold fluence. There are two ways to define the ablation rate: the linear fit for the plot of the ablation depth versus the pulse number for a given fluence, or the depth of the ablation crater giving one pulse at a given fluence. As previously described, the method used to measure the ablation threshold can dramatically change the result, depending on whether the material begins to ablate after the first pulse or after multiple pulses, or when the ablation crater is too small to measure after the first pulse. Incubation is the process that arises if ablation does not start with the application of the first laser pulse. The phenomenon is related to physical or chemical changes in the material due to the first few laser pulses, often resulting in an increase in the absorption at the irradiation wavelength. To determine the laser ablation threshold, the etch rate per pulse has been found. This was used for all materials: PC, PMMA, SU-8, and chitosan materials at the 193 nm irradiation wavelength. The depth for each sample was investigated by measuring the ablation craters depth using the white light interferometer (WLI), WYKO NT 1100, see Figure 2-12. Etch depths were measured at several distinctive locations of the sample for every fluence of the laser.

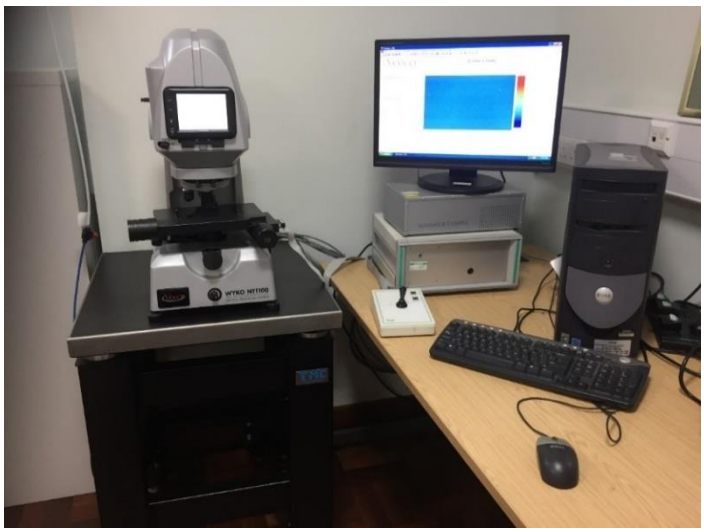

Figure 2-12 White light interferometry (WLI, WYKO NT 1100) setup.

The used laser fluence ranged from 10 mJ cm^{-2} to a maximum of 200 mJ cm^{-2} for PC, from 80 mJ cm^{-2} to a maximum of 2.5 J cm^{-2} for PMMA (see Figure 2-13, from 20 mJ cm^{-2} to a maximum of 300 mJ cm^{-2} for SU-8 and from 60 mJ cm^{-2} to a maximum of 3.5J cm^{-2} for chitosan (see Figure 2-14).

As shown in the figures below, the illustrated plots describe the feature depth machined against the required natural log of the laser fluence. The plot has been fitted using a linear trend that has been extended to the value to predict the natural log of the minimum laser fluence required to etch the material as per the standard method. Figure 2-13 shows the ablation thresholds of PC (A) and PMMA (B) are 25 $mJ.cm^{-2}$, 110 $mJ.cm^{-2}$, respectively. The geometry of ablation is strongly dependent on the distribution of the temperature governed by the absorption profile of the laser and the heat diffusion length, which produces the heat-affected zone (HAZ) around the spot of ablation. The etch rate of ablation close to the ablation threshold shows a relatively low trend at a nanometre per pulse level for all materials. At the higher fluence of the incident laser, the etch rates were started to plateau. This is due to several effects: photon shielding by ablation products and surface re-structuring, causing the effective surface area to rise. For SU-8, as compared to chitosan, lower ablation rates, and lower threshold fluences were detected as shown in Figure 2-14 A, B. It is clear that the ablation threshold of chitosan at 193 nm is 95 $mJ.cm^{-2}$, much higher than the ablation threshold of SU-8 40$mJ.cm^{-2}$ and the etch rate depth is greater too because the absorption coefficient of chitosan is lower compared to SU-8 at 193 nm wavelength and the difference in their optical properties. At relatively

high-power range density the ablation rate can be increased; however, the advantage of the small thermal effect in SU-8 is seen as shown in Figure 2-14.

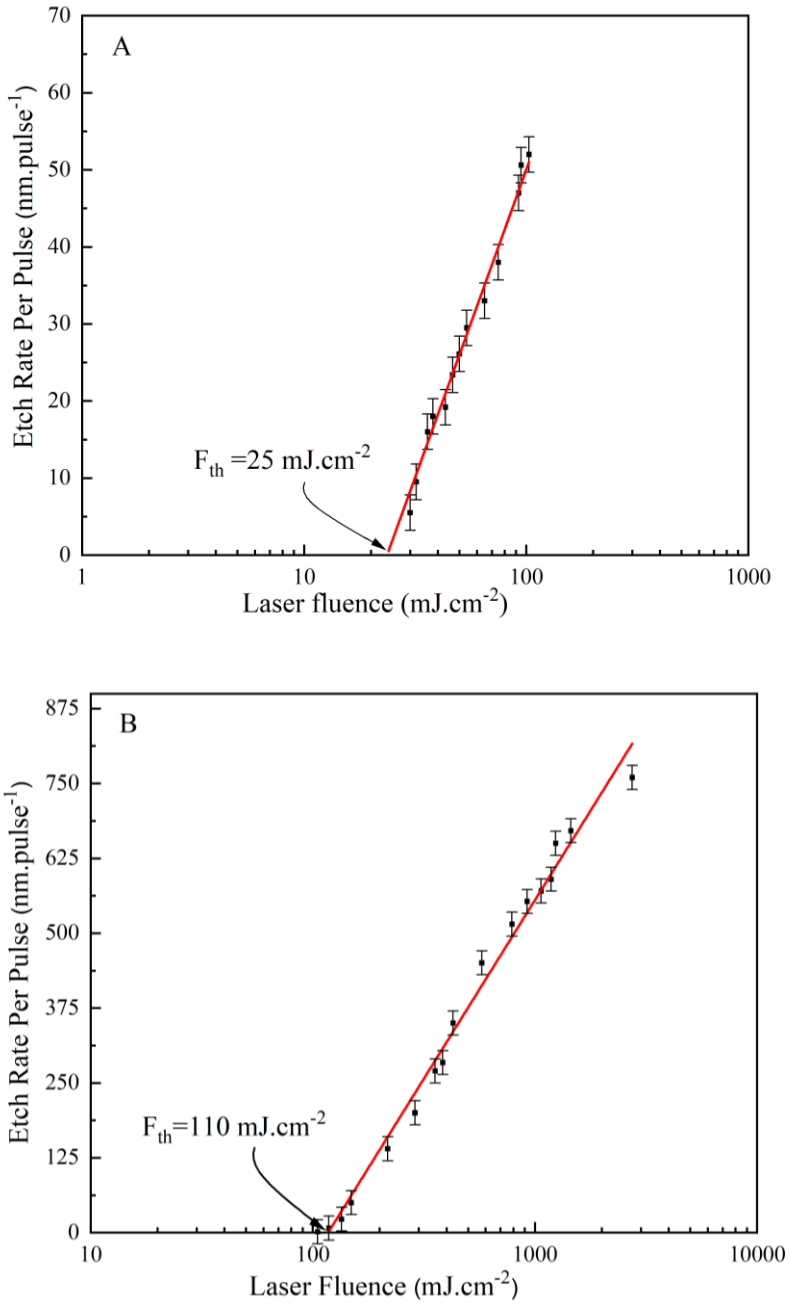

Figure 2-13. Ablation threshold vs laser fluence of PC (A) and PMMA (B). It shows that ablation thresholds at 193 nm wavelength are 25 mJ.cm^{-2} and 110 mJ.cm^{-2} for PC and PMMA respectively.

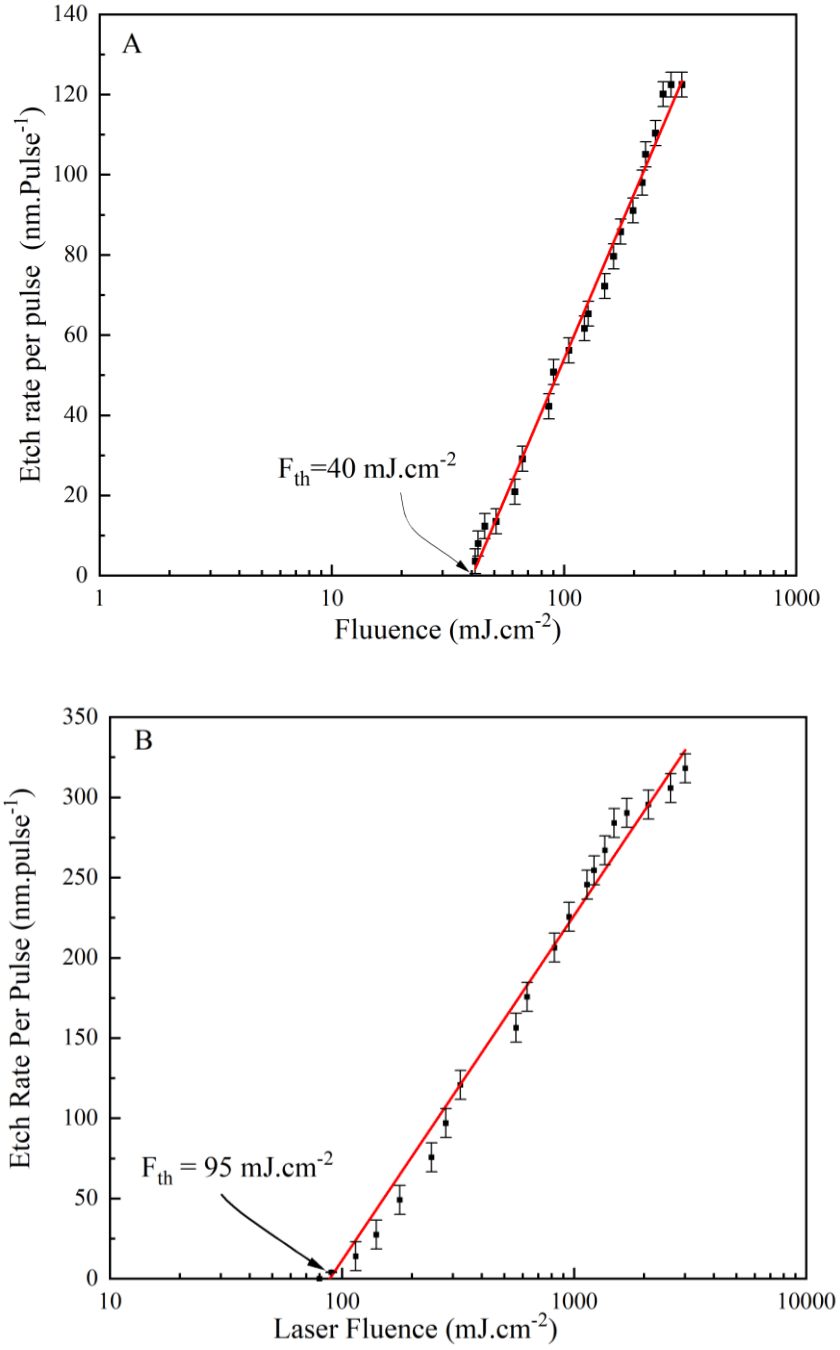

Figure 2-14 A. The ablation threshold of SU-8 film in a thickness of 5 µm, it shows that the ablation threshold is 40mJ.cm^{-2} at 193 nm wavelength. B. Ablation threshold of chitosan film in thickness 2 µm, it shows that the ablation threshold is 95 mJ.cm^{-2} at 193 nm wavelength.

Figure 2-15 shows WLI images of craters ablated on SU-8 surface by 10 laser pulses of excimer laser (λ=193 nm) using different laser fluences (50, 70, and 100 mJ cm^{-2}, 10 pulses and a repetition rate of 1 Hz. It is clear from the images that the depth of ablation depends on laser fluence while the diameters of holes are the same. Figure 2-16 shows the WLI images of craters ablated on chitosan surface by using the same laser parameter except for the laser fluence which is larger than fluences that used to ablate SU-8 (see

Figure 2-15.C), different laser fluences were used (120, 180, and 330 mJ cm^{-2}) as shown in Figure 2-16.C.

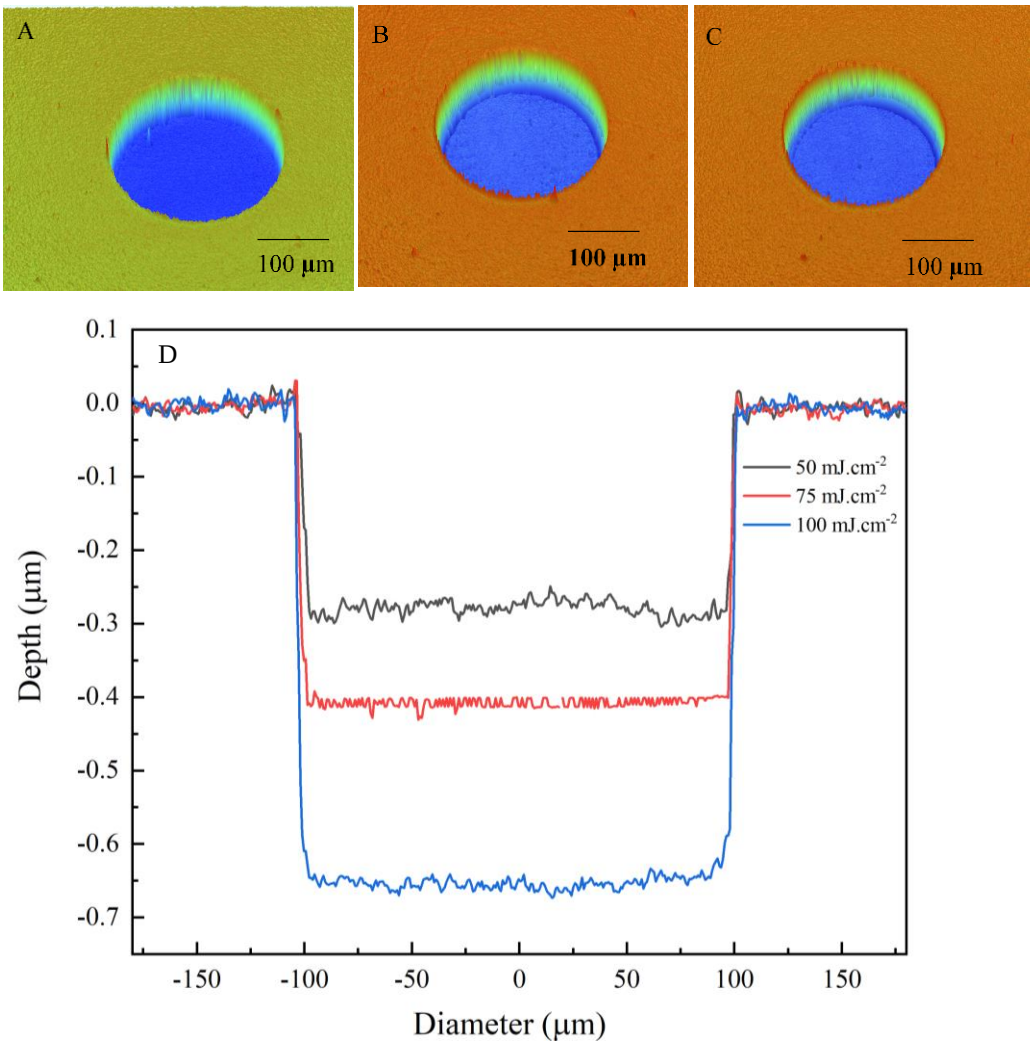

Figure 2-15 WLI images of Su-8 ablation (A) 50mJ.$cm^{-2,}$ 10 pulse, (B) 75 mJ.$cm^{-2,}$ 10 pulse, (C) 100mJ.$cm^{-2,}$ 10 pulse and (D) 2D cross section of each hole.

As a result, it can be seen the depth of craters ablated on chitosan film (~300 nm at 100 mJ.cm^{-2}) less than the depth of craters ablated on SU-8 film ~650 nm at 100 mJ.cm^{-2}) due to the optical properties of both surfaces. Furthermore, the mechanism of ablation for chitosan is different from others because of the growth of the effective surface area as laser-driven acoustic wave influences tensile stresses and the bubbles nucleate, changing the surface topology. Laser ablation has also caused the bubble formation and foaming on the surface of the irradiated area. The photoacoustic mechanism plays a significant role in laser ablation, particularly in biocompatible materials.

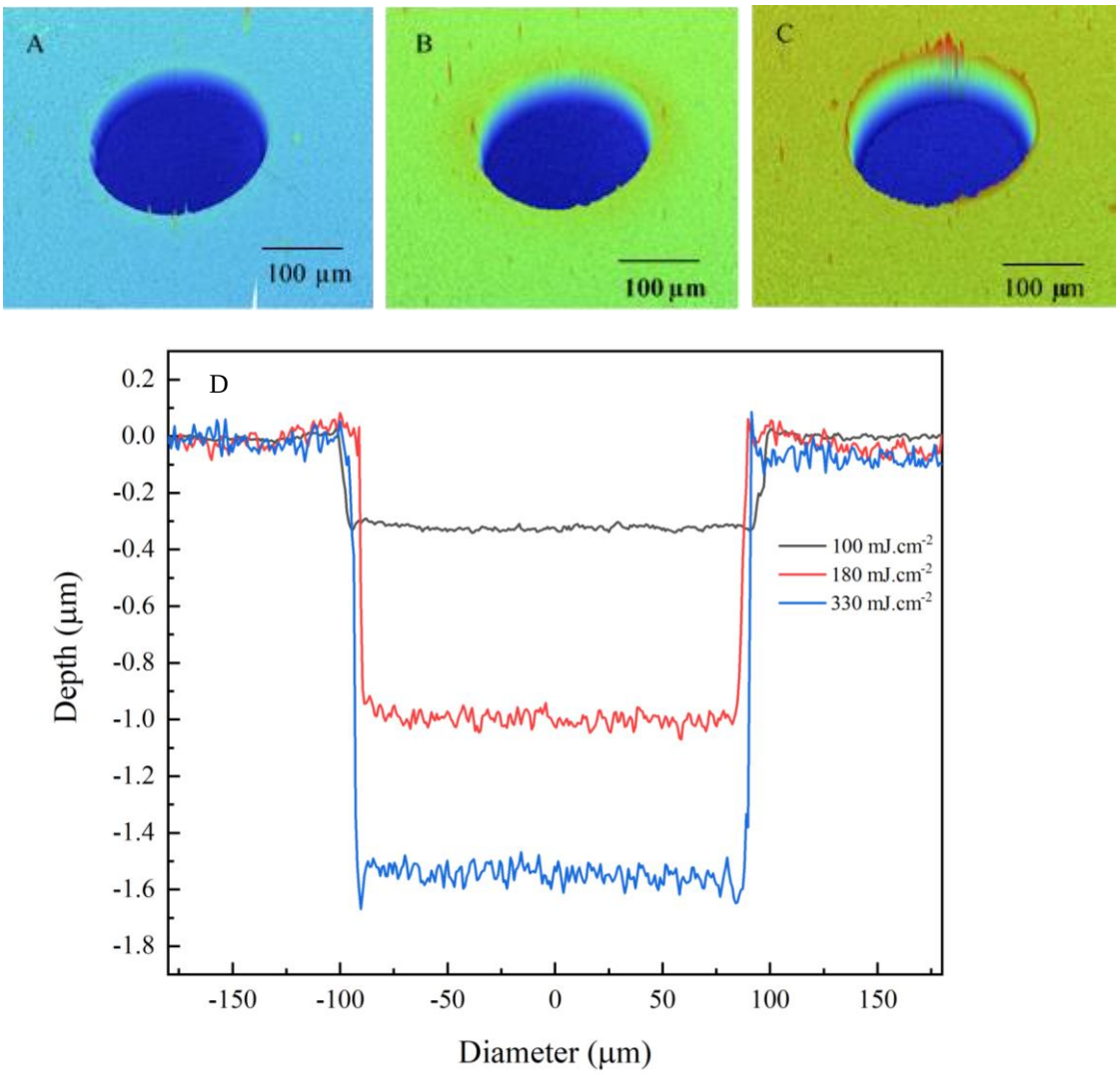

Figure 2-16 WLI images of chitosan ablation (A) 100mJ.cm$^{-2,}$ 10 pulse, (B) 180 mJ.cm$^{-2,}$ 10 pulse, (C) 330 mJ.cm$^{-2,}$ 10 pulse and (D) 2D cross section of each hole.

2.7 Conclusion

Laser material processing of polymer is an important field that has attracted attention in various applications related to academic research. It may be possible to identify biological applications by modifying the surface of polymeric materials which may improve the biomimetic and biocompatible properties. The work reported in this chapter investigated the absorption and transmission of PC, PMMA, SU-8, and chitosan at a range of wavelengths 190 nm -1000nm. A suitable wavelength to ablate material can be determined by measuring the absorption spectrum of the material needed to ablate and choosing the wavelength where maximum absorption occurs. Laser ablation processing, which employs a pulsed laser of ArF (193 nm wavelength) to remove materials from a

substrate over a fluence range from 10 $mJcm^{-2}$ to 1000 $mJcm^{-2}$, As a result, the ablation thresholds 25, 110, 40 and 95 $mJ.cm^{-2}$ were measured for PC, PMMA, SU-8, and chitosan respectively. The biocompatible materials photoresist SU-8 and chitosan were chosen because both materials are biocompatible, and they have high glass transition temperature and other properties mentioned previously. Optical properties that measured for these materials show that both materials have much higher absorption coefficients ($\alpha_{SU-8} = 4.2\times10^{5}m^{-1}$and $\alpha_{chitosan}=3.3\times10^{5}m^{-1}$) at 193nm wavelength which used in next chapter. Finally, it should be underlined that the quality of the ablation of craters made in different materials is powerfully dependent on several parameters which include not only the width of the laser pulse but also repetition rate, wavelength, fluence, beam profile, number of pulses, focusing objective, and the ablation environment.

Chapter 3 The realisation of Sub-wavelength features in SU-8 and chitosan

3.1 Introduction

Using lenses to focus light is a huge scientific area. In many systems there is sufficient space to use almost any size of lens. However, there are many systems that have restricted space and novel beam delivery systems are required. This is especially true in the area of micro and nano-fluidics, so-called Lab-on-Chip. It is the latter from which we have an application interest. Lab-on-Chip systems are typically a few centimetres in size and therefore a lens of a similar dimension is difficult to incorporate. Ball lenses on the other hand can be quite small. It is not unusual to have 1mm diameter ball lenses. Frequently ball lenses are used along with optical cables and this combination provide a compact optical delivery system. However, one can push towards smaller dimensions and use spherical particles to focus light. The work in this chapter uses spherical particles of 1 μm diameter and we investigate their focal properties. Many optical physicists and engineers strive to confine light to smaller and smaller spot sizes in small systems that gave so-called small foot-print architectures. We note the optical system can be one that focus light or a lens that is being used to receive light. For example, in microscopy and photoluminescence where one might like to probe the emission of light from a small emission volume. In microscopy high spatial resolution is sought after when probing fluorescent molecules and similar light-emitting structures [230]. In contrast, direct-write laser processing, data recording or as in this work, laser surface modifications, light is focussed onto a substrate material for applications such as laser: annealing, ablation, cutting, patterning etcetera. A good example of two applications using high and low in put powers at the lens are: high power laser welding and laser tweezing. Although the latter utilises power on the milliwatt scale the laser beam is tightly focussed and very large irradiances can be realised. As a result very large electric field gradients can be set up and light can be sued to trap molecules and particles [231–233].

In this chapter we report experimental and computational results of microsphere lithography carried out at a wavelength of 193 nm. Much of previous work has been carried out at longer wavelengths with limited work below 200nm [234]. As spot sizes scale with wavelength, as is shown in this chapter, impressive sub-wavelength patterning can be achieved using so-called photonic nano-jets. To complement the experimental

work we have carried out FDTD simulations using the software, Lumrical. Optical simulations are extremely useful for visualising and quantifying the electric field and intensity of light and in particular light propagating through focussing elements. The system in our case consist of a SiO_2 microsphere that is supported on an underlying substrate. An interesting question might be, what is the size and distribution of the electric field in the focal region? The spot size (focal region) is dependent on diffraction, wavelength of light used, laser beam divergence, optical aberrations and scattering of light. Hence it is useful to compare experimental results with that of optical simulations.

In this chapter, an experiment using a 193 nm Argon Fluoride excimer laser has been used to realise a sub-micron sized dimples in materials SU-8 photoresist and chitosan. UV laser radiation is focussed by a small spherical particle that acts to all intense and purposes as a ball lens. Optical enhancement is achieved by tightly focussing light into a small focal volume. A 1 μm diameter SiO_2 microsphere is located on the surface of two materials, SU-8 and chitosan in two separate experiments. The microsphere is illuminated with light from a 193 nm wavelength ArF laser. The spatial location of the focal region can be estimated using equations 3. However, these equations are for ideal cases and they do not take into account optical aberrations and effects of depolarisation of the electric field in the focal region. To quantify theses effects, finite difference time domain (FDTD) was used. More detailed information is given later in this chapter. It is also of interest to estimate the surface temperature of the underlying substrate. This we have done using a Finite Element Method (FEM) for both materials SU-8 and chitosan. Temperature information assists in understanding material modification and in this work it is useful to analyse the microsphere ejection mechanisms.

The magnitude of temperature increase and concomitant substrate acceleration, therefore, depends on optical and physical properties of the sphere and substrate system. We report computational simulations of the temperature change induced by the laser of the illuminated microsphere supported on a photoresist, SU-8 and on chitosan. Theoretically, computational, and experimentally are demonstrated in this chapter. Experimental and computational results of an irradiated laser microsphere supported on biocompatible SU-8 photoresist and chitosan. A single pulse from an ArF excimer laser (λ= 193 nm) was used to modify the underlying substrate producing a single concave dimple.(FDTD) simulations were carried out to simulate the propagation of 193 nm laser radiation focussed through a 1 μm diameter silica sphere. Numerical simulation results are in good agreement with not only the analytical solution but also the experimental data. The

photonic nanojets properties, such as FWHM, effective length, focal distance, and light intensity, can be controlled for further experimental study. A novel kind of microsphere-based optical lithography technique using photonic nanojets have proved that the high subwavelength resolution of nanoholes or nanopillars can be easily fabricated using UV light source. Atomic force microscopy (AFM) and scanning electron microscope (SEM) measurements have been used to quantify the shape and size of laser inscribed dimple. SEM and AFM are powerful characterisation tools in material science, capable of revealing surface structures. In this work we aim to provide an overview of the various computational approaches to understand not only the architecture of photonic nanojet, but also the mechanism of their formation.

3.2 Theory

3.2.1 Focal proprties of spherical lenses

Ball lenses are a special form of optical lenses with a spherical shape which produces spherical aberration. An optical aberration is a distortion in the image formed by an optical system compared to the original. Rays passing through the lens close to its center are focused farther away than rays passing through a circular zone near its rim [235]. Figure 3-1shows a cross-section of the geometry of a ball lens.

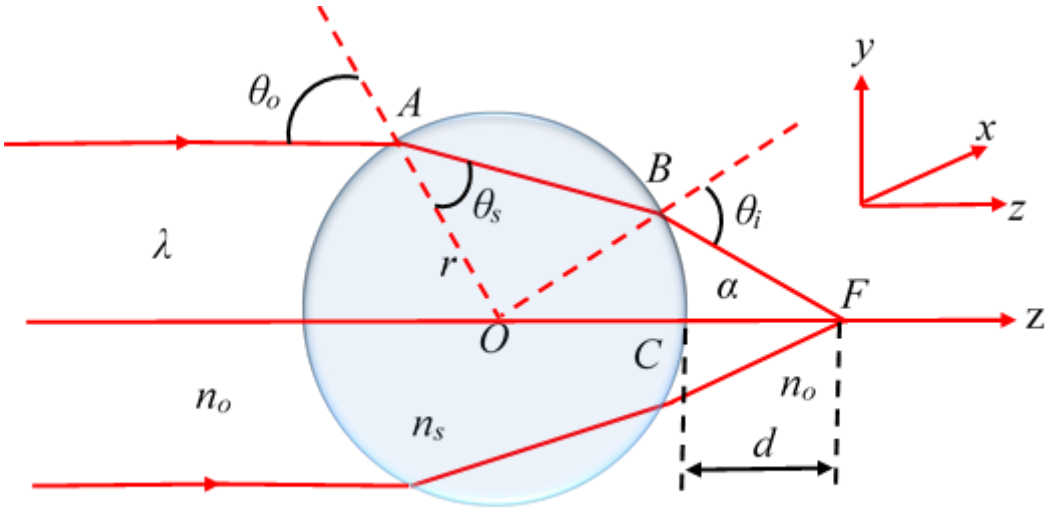

Figure 3-1. Schematic of ball lens illuminated by a incident plane-wave [235].

The effective focal length (*EFL*) and the back focal length (*BFL*) serve as useful descriptors to quantify lens properties. For an ideal lens the *EFL* and *BFL* can be expressed in terms of the refractive index, *n* of the lens and the lens radius *R* [236].

$$EFL = \frac{nR}{2(n-1)} \tag{3.1}$$

$$BFL = EFL - R \tag{3.2}$$

The two parameters above are illustrated in Figure 3-1, the *BFL* can be calculated from refracted angles using Snell's law [235].

$$d = r\left[\cos(\theta_0 - \alpha) + \sin(\theta_0 - \alpha)\cot\alpha - 1\right] \tag{3.3}$$

where $\alpha = 2\theta_0 - \theta_s$. The minimal size of the laser spot (2w0) is defined by the diffraction limit as:

$$2w_0 = \left(\frac{4\lambda}{\pi}\right)\left(\frac{f}{D}\right) \tag{3.4}$$

where λ is the wavelength, f and D are lens focal length and the diameter of the input pupil of the lens respectively. Depth-of-focus (DOF) is also important in many optical systems especially optical lithography. It is often used as a catch all for any focus effect in optical lithography [237]. Generally, DOF decreases linearly with wavelength and as the square of numerical aperture.

$$DOF = \left(\frac{8\lambda}{\pi}\right)\left(\frac{f}{D}\right)^2 \tag{3.5}$$

Equation 3.5 serves well for typical macroscopic lenses. However, in the case of small micro-spheres the short focal length and refractive index play an important role in focusing. In the case of microspheres, the position of a focal point can lie inside instead of outside the sphere. We note the position of the focal point is dependent on the refractive index contrast, that is the focal position also depends on refractive index of the medium surrounding the microsphere. Optical aberrations are inherent in one form or another in optical systems and in some optical systems a great deal of time and effort has gone into reducing the aberrations as in general they are detrimental to the system or process. One of the main aberrations of ball lenses is spherical aberration (*SA*). A ball lens can be described as a double convex lens that has equal radii. Spherical lenses, commonly called a ball-lenses, are a good example of an imperfect lens as they are subject to *SA*. Shown below are expressions for different aberrations, Coma aberration (CA) results when refraction differences are produced due to the light rays, which passes through various lenses zones, as the incidence angle increases and derives name from comet shape aberrated image. Astigmatic aberration (AA) is opposite to spherical aberration and coma in production, it results when the focus of single lens zone fails to produce image of an off-axis point at a single point [238].

$$SA = \frac{\left[n(n-3)+1\right]y^3}{2n^2R^2} \tag{3.6}$$

$$CA = \frac{\left[n(n-3)+1\right]y^2u_p}{2n^2R} \tag{3.7}$$

$$AA = \frac{\left[n(n-3)+1\right]yu_p^2}{2n^2} \tag{3.8}$$

where y is the ray height at the first surface, and u_p is the half-field angle. These expressions can be used when carrying out ray analysis of aberrated lenses.

There is a wide amount of published work describing optical field enhancement [17, 18, 107]. A particular good application of enhanced resolution using microspheres can be found in reference [239] and references within. Some published works have demonstrated that using silica microspheres as a lens in optical microscopy that the diffraction limit can

be surpassed. Turning our attention back to focussing light It has been shown that micron sized dielectric spheres illuminated by a plane wave, can produce a narrow, high-intensity, sub-diffraction beam waist can be produced is referred to as a photonic nanojet, (PNJ). that propagates into the background medium from the shadow-side surface [240]. Formation of the PNJ as a result of focused near-field diffraction [241]. At high numerical aperture of microsphere lens, its resolutions can be improved. The improvement in resolution is due to an increase in the effective numerical aperture of the micro-sphere lens. PNJ's have emerged as a useful aid in high resolution imaging and spectroscopy applications due to their ability to confine electromagnetic waves in sub wavelength scale dimension [119] .

3.2.2 Optical field enhancement

A function of a lens when used for focusing is to increase the light intensity. Confining light in this way when using a large Numerical Aperture (*NA*) lens is sometimes referred to as tight focusing [50]. In such systems light is focused to a small spot size, w. One can express the spot size in terms of the Radius *R* and the refractive index *n* [242]

$$w = R\sqrt{\frac{\left(4-n^2\right)^3}{27n^4}} \tag{3.9}$$

And noting that the value of *n* is is wavelength dependent, in this work 193 nm (6.7 eV). A simple way of quantifying any field enhancement is to consider the ratio between the intensity of the incident beam, I_0 to that of the intensity in the focal region I_t,

$$\frac{I_t}{I_0} = \frac{a^2}{w^2} \approx \frac{27n^4}{\left(4-n^2\right)^3} \qquad \text{for} \quad n < \sqrt{2} \tag{3.10}$$

$$\frac{I_t}{I_0} = \frac{27n^4}{\left(4-n^2\right)^3}\frac{n^2}{2n\left(n-\sqrt{2}\right)+2} \text{ for} \quad n > \sqrt{2} \tag{3.11}$$

However, these simplified expressions do not take into account Fabry-Perot type reflections between the sphere and the underlying substrate. It is interesting to note that

the focal spot can be located either inside or outside of the sphere depending on the value of the refractive index and the size of the sphere. Therefore, the lens material and size can select to engineer the spatial location and electric filed enhancement factor.

3.2.3 Temperature calculations of the substrate beneath the microsphere.

Information about the mechanism of dimple formation can be gathered from temperature calculations. Electric field enhancement at the sphere-substrate interface manifests in an increased temperature of the SU-8 film. The magnitude of the temperature increase provides useful information that can be used to explain possible mass transport mechanisms in the vicinity of the dimple [139, 242]. For analysis purposes, we estimate the temperature rise in the SU-8 layer by assuming a Gaussian temporal intensity profile. An intensity distribution of the laser pulse was defined as [242]:

$$I_0(t) = \frac{\Phi t}{t_l^{\,2}} \exp\left[-\frac{t}{t_l}\right] \tag{3.12}$$

$$T(r,z,t) = S_0 \frac{A_0 \alpha}{C_s \rho_s} \int_0^t dt_1 I_0(t-t_1) \frac{\exp\left(-\frac{r^2}{r_0^2 + 4\chi t}\right)}{1+\frac{4\chi t_1}{r_0^2}} F(z,t_1) \tag{3.13}$$

Where, $t_l = 0-409\,\mathrm{t}_{FWHM}$, where t_{FWHM} is the pulse duration at the FWHM, and Φ is the incident fluence of laser on the silica sphere, S_0 is the intensity enhancement factor, r_0 is the width of corresponding Gaussian, r is the radial coordinate, α is the absorption coefficient, C_s is the specific heat capacity, ρ_s is the thermal conductivity, A_0 is the absorptivity, χ is the thermal diffusivity of the substrate,

$$\chi = \frac{k_s}{c_s \rho} \tag{3.14}$$

and the $F(z,t)$ is the following function as shown below [242]:

$$F(z,t)=\frac{1}{2}e^{\alpha^2\chi t}\left\{e^{\alpha z}erfc\left[\alpha\sqrt{\chi t}+\frac{z}{2\sqrt{\chi t}}\right]+e^{-\alpha z}erfc\left[\alpha\sqrt{\chi t}-\frac{z}{2\sqrt{\chi t}}\right]\right\} \quad (3.15)$$

3.2.4 Sphere-substrate adhesion and detachment mechanism

Silica spheres, diluted in water, were placed on the surface of the SU-8 and chitosan films. The film layer is mildly compliant; therefore, due to adhesive force between the spherical particle and substrate (film), the contact area increases ever so slightly as the sphere embeds into the film. There is an associated surface roughness of both the sphere and the substrate, which modifies the adhesion force. Although work on PNJ's is primarily concerned with the optical effects, we give some consideration in this work to the adhesion and detachment forces.

After laser irradiation has taken place, there are three main scenarios to consider; the sphere may eject from the substrate, the sphere may appear undamaged and remain on the substrate, or the particle may become damaged. The laser fluence for each of these scenarios can be found by quantifying the magnitude of the adhesion force and hence calculating the laser fluence for particle ejection. This is especially relevant if the particulates are in the form of debris. In such cases, we can approach the system from a laser cleaning perspective [243]. Adhesive forces of small microspheres and particulates to a surface can be calculated using Van der Waals force equations. Although in this work we are primarily interested in optical field enhancement, it is informative to consider the fate of laser-illuminated particles and microspheres and identify upper limits of laser fluence for microsphere removal.

In this work, it can be assumed that the SiO_2 microsphere is optically transparent. This is supported by the low transmission loss over a path length of one micron. Taking into consideration reflection losses at both interfaces the transmission loss corresponds to ~10%. Laser heating of the particle is assumed negligible and energy from the laser pulse is deposited into the underlying substrate. Subsequently, detachment is primarily associated with substrate expansion caused by absorption of energy over the short 12 ns duration of the laser pulse at FWHM. Interaction of short nanosecond pulses from excimer lasers result in rapid temperature changes of typically 10^9 Ks^{-1}. Consequently, rapid heating can manifest in rapid substrate acceleration.

The magnitude of temperature increase and concomitant substrate acceleration, therefore, depends on optical and physical properties of the sphere and substrate system. Front side reflectivity of SiO_2 is typically 5% at a wavelength of 193 nm which slightly reduces the laser fluence passing through the microsphere. However, the small loss of energy is offset by an increase in laser fluence due to the refractive focusing of the microsphere. As mentioned, particle ejection may occur by several mechanisms depending on the magnitude and the degree to which energy is absorbed by the substrate. If the laser fluence beneath the microsphere is sufficiently high substrate melting and boiling points may be exceeded such that ablation and evaporation contribute to mass transfer of substrate material. Evaporating and ablative species will generate forces in the region beneath the microsphere. Plume expansion and gas dynamics may play a significant role in sphere displacement. Substrate acceleration due to an increase in temperature and plume expansion may not be totally independent and both mechanisms may play a role in particle ejection. Therefore, optical focusing, energy confinement and substrate response to pulsed laser energy may play important roles in modifications to the substrate. This work, therefore, uses FEM methods to estimate the substrate temperature beneath the microsphere during the absorption of a laser pulse.

In these experiments, a SiO_2 microsphere is supported on spun coated SU-8 and chitosan. Adhesion is primarily associated with Van der Waals forces between the sphere and substrate. From Equation (3.16) one observes a reduced sphere-substrate spatial separation, z, results in an increased force [244, 245].

$$F_1 = \frac{hr}{8\pi z^2} \tag{3.16}$$

Where *r* and *h* are the microsphere radius and material-dependent Liftshitz-Van der Waals constant respectively. Due to the adhesion force and compliance of the substrate surface roughness is reduced from its spun state and the contact area of the microsphere increases. For a compliant system the force is given by

$$F_2 = \frac{h\delta^2}{8\pi z^3} \tag{3.17}$$

where δ is the contact area radius, addition of these terms gives an estimate of the total force of adhesion.

$$F_T = \frac{hr}{8\pi z^2} + \frac{h\delta^2}{8\pi z^3} \tag{3.18}$$

Observation of Equation (3.18) one observes the importance of accurately quantifying the microsphere-interface separation distance, *z.* The latter magnitude this contact distance plays a significant contribution to the interfacial force. Using equation (3.18) the calculated adhesion force corresponds to F_T~ 280 nN and F_T ~170 nN for a sphere - SU-8 and sphere-Chitosan respectively. For a 1μm diameter microsphere the gravitational force acting on the particle, F_g corresponds to a force of F_g ~130 pN. Hence, there is a relatively strong adhesion force between a small microspheres sphere and substrate.

Returning to the microsphere removal mechanism, if the laser fluence beneath the microsphere exceeds the laser ablation threshold of the substrate the temperature may exceed both the melting and boiling point [246]. Ablation plume dynamics is a subject in its own right and to avoid the risk of oversimplifying the mechanism which direct readers to. The normal expansion *H* of the surface due to the above temperature rise is given by [243],

$$H = \alpha\left[\left(1-R_s\right)\frac{F}{\rho_s C_s}\right] \tag{3.19}$$

where α is the coefficient of thermal expansion. Inserting the corresponding numerical values (see Table 3-1) and using a fluence underneath the particle, F = 1.045 Jcm^{-2}, we calculate a particle displacement H≈280 nm for SU-8 and H≈100 nm for chitosan. However, if this expansion is realised over a duration of τ = 12 ns, and using equation (3.18),

$$a = \frac{H}{\tau^2} \tag{3.20}$$

An acceleration, a = 2.146×10^{11} m.sec^{-2} for SU-8 substrate and a= 0.7×10^{9} m.sec^{-2} for chitosan substrate. Thus, the acceleration is larger than gravitational acceleration (g) (a>>g). For a time-dependent absorption of energy as is the case for an excimer laser pulse, one can calculate the substrate displacement of the substrate [242].

$$Z_s(t) = S_0 \frac{\beta_3 A_0}{C_s \rho_s} \int_0^t \frac{I(t-t_1)\,dt_1}{1+\frac{4\chi t_1}{r_0^2}} \times \int_0^\infty \alpha dz \left[1-\sqrt{\pi}\varsigma e^{\varsigma^2} erfc(\varsigma)\right] F(z,t_1) \qquad (3.21)$$

where S_0 is the optical enhancement factor, $r_0 = (x_o\, y_o)^{1/2}$ is the width of corresponding Gaussian beam, r is the radial coordinate, α_A is the absorption coefficient, C_s is the specific heat capacity, ρ_s is the thermal conductivity, A_0 is the absorptivity, $\chi = k_s / C_s \rho$ is the thermal diffusivity of the SU-8 substrate, and the $F(z, t)$ is defined in equation (3.22).

$$F(z,t) = \frac{1}{2} e^{\alpha^2 \chi t} \left\{ e^{\alpha z} erfc\left[\alpha\sqrt{\chi t} + \frac{z}{2\sqrt{\chi t}}\right] + e^{-\alpha z} erfc\left[\alpha\sqrt{\chi t} - \frac{z}{2\sqrt{\chi t}}\right] \right\} \qquad (3.22)$$

By using Equation (3.21) if the value of the optical field enhancement, S_0=40, the SU-8 substrate displacement calculated *Zs* is close to 280 nm, while chitosan substrate displacement calculated around 100 nm.

Most of the pulse energy is absorbed by the substrate (transparent particles) resulting in a rapid rise in the substrate temperature. Due to the physical coupling between the particle and substrate momentum is transferred to the particle [3]. Microsphere ejection occurs due to the rapid pulsed laser heating. It was noted that micron sized microspheres can be ejected from the surface of a substrate at extremely low input laser fluence of ~ 45 mJ.cm^{-2}. Obviously, this low input laser fluence is due to optical filed enhancement caused by focussing. The sudden expansion of the substrate surface explains a significant microsphere ejection mechanism. Plume expansion dynamics will no doubt contribute to microsphere ejection but for the present work the ejection due to acceleration of the substrate only has considered. The timescale for this expansion is also very short (in the order of nanoseconds). The expansion amplitude can be very small, which results in strong acceleration. To quantify this acceleration, consider a free-solid surface that is completely irradiated by a uniform laser pulse of fluence, F, and pulse duration, τ. This acceleration would be much larger than gravitational acceleration. As a result, this is huge substrate acceleration that ejects the particles from substrate surface.

Sphere adhesion force was calculated by using Equations (3.16), and Table 3-1, it was found to be 280 nN, the gravitational force F_g is close to 130 *pN*. Most of the energy from

the laser is absorbed by the substrate causing the surface to vibrate, a quick thermal extension of the substrate will then appear [243]. The vibration substrate results in a force that moves the particles and is then launched out from the surface.

Table 3-1 Physical properties of SU-8 [82] *and chitosan* [247] .

Parameters	SU-8 film	Chitosan film
Coefficient of thermal expansion (K^{-1})	52×10^{-6}	0.05×10^{-6}
Reflectivity	0.05	0.04
Material density, ρ (g. cm^{-3})	1.2	1.3
Specific heat capacity, C ($J.g^{-1}K^{-1}$)	1.5	3.9
Sphere adhesion force F_T (pN)	280	170
Gravitational force *Fg* (pN)	0.013	0.013
The normal expansion, *H* (nm)	280	100
Acceleration, a (m. sec^{-2})	2.14×10^{11}	0.7×10^{9}

From Equation (3.17), we can estimate that $H\approx280$ nm between the silica particle and SU-8 substrate, compared to $H\approx100$ nm between the silica particle and chitosan substrate. However, if this expansion is achieved in the laser pulse duration of 12 ns, and by using equation (3.20), the acceleration of the SU-8 and chitosan substrates due to increasing temperature, $a_{su\text{-}8} = 2.146\times10^{11}$ m.sec^{-2}, $a_{ch} = 0.7\times10^{9}$ m.sec^{-2} respectively. These accelerations for both SU-8 and chitosan substrates are about much larger than gravitational acceleration. So the substrate vibration results in momentum transfer to the particles that accelerate then eject from the substrate.

Depending on the magnitude of laser energy absorbed, other mechanisms may contribute to particle detachment. If the laser fluence beneath the microsphere exceeds the laser ablation threshold, the substrate may exceed the melting and boiling point. In such cases, the evaporating gaseous species will impart forces in the region beneath the microsphere.

These two mechanisms are not independent, and both mechanisms play a role in the particle becoming detached. However, we have not made an attempt to deconvolve these two mechanisms. The increase in temperature, and hence boiling and physical expansion of the substrate is dependent on the degree to which the laser beam has been focussed by the microsphere.

Since the development of near-field optical microscopy and their use in characterising nanostructures. Many numerical methods have been used and developed to simulate the interaction between fabrications of nanomaterials and the electromagnetic field [248]. Two common numerical methods are used for calculating irradiation temperature and electromagnetic problems of nanostructuring materials by laser; The finite-element method (FE) and the finite-difference-time-domain (FDTD) method [249]. In this chapter, an FE model using the Finite Element Method (COMSOL®, version 5.3) simulations were also carried out to calculate the laser induced temperature rise of SU-8 and chitosan in the region beneath the microsphere. In addition, Finite Difference Time Domain (FDTD, LUMERICAL™, version 8) simulations were carried out to visualise the propagation of 193 nm radiation through a microsphere to quantify the electric field enhancement. Simulations indicate the presence of a nanojet penetrating the underlying substrate.

3.3 Laser induced temperature rise simulation using COMSOL Multi-Physics.

Development and research in the areas of heat transfer, heat exchangers and their related technologies have witnessed a prolific increase over the past few decades. The laser is usually seen as a very special and intense heat source, and only its thermal effects are to be considered [18][97]. It is important that we are capable of using the rate equations that calculate the energy amount being transferred per unit time and that we know the physical mechanisms that cause the modes of heat transfer.

3.3.1 Heat Transfer

Thermal energy is related to the matter temperature. The higher the temperature, the greater the thermal energy for a given material and mass. The study of the thermal energy exchange inside a material or between materials happens when there is a temperature variance [250]. Table 4.1 shows the standard international system (SI)and English units used for heat and heat transfer rates, including the conversion factors [251].

Table 3-2 Units and conversion factors for heat measurements

	SI units	English units

Thermal energy	1 J	9.478×10^{-4} Btu
Heat transfer rate	1 $J.s^{-1}$ or 1W	3.412 $Btu.h^{-1}$
Heat flux	1 $W.m^{-2}$	0.317 $Btu.h^{-1}.ft^{-2}$

3.3.2 Mechanisms of heat transfer

Heat can be transferred from one body to another in three mechanisms conduction, convection, and radiation mode. One of these or a combination of them is responsible for any energy exchange between bodies. While conduction is the heat transfer through solids or stationary fluids and occurs via direct contact, convection uses the mass movement of fluid to transfer heat; the fluid can be a liquid or a gas. In general, the terms natural or free convection is used if the flow is induced by heat transfer [140]. The electromagnetic radiation emitted by an object for exchanging is the heat radiation mode [252] and hence does not require a medium for heat transfer. So, heat transfer as a result of the emission of the electromagnetic waves is known as thermal radiation.

Consequently, there is a net heat transfer from a matter of high temperature to matter of lower temperature. The laser heating nature is to change the internal microstructure of material by absorption of energy. The material absorptivity of laser light is a serious factor that affects the deformation process. The temperature rises with the absorbed energy and the constant of heat transfer [253]. In general, there are three types of heat transfer by (a) conduction, (b) convection and (c) radiation.

Figure 3-2 shows the schematic diagram of the laser-material interaction process. When the laser beam is irradiated on the top surface of the target, a series of complicated physical and chemical phenomena happen in the laser interaction process and irradiated material, which contains two phases: the first phase is the absorptivity and reflectivity of the material's surface to the incident laser and the second phase is the heat transfer modes

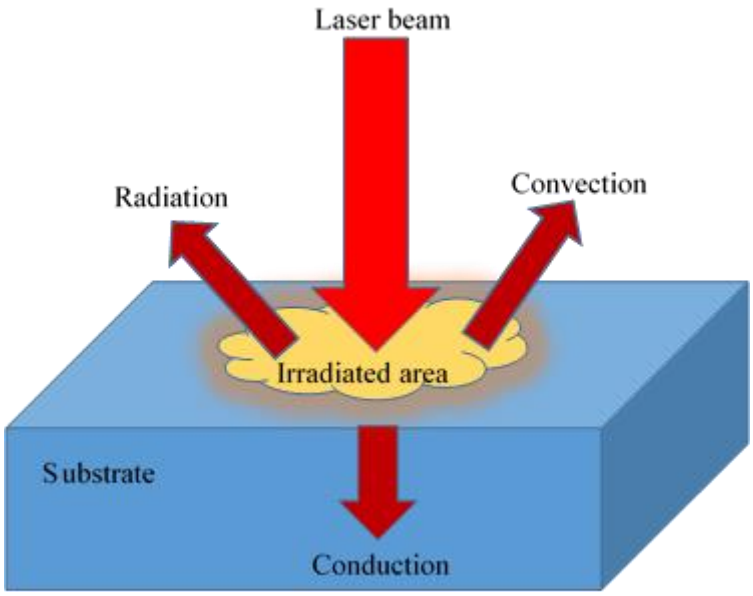

Figure 3-2. Modes of heat transfer

3.3.3 Finite element method

The standard numerical calculation scheme for the computer simulation of physical systems has become the finite element (FE) method, for example, the heat equation or integral equations with a numerical approximation [254]. The matter of interest is, therefore divided in a finite number of elements. In these elements, functions are applied to find approximate solutions in combination with the starting and the boundary conditions [140]. For the discretisation of both structures, 2D and 3D, the finite element (FE) approach is superior. Due to the implicit or iterative form or the mass matrix formulation, for example, most of the Finite element -based time-domain methods informed so far suffer from limitations. Therefore, its simulation speed is much slower than the FDTD method. A very resource-intensive numerical technique is the time domain analysis of electromagnetic [255].

Dividing the region of interest into sub-regions, or elements, which consist of nodal points and defining the type of "shape" at each an element end is the first step. A quadratic element has a third node placed at the element midpoint; a cubic element contains four nodes, spread out at intervals. FE mesh is the term used for the collection of elements and nodal points. The shape functions typically used in the procedure is directly linked to the type of mesh chosen [256].

3.3.4 COMSOL™

Computer programs like COMSOL ™ Metaphysics can be applied to solve the numerical problem. COMSOL ™ Multiphysics is a cross-platform finite element analysis, solver and multiphysics simulation software. There are different modules available, to provide software solutions for multiphysics problems are available in the software package. The individuality of COMSOL ™ Multiphysics, over other FEA software packages, is its capability to solve coupled phenomena [257]. These are phenomena for which the solution of each physical problem cannot be achieved independently of the others.

Numerous engineering and physics-based problems can be easily solved by these modules. Other than the designed modules, it also offers partial differential equations (PDEs) based modelling which can be entered directly. PDEs describe many phenomena in nature. While these equations can be simplified and solved theoretically for simple problems, it is not possible to find the answer analytically for complicated structures, which exist in the real world, to solve this issue, numerical methods and simulation software like COMSOL™ Multiphysics® is used.

One can easily access all the functionality and get an overview of a built-in model builder in a powerful integrated desktop environment provided by the software.

Finite element method (FEM) is used by COMSOL ™ Multiphysics to solve equations. It is possible to identify material and physical properties and define parameters [88], [139] using the built-in physics interfaces. The COMSOL ™ 5.3 interface is divided into several sections, which are described as;

1- Parameters: In this section, the non-variable parameters are defined, which stay constant during the simulation. These include pulse energy, laser spot radius, laser fluence, reflectivity, absorption coefficient, and the laser pulse duration.

2- Variables: the variables of the simulation are defined. Variables are defined as anything which varies with the dependents of the simulation, in this lattice temperature (T) and time (t).

3- Geometry: Here, the geometry of the simulation is defined. In this case, two rectangles are created, representing the film and substrate.

4- Materials: The material parameters are defined in this section, for both the film and substrate. This includes the thermal conductivity, heat capacity at constant pressure, and the density.

5- Heat Transfer Module: The 2-D heat equation is solved concerning the parameters and variables defined.

6- Mesh: The mesh of the geometry is defined. The mesh was set as a free triangular mesh, and the size of the mesh set to 5 nm.

7- Study Sequence: The model sequence is generated. The time step variables are set, typically starting at 0 ns, to 2000 ns, in 1 ns steps.

3.3.5 Modelling the temperature rise of irradiated laser SU-8

The Electric field enhancement under the microsphere causes an increase in temperature under the microsphere (inside the substrate). Knowledge of the localised SU8 substrate temperature is a useful quantity for understanding the mechanism of hole formation. Simulations of temperature were carried out using COMSOL® Multiphysics 5.3 software. A one dimensional, 1D, model was set up by scaling the incident laser fluence by the field enhancement due to the focusing effect of the microsphere. Numerical simulation based on the finite element method makes it possible to address problems related to applications of physics and engineering, particularly coupled phenomena and multiphysics [257].

When a laser irradiates a solid material, its temperature rises, and it will eventually undergo a phase transition. This transition can be either via a liquid phase or directly to a gas phase. The ability to precisely control material heating, penetration depth, and removal rate can be achieved by manipulating laser beam parameters such as the pulse duration, wavelength, and fluence (or intensity) [91]. It is assumed that the process occurs due to material evaporation caused by heating from nanosecond pulses. Boundary conditions were used to simulate the heat increase due to the ablation of the material. When it reaches its ablation temperature, it changes to the gaseous state and is removed from the modelling domain. Therefore, the solid material cannot become hotter than its ablation temperature, and when the material reaches this temperature, there is a loss of mass from the surface (SU-8). This is governed by the material density and the heat of the simulation. The solids module of the software simulates heat conduction by

calculating heating and cooling rates in a substrate due to conduction, convection and radiation. For solid materials over short time durations, heat conduction is the dominant mechanism. Temperature gradients in the material drive conduction. The diffusion of heat in a substrate due to conduction can be calculated using the heat equation (3.23)

$$\rho C_\rho \frac{\partial T}{\partial t} + \rho C_\rho U \cdot \nabla T + \nabla \cdot q = Q + Q_{ted} \tag{3.23}$$

This module takes the material density (ρ), material temperature (T), thermal conductivity (k), and specific heat capacity (C_ρ) as inputs. The user defines the heat source (Q); for laser heating models, Q_{ted} the thermoelastic damping, the source has a top-hat spatial distribution and pulses periodically over time. Typically, k and C_ρ are dependent on temperature and are recalculated at each iteration of the solver.

An important condition for solving the heat equation is the description of boundary conditions. The boundary conditions might be defined as constant values or variables as functions of different parameters. There are three different boundary conditions specified below [258]. Figure 3-3 illustrates the Schematic diagram of boundary conditions for heat diffusion equation at the surface (x=0).

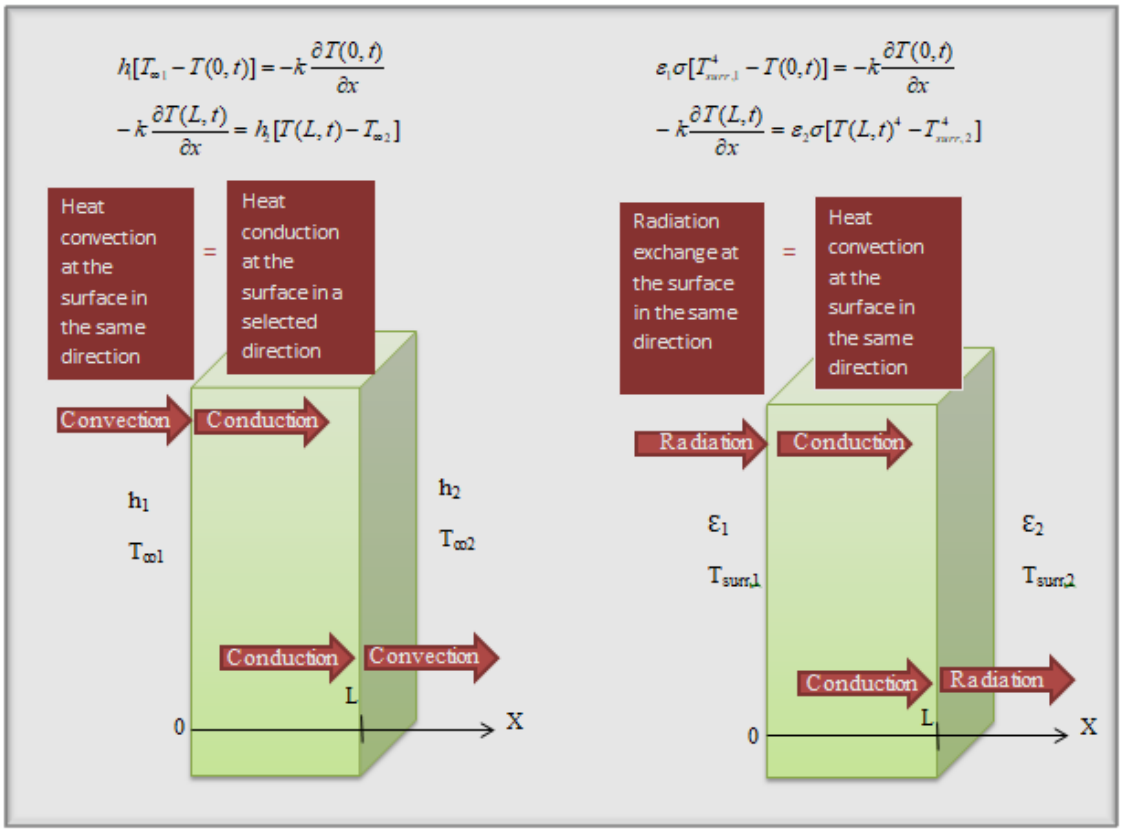

Figure 3-3. Schematic diagram of boundary conditions for heat diffusion equation at the surface (x=0 and x=L)

Where T_∞ is the convection boundary condition. Heat-diffusion coefficient is an important property of all materials, it is the thermal conductivity divided by both density and specific heat capacity at constant pressure as shown in equation (3.24) [102].

$$D = \frac{K}{\rho C} \tag{3.24}$$

To model this element, the default solver settings are used for heat transfer studies, except the time step, which was set to 'strict'. This forces the solver to recalculate at each of the manually defined individual time steps, as well as any necessary intermediate steps. A triangular mesh was chosen for all simulations. Two-layer geometry was implemented, consisting of air at the front surface of the solid SU-8. Both conduction and convection at the surface were used in the simulation, and radiation losses were assumed to be negligible. To represent the gas state, when the material temperature exceeds its boiling point, it is assumed that the material evaporates, and elements of the part would be removed.

Figure 3-4. A and B shows the temperature distribution of a SU-8 material during one laser shot compared with the analytical solution. When the temperature of a part exceeds the boiling point of ~500 K, the portion is removed and its property changes to a gas phase. The temperature calculations correspond to laser fluences of 1045 $mJ.cm^{-2}$ at 193 nm wavelength and 11.5 ns pulse duration. The optical penetration depth of the laser is reciprocal to the absorption coefficient. It becomes high in the UV range because photo-resist material (5 µm film thickness) has a high absorption coefficient of around 3.9×10^{5} cm^{-1} at 193 nm wavelength. Therefore, the ablation efficiency is affected more by the absorption coefficient value rather than the surface reflectivity. Simulations were performed as a function of time and distance moreover, simulation results produce an overestimated ablated zone radius compared to the measurements made using an SEM (250 nm simulated instead of 150 nm experimental for a laser fluence of 1045 $mJ.cm^{-2}$). This difference can be explained by the fact that the changing of the optical properties of the sample surface through irradiation were not taken into account in this simulation. The parameter study is performed to see the most effective condition of the ablation process. It is notable that the optimal ablation condition depends on the type of material, wavelength of the laser and laser fluence, and so forth. However, it is expected that the simulation results recognised in this study may contribute to the improvement of the ablation process using the nanosecond pulsed laser.

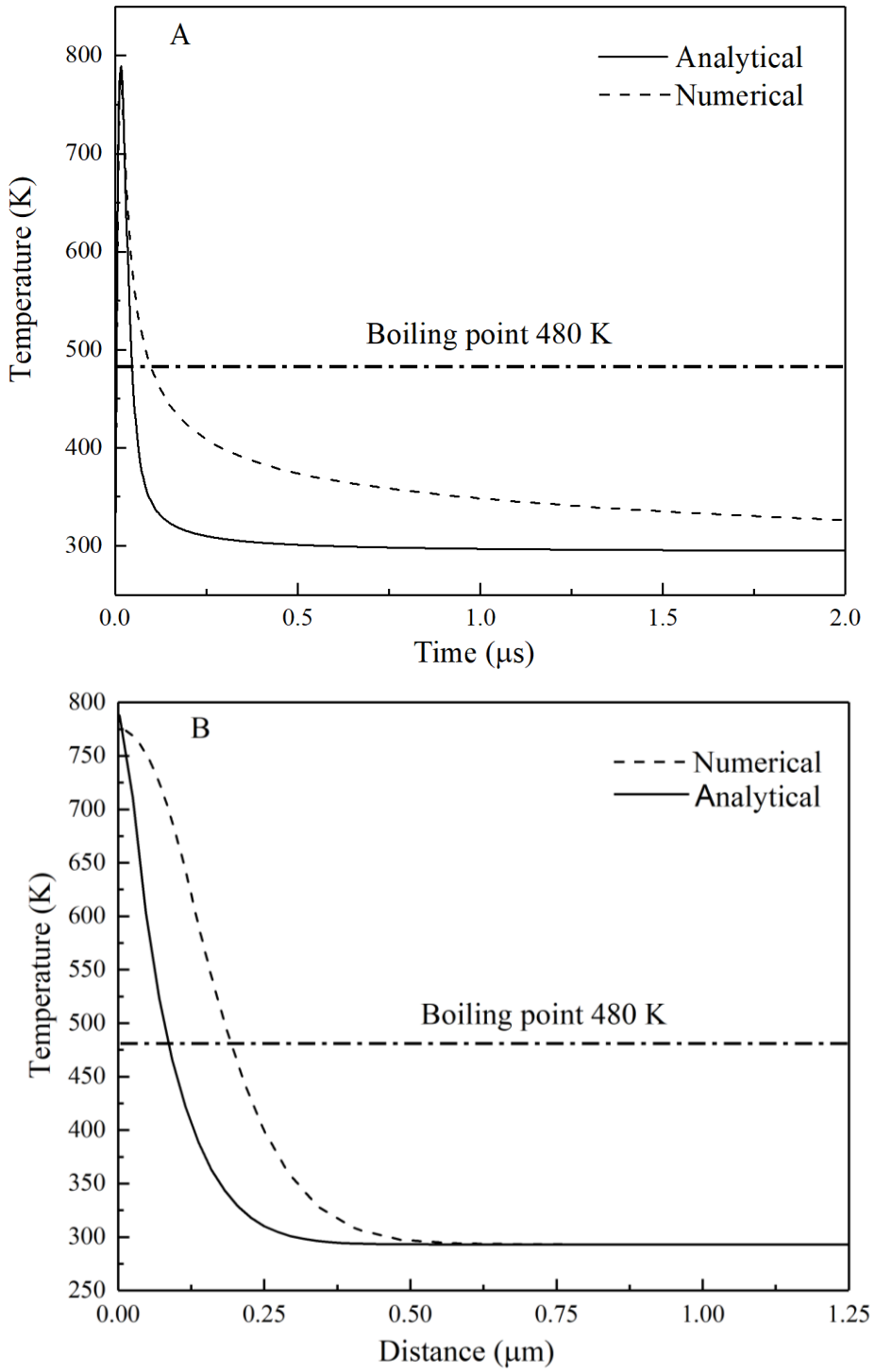

Figure 3-4. A and B show the temperature profile modelling by COMSOL (Numerical) and analytical by using equation (4.1) as a function of time and depth, respectively. The results show temperature inside the SU-8 substrates under the microlens (silica particles) of 1μm diameter within 193 nm laser radiation using an incident laser fluence of 45 mJ. cm^{-2}, in the temporal domain (A) and the spatial domain (B). The initial temperature of the substrates was 295.15 K in both (A) and (B).

3.3.6 The temperature rise of laser irradiated chitosan

Laser-irradiated chitosan was simulated, again with a triangular mesh. A two-layer geometry of solid Chitosan was created to an air interface. Radiation losses were assumed to be negligible, and both conduction and convection at the surface were used in the simulation. FE model is used to predict temperature rise and quantify the thermal dose resulting from laser irradiation of excited chitosan film sample. The laser pulse duration used in the simulations is 11.5 ns at FWHM. The computations were carried out using COMSOL™ Multiphysics 5.3 software to calculate the temperature rise of chitosan due to pulsed laser irradiation at fluence of 45 $mJ.cm^{-2}$ underneath the microparticle.

The results for the temporary and spatial temperature compared with the analytical solution. are shown in Figure 3-5. The curve has been calculated using the corresponding laser fluence to ablate the chitosan material due to rising temperature less than degradation temperature of chitosan (490 K). The point reached the peak temperature of 460 K at 11.5 ns after the laser began to heat the surface. The temperature of the target mostly depended on the effect of the laser heating and the thermal diffusion in a three-layer geometry which consists of air, chitosan film that was coated on a soda-lime glass substrate. The results show temperature inside the chitosan substrates underneath the silica particle of 1μm diameter within 193 nm laser radiation using an incident laser fluence of 45 $mJ.cm^{-2}$, in the temporal domain (Figure 3-5. A) and the spatial domain (Figure 3-5 B). The initial temperature of the substrates was 295.15 K.

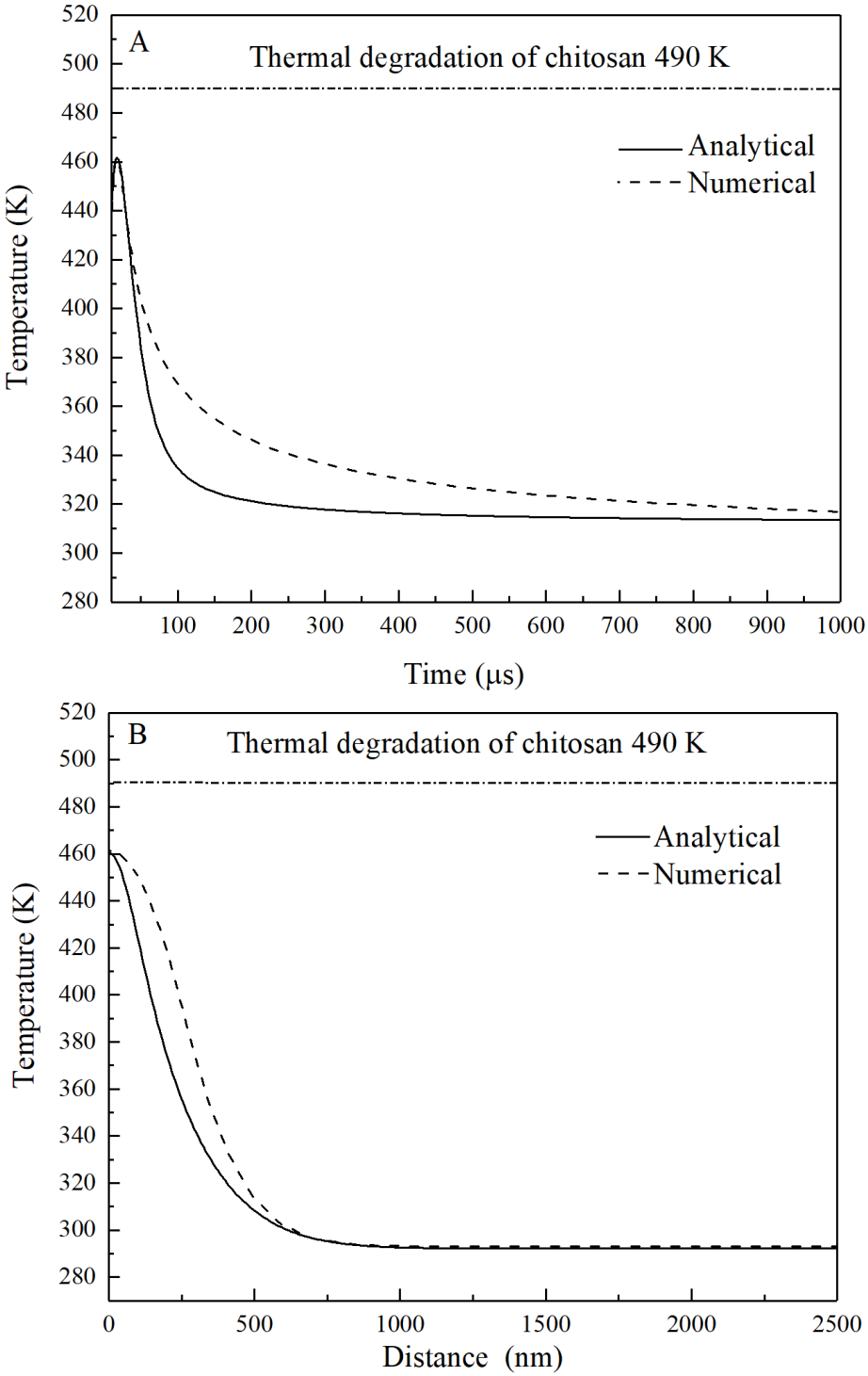

Figure 3-5. A and B show the temperature profile modelling by COMSOL (Numerical) and analytical by using equation (4.1) as a function of time and depth, respectively. The results show temperature inside the chitosan substrates under the microlens (silica particles) of 1μm diameter within 193 nm laser radiation using an incident laser fluence of 45 mJ.cm^{-2}, in the temporal domain (A) and the spatial domain (B). The initial temperature of the substrates was 295.15 K in both (A) and (B).

3.4 Electric field modelling

Much attention has been given to the Near-field patterning of a substrate surface, produced by irradiation of the laser, at a spatial resolution under the diffraction limit. This technique has been used in the fields of medical diagnostics, non-linear optics, biophotonics, optical data storage systems, solar cell and plasmonics nanostructure [118]. Using an AFM tip in scanning tunnelling microscopy mode and illuminated by a laser is one typical method for near field nanofabrication. Between the tip and substrate surface, field-enhancement and thermal-induced mechanical contact are provoked, causing nanopatterns to be written [259]. Optically controlled nanolithography and nanofabrication, due to photothermal energy and optical force generated by a tightly focused laser beam [260]. Illuminating of spherical particles on substrates by a laser has also been widely investigated [107], [111], [119], [134], [235] regarding high throughput nanofabrication. Problems arising in nanophotonics are often investigated using the finite-difference-time-domain (FDTD) numerical electromagnetic method. In the FDTD method, the electromagnetic field is defined for a finite number of discrete spatial positions and calculated at consecutive discrete time intervals using an explicit leapfrogging algorithm [261].

3.4.1 Finite-difference time-domain method

The Finite Difference Time Domain (FDTD) method is a multipurpose technique and a powerful tool that can allow for the efficient and accurate simulation of electromagnetic phenomena which are governed by Maxwell's equations over the last decade since Yee [262] proposed it in 1966. It has been applied to numerous problems of propagation, radiation, and scattering of electromagnetic waves. It is a numerical technique based on the finite-difference concept used to solve Maxwell’s equations for electric and magnetic field distributions in the time and space provided that an accurate analytical law of dispersion is used, FDTD is well adapted for studies of spectroscopic. Full-spectrum results can be found in a single run of the program [263] and are offered by this method. The majority of the FE-based time-domain methods stated so far suffer from limitations because of the implicit or iterative form or the mass matrix formulation, for instance, the FE approach is superior for the discretisation of both 2D and 3D structures. Thus, the simulation speed of FE is much slower than the FDTD method.

Time-domain analysis of electromagnetism is a very resource-intensive numerical technique. The FE based methods are not as common as the FDTD method [255] due to the slow performance. The equations with second-order accuracy can be discretised by FDTD methods which store different field components located at different points in a unit cell (grid). This discretization is known as a Yee lattice. All calculated results are done locally to each Yee's lattice, the only memory it occupies is the memories for electric and magnetic field components and the material properties for each cell in the computational domain. Compared to methods forming global matrices, the method's memory requirement is very low [264].

3.4.2 LUMERICAL Finite-difference time-domain

Using a commercial 3D Maxwell solver called Lumerical FDTD, analyses the interaction of IR – UV radiation with complicated structures employing subwavelength scale features. The Numerical FDTD was performed using this program. The software employs an FDTD method in the form of a 3D Maxwell solver [118]. To better understand the near-field underneath the micro-particles, we carried out three-dimensional (3D) FDTD simulations, using a commercial software package (Lumerical Solutions). Optical simulations are useful for visualising field enhancement and near field effects. The particular choice of software is often dictated by the scale size of the optical system. For example, for a microsphere of one micron in diameter, we chose to adopt the software package Lumerical™ version 8.19.1522.

3.4.3 Results of finite difference time domain simulations.

Figure 3-6. (A-C, top)and (A-C,down) shows the electric field distribution in the xz plane calculated by FDTD for 193 nm laser propagation through 1µm sapphire (n= 1.92 at 193 nm wavelength) microsphere and 1µm diamond (*n*= 2.93 at 193 nm wavelength) microsphere respectively, The incident light is the plane wave in the z-direction and it is linearly polarized along x-direction , the substrate is a flat SU-8 (*n*=1.8 at 193 nm wavelength) surface (left) and chitosan (*n*=1.75 at 193 nm wavelength) surface (right). Figure 3-6. A. presents the cross-section of the electric field distribution below the microsphere at the centre of the nanojet along the x-axis. Figure 3-6.C. shows the cross-section of the electric field distribution along the beam propagation direction in the z-direction.

Figure 3-7. (A-C, top)and (A-C, down) explains the peak intensity distribution in xz plane calculated by FDTD for 193 nm laser propagation through 1µm sapphire microsphere and 1µm diamond microsphere respectively, the incident light is the plane wave in the z-direction and it is linearly polarized along x-direction , the substrate is a flat SU-8 surface (left) and chitosan surface (right). Figure 3-7. A. shows the ross-section of the peak intensity distribution below the microsphere at the centre of the nanojet along the x-axis. Figure.C. illustrates the Cross-section of the peak intensity distribution along the beam propagation direction in the z-direction. From both figures below it can be seen that the particle nanojet is produced near to the centre of the diamond micro particle while it is near to the bottom of the sapphire micro particle because of the refractive index of the diamond material higher than the refractive index of the sapphire material at 193 nm wavelength. However, the spot diameter at FWHM is inversely proportional with refractive index of microparticle. As a result, the spot diameter of the laser beam in focal region of the sapphire and diamond microlenses are ~ 68 nm and ~ 45 nm respectively.

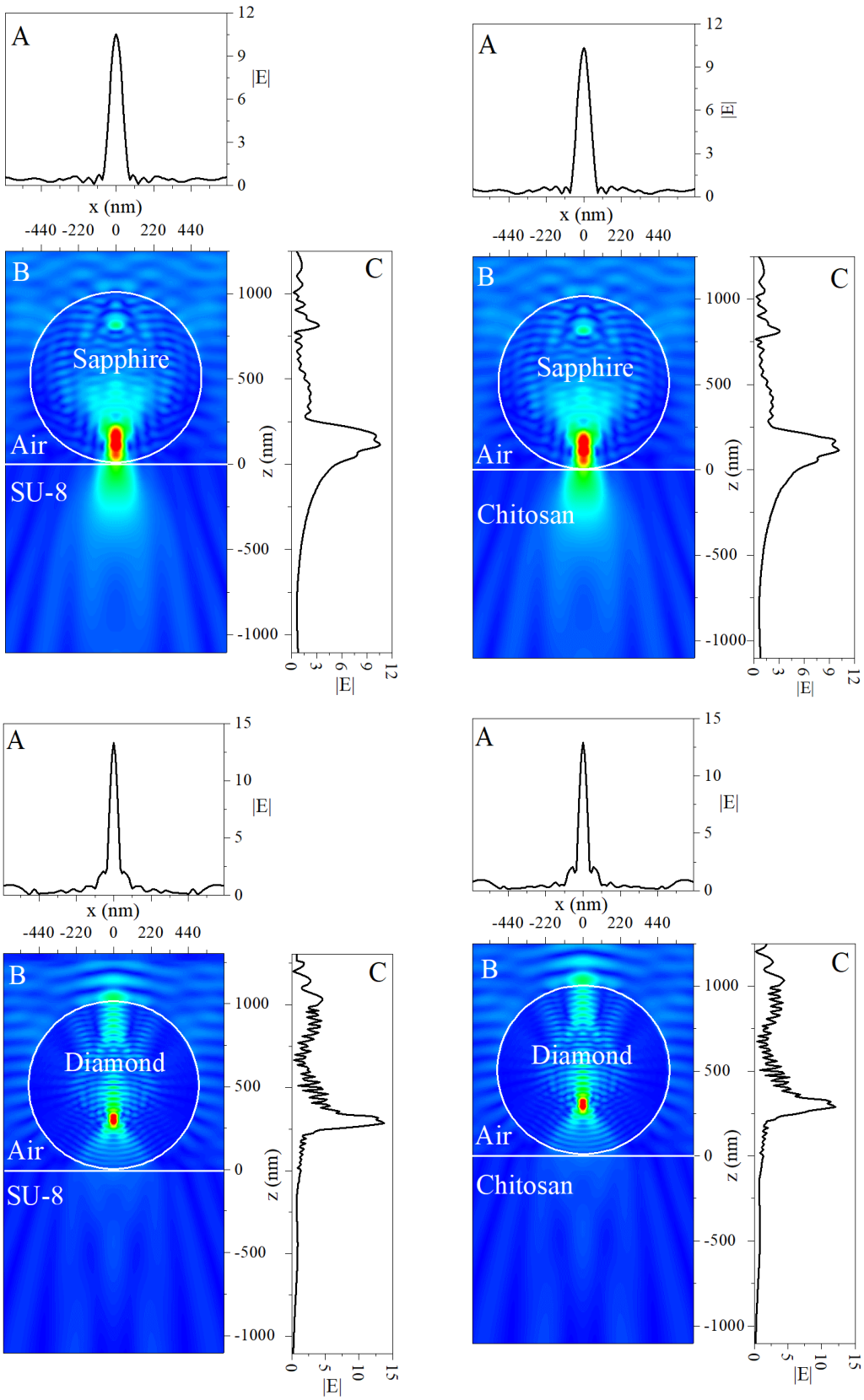

Figure 3-6. (A-C, top) and (A-C, down) The electric field distribution in xz plane calculated by FDTD for 193 nm laser propagation through 1μm sapphire microsphere and 1μm diamond microsphere respectively. The incident light is the plane wave in the z-direction and it is linearly polarized along x-direction, the substrate is a flat SU-8 surface (left) and chitosan surface (right). (A) Cross-section of the electric field distribution below the microsphere at the centre of the nanojet along the x-axis. (C) Cross-section of the electric field distribution along the beam propagation direction in the z-direction.

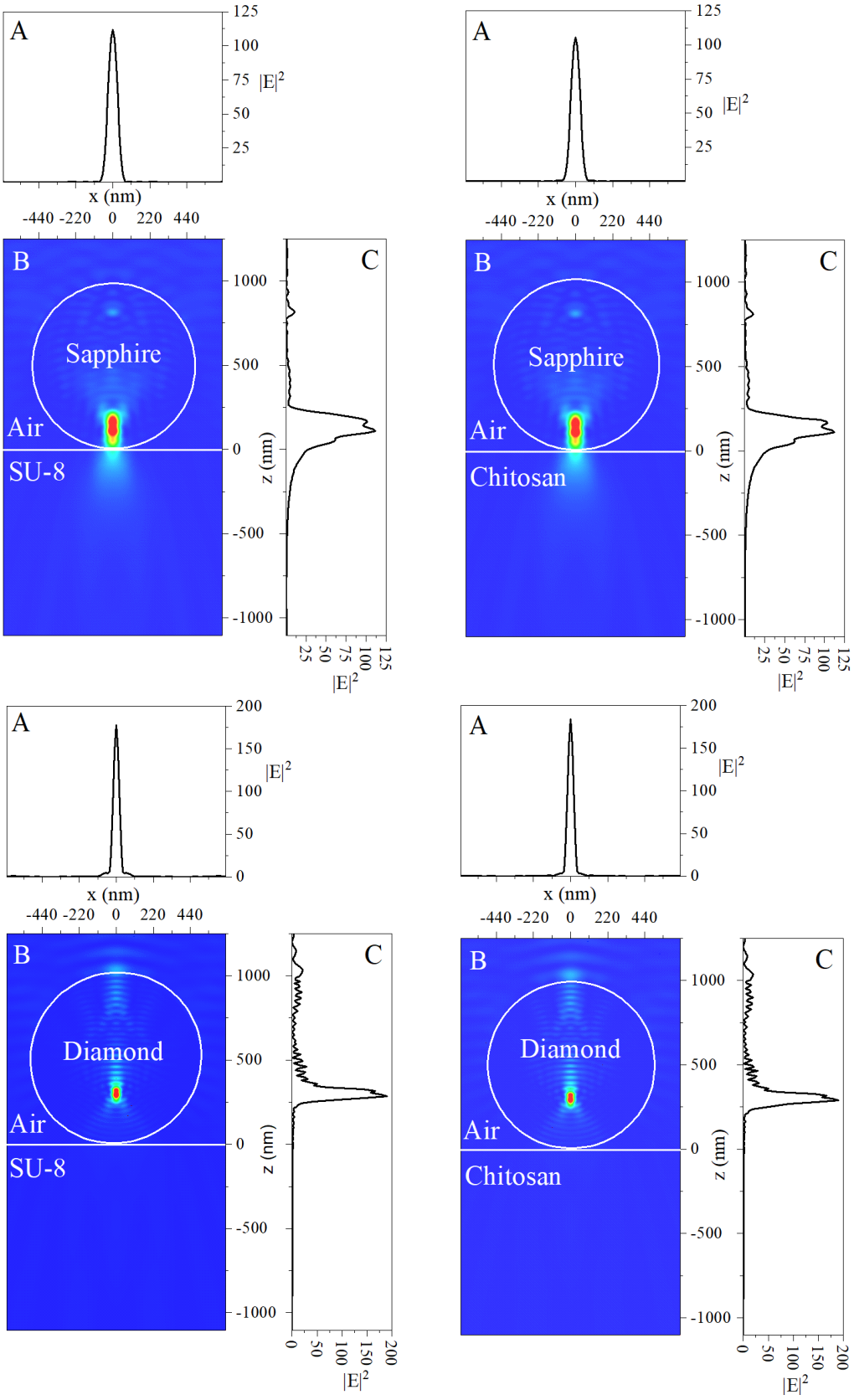

Figure 3-7. (A-C, top)and (A-C, down) The peak intensity distribution in xz plane calculated by FDTD for 193 nm laser propagation through 1µm sapphire microsphere and 1µm diamond microsphere respectively, The incident light is the plane wave in the z-direction and it is linearly polarized along x-direction , the substrate is a flat SU-8 surface (left) and chitosan surface (right). (A) Cross-section of the peak intensity distribution below the microsphere at the centre of the nanojet along the x-axis. (C) Cross-section of the peak intensity distribution along the beam propagation direction in the z-direction.

Due to sub-micro dimple needs to be simulated on flat substrate, two systems were simulated by using silica microsphere which has refractive index (1.56 at 193 nm wavelength) lower than refractive index of substrate. The first computational domain simulates a one-micron diameter silica (SiO_2) spherical focusing element in the air. The other a microsphere located on a 1µm thick SU8 and chitosan substrates. The optical system was illuminated with linearly polarised light in the x-direction using 193 nm EM radiation. The software employs a finite-difference-time-domain (FDTD) method in the form of a 3D full numerical solution of Maxwell's equations [15].

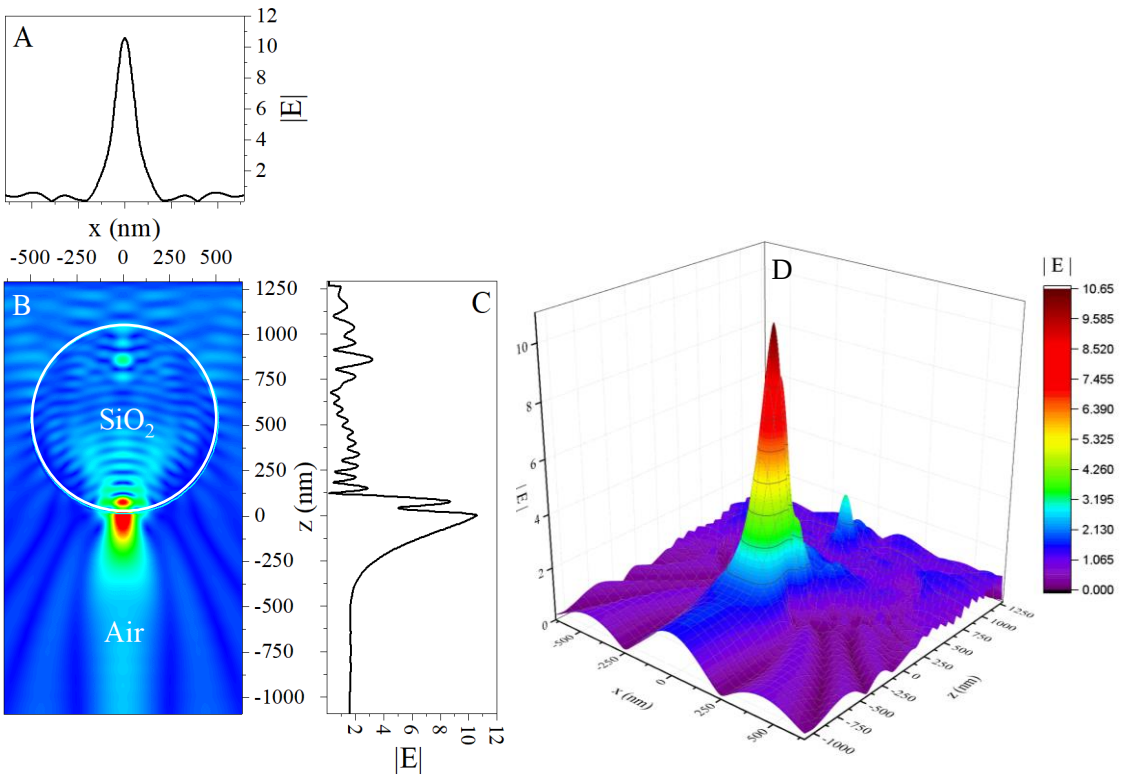

Figure 3-8. FDTD modelling of the laser propagation through a silica microsphere (1 µm diameter) and air. (A) |E| distribution in xz-plane underneath the microsphere, (B) and (C) is the beam profile of absolute intensity in x and z-direction respectively. (D) 3D surface plot of the optical intensity at the focal length ~10 nm under the microparticle silica.

Figure 3-8 show FDTD modelling of the laser propagation through a silica microsphere (1 µm diameter) and air (no substrate). Figure 3-8.A. shows electric field distribution in xz-plane underneath the microsphere, Figure 3-8 .B and C present the beam profile of absolute intensity in x and z-direction respectively. Figure 3-8 .D. shows the 3D surface plot of the optical intensity at the focal length ~10 nm under the microparticle silica.

Figure 3-9.A. shows |intensity distribution in xz-plane underneath the microsphere, while (B) and (C) show the beam profile of absolute intensity in x and z-direction respectively. Finally (D) shows the 3D surface plot of the optical intensity at the focal length, ~10nm under the microparticle silica.

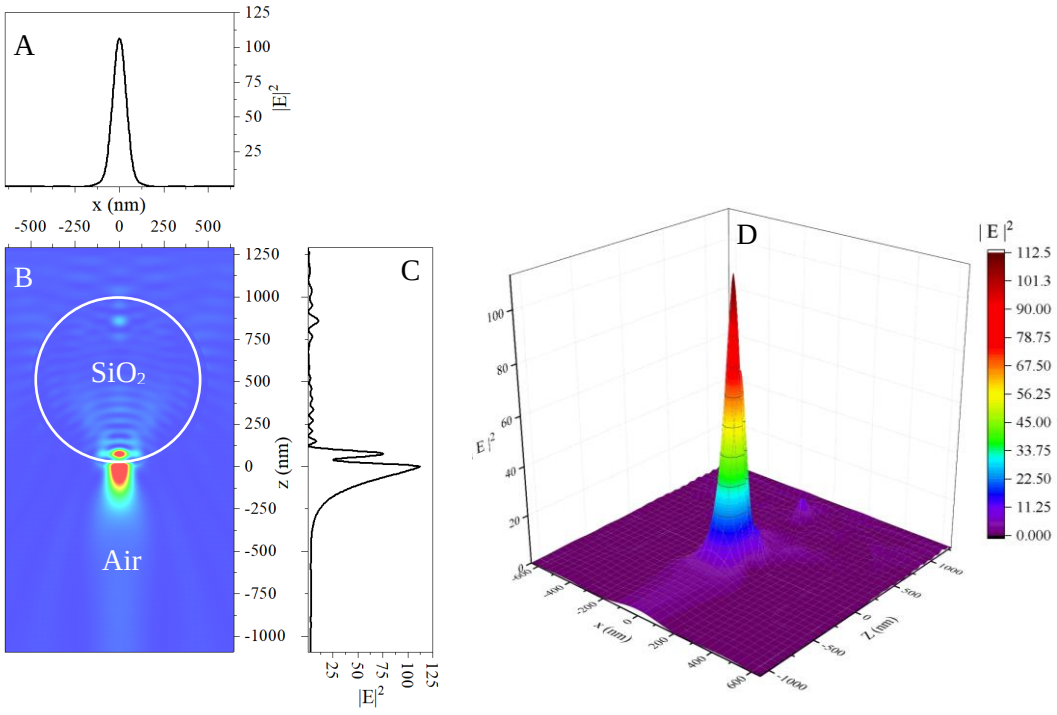

Figure 3-9: FDTD modelling of the laser propagation through a silica microsphere (1 µm diameter) and air. (A) $|E|^2$ distribution in xz-plane underneath the microsphere, (B) and (C) show the beam profile of absolute intensity in x and z-direction respectively. (D) 3D surface plot of the optical intensity at the focal length, ~10nm under the microparticle silica.

It can be seen, the diameter of the electric field profile in the x-direction is 106 nm and close to 400 nm in the z-direction (see Figure 3-8) .while the shape of intensity profile produced the diameter of intensity shape about 80 nm in the x-direction and about 300nm in as shown in in the z-direction Figure 3-9.

3.4.4 The electric field of SU-8 (GLM2060) and micro-silica (SiO_2)

The refractive index used in the simulations were n = 1.56 at 193 nm wavelength for the SiO_2 microsphere [24]. For the SU-8 (GM1060) substrate, we set the thickness to be 1 µm and a complex refractive index of n= 1.8 + 0.006i at a wavelength of 193 nm [25]. In the calculations, we used a 2 nm grid spacing in each direction. The boundary conditions

were implemented by introducing a stretched coordinate perfect matching layer around the structure. Calculations were terminated when the field decayed to 10^{-5} of its original value. The aims of the simulations are to find the spatial shape of the intense field region, to identify the location of the focal region along the beam propagation direction and to investigate the lateral spot size. This information can then be used to predict the temperature of the underlying SU-8 substrate and to compare the focal region with the physical hole in the SU-8 substrate.

Figure 3-10 shows the shape of the electric field enhancements is elliptical, with an about 95 nm diameter in the x-direction and a 500 nm diameter in the z-direction at FWHM. Most of the laser energy is absorbed inside the SU-8 substrate normally beneath the particle.

D

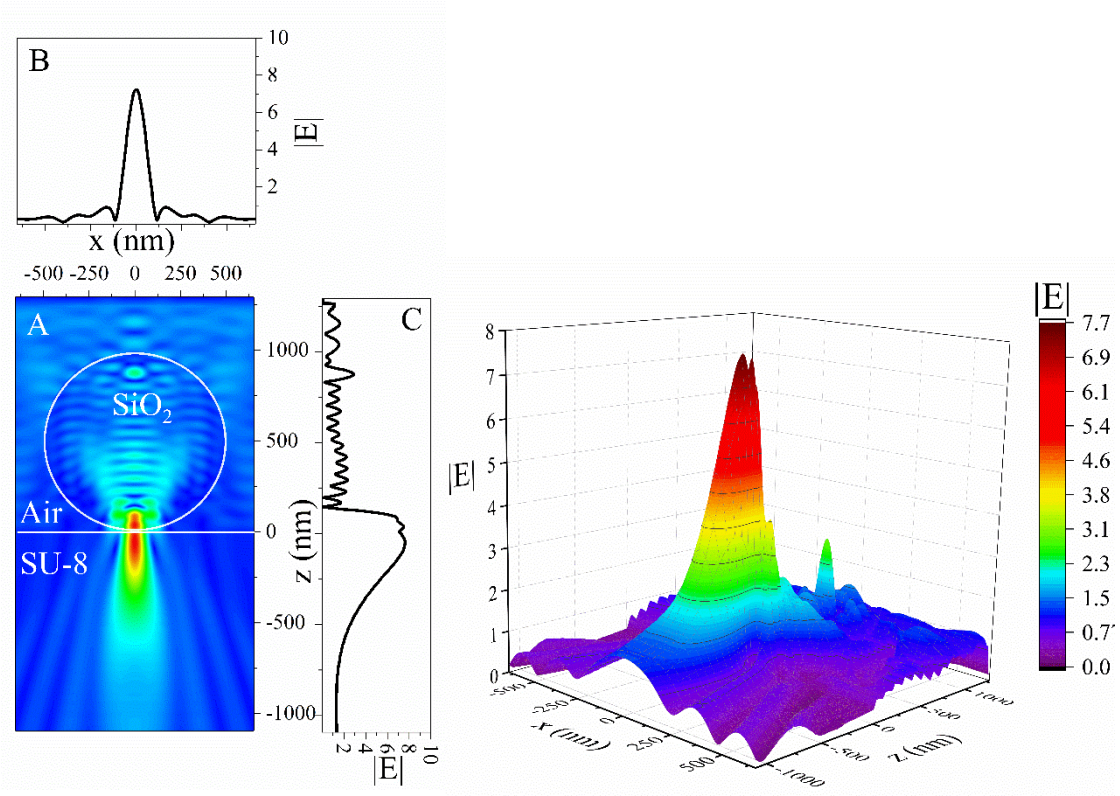

Figure 3-10 FDTD simulation of the Electric Field for 193 nm laser propagation through a silica microsphere (1um diameter in the focal region (A), cross-section of the peak electric field along the x-plane

(B), cross-section of the peak electric field along the beam propagation direction in the z-plane (C) and 3D surface plot of the electric field in the focal region under the microparticle silica (z=130nm) (D).

Figure 3-11 shows the distribution of the intensity, or $|E|^2$,(the diameter of intensity profile 70 nm at FWHM) under a single microsphere in the presence of the SU-8 substrate. The laser propagation direction is indicated by z-direction, and the electric field and Intensity is calculated in both xz-plane. It can be seen that a very small area in the substrate underneath the microsphere absorbed the laser energy. The profile of the intensity approximates a Gaussian distribution; the electric field intensity is the highest in the focal point (130nm) of microparticle (lens) inside the substrate. The intensity distribution ($|E|^2$) also changes at a later stage when SU-8 ablation starts, by the time of which the initial setup for the simulation is violated

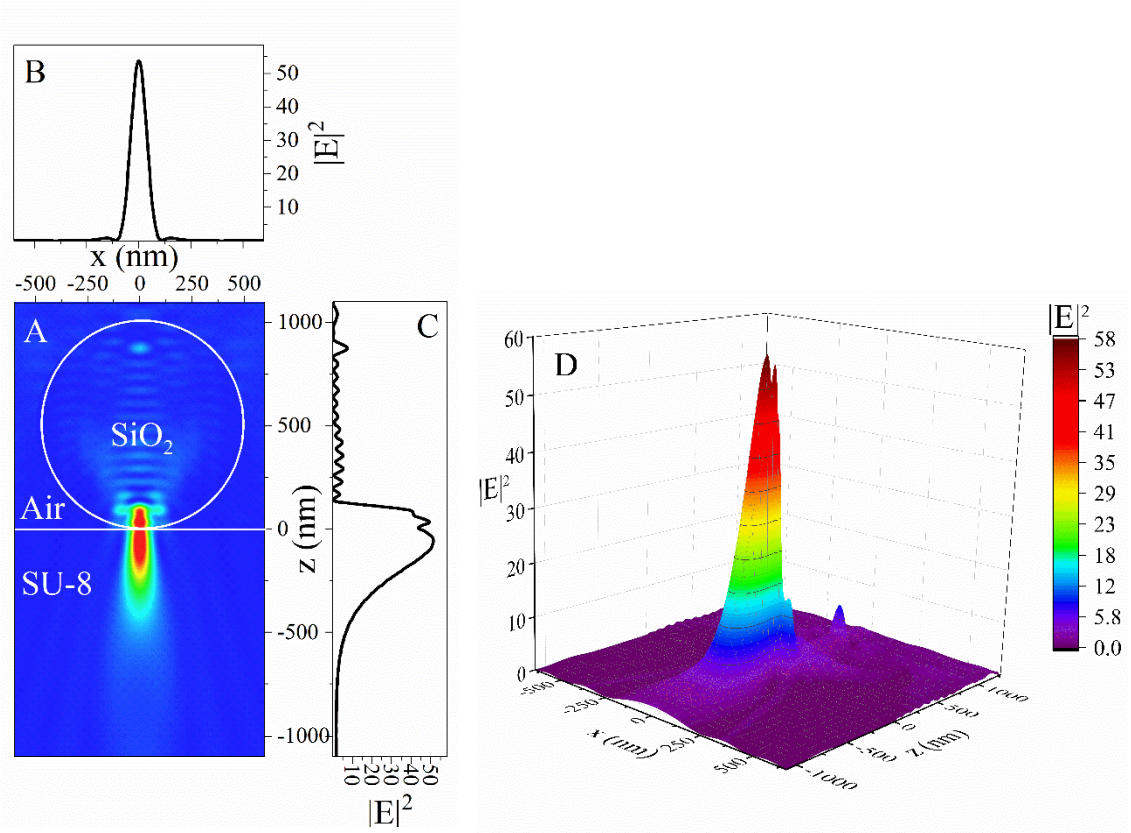

Figure 3-11 FDTD simulation of the intensity for 193 nm laser propagation through a silica microsphere (1um diameter in the focal region (A), cross-section intensity of the peak intensity along the x-plane (B) and in the z-plane (C) and 3D surface plot of the intensity in the focal region under the microparticle silica (z=130nm) (D).

3.4.5 The electric field of chitosan and micro-silica (SiO_2)

The same parameters of simulation that done above were repeated only the substrate was changed by using chitosan film with a complex refractive index of n= 1.7 + 0.0046i as a substrate and the modelling results as shown below in

Figure 3-12 and 13. Electric field profile underneath the particle investigated (see

Figure 3-12) which signifies the electric filed diameter 102 nm in the x-direction and about 600 nm in the z-direction at FWHM, while the intensity is represented in Figure 3-13 which shows the diameter of the intensity profile 76 nm at FWHM too.

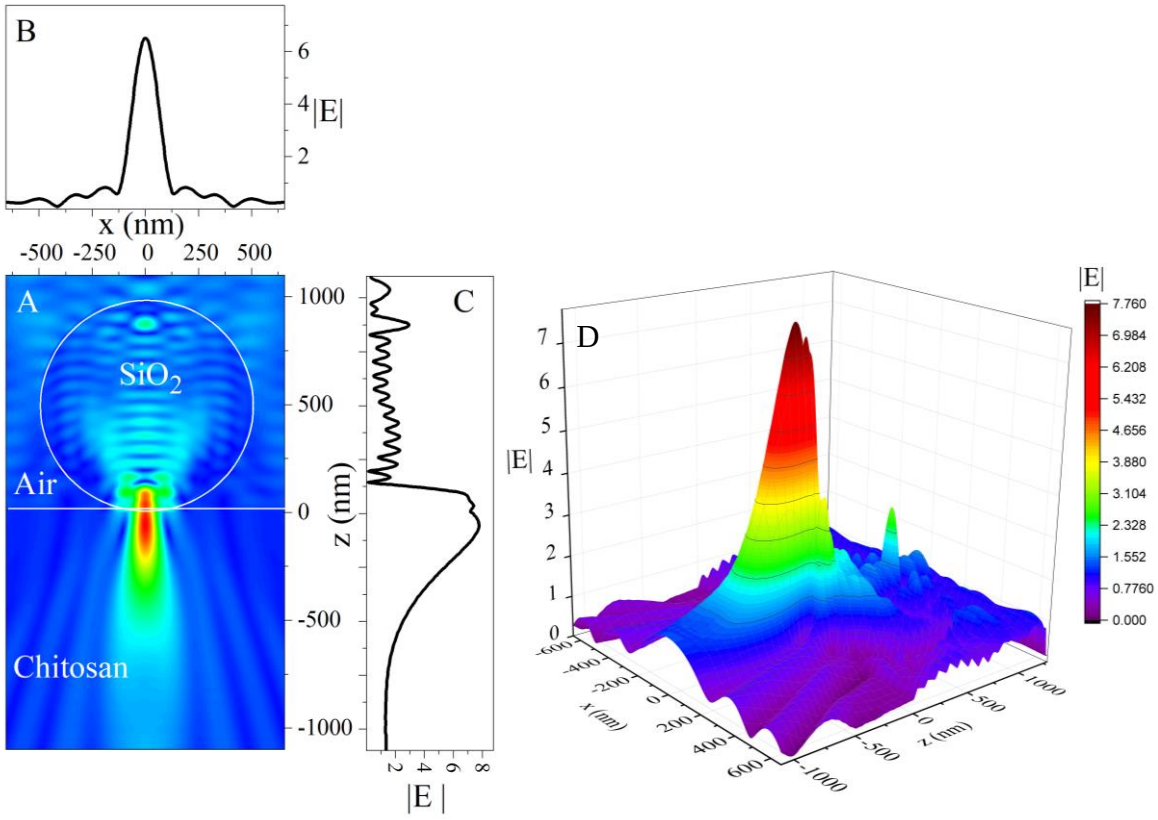

Figure 3-12 FDTD modelling of the laser propagation through a silica microsphere (1 µm diameter). (A) |E| distribution in xz-plane inside the microsphere and chitosan substrate, (B) and (C) are the beam profile of absolute electric field in x and z-direction respectively. (D) 3D surface plot of the optical electric field at the focal length under the microparticle silica (z=130 nm).

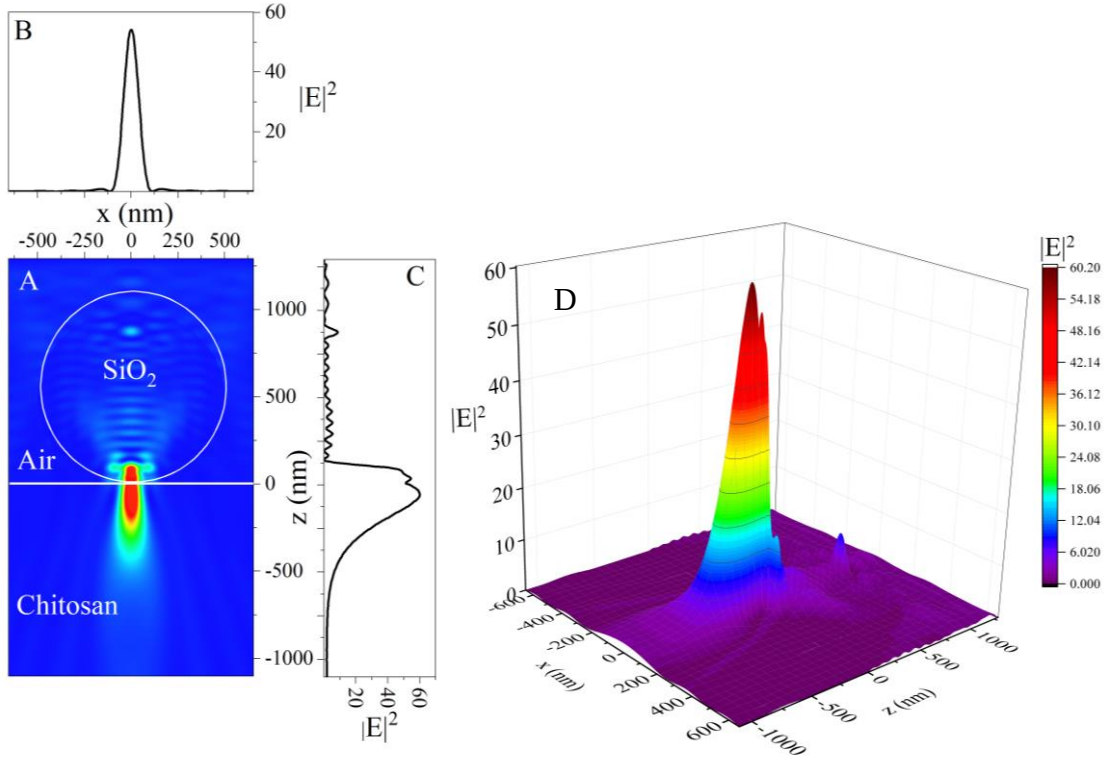

Figure 3-13 FDTD simulation of the laser propagation through a silica microsphere (1 µm diameter in the focal region (A) Absolute intensity in xz-plane inside the microsphere and chitosan substrate, (B) and (C) are the beam profile of absolute intensity in x and z-direction respectively. (D) 3D surface plot of the optical intensity at the focal length, ~140 nm under the microparticle silica.

Table 3-3 FDTD results for both silica:SU-8 and silica:chitosan

Material System	Focal length (nm)	Electric field | E | , $V.m^{-1}$	Intensity | E |2 , $W.m^{-2}$	Spot diameter at FWHM |E| profile, (nm)
Silica: Air	10	10.5	110	110
Silica:SU-8	130	7.5	55	91
Silica: Chitosan	140	8	60	102

3.5 Methodology

3.5.1 SU-8 and silica particle film preparation

The substrate consisted of standard soda lime glass microscope slides were sonicated using Deionized water, Acetone and Isopropanol for 10 min, respectively (UW ultra-wave mode QS5, ultrasonic cleaner). The substrate was blown dry using nitrogen gas for two minutes to remove residual solvent. After a short period the substrates were left to cool back down to ambient temperature. SU-8-negative tone photo-epoxy (GM1060, Gersteltec Sarl.) was spin coated (SUSS Micro Tec Lithography, GmbH, Type DELTA 10TT) at 5000 rpm for 30 seconds producing a 5 μm thick film. The sample was left to relax for 40 minutes before placing on a hot plate. SU8 substrates were heated in a two-stage heating process, 65 ^{o}C for 5 min then 95 ^{o}C for 5 min and cured using a UV lamp, emitting at a wavelength of 365 nm, Irradiance 10 mW.cm^{-2}. Silica microparticles (Kisker Biotech), 1.0 μm diameter suspended in water were dropped on the SU8 surface substrate fixed on the spin coater. The microparticle-substrate was exposed to a single pulse from a Lambda Physik LPX 202 ArF excimer laser emitting at a wavelength λ = 193 nm. The pulse width was measured as τ = 11.5 ns (FWHM) at a charging voltage of 26 kV (photodiode, Hamamatsu, S7911 measured with an oscilloscope, (Infinium, 500 MHz, 2 GB samples s^{-1}). A mask projection optical technique consisting of a stainless-steel projection mask, 2 mm diameter aperture was used to select a near-uniform laser fluence on the sample. The laser beam was steered using dielectric mirrors, which were optimised for reflection at 45°, see Figure 3-14). A plano-convex silica lens, focal length of 81.8 mm at 193 nm was used to image the projection mask aperture using a 1/10 magnification. The laser energy was measured after the lens to account for optical losses along with the beam delivery system. A variable angle dual plate beam attenuator (ML2110-Metrolux-Germany) reduced the laser fluence to 45 mJ.cm^{-2} measured with Joulemeter (Molectron). The sample, (see Figure 3-15), was irradiated using a single laser pulse in the air with a vacuum fume extractor in close proximity. A solving cleaning process was used to clean the Soda lime glass. Using Ionized water, Acetone and Isopropanol respectively, each of them sonicating for10 min using ultrasonic bath (UW ultra-wave mode QS5, ultrasonic cleaner) to clean the substrates. The substrates were cleaned using Ionized water to eliminate the influence of the oxidation on the substrate surface. The substrate was then dried by using nitrogen gas for two minutes to remove adsorbed solvent from the substrate surface. SU-8-negative tone photo-epoxy (GM1060, Gersteltec Sarl.) was spin coated

(SUSS Micro Tec Lithography, GmbH, Type DELTA 10TT) at 5000 rpm for 30 seconds to produce 5 µm film thickness, after cooling down the substrate. The sample was placed on a hot plate (65 °C) for five minutes, the temperature was increased to 95 °C and the sample was left for another five minutes. The coated substrate was then exposed to a UV lamp of 365 nm, (10mW.cm^{-2} intensity) to be cured. The sample was left at room temperature for ten minutes and finally coated in silica microparticles, suspended in ionized water (1.0 µm particle diameter, 2.0g.cm^{-3} density, Kisker Biotech). The microparticles of silica array were exposed to a single shot of a Lambda Physik LPX 202 ArF excimer laser. The excimer laser beam was focused into a smaller area (400 µm spot diameter) by a fused silica plano-convex lens (focal length is 81.8 mm at 193 nm) and normally irradiated the microparticle-substrate structure. The laser fluence was fixed at 45 mJ .cm^{-2}. The sample was irradiated with a single pulse (τ = 11.5 ns). During the laser irradiation, the silica particles focussed the laser beam into SU-8 substrates and hemispherical cavities were produced on the SU-8 substrate surface. After the laser irradiation, the sample surface was by characterised by Scanning Electron Microscopy, SEM (Zeiss EVO60) and Atomic Force Microscope AFM(Bruker edge).

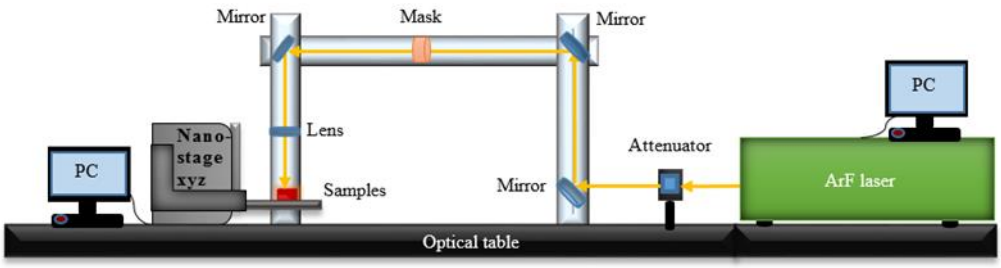

Figure 3-14. Schematic illustration of the 193 nm laser system and beam delivery

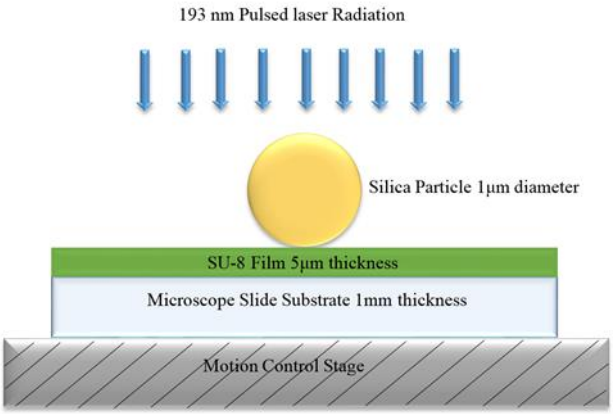

Figure 3-15. Schematic of a silica particle 1μm diameter in near contact with SU8 layer of thickness 5 μm

3.5.2 Chitosan and silica particle film preparation

A soda-lime microscope slide (Thermo Scientific) was used to support a chitosan film. The microscope slide was sonicated in deionized water, acetone and isopropanol for 10 minutes respectively using an ultrasound cleaner (UW ultra-wave QS5). The substrate was blown dry with nitrogen gas for two minutes to remove residual solvent. Substrates were left in the air to cool back down to ambient temperature. The Chitosan and its solution used in these experiments were purchased from (Sigma-Aldrich, Chitosan-448869, 0.1 M acetic acid). To achieve a 2% concentration, the chitosan solution was prepared by dissolving 0.2 mg chitosan in 10 mL acetic acid. Chitosan film was spin-coated (SUSS Micro Tec Lithography, DELTA 10TT) at a speed of 1000 rpm for 30 seconds which produced a film thickness of 2 μm. A calibration curve can be found in chapter 2 to identify the spin speed for samples having thicknesses in the range 300 nm to 10 μm. Before carrying out the laser ablation experiments, the samples were left to dry for one day. The substrate was coated again by a silica microparticles suspended in ionized water (1.0 μm particle diameter, 2.0 $g.cm^{-3}$ density, Kisker Biotech). The micro-particles of silica array was exposed to a single shot of the same laser parameters used above with SU-8 sample (see the setup in Figure 3-14). The laser fluence was fixed at 45 $mJ.\ cm^{-2}$ too and a single pulse irradiated the sample. The silica particles focussed the laser beam into the chitosan substrate during the laser irradiation. Hemispherical cavities were shaped on the chitosan substrate surface. The irradiated sample was characterized by AFM and SEM.

3.6 . Results and discussion

3.6.1 Submicron hole dimple in SU8

Nano-holes fabrication starts with the convective assembly of 1 µm silica microspheres coated SU-8 substrate (5 µm thickness). A ns-laser pulse generated by ArF laser (λ=193 nm, τ =12 ns) is focused into 250 µm -sized spot on the sample that moves on a nano XYZ translation stage (Figure 3-14). The silica spheres work as micro-lenses for a single laser pulse that generates an ordered array of well-defined holes into the SU-8 and chitosan layers, respectively. Figure 3-16. (A) Shows scanning electron microscopy (SEM) image of a microflowers of silica microspheres with 1 µm diameter formed by self-assembly method. The SEM image presented in Figure 3-16. (B) Shows a surfaced SU-8 substrate after a single laser shot, at a laser pulse fluence of 45 $mJ.cm^{-2}$. The focusing of the laser beam underneath the particles produced 150 nm diameter of holes on the surface of the substrate. From the literature (Chapter1),it was noted that the fabricated cavities become bigger as the laser fluence is increased. Therefore, a laser fluence of 45 $mJ.cm^{-2}$, above the ablation threshold of SU-8 ,40 $mJ.cm^{-2}$(chapter 2) at a wavelength of 193 nm, was determined to be the optimum fluence for nanofabrication by laser irradiation of 1 µm particles of silica. Figure 3-16. B. shows rims and some nanometer-sized particles at the edges of the holes. These are thought to be formed as a result of redeposition of laser-ablated species. SEM image of the nano-holes structure (150 nm diameter) fabricated underneath the microsphere of diameter (1.0 µm) on the SU-8 substrate.

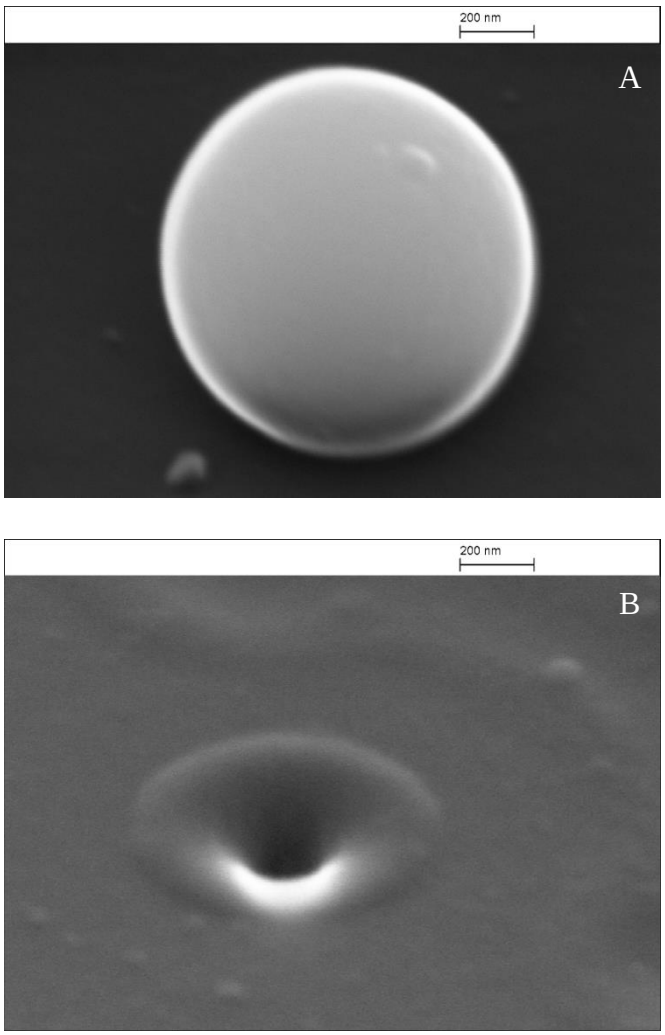

Figure 3-16. The SEM images of 1.0 μm silica microspheres on a (5 μm) SU-8 substrate before laser irradiation. B is the SEM images of the nanohole structures (150 nm diameter) formed on SU-8 by single-shot ArF (λ=193 nm) laser radiation of the silica microspheres with a laser fluence of 45 mJ cm^{-2}. laser fluence underneath the microsphere of 1.045 J cm^{-2}.

Figure 3-17. A and B shows the SEM images of silica microparticles of 1.0 μm diameter and the sub-microholes produced on SU-8 substrate by focusing the laser beam underneath the microparticles which are operated as a microlens.It can be seen from

Figure 3-17.B, the spacing between nanoholes centres was close to the diameter of the microspheres. These results indicate that further enhancement of intensity underneath the particles produced nanostructures surface.

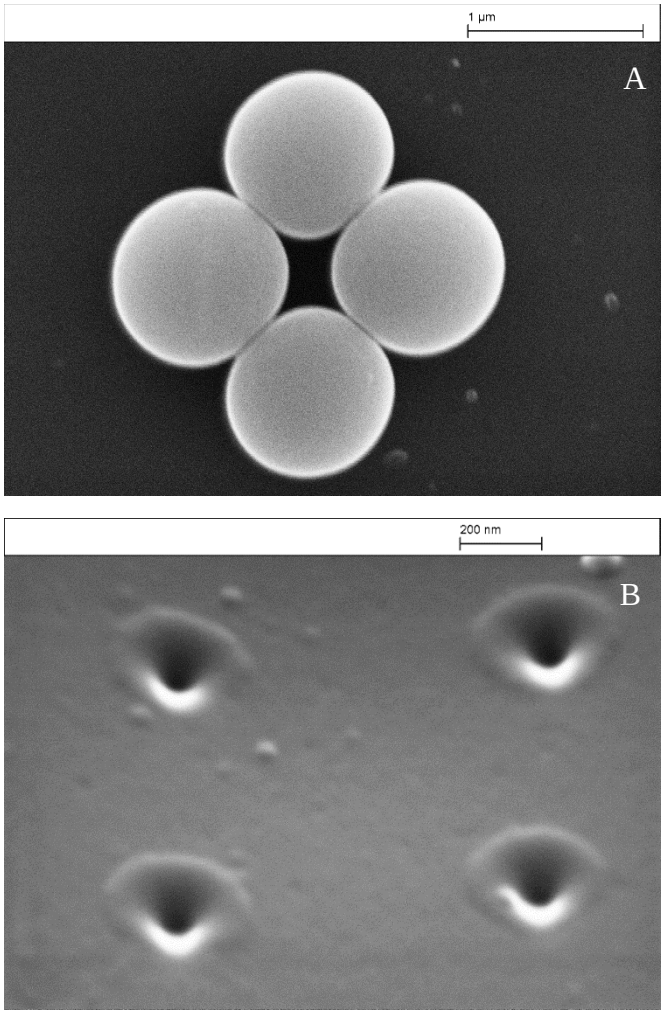

Figure 3-17. A. Electron microscopy micrograph of the surface morphology of silica sphere arrays (1.0 µm diameter) prepared by spin coating on SU-8 substrate. B. The sub-microholes produced on the substrate by focusing the laser beam underneath the microparticles which are operated as a microlens. The distance between the holes around 1.0 µm.

AFM was used to characterize the surface morphology of the patterned SU-8 substrate samples.

Figure 3-18 shows typical 3D AFM images of the surface topology after illumination of the cavities formed on SU-8 substrates underneath the 1 µm silica particles by a single laser pulse of ArF laser.

Figure 3-18. A depicts the surface profile after laser irradiation and illustrates the spacing between individual nanoholes is 0.9 µm, corresponding to the microsphere diameter. The nanoholes are slightly elongated along the laser scanning direction.

Figure 3-18. C shows the 2D line profile shows the diameter of this nanohole which is approximately 150 nm at FWHM and the depth of the nanoholes measures approximately

180 nm. The microspheres at the centre of the laser-material interaction zone were removed during irradiation. Due to laser ablation and material removal and high value of acceleration one may assume that the accelerating substrate provides the driving force for ejection of the microsphere as discussed previously. The surface level underneath the microspheres recedes, and a nanometre-sized hole is formed. An air gap forms between the microsphere and the bottom of the nanohole being drilled into the substrate. The diameter of this nanohole is approximately 150 nm at FWHM (experimentally), which compares favourably with the estimation of a maximum diameter of 91 nm made in the electric field intensity simulation by FDTD (LUMERICAL) in the first section of this chapter. Beneath the microsphere the incident laser fluence is considerably higher at 1045 $mJ.cm^{-2}$ which is considerably higher than the laser ablation threshold of SU-8. After the end of the laser pulse, 12 ns FWHM, the temperature of the dimple wall remains momentarily higher than the boiling point (T=480 K) of SU-8 further contributing to mass transport and growth of the dimple feature. Lower and (higher) laser incident laser fluence could be used to realise more subtle and (deeper) surface relief features. In both computational and experimental results, the FWHM of the nanojet (FDTD) nanodimple (experimental) are smaller than the diffraction limit, thus allowing for the fabrication of structures at the nano dimensions.

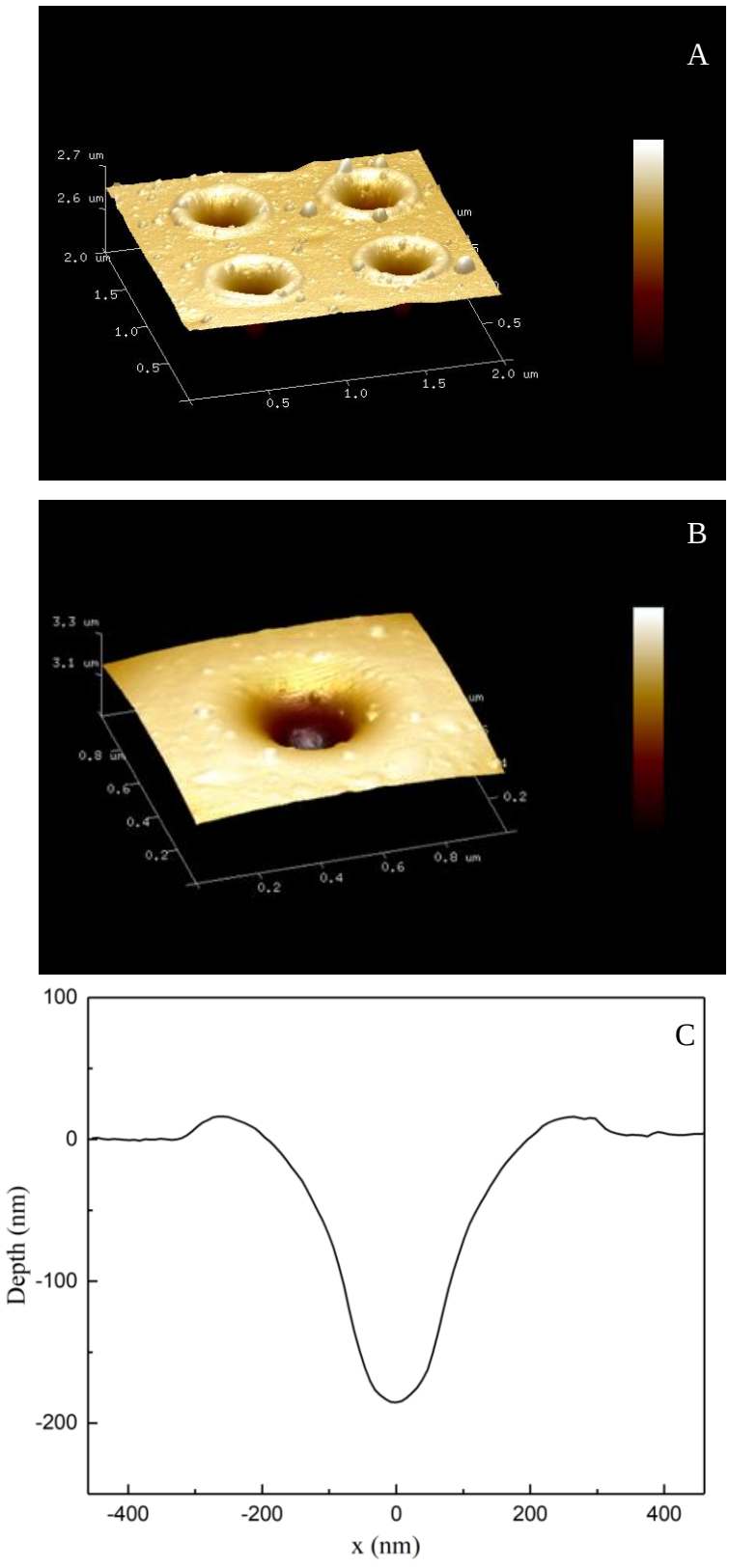

Figure 3-18. A and B is the 3D AFM images of the nanostructures holes (150 nm diameter) formed on SU-8 by single-shot ArF laser radiation of the silica microspheres with a laser fluence of 45 mJ cm^{-2}, C is the 2 D section profile for nanoholes.

3.6.2 Sub-micron hole - Dimple in chitosan

The same parameters of the optical system used above (silica and SU-8 substrate) have been used again to fabricate the nanohole structure, but with a chitosan substrate. The chitosan film (2 μm thickness) was prepared and used as a substrate for this experiment. Both SEM and AFM are used to characterise the morphology of the Chitosan nanostructure. SEM image of a hexagonal array produced structures produced on chitosan substrate by ArF laser irradiation at a laser fluence of 1045 mJ cm^{-2}. Hole array with a period of 1 μm in all directions. Figure 3-19. A shows SEM images of top view for a chitosan template self-assembled from SiO_2 spheres with diameters of 1 μm which enhance the intensity underneath the particles by focusing the laser beam to fabricated nanohole at 180 nm diameter. It is noted that in Figure 3-19. B the rims also appear at the edge of the holes, but they are much pronounced compared to rims on SU-8 nanostructure (see

Figure 3-17 and 18), this could be due to the negative thermal expansion coefficient of chitosan. This can be explained by the fact that less ablation on SU-8 substrate and hence less redeposition is occurring due to substrate properties. The coefficient of thermal expansion is an important mechanical property for thin film materials. There are some problems that arise from effect of the thermal expansion; for example, the mismatch of thermal expansion between the thin films and the underlying substrate may lead to residual stresses in the thin films. Instead, the thermal expansion effect can be exploited to guide nanostructures. The substrate reaches its maximum acceleration value due to the substrate thermal expansion during the irradiation of the short-pulsed laser until the peak fluence of the beam is reached. The magnitude of substrate acceleration is proportional to the level of fluence due to linearity assumption of thermoelastic effects and is inversely proportional to the duration of the laser pulse squared. In addition, Material properties, the thermal stability, the glass transition behavior and the mechanical properties above glass transition should take into account to understand the behavior upon laser irradiation.

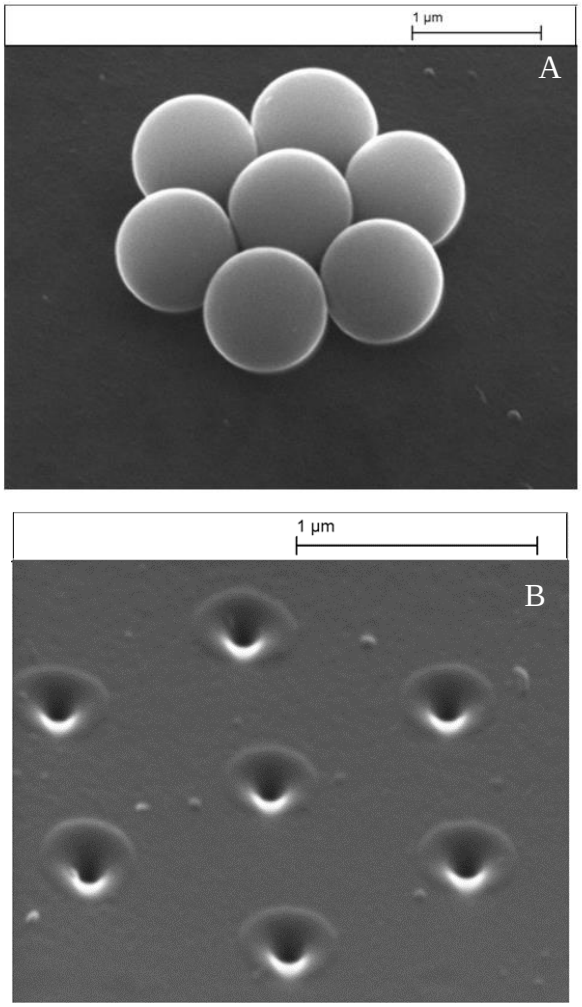

Figure 3-19.A. SEM images of a hexagonal monolayer of silica spheres (1 µm diameter) formed by the self-assembling process, B SEM image of a hexagonal array produced structures produced on chitosan substrate by ArF laser irradiation at a laser fluence of 1045 mJ cm^{-2}. Hole array with a period of 1 µm in all directions.

A different self-assembly structure of spherical microparticles formed on chitosan substrate after coating is shown in Figure 3-20.A. The nanoholes array produced underneath these self-assembly particles are a result of the focused laser beam to sub-micro dimensions during irradiation (see Figure 3-20.B). The distance between the nano holes is approximately the diameter of the silica particles.

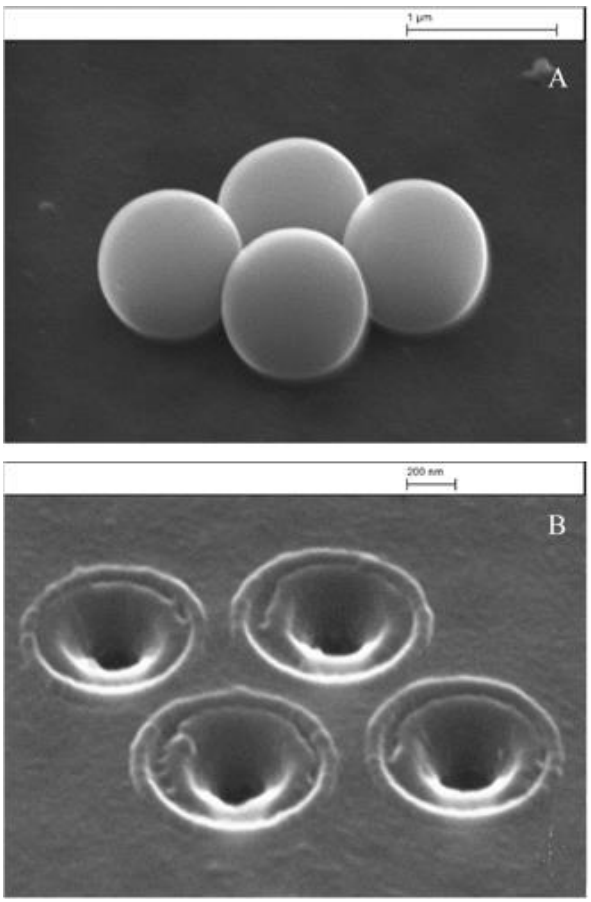

Figure 3-20. A is the SEM images of self-assembly micro-particles silica of 1.0 µm diameter on a (2 µm) chitosan substrate before laser irradiation. B is the SEM of four nanoholes structure (180 nm diameters) produced on chitosan by single-shot ArF laser radiation of the silica microspheres with a laser fluence of 1045 mJ cm^{-2}. A period between any two holes about 1.0 µm.

The morphologies and the depth of the nanohole on chitosan substrate were investigated again by AFM as shown in Figure 3-21.A, the AFM image of the hole arrays in chitosan film with a period of 1.0 µm Figure 3-21. B shows the nanohole was found to have a diameter of 180 nm at FWHM, this agrees with the SEM measurements. Figure 3-21.C specifies the 2D profile of nanohole close to 300 nm depth.

Compared with results above, it can be seen the depth of nanohole on chitosan film is deeper than the hole on SU-8 film. This is due to the Chitosan substrate having a higher thermal conductivity, therefore, producing a larger nanohole for given laser power and other system parameters [265]. Once within the material, absorption causes the light intensity to decay with depth at a rate determined by absorption coefficient (α) of the material. In general, it is a function of wavelength and temperature, but for constant intensity, I decline exponentially with depth z according to the Beer-Lambert law

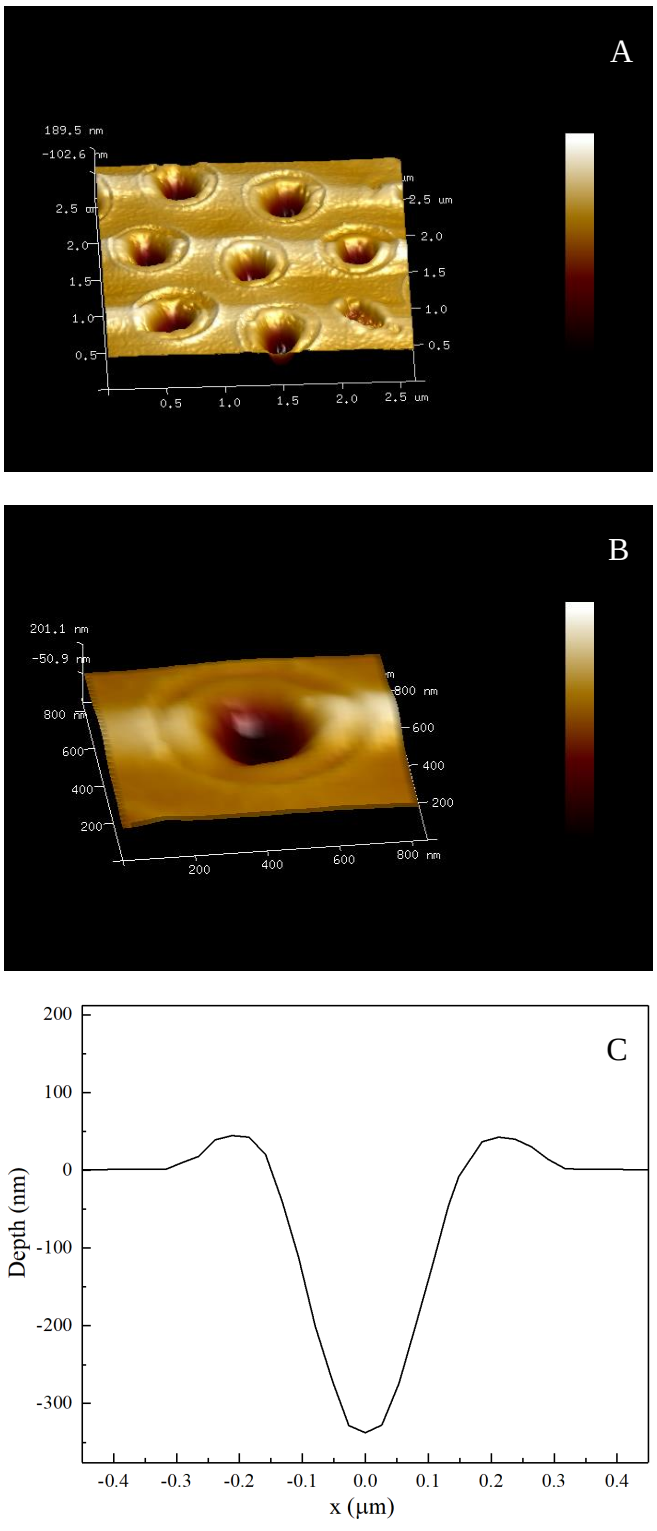

Figure 3-21. A is the AFM images of the nanostructure's holes (180 nm diameter) formed on chitosan by single-shot ArF laser radiation of the silica microspheres with a laser fluence of 10 45 mJ cm^{-2}. B is the 2d profile

Figure 3-22. A and B shows the intensity profiles that are investigated by LUMERICAL (FDTD) and analytical (Richard-Wolf integrals) for both SU-8 and chitosan substrates. These results are compared with the 2D profile of nanoholes that are fabricated on both

substrates and measured by AFM. Table 3-4 shows the nanoholes diameter and depth for both SU-8 and chitosan substrates demonstrates the nanoholes diameter at FWHM and the depth, for both substrates.

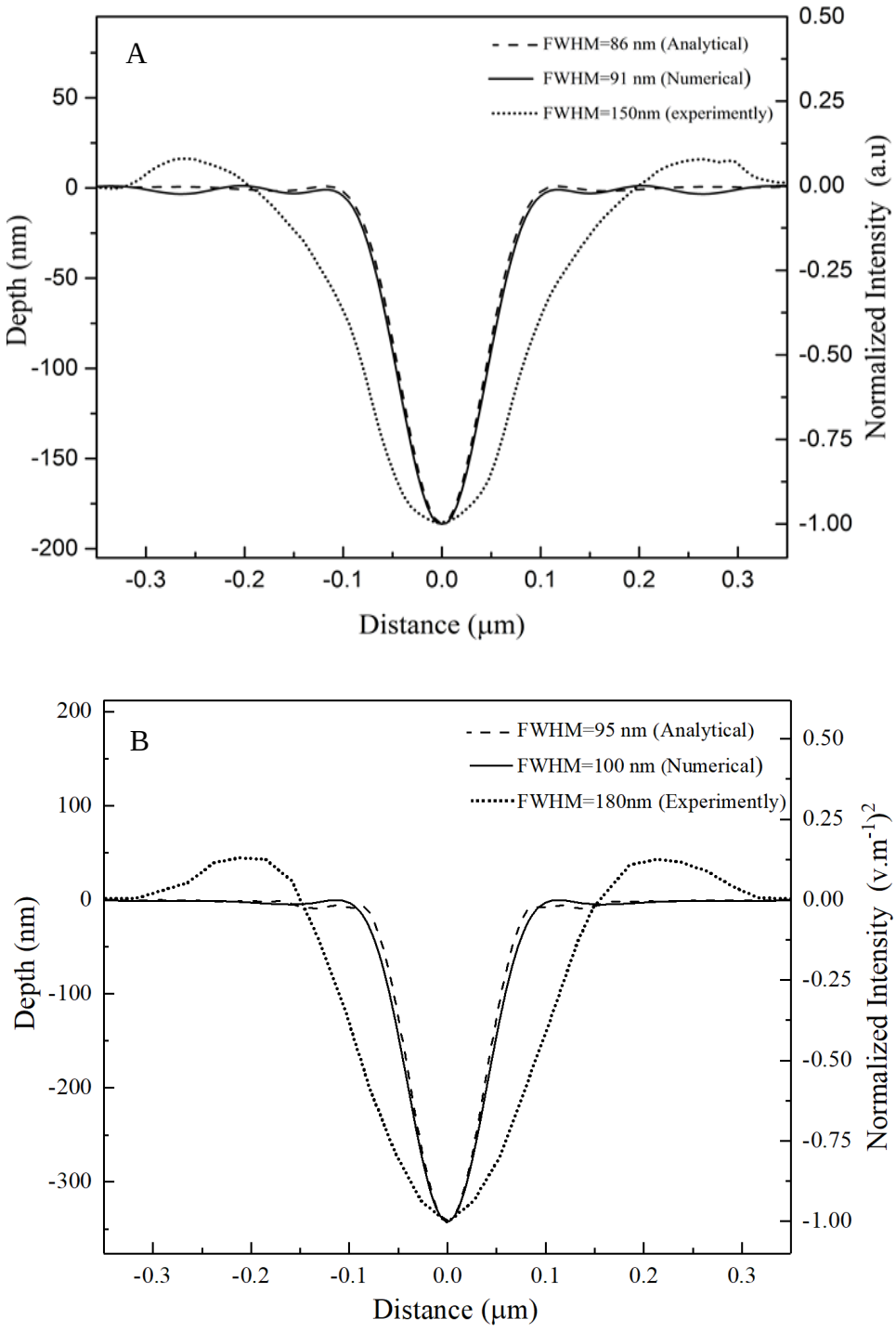

Figure 3-22 Analytical, numerical and experimental data of intensity profile underneath the silica micro sphere through (A) SU-8 substrate and (B) chitosan substrate.

Table 3-4 shows the nanoholes diameter and depth for both SU-8 and chitosan substrates

The diameter of nanohole at FWHM	SU-8 substrate	Chitosan substrate
Experimentally (nm).	150	180
Numerically (FDTD), (nm)	91	100
Theoretically (nm)	86	95

3.7 Conclusion

laser processing method have demonstrated to create small sub-wavelength, 150 nm, 180 nm at FWHM sized cavities in SU-8 and chitosan substrates respectively using an ArF laser emitting at a wavelength of 193 nm and 1045 $mJ.cm^{-2}$ fluence . The spherical microsphere acts as a small ball lens and tightly focuses laser radiation. Delivery of laser energy takes place within 11.5 ns, and consequently, the microsphere is removed in a single laser pulse due to a rapid change in temperature of the substrate and a concomitant rapid acceleration of the supporting layer. Several mechanisms can contribute to the ejection of a particle from a substrate. When the laser fluence beneath the microsphere is sufficiently high, melting and boiling points may be exceeded, this may result in ablation and evaporation of substrate species which in turn contribute to the transfer of momentum to the microsphere. In addition, laser ablation and material removal and high value of acceleration one may assume that the accelerating substrate provides the driving force for the ejection of the microsphere. Using the refractive index of the microsphere at 193 nm and field enhancement of S0=40 was estimated. Experimental data resulting in minimum focal diameter for both SU-8 and chitosan are an in close agreement with computational results FDTD simulations and theory calculations as shown in Table 3-4. Computational results FE simulations produce an overestimated ablated zone radius compared to the measurements made using an SEM (250 nm simulated instead of 150 nm experimental for a laser fluence of 1045 $mJ.cm^{-2}$) on SU-8 while (300 nm simulated instead of 180 nm experimental for a laser fluence of 1045 $mJ.cm^{-2}$) on chitosan. As well the depth of nanodimple on chitosan (~300 nm) deeper the dimple depth on SU-8 (~180 nm) due to material properties.

In summary, laser processing of SU-8 and chitosan films using a PNJ emitting at a wavelength of 193 nm to realise small sub-wavelength dimple shaped cavity. The dimple measures 150 nm (SU-8) and 180 nm (chitosan) in size at the FWHM point. The SiO2

microsphere acts as a small ball lens that tightly focuses laser radiation. As a consequence, 193 nm laser radiation locally heats substrate above its boiling point in the region beneath the microsphere. FDTD simulations provide a useful information about PNJ's spatial extent and as such the simulations can be used to engineer the position and geometry of a PNJ. We note that PNJs can be realised from other refracting elements that are not necessarily spherical and work in this area is ongoing. Similarly, surface modification need not be restricted to planar surfaces. Work is presently underway to couple laser radiation into microspheres and nanospheres in contact with biological cells. Utilization of subwavelength photonic PNJs may open up novel opportunities within the biomedical field to controllably disrupt cell membranes for drug delivery and transfection studies.

Chapter 4 CO_2 laser shaping of silica optical fibres

4.1 Introduction

Among the focusing head and laser source, fibre optics or reflective optics can be used to deliver industrial laser beams [266]. The type of the laser and the power, which is involved in different applications, are dependent on the delivery method, the delivery method can be comprised of two methods of characterization of either laser system or the application used [267]. In comparison with the free space, the use of fibre beam transport has many advantages. The most important advantage that can be observed is the flexibility in use of the laser at different places; however, the beam properties remain same [268]. Fibre optic laser cables are more reliable to deliver laser power having high beam quality and more brightness. The loss is negligibly small when the light rays travel long distances with no emission of light outside the cable [269]. It is important to choose the appropriate type of fibre due to the output beam characteristics which can increase or decrease the utility of optical fibre delivered beam for many applications [183]. However, there are many advantages of single-mode optical fibre with respect to bandwidth and to transmit to long distances, on the other hand, the design of multi-mode optical fibre is used for short distance transmission. The multimode fibre cost more than single mode which is of 550m. There are many new opportunities for Micro/nanofibers (MNF) in vast region ranging from nanophotonic, nonlinear optics to quantum optics, as it is very interesting field for optical sensing using micro and nanometre scale. It brings better platform by merging nanotechnology and fibre optics. Now a days, the demand of better Nano sensors or microsensors is increasing from scientific research world [270].

The ability to structure surfaces on a submicron scale is becoming increasingly important for a broad range of technical and biological applications [271]. The first reason is the possibility the unique properties of nanostructures will result in novel applications and devices. Another reason for the great popularity of this field is that phenomena occurring on sub micro scale are of interest to physicists, chemists, biologists, electrical and mechanical engineers, and computer scientists. An incentive in nanoscience is also to try to understand behave of materials when sample sizes are close to atomic dimensions. There is also the opportunity to use nanostructures for technology [272].

The size of the spot is limited by numerical aperture which sets the maximum achievable spatial frequency (NA/λ). The laser beam can be focused into a very small spot size,

which can then be used effectively to fabricate the microstructures and functional components with fine microstructure by micro-additive fabrication via laser heating [273].

Optical fibres (OF) are in general circular symmetric and come in a range of core diameters. The ends of OF are cleaved flat to facilitate both launching light efficiently into and out of the fibre. As the light exits the fibre the beam diverges. This beam divergence is not desirable in most applications. A more desirable beam profile is one that is either focussed or collimated. The use of micro-lenses is just one solution [155]. However, due to precise polishing requirements, fabrication of such micro-optic components is technically challenging. Components also need proper housings to hold both the fibre and micro-optic components. This would make the overall size of the device at least one order of magnitude larger, compared to the diameter of the actual optical fibre. An alternative approach is to fabricate microlens structures at the tip of an optical fibre, thus not significantly increasing the total size of the device [173, 274].

Different lenses, for example, spherical (ball) and tapered fibre micro lenses can be contrived as fibre micro components. These optical elements are valuable for controlling the beam direction and focussed spot size. Lenses spliced to fibres reduce Fresnel reflection coupling losses, they are robust, the splicing technique minimises potential failure mechanisms and in many cases it is a cheaper form of fibre termination [182]. There are many applications where microlenses are adopted for low-and high-power lasers [156]. As will be discussed the position of focussed 10.6 μm radiation onto the fibre and concomitant laser operating parameters effects fibre re-shaping. The fabrication of aspheric shapes is achieved by the ability of laser micro-machining to modify the fibre tip. Otherwise, this would be difficult to achieve small feature size because of the long wavelength [23]. Better reproducibility is achieved by more consistent lens curvature in CO_2 laser heating fabrication than the arc discharge technique.

This chapter first describes the principle operation of the carbon dioxide (CO_2) laser. Then discusses the interaction between silica optical fibres and electromagnetic radiation from a CO_2 laser. Moreover, the realisation of micro lensed optical fibres such as ball, tapered optical fibre micolens fabricated using 10.6 μm radiation are discussed. Finally, the experimental results are presented as two sections, firstly characterisation of the surface roughness of the reformed glass for a range of fibre rotation speeds, irradiation time and irradiated power. Secondly the knife-edge technique was used to characterize the beam

profile as light, at a wavelength of 632.8 nm, from a HeNe laser exits micro structured optical fibres. Laser processed fibres were investigated optically using an Optical Microscope (LEICA DMLM) and scanning electron microscope, SEM (Zeiss, EVO60). In this study, a laser micro-machining technique was chosen to modify the tips of OFs. A CO_2 laser was chosen as a heat source as the emission wavelength couples strongly with the vibrational modes.

Fibres that are used for CO_2 glass reforming applications are generally made of glass (fused silica), glass protected with a polymers jacket, or all polymer (plastic optical fibres). Fused silica (fused quartz) is silica glass having amorphous (non-crystalline) structure, and it is produced by fusing (melting) high purity silica sand. An advantage of using fused silica optical fibres is that the optical transmission is higher than that in glass optical fibres at ultra-violet wavelengths. It has been reported that CO_2 laser heating of fibre tips results in more consistent lens curvature than the other techniques used in microlens fabrication [185]. There has been lots of interest using a CO_2 laser for the surface treatment of silica. The CO_2 laser used in this work is a sealed unit and essentially this type of laser can be used as a simple trouble-free turn-key laser source. CO_2 laser relatively low cost, have a wide range of output powers, and silica glasses have a high absorption coefficient ($\sim 5\times10^5\ m^{-1}$) at CO_2 laser wavelength (10.6 μm) [275].

Some examples of applications of CO_2 laser processing are: laser polishing [89], [153], [276], improving low loss fibre core with arbitrarily long lengths, to melt and recrystallize the core of silicon OF, CO_2 laser is scanned along the fibre's length. The process can make single-crystal silicon cores over the length of the scanned region to precisely control the temperature and the cooling, hence greatly decreasing the optical transmission losses [277], thermal treatment of interfaces of fibre optics and as in this work, micro-structuring glass materials [274]. Surface smoothing and polishing occurs by raising the glass temperature to reduce its viscosity to controllably reflow the near-surface [5].

Fibres can be either pulled to neck-down the diameter and subsequently split the fibre into two or be cleaved at a required position before melting the tip to form a lens. Using this method, very sharp tips can be obtained, and they have been widely used as scanning probes in the field of scanning near-field microscopy [167] and used as nano-pipettes in cell biology [279] Silica (SiO_2) is the main ingredient of most glasses and has a tetrahedral structure. This consists of four oxygen (O) atoms surrounding the silicon (Si) atom at the centre as shown in Figure 4-1.

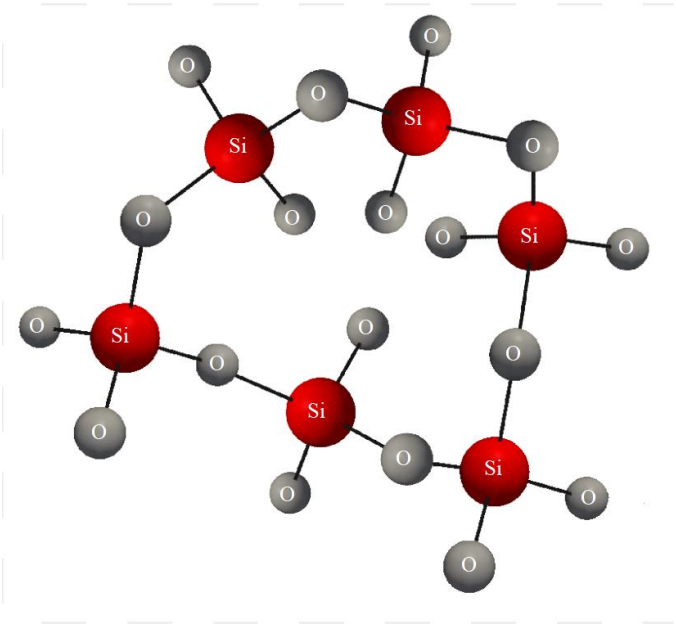

Figure 4-1. Illustration of Silicon Dioxide (SiO_2) lattice structure

4.1.1 Operation of the carbon dioxide (CO_2) lasers

The carbon dioxide laser is a molecular gas laser. It was invented by Indian born American scientist Prof, Kumar Patel at Bell Labs (1964) [280]. It produces a beam of electromagnetic Infra-red (IR) radiation which has a relatively long laser wavelength (10.6 µm). Carbon dioxide laser gas mixtures contain CO_2, Nitrogen, and Helium. All these gases are mixed to produce the gain medium which is created by transitions between different vibrational energy levels in the carbon dioxide molecule. The nitrogen molecules help to excite CO_2 to the upper laser level. Firstly, a high voltage direct current is used to excite nitrogen molecules to the first vibrational energy state. This first energy level of nitrogen has almost the same energy as the upper level of CO_2. Secondly, transfer of vibrational energy from N_2 to CO_2 is achieved through collisions between the two molecules. Carbon dioxide molecules are excited by vibrating nitrogen molecules to the point where the gain medium becomes an effective optical amplifier [23, 281]. Helium gas is added to the gas mixture to help CO_2 molecules to relax and increase efficiency of lasing. The output power increases by adding helium which help CO_2 molecules to move from the lower laser level to the ground state, thus maintaining the population inversion needed for operation. Atoms of helium collide with molecules of CO_2 and vibrational energy is transferred from CO_2 molecules to the helium atoms. Consequently, higher laser powers can be produced [281]. These processes are illustrated in the Figure 4-2 below.

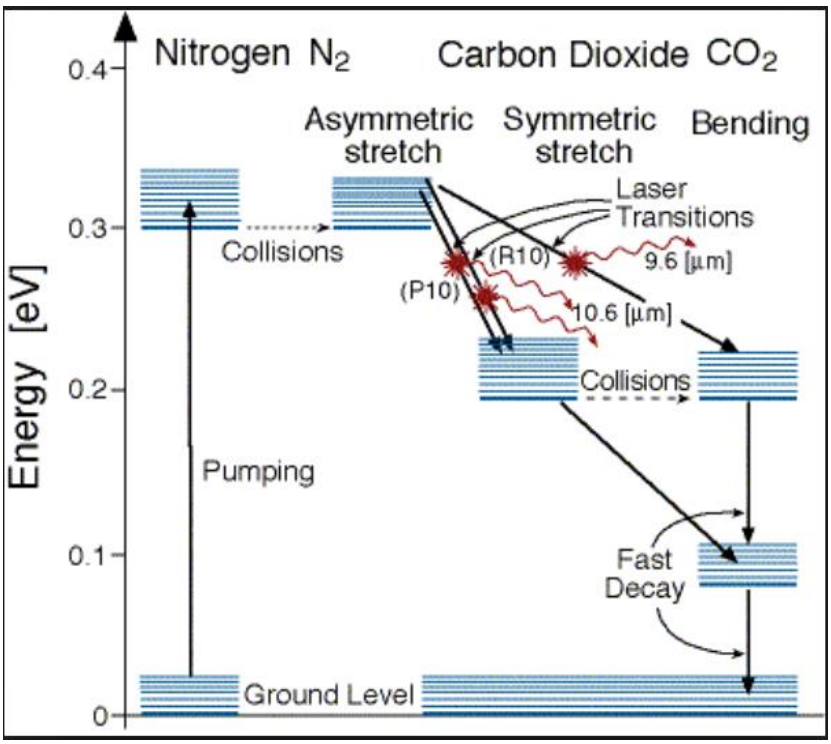

Figure 4-2. CO_2 laser energy level diagram [281].

Heating of silica glass by CO_2 laser radiation is used in various scientific and industrial applications, for example, micromachining to produce lensed optical fibre, processing of optical fibres, polishing of micro-optical components, production of free form optics, and generation of holographic structures. All these applications take advantage of the high power available for carbon dioxide laser and the high absorption coefficient of silica at the corresponding laser wavelength [282]. Using CO_2 laser as a heat source for post-processing of optical fibres are proven to be the most responsive heating source that offers the flexibility and resolution needed for the fabrication of these optical components [186]. It is, therefore, possible to realise tapers and micro-ball lenses using CO_2 lasers easily compared with electrical filaments, open flames and arc discharge [153].

4.1.2 Interaction between silica optical fibre and CO_2 laser irradiation.

When a beam of Laser radiation incidence on silica fibre, following effects can be observed: reflection, absorption, scattering and transmission [283]. The interaction between laser radiation and materials in general, depends on parameters that are linked with the laser source (wavelength and absorption coefficient)) and also on the materials thermophysical properties [179]. Through laser interaction with solids, a variety of physical processes occur such as sublimation, melting and vaporization [284]. Pure silica

has a high-melting temperature (T_m ~1700 °C), The drawing temperature of conventional silica glass is close to 2000 °C and it has a very high viscosity, and this property allows the glass to be formed, cooled and annealed without crystallizing [285]. Since the viscosity of fused silica cannot be significantly reduced by simply increasing the temperature, this glass is very difficult to produce by conventional glass-melting techniques. Through laser irradiation, and depending on the mentioned laser parameters, the main physical mechanisms can be divided in two types, thermal and non-thermal [286]. These physical processes are used to fabricate different optical lensed fibre as it will be explained in the following sections. As the temperature of the fibre increases, the glass materials begins to melt and application of opposing forces permits stretching of a fibre, referred to as fibre pulling [287]. Heat affected area, and mechanical stresses are very important for lensed fibre fabrication. So, it is required to understand the optical and thermo-mechanical interactions of 10.6 µm CO_2 radiation with fused silica [288]. The high absorption coefficient of silica at this wavelength causes the temperature of the glass surface to be increased above its vaporisation temperature and begins to evaporate. Heat is conducted into the fibre bulk permitting fibre reconstruction. Conservation of energy and momentum and the presence of coupling mechanisms are required for effective energy transfer from laser radiation into a material [289]. Researchers have shown, through theoretical analysis, that the amount of material removed during laser irradiation can be controlled by using intense short laser pulses. This causes ablation of the surface with minimal melting of the underlying material, preserving the fibre structure [23]. This has been used to round fibre ends and to splice fibres together [185].

4.1.3 Absorption of 10.6 µm radiation in silica

OFs are essentially optical waveguides shaped like long, thin, cylindrical rods. Light propagating in free space behaves very differently to light propagating in optical fibres. This is because the optical field is now confined within the fibre and guided in a manner determined by the material or materials and the geometry of the fibre. There are also restrictions on the frequencies (wavelengths) allowed to propagate within the fibre. Common OFs are composed of many different types of materials; generally, glass materials or polymeric materials. In general, an optically transparent material can potentially be utilised as an optical fibre [290].

The choice of material and geometry of the fibre depends very strongly on the optical fibre application. These range from low-loss optical transmission for telecommunication (1550 nm region), illumination or imaging purposes, laser beam delivery systems amongst many other applications [287]. More specifically, active Erbium-doped fibres are used to boost telecommunication signals at predetermined positions in systems that cover large distances [261].

Plastic fibres are mainly used for lightning, light-decoration and short length systems and devices. In more sophisticated applications, glass is the most common material. Silica-based glasses have low transmission within in the short wavelength region of the spectrum typically less than 200 nm by absorption of the electronic origin of intrinsic defects (see Figure 4-3. A), above, typically 2 µm, the absorption coefficient increases as shown in Figure 4-3. B, increased absorption is primarily associated with complex phenomena such as the generation of phonons. Within this range of the spectrum, the material can be considered to be transparent. CO_2 lasers have peak emission wavelengths in the far IR and are operated at a wavelength of 9.2 or 10.6 µm. In silica glasses, strong absorption peaks are observed between 8.5 – 13 µm. The observed peaks are related to vibrational modes within the material. The peaks are also due to additional vibrational modes of impurities or dopants present within the fibre [262]. Figure 4-3. B, illustrates the absorption spectra of silica, here it can be seen that there is strong optical absorption between ~8-12 µm. There is also a small peak close to the emission wavelength of the CO_2 laser.

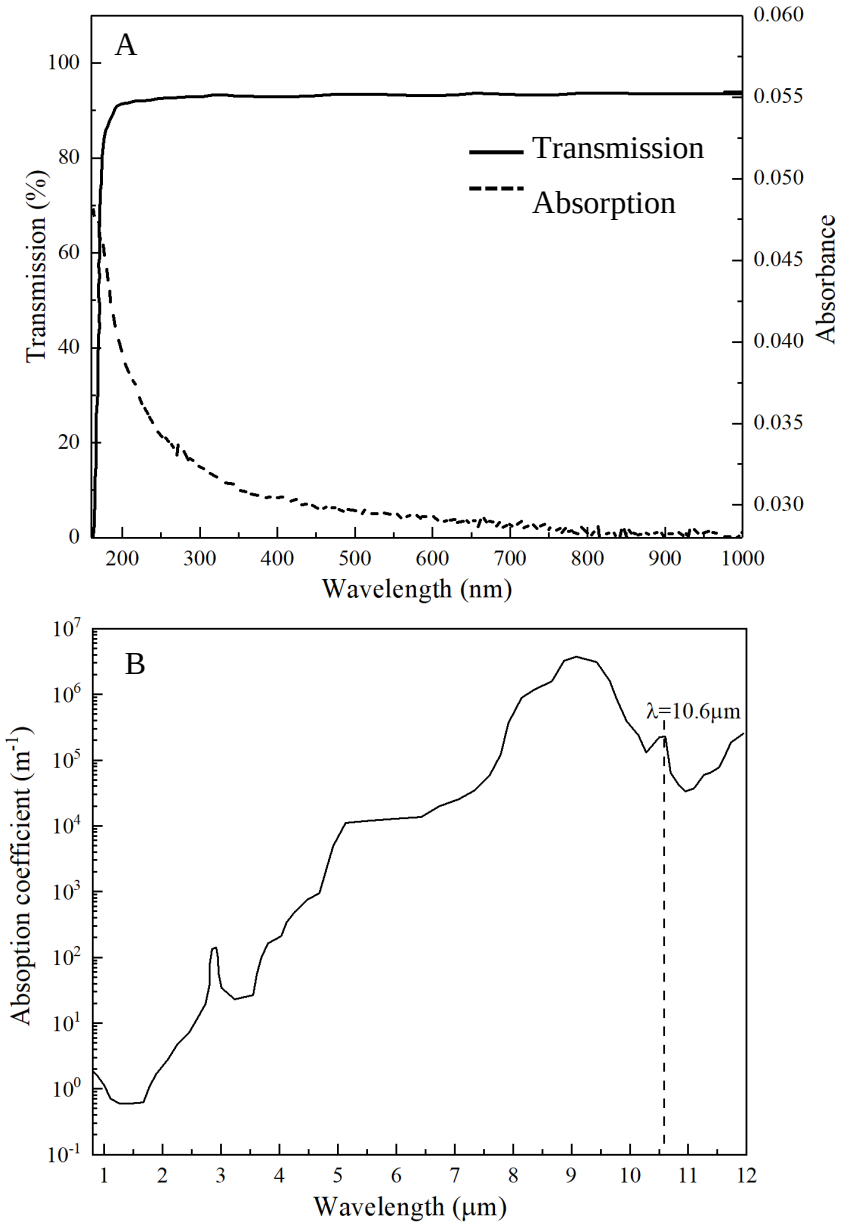

Figure 4-3 A. Transmission of silica at wavelength range (190 nm -1000 nm). B. The absorption coefficient of fused Silica at IR wavelengths [261].

Figure 4-4 (A) shows how the reflectivity as a function of angle of incidence for silica at 10.6μm wavelength. Figure 4-4 shows the transmittance spectrum through the silica as a function of a wavelength. It can be seen the minimum values of reflectivity and transmittance at incident angle 0° and wavelength 10.6 μm respectively.

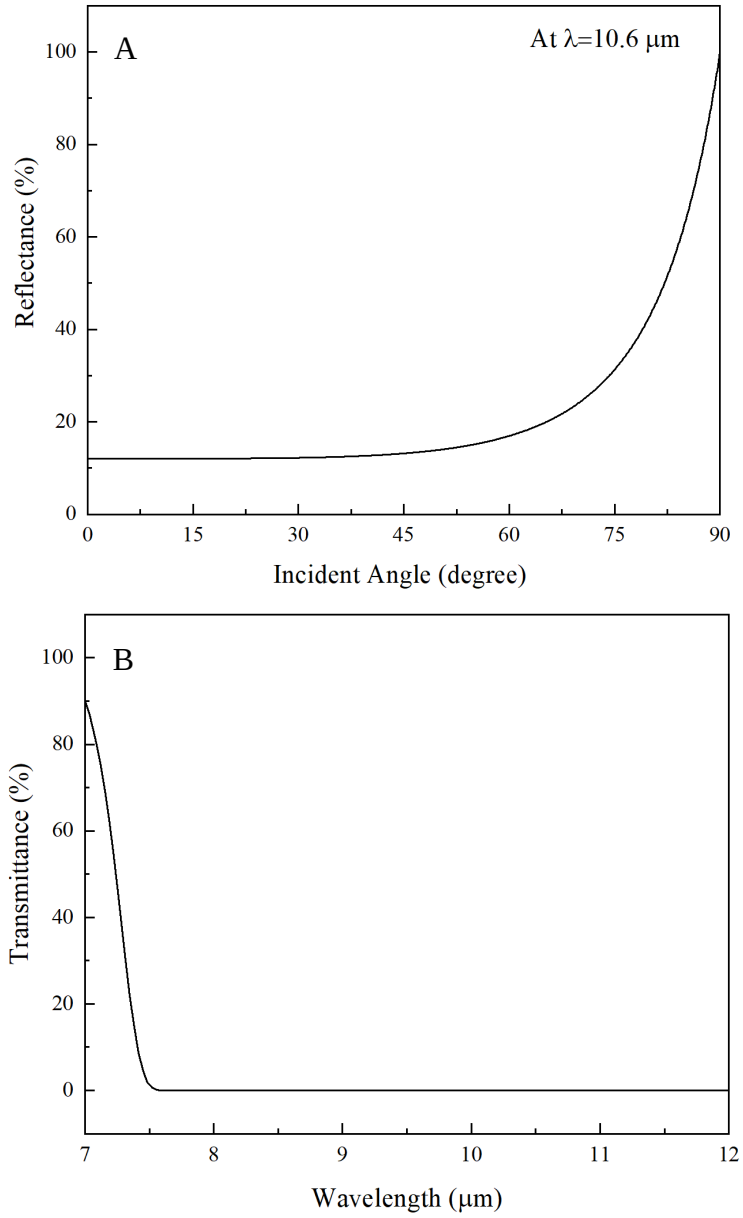

Figure 4-4. A. Reflectivity R against light incident angle and B. Transmittance T against wavelength at silica surface [291].

4.1.4 Multimode optical fibres

Within our society, optical fibres have become a major conduit for communication. Not only are optical fibres used for telecommunications, but also more importantly as fibre optic sensors, medical applications, and defense sector for vehicle navigation [292]. They are also used in mechanical and chemical sensors for remote sensing applications[179, 270], as well as delivering high power laser beams for applications such as laser cutting. Bio-medical optics is another emerging area where fibre optics plays a major role. Following the process after years and assuming group works, Multi-Mode Fibre (MMF) optic has a large diameter core that enables different optical modes to propagate [183].

Along these lines, the number of light reflections is created as the light goes through the core making capacity for more information to go through at a given time [270]. MMFs have more advantages than SMFs in comparison. The larger core radii of MMFs make it easy to deliver optical power in the fibre and to get the emitted or reflected light from sample [293]. MMFs are chiefly utilized in short-range transmissions because of their larger numerical aperture (NA) and core radius [271]. Transmission capacity single-mode fibre (SMF) holds preferences and a larger range of distances, MMF effectively supports most distances required for enterprise and systems of the data centre network, at an expense essentially not exactly single-mode [273]. A rich and complex mix of spatial and temporal nonlinear phenomena support by MMFs [294]. An advantage of a fibre having a large core diameter, MMFs make it simpler to deliver optical radiation into the fibre and to gather light emitted or reflected from an objective [293]. When the requirement for each photon matters, the benefits of large core (greater than 200 microns) multimode fibres are taking the top. As the name infers, multimode fibre is intended to convey numerous beams of light or modes. There are two sorts of multimode strands: graded index and step index [270]. In this chapter, large-core step-index MMFs have been chosen for lensed fibre fabrication (Technology Enhanced Clad Silica (TECS) multimode fibres, Thorlabs). The fibres of TECS multimode are perfect for applications, including spectroscopy, ontogenetic, and therapeutic diagnostics [155]. The structure of the fibre is commonly a pure silica core with a cladding of a thin hard polymer material and an outer jacket. Table 4-1 below shows the important parameters of the OF that used in this work.

Table 4-1 Pure silica OF properties

Core Diameter µm	Clad Diameter µm	Coating Diameter µm	Refractive index(n) at 10.6 µm	Numerical aperture	The glass transition temperature	Reflectance	Absorption Coefficient cm^{-1}
50	125	250	2.1248	0.22	1200°C	0.13428	2755.1
400	425	730	2.1248	0.39	1200°C	0.13428	2755.1
600	630	1040	2.1248	0.39	1200°C	0.13428	2755.1
1000	1035	1400	2.1248	0.39	1200°C	0.13428	2755.1
1500	1550	2000	2.1248	0.39	1200°C	0.13428	2755.1

As the fibres have high core-to-clad proportion and the cladding remains same during termination. The fibre coating does not have any optical properties that might affect the light propagation within the fibre-optic cable [295] . During the installation process, this coating is stripped away from the cladding to allow proper termination to an optical transmission system. Fibre can be cut and connected in field conditions, also works incredible for military purposes, mining and oilfield detecting application. For medical field, the mechanical, optical and auxiliary properties of fibre are very helpful in the applications of laser conveyance, endoscopic and biosensing systems [270].

For better coupling, high core – to – clad proportions are used. It increases the capability of receiving higher energy density and decrease the losses due to bending or flexibility conditions [296]. For medical purposes, the requirements are scope of geometries, clad-core proportions and numeric aperture (NA) of step – index multimode fibre, these all rely on the condition of using it as for Laser medical procedure, brightening or detecting. The fibre core geometries range from 100 μm to 1000 μm and clad – core proportions can extend this range from 1.05 to 1.20. According to rule, the more the NA accessibility the smaller the clad – core proportion will be. Similarly, the fibre cone is proportional to NA. Smaller core and clad – core proportions bring less material cost and increasing adaptable filaments [297].

4.2 Surface deformations induced by laser melting

From this study, micromaching fabrication technique can be developed. It is used for production of micro lensed fibre with optimization. These micro lensed fibres have been designed and been fabricated for optimal use. In general, micro lenses are fabricated by irradiating the fibre down to a point and melting the end. The shape and size of the resultant lenses are like ball, hemispherical and tapered fibre lenses. Following are the basic steps in sequence of deformation using laser melting; first the material melts, the molten layer of material is allowed to flow and for final step it again solidifies with irradiation, which makes the deformation permanently. The deformation mechanism depends upon the material composition as well as the fluency of absorption. It has been observed that the silica fibre at surface temperature can bring melting at irradiance values near to ablation threshold irradiance [298]. The corresponding irradiances are important parameters unique to the material and are often referred to as the melting and boiling irradiance thresholds [259]. Now, it is prudent to consider the situation in which the

surface temperature of the material exceeds the melting temperature after being irradiated with laser radiation [261]. In this case, it becomes important to analyse the temporal evolution of depth of melting during laser irradiation.

4.2.1 Fabrication mechanism of microlensed fibre

The surface tension, γ, is a valuable property of glass as it is an essential factor on the working states of glass production and its uses. This surface tension is an acute factor for glass manufacturing and formulating [299]. Surface tension is an essential parameter for the controlled fabrication and tapering of micro-lensed fibres. The weight of an OF end underneath the irradiated area are required to effectively control the inner structure can be found, as the surface tension manages the level of microstructure breakdown or development [300]. Moreover, the lens of convex and ball lens can be formed at the end of an optical fibre by heating the fibre tip until the fibre reaches its softening point and surface tension reshapes the fibre tip [301].

Surface tension can be legitimately estimated by utilizing optical fibre material with radius, r. With keeping the balance between the downforce, F_w, hanging underneath a heated volume of optical fibre with mass, m, fibre and the upward force from the surface tension F_s (Figure 4-5). At the point when the downwards force is bigger than the upwards force from the surface tension, the fibre will taper. Whereas, when the upwards force is greater, the length of the fibre below the heated volume will restructure and a semi-spherical volume will be produced.

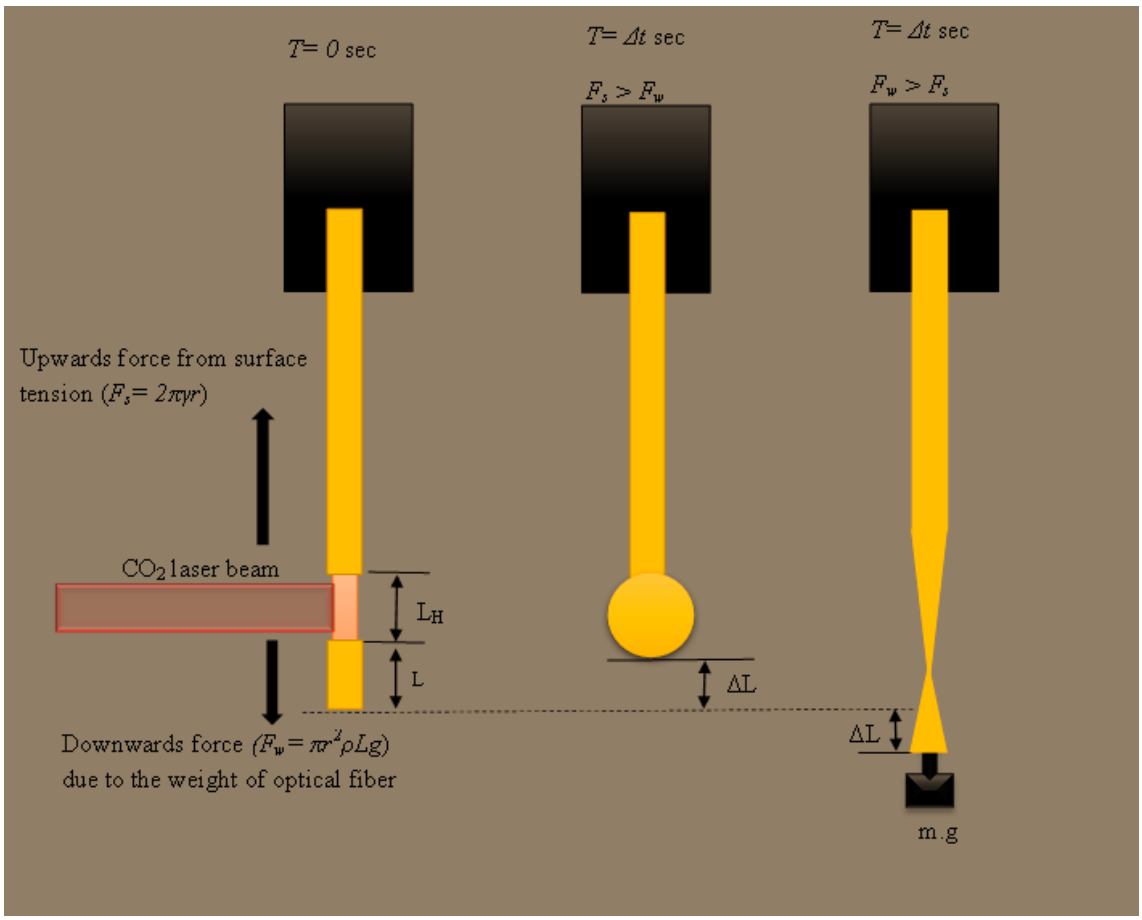

Figure 4-5. (A) An OF of length L and density ρ below the length of irradiated fibre L_H (close to to the beam of CO_2 laser with diameter D), is liable to the force F_s up because of the surface tension, and the force of F_w down because of the fibre weight underneath the irradiated area. (B) If $F_s >> F_w$, the fibre will rise a length L upwards after Δt seconds, fabricating a sphere bulb as the heated fibre moves towards a shape that limits the surface tension (C) If $F_w > F_s$ the fibre will taper, increasing the length by L after t seconds.

When the two forces are in the equilibrium, the following expression can be inferred [302], for the surface tension (γ):

$$\gamma = \frac{mg}{\pi r} \tag{4.1}$$

$$f_s = 2\pi r\gamma \tag{4.2}$$

$$f_w = \pi r^2 \rho L g \tag{4.3}$$

Figure 4-6 below, shows the analytical results by using Equations (4.1), (4.2) and (4.3). These calculations shows the fabrication mechanism of ball end fibre (at $F_w<F_s$) or

tapered fibre(at $F_w > F_s$) depends on the values of downward force (F_w) ,upward force (F_s) which is constant (62.5 µN) and the effect of adding weight (6 g) that is fixed to the end of OF below the irradiated site. As a result of using 6 mg weight minimized the waist of OF (taper length) from 20 mm to 1.5 mm.

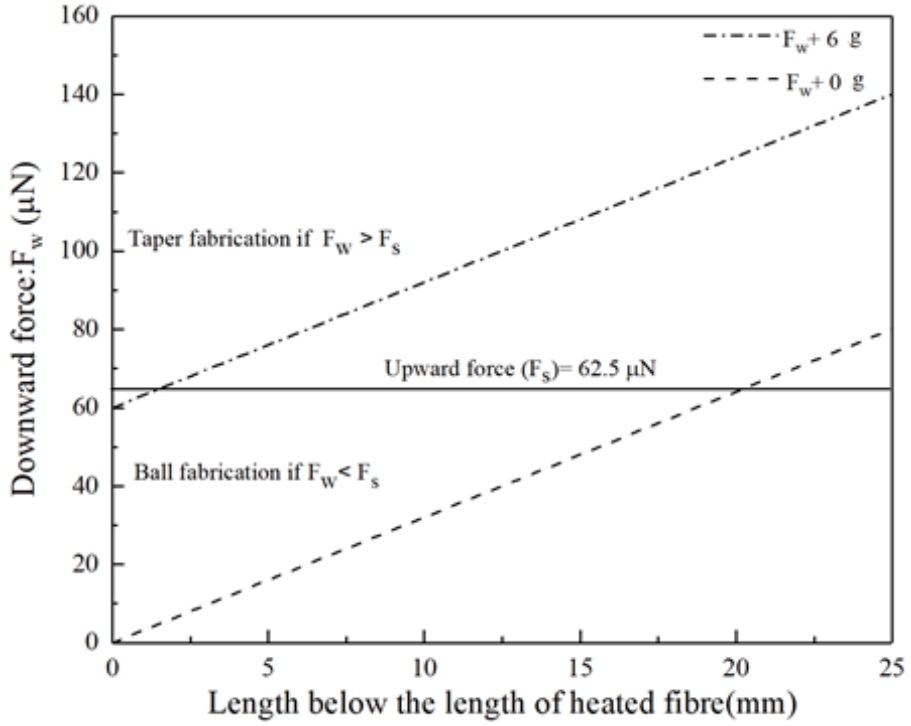

Figure 4-6. Microlensed fibre mechanism to fabricate both micro ball end and tapered OF.

To soften the material, the fibre end is heated, in general, it will become spherical because of surface tension forces [271, 285]. The spherical lens operating single fibre is the simplest one. By feeding the stripped fibre into a heat zone which is irradiated by high power CO_2 laser, the end of silica fibre melts and forms a ball shape due to heat source from laser beam and surface tension forces. A schematic of the experimental set-up is shown in Figure 4-7.

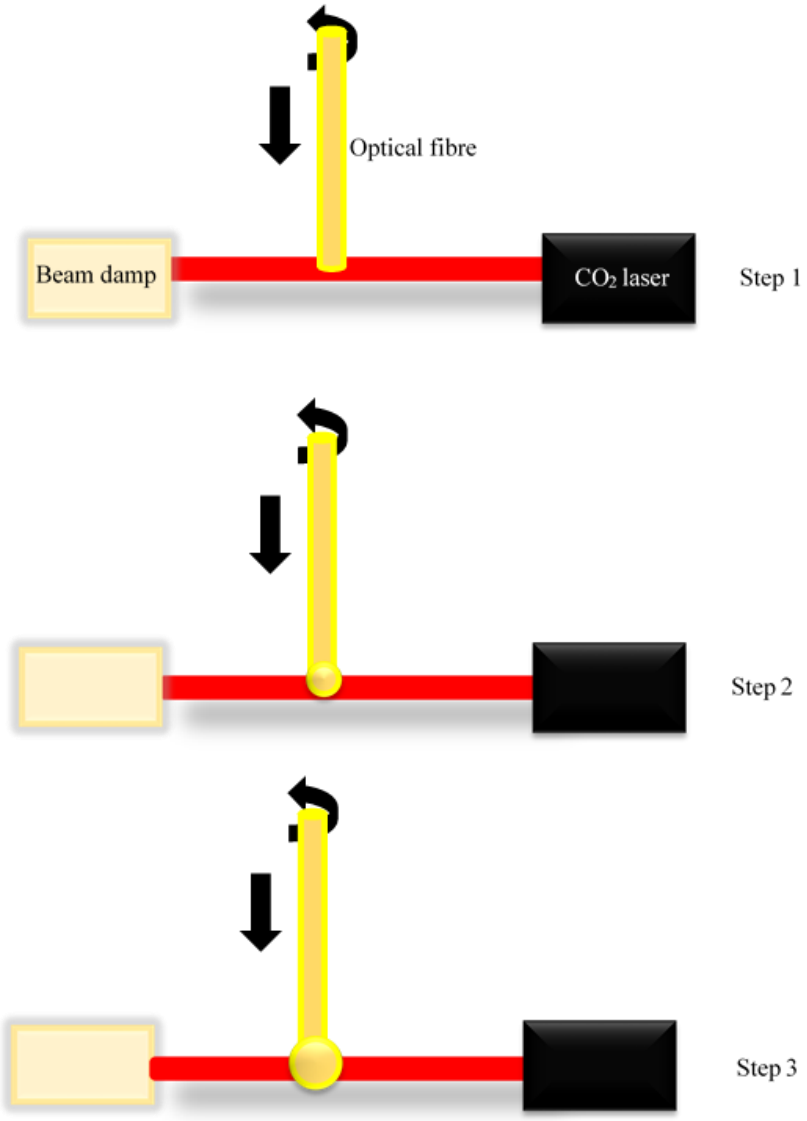

Figure 4-7 Spherical lense prepared with single fibre by pulling fibre to heat zone with constant revolution and pre-set speed. The encouraging length is determined to focus on the desired size of the ball lens. The size of the ball can be measure during the process increasingly, and the power of the laser in the ongoing capacity of the size of the ball.

Pushed-trapper construction is an example of a process for tapered -end fiber microlens. Whereas, for the endcaps in the fibre laser system, the up-tapered lens is frequently required. Figure 4-8 demonstrates the general process of fabricating such fibre lenses. As shown in Figure 4-7, the change in temperature when heated irradiated area of OF using a CO_2 laser depends strongly on the optical absorption coefficient and the incident laser power. Therefore, the ideal configuration, which is the best location of the CO_2 laser beam is shown as in Figure 4-8. It can be founded that irradiating silica at low power and irradiating silica fibre at acute angles can be used to polish silica surfaces. Therefore, the machining process must be carefully optimized to minimize roughness.

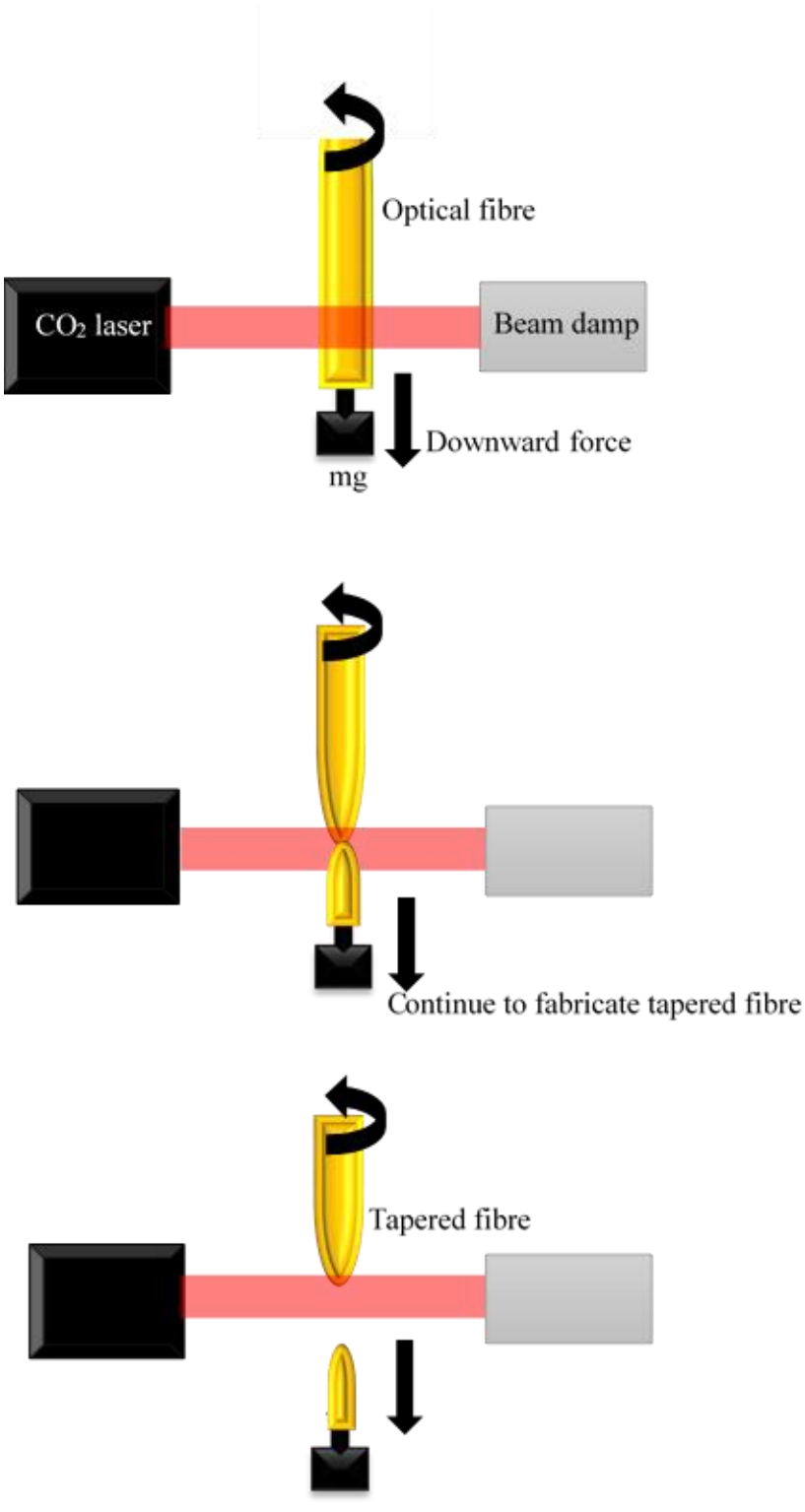

Figure 4-8 A schematic of the tapered fibre techniques, illustration of taper lens processing with both of transition fibre and lens-fibre till breaking fibre , then tapered fibre continue rotating about 20 sec to reduce surface roughness of lens.

4.2.2 Calculating the CO_2 laser beam spot size.

The Gaussian beam output of a laser is frequently characterised using the well-known ABCD matrix technique [303]. The output beam waist at the focal length is expressed by:

$$\omega_{01} = \omega_0 \left[\left(\frac{n_1}{n_2} \right) \frac{A^2 + \alpha^2 B^2}{AD - BC} \right]^{1/2} \quad (4.4)$$

Where, n_1 and n_2 are the refractive indices of the OF core and air, respectively. The terms A to D are the elements of the ray matrix, derived from the input and output planes obtained from.

$$\begin{bmatrix} A & B \\ C & D \end{bmatrix} = M_{34} M_{23} M_{12}, M_{12} = \begin{bmatrix} 1 & L_c \\ 0 & 1 \end{bmatrix}, M_{23} = \begin{bmatrix} 1 & 0 \\ \frac{n_2 - n_1}{n_2 R} & \frac{n_1}{n_2} \end{bmatrix}, M_{34} = \begin{bmatrix} 1 & L_f \\ 0 & 1 \end{bmatrix} \quad (4.5)$$

L_c is the length of the microlens fibre, R is the radius of curvature of the lens, L_f is the focal location relative to distance between the surface of the lens and the final beam waist. The matrix should satisfy: $AC - \alpha^2 BD = 0$ in which $\alpha = \lambda / \left(n_1 \pi w_0^2 \right)$. Where, λ is the wavelength, and ω_0 is a beam waist of the end face of the OF referred to as the core diameter. The beam radius at point z is given by,

$$\omega_1(z) = \omega_{01} \left\{ 1 + \left[\left(z - L_f \right) \lambda / \left(\pi n \omega_{01}^2 \right) \right]^2 \right\}^{1/2} \quad (4.6)$$

Equations 4.4 to 4.6 are used later when discussing the mechanism of fibre re-shaping.

4.2.3 CO_2 laser polishing of microlensed optical fibre end surface

In micro lensed optical fibres, to fabricate transmission loss, the required condition is to identify the mechanism of all losses which helps to avoid in composition of given glass [153]. The light propagation in material begins at its surface and the transmittance T is the factor responsible for the entrance of light, it is related to surface reflectance R represented as $T = 1 - R$, where R is the reflectivity derived from refractive index of material, angle of incidence and surrounding media [289].

The scattering mechanism is mainly due to forward scattering (Mie scattering), this mechanism is appear because of material inhomogeneities at longer wavelengths [276]. For low scatter loss in these components, laser melting treatment (polishing) is introduced to reduce the roughness of surface to 10nm without changing the initial surface shape

(laser - machined shape) significantly [298]. Also, better polishing of core/cladding regions can decrease the overall losses by decreasing the end surface scattering losses.

The surface roughness of a lens strongly influences its properties and functions, such as; optical properties of the OF. Surface roughness reduction is important when it comes to coupling and propagation of electromagnetic radiation in optical fibres and optical components [284]. OFs are passive waveguides that may require additional active and passive devices [304]. Integrating these devices may introduce additional optical losses at the adjoining interfaces. For example, if coupling lenses and collimators are introduced in the optical fibre system. Interfaces may become damaged especially if the power delivered down the fibre is high. Surface smoothing is often required to reduce losses, which can be achieved through various techniques [156]. The most promising technique to resolve these issues is to integrate components by permanently splicing them in fibre system. Hence polishing surfaces at the input or distal end of the fibre serves to reduce optical transmission losses.

Therefore, in industrial manufacturing polishing techniques are widely used to reduce the roughness of surfaces [305]. This can be accomplished by various heat sources, such as: heating the ends of the fibres to be joined with a flame torch, by a spark discharge, filament heater, or a CO_2 laser. Heating elements can introduce contaminants into the melted fibre end face, thus lowering the damage threshold. Spark discharge can lead to arcing onto the fibre connector and can present an electrical hazard therefore, laser heating is the preferred method of melting the fibre end face [306, 307]. CO_2 lasers at 10.6 μm are an excellent choice for fused silica fibre. CO_2 laser polishing promises a non-contact approach with fast preparation times and high quality surface finishes for silica glass fibres [308].

Nowadays, CO_2 lasers have been widely used for micro-patterning of various materials [89] and micro-lens formation inside transparent materials . The polishing process with laser radiation can significantly reduce the surface roughness from not polished glass material. Although mechanical polishing can decrease the roughness of the end faces of optical fibres, CO_2 laser-assisted polishing can reduce the roughness of the OFs significantly, and the technique is simpler compared to traditional mechanical polishing [309]. A decrease in the roughness from 2.5 μm average to less than one hundred nanometres was achieved. The microstructure of the surfaces has been measured using White Light Interferometry (WLI).

4.3 Calculation of silica fibre melt temperature

Splicing and shaping of OFs via lasers has several significant advantages over other electric heating methods which include nichrome wire resistance heating and electric arc heating. The output power of the laser beam can be more easily controlled, and it can be directed accurately to the butted fibre ends by using laser optics [156]. The main advantage is that heating through absorption is characteristically different compared to other electrical surface-heating methods. Due to absorption, the heating process can be directed to exactly the places that are decisive for the process. Directed heating not only improves the quality of available OF components, but allows unique fabrication of fibre shapes and designs [310] . The feasibility of using a CO_2 laser to make micro-spherical ball lenses on the end of the fibres was also investigated. Inclusion of micro-lenses present significant promise in the drive to create fibres for high-efficiency coupling and transmission of light [149].

Microspheres integrated into optical fibre devices have been at the forefront of research over the last two decades. Microspheres created on top of OFs were explored for the possibility of exciting whispering gallery modes. They opened new paths in different fields of research. In addition, such kind of structures can also be produced for interferometric cavities [311].In this study, heat conduction within optical fibres during CO_2 laser splicing is calculated .

Radio frequency excited CO_2 laser beams have a Gaussian irradiance distribution when operating on the TEM00 fundamental mode. Within the study, various operational parameters were varied to determine the optimal conditions for the fabrication of spliced fibres. The examined parameters include beam fluence, duty cycle, the standoff height of the fibres, translational speed of the piezo stage, and finally the assist gas pressure. This investigation will allow for the optimisation of the parameters [153]. In the following text, the temperature as a function of time and position is obtained from first principles. It is then applied in the specific case of absorption of a Gaussian beam by thermally optical fibre.

The surface temperature of a heated OF can be found theoretically by considering the heat generated by a CO_2 laser fluence incident on the OF by utilising the heat equation. The heat losses through conduction, convection, and radiation as a function of time and axial

position are also considered like this giving a more realistic model. The heat equation utilised within the study is given by the equation below [160].

$$\frac{\partial^2 T}{\partial x^2} - \frac{1}{k}\frac{\partial T}{\partial t} - \frac{4H}{Kd}T = 0 \tag{4.7}$$

Where H is the conductance of the material surface. The terms within this equation are detailed in Table 4-2.

$$T(x,t) = \frac{P}{\pi^{3/2} d^2 C\rho (kt)^{1/2}} \exp\left(-\nu t' - \frac{x^2}{4kt}\right) \tag{4. 8}$$

Where P is the quantity of heat liberated by the instantaneous point source, and

$$\nu = \frac{4H}{C\rho d} \tag{4.9}$$

The analytical solution for temperature is derived as a function of time, position, and beam radius, all equations parameters are reported in Table 4-2. Figure 4-9 shows the temperature (*T)* calculated as a function of the ratio of the distance from junction point to fibre diameter (*w/d*). It can be seen the gradient of temperature is very sharp at a small value of *w*. At a distance equal to the fibre diameter ($w = d$) is estimated to be 82% of that at $w = 0$. The minimum required laser power P_o against fibre diameter is calculated by using Equation 4.10 [312]. As shown in Figure 4-10 the minimum required power is proportional to the fibre diameter.

$$P_0 = \pi d^{3/2} (KH)^{1/2} \frac{T_m}{(1-R)} \tag{4.10}$$

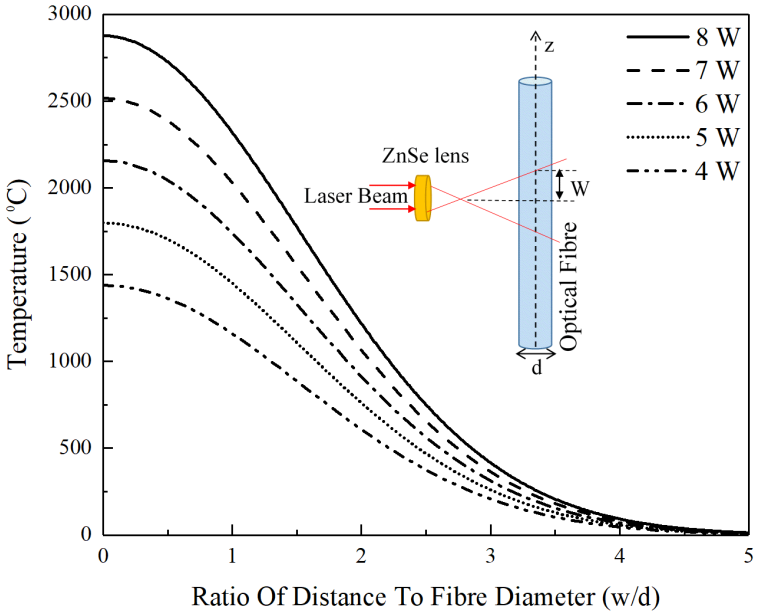

Figure 4-9. Temperature *T* as a function of the ratio of distance from junction point z to fibre diameter (*w/d*).

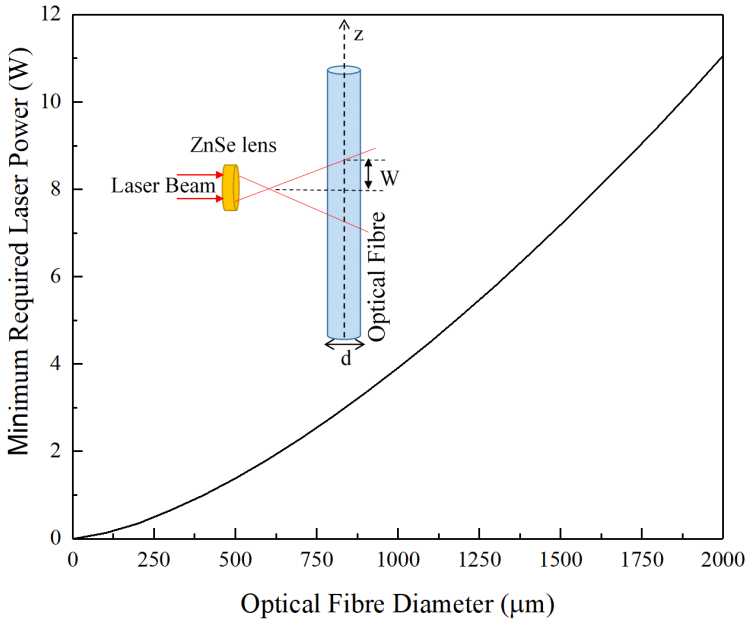

Figure 4-10. Gaussian spot of fix diameter *2w* heats an optical fibre of diameter *d*, and the minimum required power for melting silica optical fibre as a function of OP diameter.

Table 4-2 Values of optical and physical parameters

Term	Value	Units
Λ	10.6	μm
C	7.7×10^{3}	$J.kg^{-1}.K^{-1}$
H	418.68	$W .m^{-2} .K^{-1}$
K	0.015	dimensionless
K	1.1-1.4	$W m^{-1} K^{-1}$
N	2.0–2.2	dimensionless,
W	100	μm
Tair	293	K
Tm	1800-2000	K
P	2.2×10^{3}	$kg m^{-3}$
R	0.15	dimensionless

4.4 Methodology

Experiments to re-shape SiO_2 OF fibres were carried out using a CO_2 laser (OEM10ix(PP), Rofin, maximum average output power 115W, wavelength 10.6 μm, the maximum pulse repetition rate of 130 kHz at duty cycle 60% and the pulse width range of the CO_2 laser beam 2-400 μs beam diameter 8.0 mm ± 0.2 mm at laser output optic (aperture). The laser assembly consists of a laser tube, integrated RF power supply, oscilloscope (Keysight, DS) X2002A,70 MHz), and TTL controller unit (Rs422) to drive the laser. The laser output passes through the manual attenuator (C-MA, ULO Optics), it uses for two purposes firstly, it allows the user to externally control the transmitted power of CO_2 laser beams, secondly for stopping unwanted back-reflections from reaching the laser. The operation principle is founded on the 'Brewster angle'. It provides much adjustable control of the transmitted beam from 6% to 100 %.

The CO_2 laser beam was focused using a zinc selenide lens (clear aperture: 10 mm, and a focal length of 100 mm). The laser was water-cooled although at the low powers used the chiller unit was not put under much load. Silica multi-mode optical fibre was selected with samples having core/clad diameters of 50μm/125 μm, 400μm/425μm, 600μm/630μm, 1000 μm/1035 μm, and 1500μm/1550μm. The core and cladding

refractive indexes were 1.46 and 1.40 respectively at 436 nm wavelength. The attenuation ranged from 12 dB/km to 18 dB/km at 808 nm (Thorlabs). The optical fibres were supported using a collet chuck and rotated using a Nema hollow shaft stepper motor (rated current: 0.67 Amps having a holding torque of 0.08 N.m. The motor spindle and hence fibres were oriented in the vertical position. Motion control x-y-z-stages (Aerotech, ANT130-v) having a resolution of 1 nm in the x, y, and z directions (see Figure 4-11l. A). The rotation speed of the motor was controlled by Arduino software (see appendix), and the code was written and uploaded to the board (ARDUINO UNO REV3, A000066]. Figure 4-11. B shows the schematic diagram of the setup that used to fabricate lensed fibre on the tip of an OF using a pulsed CO_2 laser. The optical fibre is suspended vertically and laser radiation is focussed onto the fibre in a horizontal orientation. The relative position and movement between the fibre and laser focus control the shape of the lens. The optical fibre is controlled by computer-controlled motion control stages. This permits precise positioning of the fibre with respect to the laser beam.

A CO_2 laser-assisted reshaping technique was used to fabricate micro-lensed fibres of various shapes, as mentioned earlier. Spherical, tapered, and cone-shaped fibre tips were included by varying the laser energy, core diameter, irradiation time and motor rotation speed. The shape profile of the fabricated lens must be controlled accurately. With the laser micromachining method, the shape of the fabricated lens is determined by the command sequence controlling the movement of the fibre through the beam once the beam parameters (pulse length, power, and period) are fixed. By simply changing this sequence of commands, lenses of different profiles can be formed. The applicability and flexibility of this unique micro-lens manufacturing procedure are expected to be enhanced by this feature.

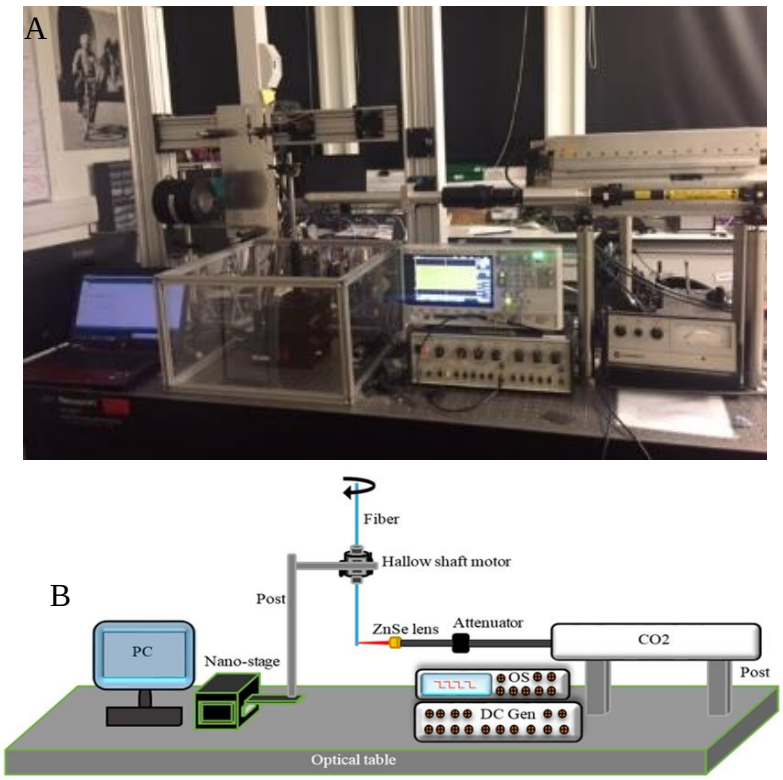

Figure 4-11. Experimental setup used to fabricate micro-lens end fibre (A) and schematic diagram of the setup which used to fabricate the spherical/ hyperbolic shape microlens on the tip of an optical fibre using a pulsed CO_2 laser (B).

All the lensed fibres were investigated by using the microscope (LEICA DMLM). The knife-edge technique was used to characterise the beam profile in the focal region of the microlensed fibre fabricated. While looking at the transmitted light on a screen, a knife-edge is mounted on the xyz-nano stage (Aerotech, ANT130-v) and moved across the beam. A helium-neon laser (632.8 nm wavelength) was used for testing the lensed OF. This technique can provide very high spatial resolution, depending on the physical limits of the aperture and the accuracy of the translation stage. It is therefore well suited for measurement of focused spots fibre-optic outputs. From simple geometric optics, if the knife-edge is before the focus, the shadow on the screen will be on the opposite side and will move in the opposite direction of the knife-edge. Similarly, the shadow on the screen will be on the same side and will move in the same direction as the knife-edge if the knife-edge is behind the focus. The transmitted beam will tend to blink on and off, with no discernible shadow motion (dependent, of course, on the waist radius and translation resolution) at the focus.

4.5 Results and discussion

4.5.1 Calibration of parameters

To convert the plane surface of the flat face OF to a spherical shape, a CO_2 laser beam of average power 5 W was focused on the end of the horizontally positioned silica MMF. Due to the exposure of the laser beam for approximately 10 mins, the end face of the optical fibre was melted and consequently reshaped to the spherical shape (micro-lensed fibre), the optical microscope image of which is depicted as shown in figures below. The calibration and optimization were done for different parameters (irradiation time, irradiation fluence, rotation speed, and irradiated distance from the end of fibre). If the laser beam diameter doesn't cover all OF the diameters, it will be difficult to fabricate the spherical shape, therefore all samples that are fabricated placed out the off-focal region of the optical system lens (focal length (100 mm) ± 10 mm). Figure 4-12. (A) Optical microscope image OF end (1500 μm core diameter) which placed in the focal length (f=100 mm) of ZnSe lens) then irradiated by CO2 laser (irradiated power 5 W, irradiation time 10 sec and fibre rotating speed=20 rpm).

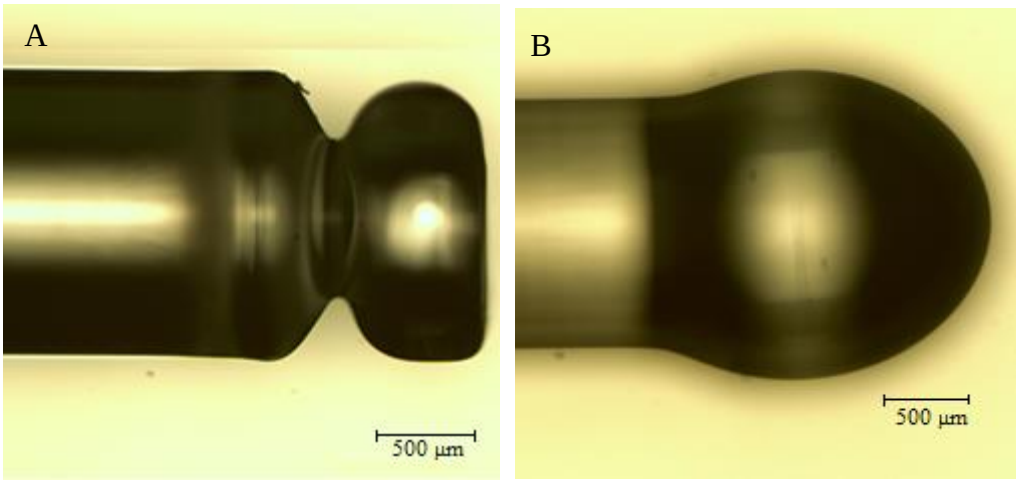

Figure 4-12. (A) Optical microscope image OF end (1500 μm core diameter) which placed in the focal length (f=100 mm) of ZnSe lens) then irradiated by CO_2 laser (irradiated power 5 W, irradiation time 10 sec and fibre rotating speed=20 rpm). (B) optical microscope image of the same OF was placed out of the focus, f ± 10mm and irradiated by CO_2 laser with the same parameters.

Figure 4-12. B shows the optical microscope image of 1500 μm core diameter of silica OF when it was placed in the lens focal length ±10mm (out of focus) because the laser beam diameter out of focus has diverged and it was covered most of the irradiated area of OF therefore the shape is spherical compared with the fabricated OF that was placed in the focus point of the lens (see Figure 4-12 A).

Surface roughness measurements of optical fibres are necessary after laser processing in order to gauge surface quality. The lensed fibre end-face roughness after laser melting or cutting has a significant influence on the transmission quality of light signals. If the fibre end-face roughness is small, the efficiency of fibre optic coupling is higher. Therefore, measuring a surface profile and surface roughness of a lensed fibre end-face is an important issue. The roughness (R_a) was measured by WLI for all samples as shown in Figure 4-13.A, B, C, and D, all calibration is done for silica optical fibre with a core diameter of 400 μm as shown below. It can be seen that the minimum roughness is produced at a laser intensity of 32 $MW.m^{-2}$, as shown in Figure 4-13. A. At this intensity, the roughness was proportional to the rotation speed of OF especially if the speed is more or less than 20 rpm (see Figure 4-13. B). Furthermore, Figure 4-13. C shows that the Ra decreased sharply when the irradiation time increased from 3 min to 5 min then Ra decreased gradually until 10 min which produced to the minimum roughness (~10 nm). After 10 min, Ra increased significantly with increasing the irradiation time. Finally, the diameter of the micro-ball lens at 32 MW.m-2 is increased with increasing the distance of irradiation from the fibre edge until 1.5 mm away from the edge (see Figure 4-13. D). The surface quality of the lens was found to have a surface roughness of $< \lambda/10$. Accurate characterisation of nanoscale surface roughness is important in many applications, and several techniques exist for this purpose. One of these techniques is polishing by CO_2 laser at low power because, without thermal treatment, the different stresses in the glass can lead to optical distortions.

Using laser radiation for polishing, a thin surface layer of the silica OF is heated up just less than evaporation temperature due to the interaction of silica material and laser radiation. It is expected that temperature is the essential determining factor for the hole smoothing process. Viscosity, stock removal, and material tensions are influenced by this value. With increasing temperature, the reduced viscosity in the surface layer leads to the reduction of the roughness due to the surface tension. Hence, a contactless polishing method can be realized nearly without any loss of material or need of a polishing agent.

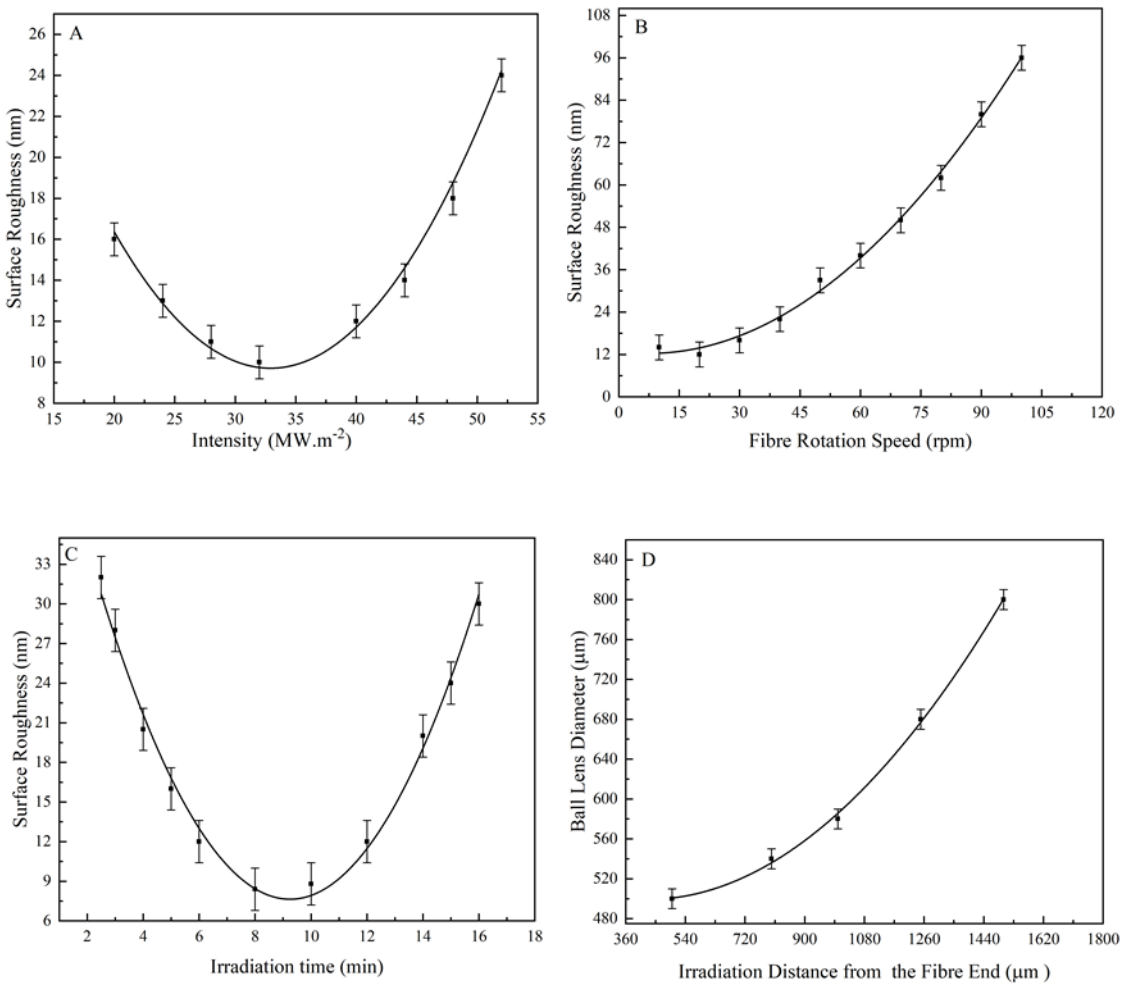

Figure 4-13 Measurements: (A) Surface Roughness *vs* incident laser intensity when irradiation time 10 min and the fibre rotation speed is 20 rpm (B) Roughness *vs* rotation speed of optical fibre when the incident laser intensity 32 MW.m^{-2} and irradiation time 10 min, (C) Roughness *vs* irradiation time when the incident laser intensity 32 MW.m^{-2} and the fibre rotation speed is 20 rpm. (D) Roughness *vs* the irradiation distance when the incident laser intensity 32 MW.m^{-2}, irradiation time 10 min and the fibre rotation speed is 20 rpm.

An experimental setup is shown inFigure 4-11 was used to fabricate microsphere lenses when the average laser power is set to 5 W, the intensity was around 32 MW.m^{-2}, the fibre is mounted vertically on the 3D translation stage, and rotated by hollow shaft motor at different rotation speed 10-50 rpm, after removing the coating layer at the end of the silica MMF. Silica strongly absorbs the emitted light at 10.6 μm, causing the fibre to soften at approximately 1800 K, forming a sphere due to surface tension which was discussed previously. The high viscosity of Silica result in spherical structures with low eccentricities of 1% or less, and low intrinsic roughness (root mean squared roughness of the order of 10 nm) results from the high viscosity of Silica. Figures below show the microscope image of silica microspheres fabricated in this manner. It can be seen that various micro-lensed optical fibre samples were placed on the stage of an optical

microscope to examine the structure of the fibre tips. The end shapes of OF depended on fibre rotation speed, the time of irradiation and the laser power (see the calibration measurement in Figure 4-13).

The mechanism of the end shape fabrication of lensed fibre due to irradiation heat reaches the thin-layered OF cladding immediately, the cladding melts and breaks when the laser beam is incident on the OF surface. Then, the heat passes to the thick-layered OF core, and the core melts gradually and finally forms different end shapes due to surface tension, irradiation time, laser power, and rotation speed. When the rotation speed is fixed between 10 to 20 rpm and the time of irradiation 10 mins, the more symmetric lens could be fabricated. All experiments performed within ± 10 mm away from the focal length of ZnSi lens that used to focus the beam of CO_2 laser to cover 400 μm core diameter of OF by a laser beam. The knife-edge technique is a beam profiling method that allows for quick, inexpensive, and accurate determination of beam parameters. The HeNe laser beam is focused on a lensed fibre and in the focal point (not correspond with the focal point in the case geometrical optic) the beam waist is located. In this technique, a knife-edge moves perpendicular to the direction of propagation of the laser beam, and the total transmitted power is measured as a function of the knife-edge position. The shift of blade in the x-axis from the position where it fully blocks the laser beam to the position where the beam is not blocked and therefore it fully incidents on the photodiode. The obtained transversal profile of the laser beam should be similar to the curve shown in the figures below.

4.5.2 Fabrication of microlens optical fibre using a pulsed CO_2 laser.

By using the setup shown in Figure 4-11, a significant role in OF end shape is played by the parameters mentioned above. Through the laser irradiating (5 W) process, rotation speed (20 rpm), 8 min irradiation time, and the irradiated area are 0.5 mm from the end face of OF, micro end lens was fabricated as shown in

Figure 4-14. A. It can be seen the shape of microlens at is not ball lens, but half ball lens. When the rotation speed is fixed at 20 rpm, time of irradiation 8 min and laser power changed to 5.5W, the absorption energy is enough to melt OF and form spherical end shape (Figure 4-14. B), then the irradiated area is increased to 1 mm from the end and irradiation time increased to be 10 min, consequently the OF end shape is close to a ball

lens as shown in Figure 4-14. C. Finally, only the irradiated area increased to 1.25 mm; the shape of the end lens is close to ellipse (see Figure 4-14. D).

In conclusion, if there is sufficient heating, the bubble expands at a faster rate, as the glass wall becomes thinner. The expansion of the bubble then suddenly stops due to the rate of heat losses at the bubble surface exceeding the heating rate from the laser. The resulting bubble (see Figure 4-14. A) an irradiated area and incident power are not enough to make a more symmetrical bubble; the heating of the bubble is stopped before it rapidly expands.

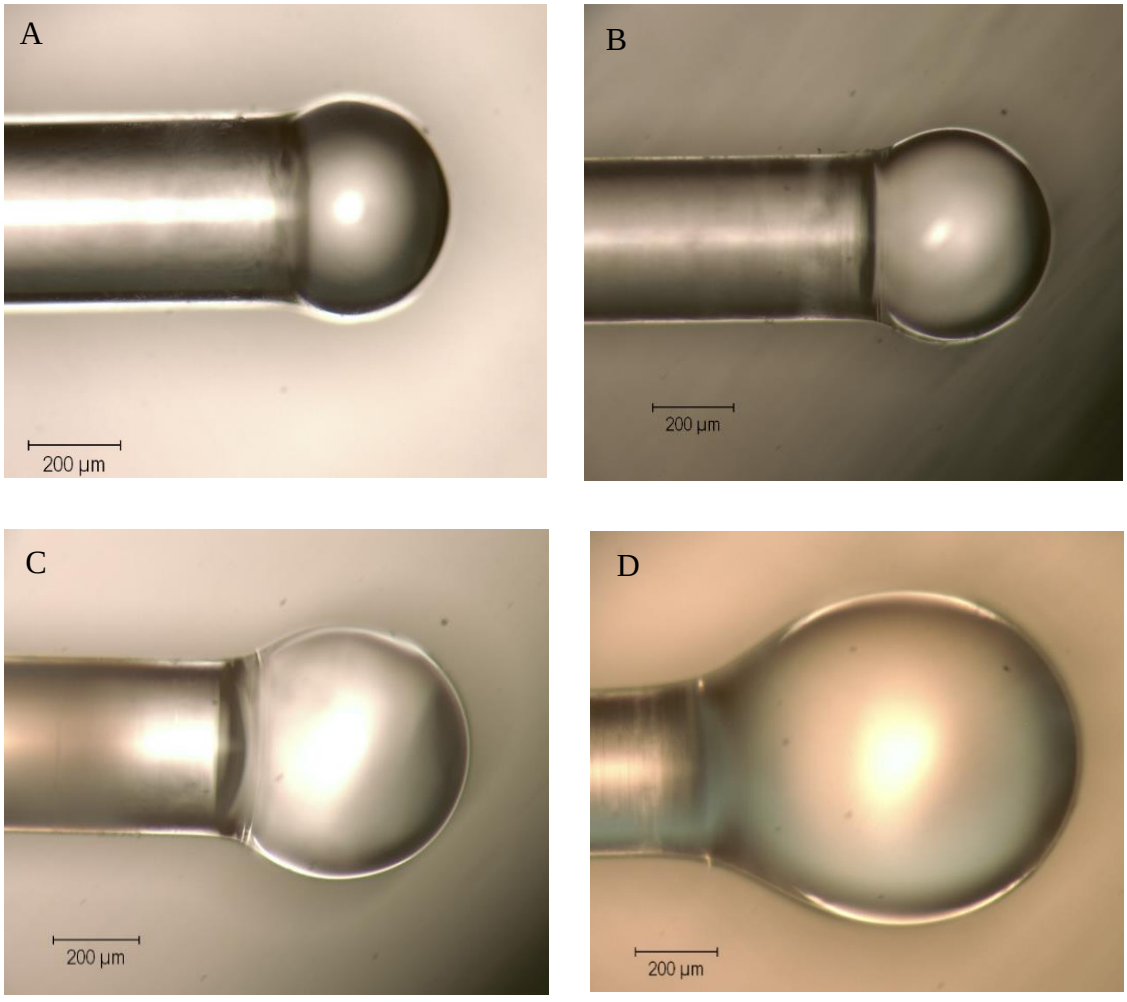

Figure 4-14 Optical microscope images of a micro-sphere lenses on the end face of silica fibre (400 µm core diameter) at different parameters fibre rotation speed (S), incident laser power (P), irradiation time (T) and irradiated area from the OF end (L) : (A) S= 10 rpm, P= 5 W, T= 8 min and L= 0.5 mm, (B) S= 20 rpm. P= 5.5 W, T= 8 min. (C) S= 20 rpm, P= 5.5 W T= 10 min and L=1mm. D) 20 rpm, P= 5.5 W, T= 10 min and L= 1.25 mm.

During this process, the sphere is filling with air which is carefully monitored and the laser is manually controlled so that the expansion does not accelerate. Polishing of the fibre tip-sample (Figure 4-14.C) several times using a CO_2 laser beam with low laser power (1-2 W at a rotation speed of 50 rpm), the roughness was reduced from around 100 nm before polishing to about 15 nm after polishing the microfiber lens (see Figure 4-14. A and B), the roughness was measured by WLI and its lower than roughness in the sample above (Figure 4-14.C) due to polishing mechanism by CO_2 laser at low power. Finally, the knife-edge method was used to characterise the intensity profile of HeNe laser (λ 632.8 nm) in the focal region of the lensed fibre which focused the HeNe laser beam as shown in Figure 4-15.C. the spot diameter at FWHM close to 160 µm.

When the CO_2 laser is used again to polish the sample (Figure 4-14. D) at low laser power (2 W) and fibre rotation speed (20 rpm) the shape of the lensed fibre is spherical/parabolic as shown in Figure 4-16.A. Its roughness reduced to 10% of the roughness before the polishing. Figure 4-16. B shows the SEM image of the spherical/parabolic lens. The beam profile of intensity behind this microlens was investigated by the Knife-edge method and produced a spot diameter of 110 µm at FWHM (see Figure 4-16. C), this microlens produced a lower spot diameter than the ball microlens (see Figure 4-15). The spherical-shaped microlenses have a stronger optical intensity and a larger elliptical field than the ball microlenses.

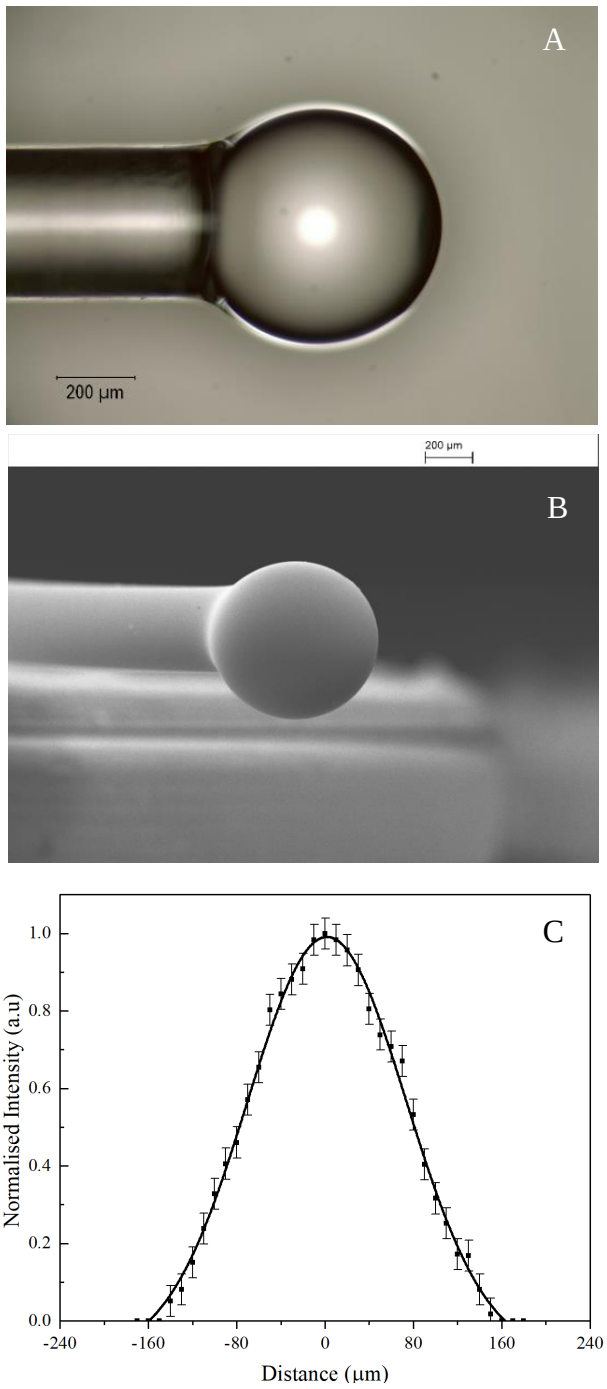

Figure 4-15 (A) Optical microscope image of micro-ball lensed fibre (400µm core diameter) after polishing the sample shown in

Figure 4-14.D by using CO_2 laser beam with low laser energy (1W) and fibre rotation speed of 20 rpm). (B) SEM image of the lens end face. (C). Normalised intensity profile of HeNe laser (λ=632.8 nm) in the focal region of the micro- ball lens, spot diameter at FWHM is 160 µm.

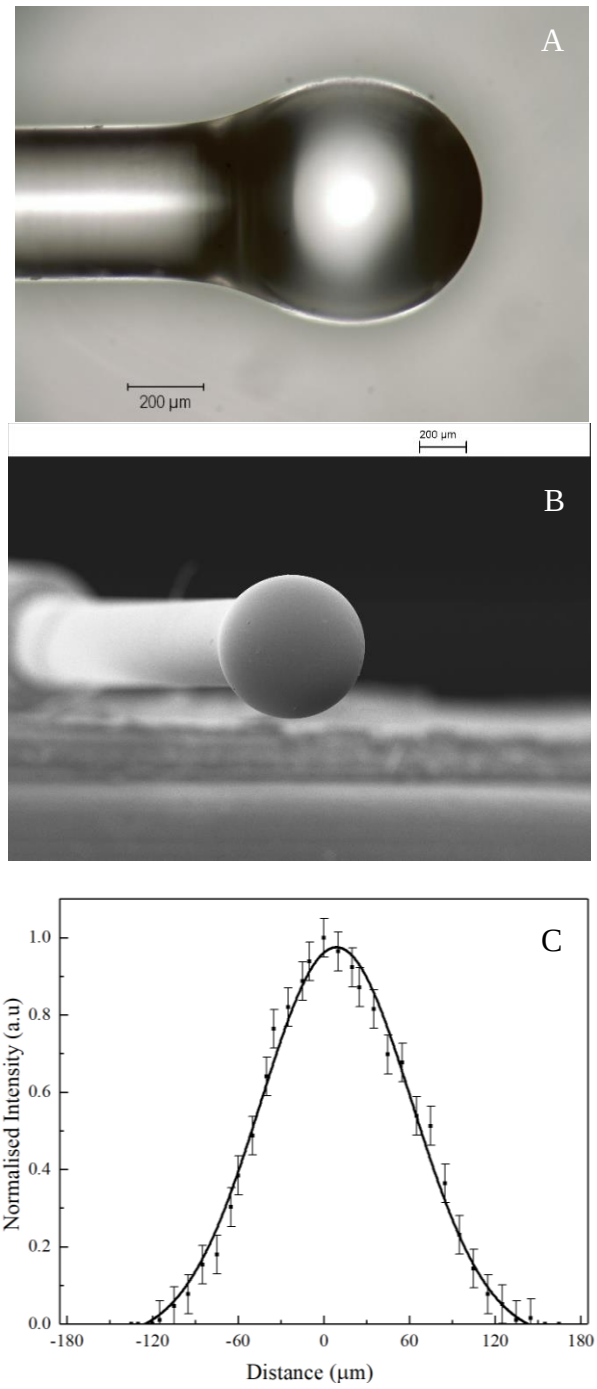

Figure 4-16. (A). Optical microscope image of the fabricated spherical-shaped microlenses lens on 400 µm core diameter of the fibre by CO_2 laser (Laser power 5.5 W, spinning fibre at 20 rpm and irradiation time is 10 min). (B) SEM image of the lens end face.(B) Normalised intensity profile of HeNe laser (λ=632.8 nm) in the focal region of the spherical-shaped microlenses, spot diameter is 110 µm at FWHM.

Figure 4-17.A. shows the optical microscope image of the spherical/parabolic lens on 1000 μm core diameter of the silica fibre. Figure 4-17. B SEM image of the lens end face the micro parabolic lens, incident laser power of 6.5 W, spinning fibre at 20 rpm and irradiation time is 10 min was used. Figure 4-17. C. presents the normalised intensity profile in the focal region of the spherical-shaped microlenses by knife-edge technique to focus HeNe laser, this lens produced a spot diameter in the focal region of about 150 μm at FWHM.

Figure 4-18, shows optical microscope image (A) and SEM image (B) of the micro hyperbolic lens that is fabricated on the end of silica OF (1000 μm core diameter) that uses an increased power of 7 W, all the other parameters were fixed the same as the sample in Figure 4-17 above. The spot size of intensity profile after this microlens was measured by knife-edge method and the proceed spot size of the beam was around 110 μm which is less than the sample above (Figure 4-17) because the latter has a higher spherical radius of the lens.

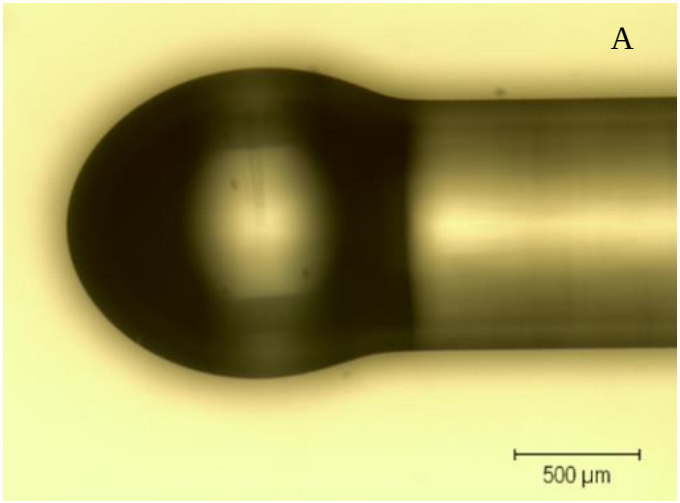

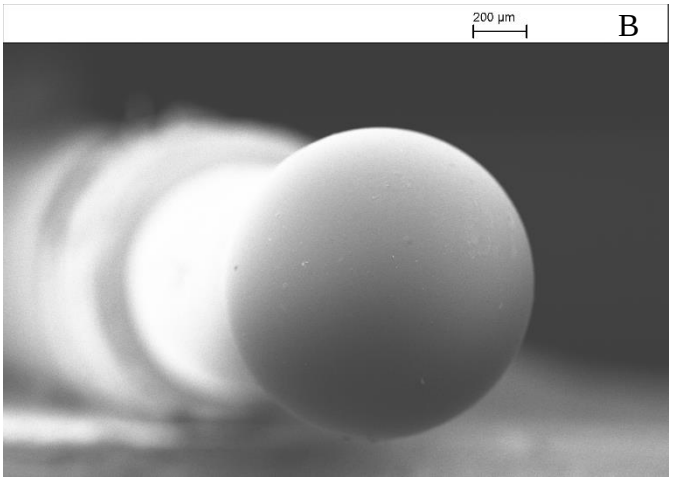

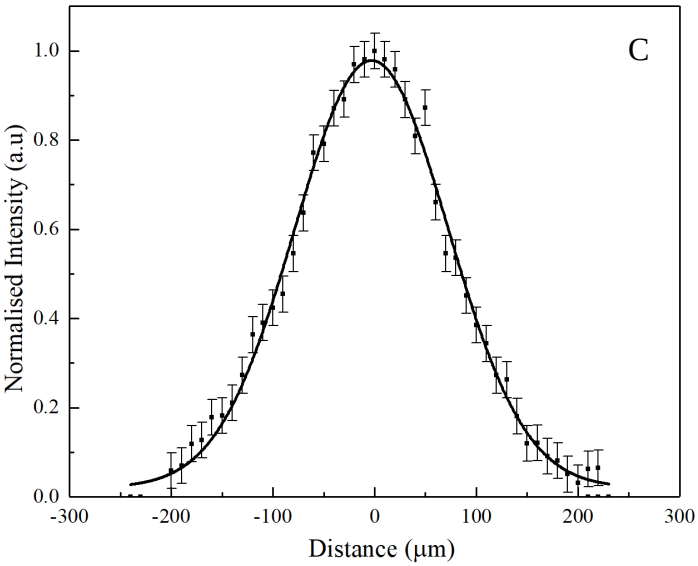

Figure 4-17. Optical microscope images of the spherical/parabolic lens on 1000 µm core diameter of the silica fibre. Laser power 6 W, spinning fibre at 20 rpm and irradiation time is 10 min. B. Normalised intensity profile of HeNe laser (λ=632.8 nm) in the focal region of the hyperbolic-shaped micro-lenses, spot diameter is 150 µm at FWHM.

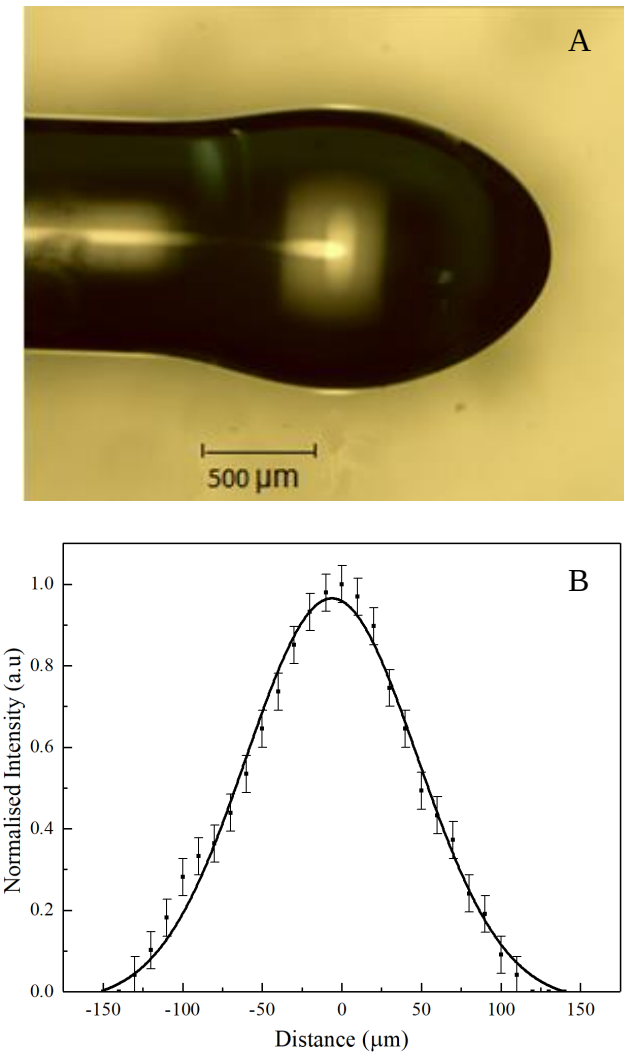

Figure 4-18.A. Optical microscope image of the fabricated spherical lens on 1000µm core diameter of the silica fibre which irradiated by CO_2 laser (incident laser power 7 W, spinning fibre at 20 rpm and irradiation time is 10 min.), B. Normalised intensity profile of HeNe laser (λ=632.8 nm) in the focal region of the spherical/hyperbolic -shaped microlenses, spot diameter is 110 µm at FWHM.

Figure 4-19. A shows optical microscope images of the spherical/parabolic –shaped lens on 1500 µm core diameter of the silica fibre was fabricated at incident CO_2 laser power 8 W, spinning fibre at 20 rpm and irradiation time of 15 min. while Figure 4-19.B. presents a normalised intensity profile of HeNe laser in the focal region of the spherical//parabolic parabolic-shaped microlenses that were investigated by the knife-edge method, spot size was found to have a diameter of 220 µm at FWHM.

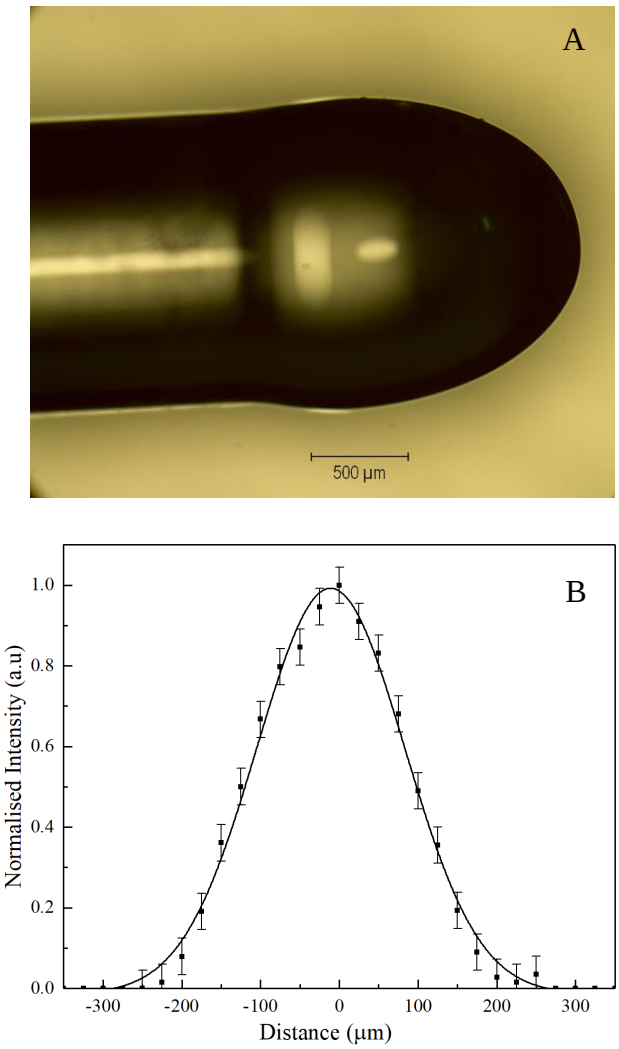

Figure 4-19. A. Optical microscope images of the parabolic lens on 1500µm core diameter of the silica fibre. Laser power 8 W, spinning fibre at 20 rpm and irradiation time is 15 min. B. Normalised intensity profile of HeNe laser (λ=632.8 nm) in the focal region of the parabolic-shaped micro-lenses, spot diameter is 220 µm at FWHM.

Results above from Figure 4-14 to Figure 4-19 show a comparison of the typical structure of a micromachined lens in the end of OF at different parameters. The technique for achieving a given desired end face radius is quite different from one to another due to the core diameter of OF and the setup parameter. The result, after this process is finished, is a fibre with parabolic-shaped microlenses and ball-end microlenses due to fibre diameter. As the tip is melted, surface tension causes the melted portion to become rounded with the diameter of the rounded tip determined by the heat distribution and by the amount of material raised above the glass melting temperature. Variations in heating and weight of the load on the fibre end can cause wide variations in the end face radius of the microlens formed since the amount of material melted is determined by the tapering angle as well as the heat distribution. The fibre tip is not chemically etched in the laser micromachining

technique. The end of the fibre is stripped and then inserted into the precision glass ferrule. The fibre is spun within the ferrule, and the shaping is achieved by directing the spinning fibre to pass through the laser beam. The fibre absorbed sufficient heat with the pulse lengths used to smooth the cut region as it is being cut. This smoothing action forms the tapered fibre. Thus cutting away excess material and formation of the microlens occurs in a single multistep pass through the beam. Tapered fibre fabrication using direct CO_2 laser irradiation.

4.5.3 Fabrication of tapered optical fibre using a pulsed CO_2

Schematic diagram of the fabrication of tapered OF using a pulsed CO_2 laser (see Figure 4-20). During the splicing process, fibre is heated up to its melting point, whereas the temperature of the fibre reaches its softening point in the tapering process. Irradiation heating with a CO_2 laser can allow the minimum taper diameter to be completely controlled via the optical intensity incident on the fibre, the rotation and nano precision movement that is available in CO_2 laser system, made flat face fibres to be tapered fibres and also capable of shaping fibres in the range between 4 μm – 10 μm.

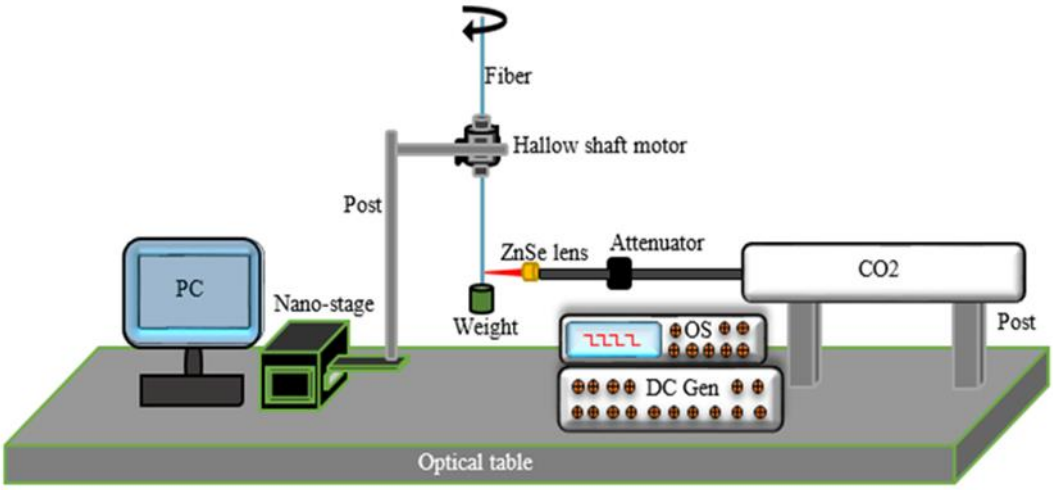

Figure 4-20. Schematic diagram of the fabrication of tapered optical fibre using a pulsed CO_2 laser.

The silica MMF (400 μm core diameter) which placed in focal length of a ZnSe lens used to focus the CO_2 laser beam on the end of the fibre. Tapering of 400 μm fibre to 5 μm is

shown in Figure 4-21. The fibre absorbed light resulting in temperature rise and under the influence of the weight, the glass softens and gradually turns into a tapered fibre. When the waist diameter of the tapered fibre reaches around 5 μm the OF is no longer being heated. Microscope images of the final taper produced can be seen in Figure 4-21. A, where the irradiation time taken for the tapering process to reach equilibrium varied from 50 sec for CO_2 laser powers fixed at 5.5 W and weight 10 g, to less than 10 sec for those fabricated at 6.5 W and the weight is 10 g (see Figure 4-21. B), due to significantly higher viscosity, surface tension and the incident power that is fixed on the optical fibre. In addition the length of tapered fibre (~ 3.5mm) in (A) is much longer than the tapered fibre in (B), the fabricated taper had an aspect ratio of 1:1000 (A) and 1:40 (B) while the taper diameter of ~5 μm in both A and B. So an aspect ratio of the taper is the most important issue to be addressed for apertured near-field scanning optical microscopy. The beam spot size of HeNe laser in the focal region of the tapered fibre (see Figure 4-21. C), was investigated by the knife-edge method and it focussedthe laser beam to be 5±1 μm at FWHM. Figure 4-22. A and B show microscope images of tapered silica fibre (125 μm core diameter) irradiated with a fixed CO_2 laser spot diameter of 180 μm, incident laser power 5 W and irradiation time 4 sec, fibre spinning 20 rpm and the weight is 10 g taper diameter 4 μm at (A) 50x and at (B) 100 x, an aspect ratio of tapered fibre of 1:20,. Figure 4-22.C presents the normalised intensity profile of a HeNe laser in the focal region of the tapered fibre by using knife edge method, and the spot diameter is approximately 4.5 ±1 μm at FWHM. The fibre taper region is smooth and x − y diameters of the tapered fibre are equal as shown in figures below. Thanks to the rotation control (Arduino software) and nano-precision movement (nanostage) that is available in CO_2 laser system, this system able to taper fibres also capable of shaping tapered fibres in the range between 4μm - 10 μm.

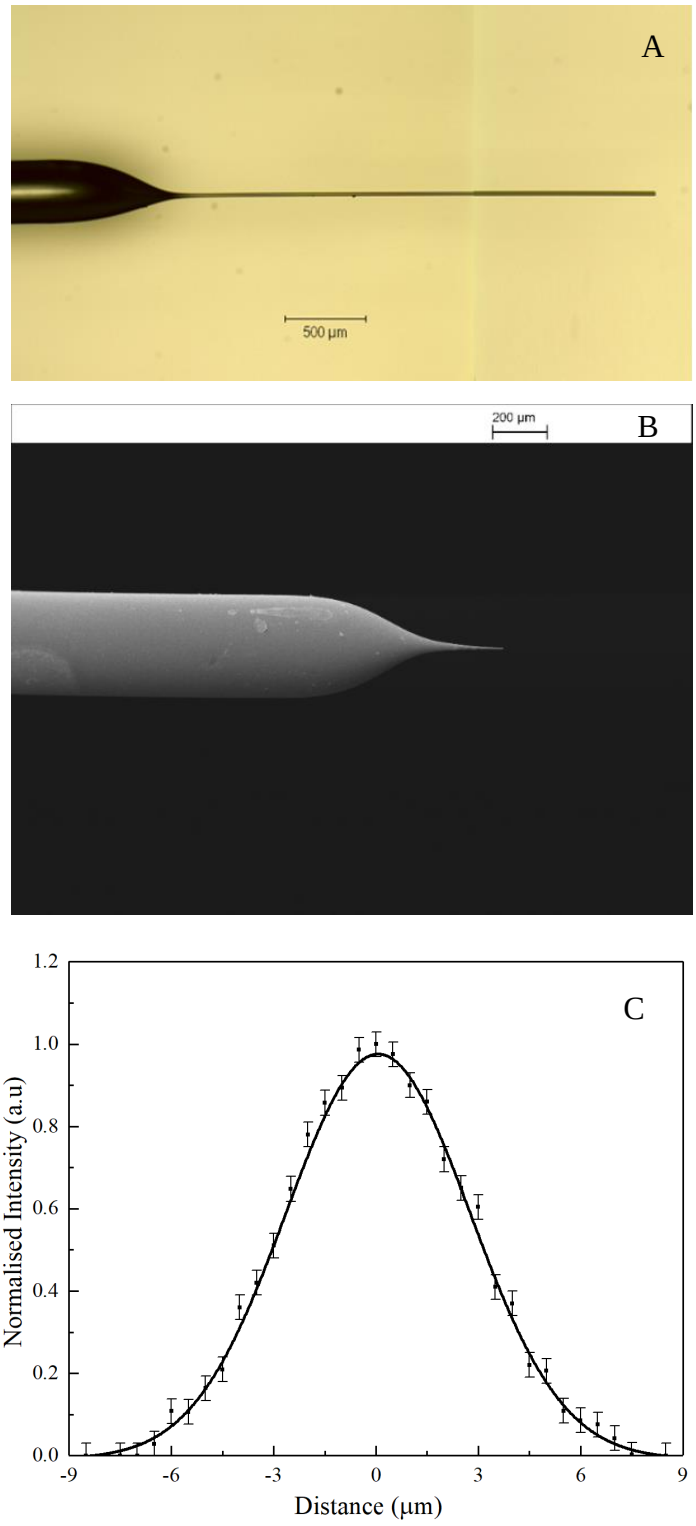

Figure 4-21. Microscope image of tapered fibres irradiated with a fixed CO_2 laser spot diameter of 180 µm for increasing the laser power. (A) 400 µm fibre core diameter was irradiated with 5.5 W for 10 sec before reaching equilibrium and the weight was 10 g, an aspect ratio of 1:1000. (B) SEM image of 400 µm fibre core diameter was irradiated with 6.5 W for 5 sec and the weight is 10 g, aspect ratio of 1:40. (C). Normalised intensity profile of HeNe (λ=632.8 nm) laser in the focal region of the hyperbolic-shaped microlenses, spot diameter is 5 ±1 µm at FWHM.

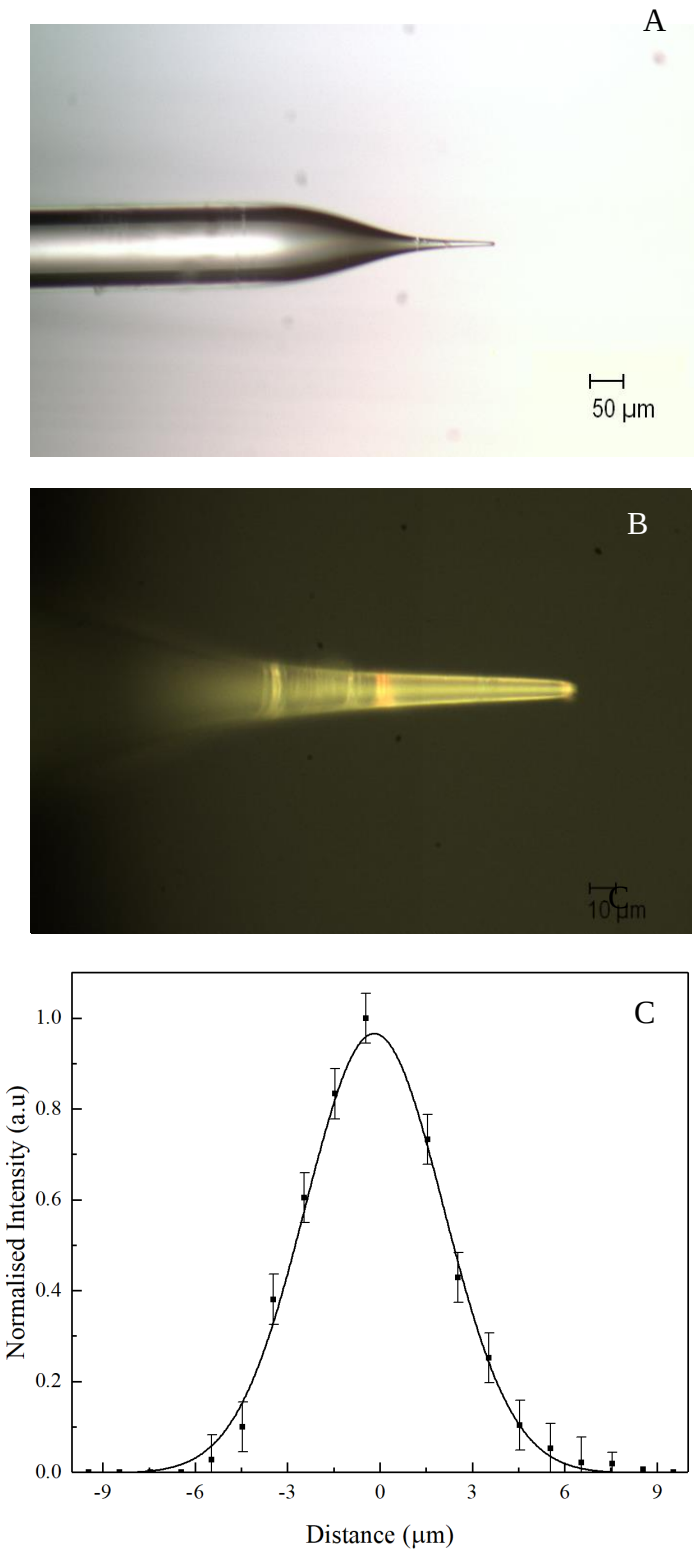

Figure 4-22. Microscope images of tapered fibres (125 µm core diameter) irradiated with a fixed CO_2 laser spot diameter of 180 µm, incident laser power 5 W and irradiation time 10 sec, fibre spinning 20 rpm and the weight is 10 g taper diameter 4 µm, an aspect ratio of tapered fibre of 1:20 (A) at 50x and (B) at 500x, (C) Normalised intensity profile of HeNe laser (λ= 632.8 nm) in the focal region of the tapered fibre, spot diameter is 4±1 µm at FWHM.

Figure 4-23.A. Shows microscope image of tapered fibres (600 µm core diameter) irradiated with a fixed CO_2 laser power at 6 W and irradiation time 10 sec, fibre spinning 20 rpm and weight of 20 g, the diameter of tapered fibre is approximately 5µm at (A) 50x and at (B) 100 x, and an aspect ratio of the tapered fibre of 1:40. (C) shows the normalised intensity profile of HeNe laser in the focal region of the tapered fibre which focuses the laser beam to be around 5 µm at FWHM.

Microscope images of the final tapered fibre (1500 µm core diameter) can be seen in Figure 4-24, where the time taken for the tapering process to reach equilibrium varied from a few milliseconds for CO_2 laser powers greater than 7 watts, to 10 times for those fabricated at around 5.5 watts, due to higher incident power. Moreover, the length of taper (400 µm length) at high incident power, 7.5 watts (Figure 4-24. B) is shorter than the taper (850 µm length) at low incident laser power, 5.5 watts (Figure 4-24. A). While the taper diameter in both cases is equal to 10 µm. Moreover, an aspect ratio of tapered fibre of1:85 and 1:40 for (A) and (B) respectively.

The HeNe laser beam was focused behind the tapered fibre lens (Figure 4-24. B) in the focal region by knife-edge method and it produced approximately 9±1 µm spot size diameter at FWHM (see Figure 4-24. C) From the tapered fibre results, the taper diameter for different core diameters of OF (125, 400, 600 and 1500 µm) are limited between 4 µm for the 125 µm core diameter OF and 10 µm for the 1500 µm core diameter OF, The tapered fibre was investigated by the knife-edge method and produced a spot size of HeNe laser beam (λ=63..8 nm) in the focal region of these microlenses of approximately from 4.5 µm to 9 µm.

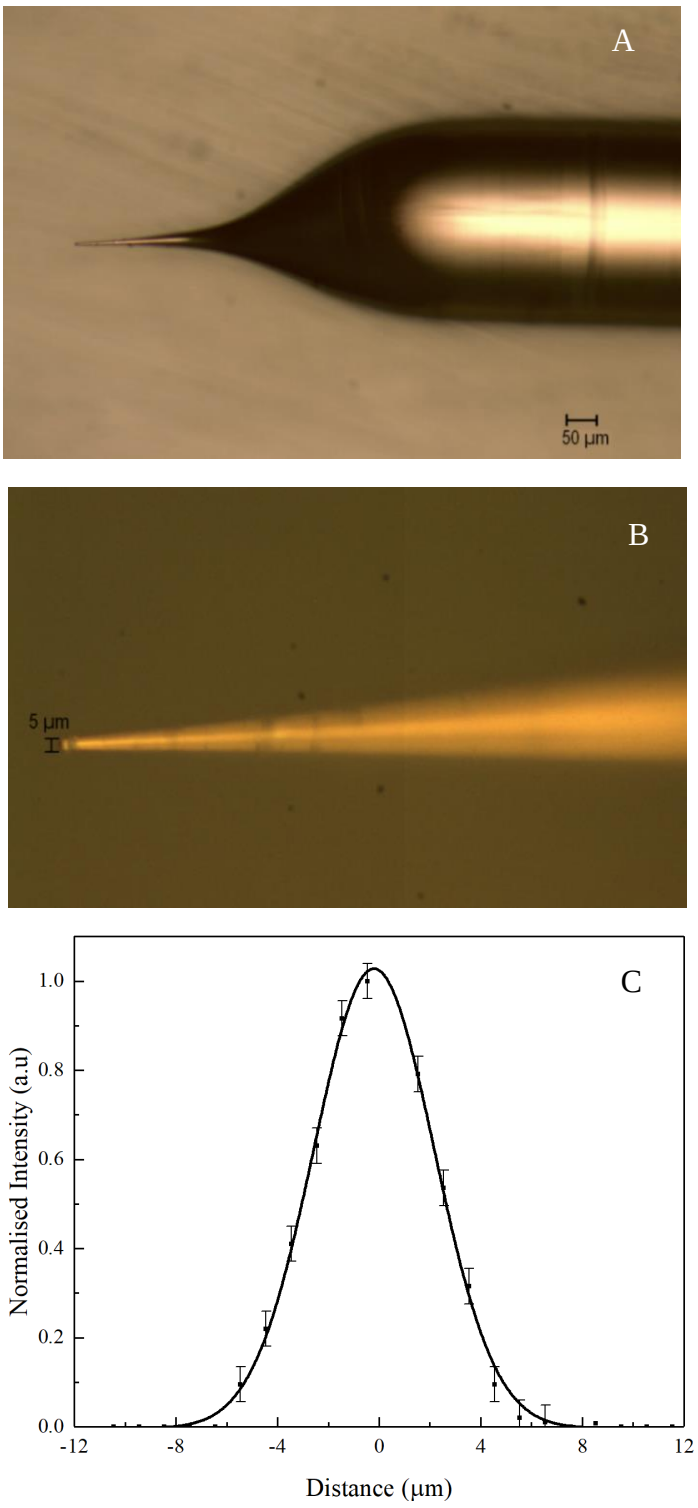

Figure 4-23 microscope image of tapered fibres (600 µm core diameter) irradiated with a fixed CO_2 laser power 6 W and irradiation time 10 sec, fibre spinning 20 rpm and the weight is 10 g, the diameter of tapered fibre is 5 µm. (C) Normalised intensity profile of HeNe laser(λ=632.8 nm) in the focal region of the tapered fibre, spot diameter is 5±1 µm at FWHM.

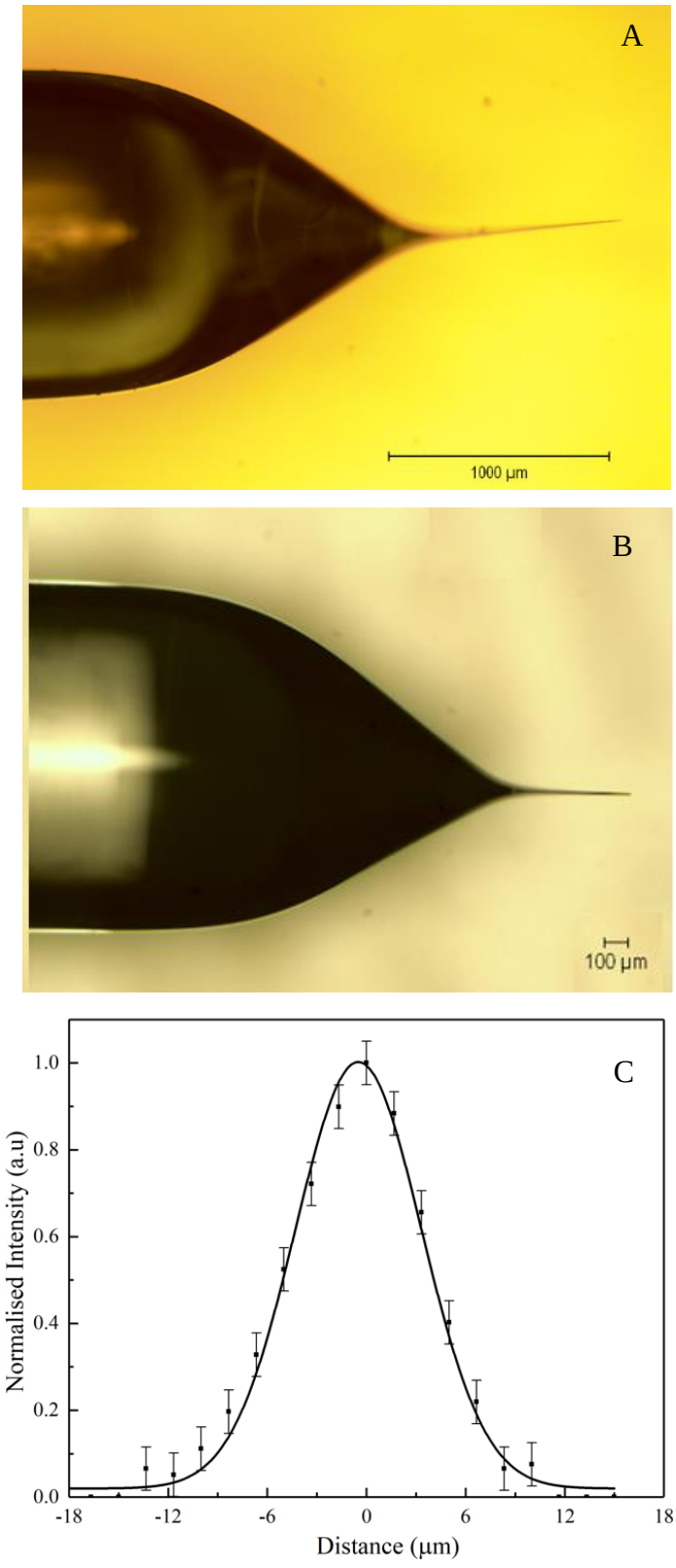

Figure 4-24 Microscope images of optical fibres (1500 µm core diameter) was irradiated with a fixed CO_2 laser spot diameter 180 µm and the OF rotated at 20 rpm, for increasing laser power going from A to B, (A) Was irradiated with 5.5 W for 100 sec before reaching equilibrium and (B) at 7.5 W for 10 sec. Taper diameter 10 µm for both cases. C) Normalised intensity profile of HeNe laser (λ=632.8 nm) in the focal region of the tapered fibre (B), spot diameter is 9±1 µm at FWHM.

A typical fibre tip structure using the micromachine method, the fibre tip was produced by firstly removing the fibre (400 µm core diameter) jacket. The fibre was on the nano stage in the focal length of the lens of the CO_2 laser system (see Figure 4-20). The weight which connects to the end face of OF is 20 g and the incident laser power fixed at 5.5 W, the fibre was spinning at 20 rpm. The Tapered fibre shape was produced first then the incident laser power was reduced gradually to 2 W to reduce the surface roughness, the fibre spinning speed was kept constant at 20 rpm. After 8 sec, the tapered hyperbolic fibre microlens was fabricated at 10 µm radius of curvature (see Figure 4-25. A). Again, the knife-edge method was used to characterize this microlens fibre and by focusing HeNe laser the spot diameter of the laser beam behind the microlens lens (in focal region) approximately 5 ±1 µm as shown in Figure 4-25. B.

Finally, an optical fibre, (600 µm core diameter) was irradiated by CO_2 laser at 7 W, 10 sec time of irradiation, and weight is 20g, thus fabricate the best exicon fibre with low radius curvature as shown in Figure 4-26. A. Then the He Ne laser beam was shined into this fibre and the knife-edge setup was used to characterise the spot of the laser beam in focal region of the optical fibre tip (see Figure 4-26. B). It can be seen the spot size diameter of this lens 5±1 µm at FWHM.

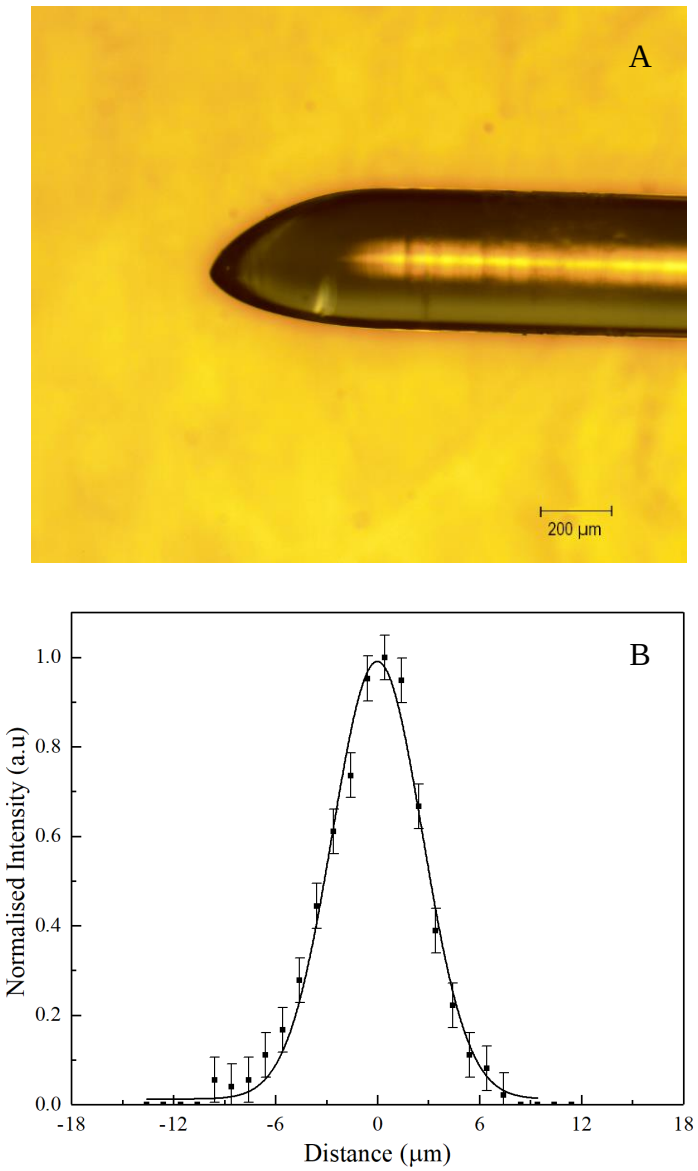

Figure 4-25. (A). Microscope image of tapered fibres (400 µm core diameter) irradiated with a fixed CO_2 laser power 5 W and irradiation time 8 sec, fibre spinning 20 rpm and the weight is 20 g, the diameter of tapered fibre is 10 µm. (B) Normalised intensity profile of HeNe laser (λ=632.8 nm) in the focal region of the tapered fibre, spot diameter is 5±1 µm at FWHM.

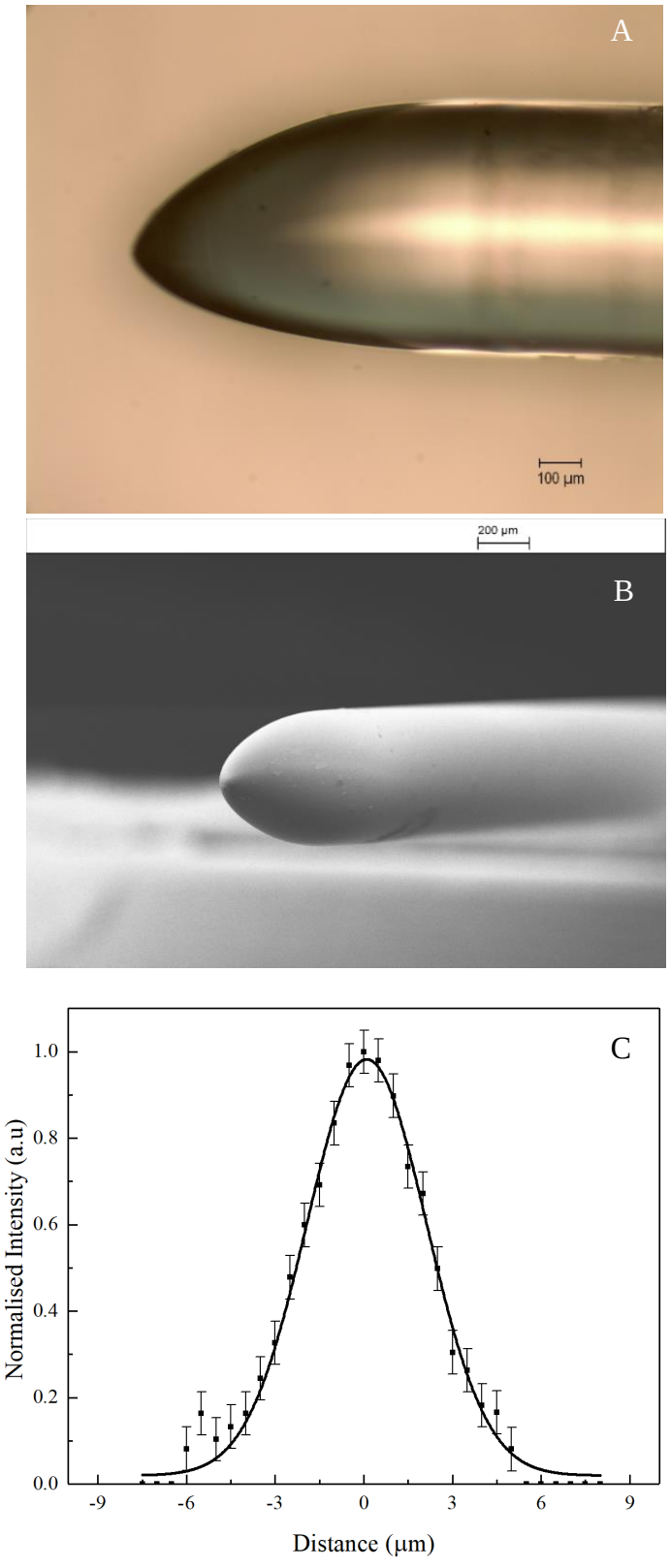

Figure 4-26. (A) SEM image of tapered fibres (600 µm core diameter) irradiated with fixed CO_2 laser power, 7 W and irradiation time 10 sec, fibre spinning 20 rpm and the weight is 20 g. (B) Normalised intensity profile of HeNe laser (λ=632.8 nm) in the focal region of the tapered fibre, spot diameter is about 5 ±1 µm µm at FWHM

4.6 Conclusion

In summary, the fabrication and characterization of lensed fibres and properties of the output beam have been discussed in detail. Various kinds of micro-lensed fibre tips have been realised including, hemispherical, hyperbolic, taper shapes using a radio frequency excited CO_2 laser. Their ability to focus light from a Helium Neon laser has been characterized using a knife-edge method. The lensed optical fibres have demonstrated the ability to tightly focus light. The use of micro lensed OF plays a vital role in the new class of microendoscopes based on individual MMFs which have been recently identified as reliable optical elements for both light delivery and detection in imaging applications. A hemispherical and hyperbolic shaped microlens was fabricated on the end of different core diameters of silica optical fibres that were heated with a CO_2 laser. The image analysis indicated that: (i) the amount of incident laser power, (ii) fibre rotation speed,(iii)irradiation time and (iv) OF diameter influence the OF end shape significantly. Excessive heat would most probably create a ball lens and increase the project area of the OF end, but the lens axis might shift from the OF axis, which will affect the optical properties. Insufficient heat could form a polynomial of the OF end and increase the project area slightly. Meanwhile the rotation speed also influences the end shapes, the faster the rotation speed, the larger the end area, and the ball lens is inclined to obtain. As a result, the minimum spot size of the laser beam was investigated behind the microlenses by the knife-edge method. A hyperbolic lens produced smaller spot diameter compared with the hemispherical lens. Hyperbolic shaped microlenses are preferred over hemispherical shaped ones for the purpose of increasing the coupling efficiency due to phase matching between the Gaussian type laser source and the fibre mode. In addition to the wave front matching between the propagating laser beam and the fibre mode, the spot-size matching of the Gaussian field distribution is a major reason for improving the coupling efficiency of the hyperbolic-shaped microlenses. These microlenses have a stronger optical intensity and a larger extent of an elliptical field compared to the hemispherical end microlenses.

A simple technique for tapering MMOF using active pressurization and direct CO_2 laser irradiation was developed and tested, fabricating different tapers of MMOF at various core diameters. Throughout this work, different tapered fibres were fabricated. These tapers had minimum waist diameters down to 4 μm and maximum taper length of ~ 3.5 mm using silica multi-mode fibre. Using the knife-edge technique produced spot

diameters of HeNe laser beam in focal region of lensed fibre are close to 5 ±1 μm at FWHM.

Fibre lensing technology is reviewed in different areas including theory, application, fabrication, and production equipment. Using a CO_2 laser as a fibre processing platform has resulted in many new products being successfully developed, with many still under development. Lensed fibres offer many advantages and cost savings compared to discrete lenses: (i) Lensed fibres are easier to align as no longer need to align a discrete lens into an OF; (ii) The back reflection is reduced for Lensed fibres as they do not have polished angled facets which is typically required at the end of an OF; (iii) lensed fibres have a single anti-reflective coated surface, compared to OFs with discrete lenses which have three anti-reflective coated surfaces; (iv) Lensed fibres have a small insertion loss and return loss penalty as they can be passively aligned.

Chapter 5 Conclusions

The choice of material is guided by its properties and the feasibility of using nanolithography to fabricate substrates of silica microparticles. The first experiment was to determine the spectral properties of the PC, PMMA, SU-8 and chitosan through absorption and transmission spectra. The optical spectrum determines the light-matter interaction and is used to find out exactly how far the wavelength infiltrates a material before the light is absorbed. The glass transition temperature of the polymer is an important factor in determining the laser ablation rate. High glass transition temperature makes it a good material candidate for optical waveguides.

Laser ablation employs a pulsed laser of ArF (193 nm wavelength) to remove materials from a substrate over a fluence range from 10 $mJcm^{-2}$ to 1000 $mJcm^{-2}$. Ablation thresholds measurements for PC, PMMA, SU-8 and chitosan are 25, 110, 40 and 95 $mJ.cm^{-2}$respectively, The photoresist SU-8 and chitosan were chosen as both materials are biocompatible and have a high glass transition temperature as well as other properties that were mentioned previously. Both SU-8 and chitosan materials were found to have much higher absorption coefficients ($\alpha_{SU-8} = 4.2\times10^{5}m^{-1}$and $\alpha_{chitosan}=3.3\times105m^{-1}$) compared with PC and PMMA ($\alpha_{PC} = 1\times10^{5}m^{-1}$ and $\alpha_{PMMA}=2\times10^{5}m^{-1}$) at 193 nm wavelength.

Experimental and computational results were obtained for an irradiated laser microsphere supported on biocompatible SU-8 photoresist and chitosan. A single pulse from an ArF excimer laser ($\lambda = 193\ nm$) was used to modify the underlying substrate, producing a single concave dimple. Atomic force microscopy and scanning electron microscope measurements were used to quantify the shape and size of the laser-inscribed dimple. The dimple had a diameter of 140 ± 10 nm FWHM and a depth of 190 ± 10nm on SU-8, and 180 ± 10 nm FWHM and a depth of 280 ± 10nm on chitosan. Both samples were irradiated at the same laser fluence (45 $mJ.cm^{-2}$) before a microlens (silica particles) and at a fluence of 1045 $mJcm^{-2}$ underneath the microlens. The difference in depth and width of the dimples in the two substrates are due to the optical properties of the substrate materials. Finite-difference time-domain (FDTD) simulations were carried outo simulate. of the propagation of 193 nm laser radiation a 1 μm diameter silica sphere which is coated on both SU-8 and chitosan substrates. From the results of the simulations, we deduced that the peak intensity along the *z*-direction is located at a position 130 ± 10 nm away from

the underside of the microsphere. The experimentally measured cross-sectional data has an FWHM diameter larger than both simulated and calculated results. This is believed to be caused by the absorption of 193 nm radiation causing the SU-8/chitosan layer to undergo a relatively high temperature rise. Finite Element Method (FEM) simulations were carried out to calculate the laser- induced temperature rise of both the SU-8 and chitosan layers beneath the microsphere. Both conduction and convection at the surface were used in the simulation, and radiation losses were assumed to be negligible. Although the incident laser fluence was relatively low (45 $mJcm^{-2}$), the peak laser fluence was increased due to the focusing effect and a concomitant and significant temperature rise resulted. The temperature calculations correspond to absorbed laser fluences of 1045 $mJ.cm^{-2}$ at 193 nm. Temporal and spatial temperature calculations of SU-8 numerically and analytically are 775 and 780 K, respectively, which are higher than the boiling point of SU-8 (480K).

The temporal and spatial temperature calculations of chitosan numerically and analytically are 460K and 462 K, respectively; these temperatures are less than the thermal degradation point of chitosan (490K). Due to the higher fluence, the temperature rise is higher than the glass transition of chitosan. Using an average fluence enhancement factor of S0, the absorbed laser fluence was calculated as 30, which was an average

The last part of this thesis presents the use of a CO_2 laser (10.6 μm wavelength) for producing microlenses at the end of silica optical fibre (Chapter 4). Silica optical fibre is irradiated by a focused CO_2 laser beam and heated to the softening point (1800 K) of the silica material. Surface tension and the parameters of the fabrication system shaped the melted material into a spherical microlens or tapered fibre that remained joined to the optical fibre. Different core diameters (125, 400, 600, 1000 and 1500 μm) of multimode fibres were used for this fabrication. The roughness of the microlens was reduced to less than 20 ±1 nm by polishing the surface with a CO_2 laser at low power (1 W). The minimum diameter at which the tapered fibre was fabricated was 5 ± 1 μm. The best ball microlenses were fabricated at the end of 400 μm core diameter due to the fibre diameter being close to the irradiated laser beam diameter, while the hyperbolic lens was fabricated at the end of a larger fibre core diameter of 600, 1000 and 1500 μm. Finally, the knife-edge technique and He-Ne laser beam (632.8 nm wavelength) were coupled into a fibre to investigate the properties of the microlenses which produced a minimum spot size 5 ±1 μm at FWHM in the focal region of the tapered fibre and axicon lenses of 125, 400 and 600 μm core diameter of the fibre.

In conclusion, Tight focussing using microspheres and lensed optical fibres could be integrated on lab-on-chip platforms for applications such as optical trapping and cell membrane modifications.

Chapter 6 Future work

Currently and in future, the application of micro and nanojets in medicine requires the development of nanobubbles for drug delivery. Materials of nanoscale size exhibit properties that macroscopic materials often do not have. Nanobubbles offer a promising strategy for non-invasive drug delivery. Nanobubbles can be used for pretreatment of the cell for optoporation, which is a technique that perforates the cell membrane, generating a nanobubble in the liquid around micro/nanoparticles after irradiation by a laser. The micro and nanoparticles in the liquid absorb the optical energy from the laser, heating the surrounding liquid, which, in turn, induces vapour bubbles around the particles. However, the incident optical fluence must exceed a specific threshold for the nanobubbles to form. Controlling the bubble generation is important, and laser radiation through microlenses provides suitable and efficient control of their growth. This technique could benefit drug delivery into cancer cells, allowing the effectiveness of the treatment to be improved.

Assembling and binding microlenses on an optical fibre probe can create parallel photonic nano jet arrays. These can be used to trap and detect nanoparticles and subwavelength cells with high-throughput, high selectivity and single-nanoparticle resolution. Waveguides of submicron dimensions that operate at visible wavelengths can be employed as integrated waveguides in photonic biosensors. However, these waveguides are often not compact and cost-effective. Therefore, devices which are cheap to produce are of interest. Vertically stacked taper with a larger input area could meet this need. Microlens optical fibres fabricated with a tapered hyperbolic end can be used for efficient coupling between a laser diode and optical fibre. Future research will also focus on empowering tapered-structured optical fibres as a tool for tailored light-delivery.

Appendix : Arduino software codes for controling fibre rotating speed.

```
#include <AFMotor.h>

AF_Stepper motor1(200, 1);


int PIN = 14;
int exposures=18;    // This is the number of AREA TO IRRADIATE
int npulses=20;  // This is the NUMBER OF PULSES FOR EACH AREA
int rotation=200*(360/exposures); // 18 exposures per sample means 20 degrees rotation


void setup() {
   pinMode(PIN, OUTPUT);          // sets the digital pin 13 as output


 motor1.setSpeed(50); // 20 rpm
 motor1.release();

 Serial.begin(9600);
 delay(100);


 Serial.println("INIZIO");

 for (int n=1;n<=exposures;n++){


       Burst(npulses);
      // ReadSynch; // Read Trigger



    motor1.step(rotation, BACKWARD, MICROSTEP);
    delay(550);


      }
  Serial.println("END OF THE PROCESS");



}

void loop() {}//KEEP LOOP EMPTY//}
```

```
void Burst(int npulses)
{


 for (int i=1;i<=npulses;i++) {

     digitalWrite(PIN, 0);//Write 0 part of the burst

     delay(1000);


     digitalWrite(PIN, 1);//Write 1 part of the burst

     delay(1000);

     digitalWrite(PIN, 0);//Write 0 part of the burst
     delay(1000);



         }



}
```

References

[1] A. A. P. Alvarez, “Micro/nano pattering of silicon and NiP/Al disks by nanosecond and femtosecond laser sources,” 2011.

[2] H. Lu, J. Wang, T. Wang, J. Zhong, Y. Bao, and H. Hao, “Recent Progress on Nanostructures for Drug Delivery Applications,” *J. Nanomater.*, vol. 2016, 2016, doi: 10.1155/2016/5762431.

[3] H. Schneckenburger, “Laser-assisted optoporation of cells and tissues – a mini-review,” *Biomed. Opt. Express*, vol. 10, no. 6, p. 2883, 2019, doi: 10.1364/boe.10.002883.

[4] R. Xiong, S. K. Samal, J. Demeester, A. G. Skirtach, S. C. De Smedt, and K. Braeckmans, “Laser-assisted photoporation: fundamentals, technological advances and applications,” *Adv. Phys. X*, vol. 1, no. 4, pp. 596–620, 2016, doi: 10.1080/23746149.2016.1228476.

[5] Hari Singh Nalwa, *Handbook of Nanostructured Materials and Nanotechnology*, vol. 3, no. 1. San Diego: A Harcourt Science and Technology Company, 2000.

[6] L. Yang, J. Wei, Z. Ma, P. Song, and J. Ma, “The Fabrication of Micro / Nano Structures by Laser Machining,” 2019.

[7] J. U. Okoli, T. A. Briggs, and I. E. Major, “Application of Nanotechnology in the Manufacturing Sector: a Review,” *Niger. J. Technol.*, vol. 32, no. 3, pp. 379–385, 2013.

[8] L. Yang, *Nanotechnology-Enhanced Orthopedic Materials Fabrications, Applications and Future Trends*. Cambridge, 2015.

[9] W. Zhou, “Recent progress of laser micro-and nano manufacturing,” no. July, 2015.

[10] J. J. P. Z. W. H. W. R.Hull C. Jagadish R.M. Osgood, *Laser Processing of Materials: Fundamentals, Applications and Developments*. 2010.

[11] J. Lawrence and D. G. Waugh, *Laser surface engineering*. Cambridge, 2015.

[12] J. A. Phys, “The art of laser ablation in aeroengine : The crown jewel of modern industry The art of laser ablation in aeroengine : The crown jewel of modern industry,” vol. 080902, no. February, 2020, doi: 10.1063/1.5134813.

[13] D. Bäuerle, *Laser Processing and Chemistry*, vol. 4. Linz: Springer Heidelberg Dordrecht London New York, 2011.

[14] V. P. Veiko and V. I. Konov, *Fundamentals of Laser-Assisted Micro- and Nanotechnologies*, vol. 195. 2014.

[15] X. Sedao, T. J. Y. Derrien, G. W. R. B. E. Romer, B. Pathiraj, and A. J. Huis In T

Veld, “Laser surface micro-/nano-structuring by a simple transportable micro-sphere lens array,” *J. Appl. Phys.*, vol. 112, no. 10, 2012, doi: 10.1063/1.4767471.

[16] D. Sands, “Pulsed Laser Heating and Melting,” *Heat Transf. - Eng. Appl.*, 2011, doi: 10.5772/28736.

[17] G. N. Makarov, “Laser applications in nanotechnology: nanofabrication using laser ablation and laser nanolithography,” *Uspekhi Fiz. Nauk*, vol. 183, no. 7, pp. 673–718, 2013, doi: 10.3367/ufnr.0183.201307a.0673.

[18] Peter Schaaf, *Laser Processing of Materials: Fundamentals, Applications and Developments*. New York: Springer Series in Materials Science, 2010.

[19] J. (Jonathan) Lawrence, *Advances in laser materials processing : technology, research and applications*, 2nd ed. Woodhead Publishing, 2017.

[20] P. Schaaf, *Laser Processing of Materials: Fundamentals, Applications and Developments*. 2010.

[21] D. C. Dumitras, *Nd: YAG laser*, 1st ed. Croatia: Janeza Trdine 9, 51000 Rijeka, Croatia, 2012.

[22] S. Calixto, M. Rosete-Aguilar, F. J. Sanchez-Marin, and L. Castañeda-Escobar, “Rod and spherical silica microlenses fabricated by CO_2 laser melting,” *Appl. Opt.*, vol. 44, no. 21, p. 4547, 2005, doi: 10.1364/ao.44.004547.

[23] S. P. H. Narendra B. Dahotre, *Laser Fabrication and Machining of Materials*, vol. 11, no. 3. 2008.

[24] L. D.Laude, *Excimer Lasers*, vol. 265. Elounda, Crete, Greece: NATO ASI Series, 1994.

[25] G. Račiukaitis *et al.*, “Laser processing by using diffractive optical laser beam shaping technique,” *J. Laser Micro Nanoeng.*, vol. 6, no. 1, pp. 37–43, 2011, doi: 10.2961/jlmn.2011.01.0009.

[26] K. Sugioka and Y. Cheng, “Ultrafast lasers-reliable tools for advanced materials processing,” *Light Sci. Appl.*, vol. 3, no. 390, pp. 1–12, 2014, doi: 10.1038/lsa.2014.30.

[27] “Optical and acoustic beam shaping for imaging and manipulation A thesis submitted for the degree of University of Dundee,” 2015.

[28] C. Wandera and A. Niyibizi, “Potential Benefits of adoption of Laser Materials Processing in East Africa’s Manufacturing Industry,” no. March, 2018.

[29] L. Li *et al.*, “Laser nano-manufacturing - State of the art and challenges,” *CIRP Ann. - Manuf. Technol.*, vol. 60, no. 2, pp. 735–755, 2011, doi:

10.1016/j.cirp.2011.05.005.

[30] A. C. Wei, J. R. Sze, and J. L. Chern, “Designs for optimizing depth of focus and spot size for UV laser ablation,” *Appl. Phys. A Mater. Sci. Process.*, vol. 101, no. 2, pp. 411–416, 2010, doi: 10.1007/s00339-010-5834-6.

[31] N. Uv, “Manipulation and Patterning of Surfaces (Nanolithography),” in *Fundamentals and Applications of Nano Silicon in Plasmonics and Fullerines*, 2018, pp. 89–137.

[32] L. Li *et al.*, “Laser nano-manufacturing - State of the art and challenges,” *CIRP Ann. - Manuf. Technol.*, vol. 60, no. 2, pp. 735–755, 2011, doi: 10.1016/j.cirp.2011.05.005.

[33] M. L. Zheng and X. M. Duan, “Laser nano-manufacturing technology and applications towards optical functional nanostructures and devices,” *2015 Opto-Electronics Commun. Conf. OECC 2015*, pp. 1–3, 2015, doi: 10.1109/OECC.2015.7340195.

[34] A. Jacassi *et al.*, “Scanning Probe Photonic Nanojet Lithography,” *ACS Appl. Mater. Interfaces*, vol. 9, no. 37, pp. 32386–32393, 2017, doi: 10.1021/acsami.7b10145.

[35] Y. J. Wang, C. A. Dai, and J. H. Li, “Numerical study of tunable photonic nanojets generated by biocompatible hydrogel core-shell microspheres for surface-enhanced Raman scattering applications,” *Polymers (Basel).*, vol. 11, no. 3, 2019, doi: 10.3390/polym11030431.

[36] 2 and Chih-Hao Chang2 Xu A. Zhang, 1 I-Te Chen, “Recent Progress in Near-Field Nanolithography using Light Interactions with Colloidal Particles: From Nanospheres to three-dimensional Nanostructures,” vol. 2, pp. 1–2, 2019, doi: 10.1016/j.vetmic.2007.04.014.

[37] J. J. Stamnes, *Waves in Focal Regions Prpagation, Dffraction and Focussing of light ,Sound and Water Waves.* 1986.

[38] J. M. Khosrofian and B. A. Garetz, “Measurement of a Gaussian laser beam diameter through the direct inversion of knife-edge data,” *Appl. Opt.*, vol. 22, no. 21, p. 3406, 1983, doi: 10.1364/AO.22.003406.

[39] I. L. Y. A. E. Poletimov, A. S. Shcheulin, “Apodizing apertures for visible and IR lasers,” *Sov. J. Quantum Electron. LASER*, vol. 22 (10), p. 5, 1992.

[40] A. N. K. Reddy, M. Hashemi, and S. N. Khonina, “Apodization of two-dimensional pupils with aberrations,” *Pramana - J. Phys.*, vol. 90, no. 6, pp. 1–8, 2018, doi: 10.1007/s12043-018-1566-5.

[41] D. R. Skinner and R. E. Whitcher, “Measurement of the radius of a high-power laser beam near the focus of a lens,” *J. Phys. E.*, vol. 5, no. 3, pp. 237–238, 1972, doi: 10.1088/0022-3735/5/3/015.

[42] S. Orlov, C. Huber, P. Marchenko, P. Banzer, and G. Leuchs, “Corrected knife-edge-based reconstruction of tightly focused higher order beams,” vol. 517520, no. 2007, pp. 10896–10904, 2016, [Online]. Available: http://arxiv.org/abs/1610.08643.

[43] P. J. Shayler, “Laser beam distribution in the focal region.,” *Appl. Opt.*, vol. 17, no. 17, pp. 2673–2674, 1978, doi: 10.1364/AO.17.002673.

[44] P. B. Chapple, “Beam waist and M2 measurement using a finite slit,” *Opt. Eng.*, vol. 33, no. 7, pp. 2461–2466, 1994, doi: 10.1117/12.169739.

[45] M. A. de Araújo, R. Silva, E. de Lima, D. P. Pereira, and P. C. de Oliveira, “Measurement of Gaussian laser beam radius using the knife-edge technique: improvement on data analysis,” *Appl. Opt.*, vol. 48, no. 2, p. 393, 2009, doi: 10.1364/AO.48.000393.

[46] J. J. Chapmana *et al.*, “An automated submicron beam profiler for characterization of high numerical aperture optics An automated submicron beam profiler for characterization of high,” vol. 095106, no. 2008, 2016, doi: 10.1063/1.2991112.

[47] P. Woźniak, P. Banzer, F. Bouchard, E. Karimi, G. Leuchs, and R. W. Boyd, “Tighter spots of light with superposed orbital-angular-momentum beams,” *Phys. Rev. A*, vol. 94, no. 2, pp. 1–6, 2016, doi: 10.1103/PhysRevA.94.021803.

[48] X. Xie, L. Li, S. Wang, Z. Wang, and J. Zhou, “Three-dimensional measurement of a tightly focused laser beam,” *AIP Adv.*, vol. 3, no. 2, 2013, doi: 10.1063/1.4791764.

[49] J.-H. Seo *et al.*, “Nanopatterning by Laser Interference Lithography: Applications to Optical Devices,” *J. Nanosci. Nanotechnol.*, vol. 14, no. 2, pp. 1521–1532, 2014, doi: 10.1166/jnn.2014.9199.

[50] A. Normatov, B. Spektor, and J. Shamir, “High numerical aperture focusing of singular beams,” vol. 7227, pp. 1–9, 2009, doi: 10.1117/12.808115.

[51] M. N. Gulari, A. Tripathi, M. Ghannad-Rezaie, and N. Chronis, “An optofluidic lens array microchip for high resolution stereo microscopy,” *Micromachines*, vol. 5, no. 3, pp. 607–621, 2014, doi: 10.3390/mi5030607.

[52] W. Ignatowsky, “Diffraction by a lens having arbitrary opening,” *Trans. Opt. Int. Petrogr.*, 1919.

[53] W. v. Ignatowsky, “Diffraktion und Reflexion, abgeleitet aus den Maxwellschen Gleichungen,” *Ann. Phys.*, 1908, doi: 10.1002/andp.19083311012.

[54] B. Richards and E. Wolf, “Electromagnetic Diffraction in Optical Systems. II. Structure of the Image Field in an Aplanatic System,” *Proc. R. Soc. A Math. Phys. Eng. Sci.*, vol. 253, no. 1274, pp. 358–379, 1959, doi: 10.1098/rspa.1959.0200.

[55] M. Born and E. Wolf, *Principles of optics*. London, 1975.

[56] Q. Li, I. Ledoux-Rak, and N. D. Lai, “Influence of incident beam polarization on intensity and polarization distributions of tight focusing spot,” *Adv. Device Mater.*, vol. 1, no. 1, pp. 4–10, 2015, doi: 10.1179/2055031614Y.0000000002.

[57] Q. Li, “Optimization of point spread function of a high numerical aperture objective lens : application to high resolution optical imaging and fabrication,” 2015.

[58] A. P. Lalanne and P. Chavel, “Metalenses at visible wavelengths : past , present , perspectives,” pp. 1–17.

[59] A. P. Mihailescu, Ion N.,Caricato, *Pulsed Laser Ablation Advances and Applications in Nanoparticles and Nanostructuring Thin Films edited*. 2018.

[60] E. Wolf, “Electromagnetic Diffraction in Optical Systems. I. An Integral Representation of the Image Field,” *Proc. R. Soc. A Math. Phys. Eng. Sci.*, vol. 253, no. 1274, pp. 349–357, 1959, doi: 10.1098/rspa.1959.0199.

[61] J. J. Stamnes, *Waves in Focal Regions Prpagation, Dffraction and Focussing of light ,Sound and Water Waves*. 1986.

[62] B. S. and J. S. Alexander Normatov*, “Tight Focusing of Wavefronts with Piecewise Constant Phase,” *Opt. Eng.*, vol. 48, no. 2, p. 028001, 2009, doi: 10.1117/1.3081093.

[63] S. Quabis, R. Dorn, M. Eberler, O. Glöckl, and G. Leuchs, “The focus of light – theoretical calculation and experimental tomographic reconstruction,” *Appl. Phys. B*, vol. 72, no. 1, pp. 109–113, 2001, doi: 10.1007/s003400000451.

[64] K. Bahlmann and S. W. Hell, “Electric field depolarization in high aperture focusing with emphasis on annular apertures,” vol. 200, no. June, pp. 59–67, 2000.

[65] A. Chipman and J. Chipman, “Polarization aberration diagrams,” vol. 28, no. 2, 1989.

[66] R. A. Chipman and W.-S. T. L. G. Young, *Polarized Light and Optical Systems*. Boca Raton,London, New York: Taylor & Francis Group, 2019.

[67] J. J. Stamnes and V. Dhayalan, “Focusing of electric-dipole waves,” *Pure Appl. Opt. (Print Ed. (United Kingdom)*, vol. 5, no. 2, pp. 195–225, 1996, doi: 10.1088/0963-9659/5/2/005.

[68] Y. L. and E. WOLF, “Focal shifts in diffracted converging spherical waves,” vol. 39, no. 4, pp. 211–215, 1981.

[69] S. S. Sherif, M. R. Foreman, and T. Peter, “Eigenfunction expansion of the electric fields in the focal region of a high numerical aperture focusing system,” vol. 16, no. 5, pp. 3397–3407, 2008.

[70] G. B. Airy, “On the Diffraction of an Object-glass with a Circular Aperture,” *Trans. Cambridge Philos. Soc.*, vol. 5, no. August, pp. 283–291, 1835, [Online]. Available: http://adsabs.harvard.edu/abs/1835TCaPS...5..283A.

[71] K. Jahn, “The vector slepian theory of high numberical aperture focussing,” Budapest University of Technology and Economics, 2017.

[72] Q. Zhan, *Vectorial Optical Fields: fundamentals and applications*. 2013.

[73] R. F. H. John C. Miller, *Laser Ablation and Desorption*. London, 1998.

[74] A. V. Gusarov and I. Smurov, “Thermal model of nanosecond pulsed laser ablation: Analysis of energy and mass transfer,” *J. Appl. Phys.*, vol. 97, no. 1, 2005, doi: 10.1063/1.1827321.

[75] M. Ganguly, “Analyzing Thermal and Mechanical Effects of Pulsed Laser Irradiation on Tissues,” 2012.

[76] S. Ravi-Kumar, B. Lies, H. Lyu, and H. Qin, “Laser ablation of polymers: A review,” *Procedia Manuf.*, vol. 34, pp. 316–327, 2019, doi: 10.1016/j.promfg.2019.06.155.

[77] K. Zimmer, *Laser Processing and Chemistry*, vol. 208, no. Part_1_2. 1999.

[78] R. S. Kappes *et al.*, “A study of photothermal laser ablation of various polymers on microsecond time scales,” vol. 3, no. 489, p. 15, 2014, doi: :10.1186/2193-1801-3-489.

[79] M. Mäder, T. Höche, J. W. Gerlach, R. Böhme, and B. Rauschenbach, “Nanostructures by diffraction mask projection laser ablation,” *Phys. Status Solidi Basic Res.*, vol. 247, no. 6, pp. 1372–1383, 2010, doi: 10.1002/pssb.200945522.

[80] P. Dyer, “Excimer laser polymer ablation: twenty years on,” *Appl. Phys. A*, vol. 173, pp. 167–173, 2003, doi: 10.1007/s00339-003-2137-1.

[81] H. N. Najeeb, G. A. Dahash, S. F. Haddawi, and M. Jassim, “Study of Changes in Optical Properties of PMMA Film before and after Irradiation by Laser,”

Chem. Mater. Eng., vol. 2, no. 6, pp. 145–147, 2014.

[82] K. Liu, Y. Kim, and H. (Moses) Noh, "ArF Excimer Laser Micromachining of MEMS Materials: Characterization and Applications," *J. Micro Nano-Manufacturing*, vol. 2, no. 2, p. 021006, 2014, doi: 10.1115/1.4027121.

[83] R. K. S. James Jacob, P. Shanmugavelu, R. Balasubramaniam, "Study of excimer laser ablation pf photoresist polymer in presence of hydroggen gas enviroment for micro-fluidic applications," 2019.

[84] S. S. Zakariyah, "Laser Ablation for Polymer Waveguide Fabrication," *Micromach. Tech. Fabr. Micro Nano Struct.*, pp. 109–130, 2012, doi: 10.5772/1364.

[85] J. P. Desbiens and P. Masson, "ArF excimer laser micromachining of Pyrex , SiC and PZT for rapid prototyping of MEMS components," vol. 136, pp. 554–563, 2007, doi: 10.1016/j.sna.2007.01.002.

[86] Y.-H. Hung, H.-L. Chien, and Y.-C. Lee, "Excimer Laser Three-Dimensional Micromachining Based on Image Projection and the Optical Diffraction Effect," *Appl. Sci.*, vol. 8, no. 9, p. 1690, 2018, doi: 10.3390/app8091690.

[87] T. Lippert, "Laser Application of Polymers," *Adv. Polym. Sci.*, vol. 168, pp. 51–246, 2004, doi: 10.1007/b12682.

[88] A. F. Mohammed *et al.*, "Ablation threshold measurements and surface modifications of 193 nm laser irradiated 4H-SiC," *Chem. Phys. Lett.*, vol. 713, no. October, pp. 194–202, 2018, doi: 10.1016/j.cplett.2018.09.057.

[89] K. L. Mittal and W. S. Lei, *Laser technology: Applications in adhesion and related areas*. 2017.

[90] Z.-L. Wu *et al.*, *Polymer-Based Device Fabrication and Applications Using Direct Laser Writing Technology*, vol. 11, no. 3. 2019.

[91] M. S. Brown and C. B. Arnold, "Fundamentals of Laser-Material Interaction and Application toMultiscale Surface Modificatio," vol. 135, 2010, pp. 91–120.

[92] R. Gernhardt *et al.*, "An Overview about the Excimer Laser Ablation of Different Polymers and Their Application for Wafer and Panel Level Packaging," *2019 Int. Wafer Lev. Packag. Conf. IWLPC 2019*, 2019, doi: 10.23919/IWLPC.2019.8914117.

[93] M. Rao, "A Brief Introduction to Excimer Lasers: Fundamental Study," *Int. J. Adv. Pharmacy, Biol. Chem.*, vol. 2, no. 3, pp. 533–536, 2013, [Online]. Available: http://www.ijapbc.com/files/20-2318.pdf.

[94] R. E. Russo, X. Mao, J. J. Gonzalez, V. Zorba, and J. Yoo, "Laser ablation in

analytical chemistry," *Anal. Chem.*, vol. 85, no. 13, pp. 6162–6177, 2013, doi: 10.1021/ac4005327.

[95] S. Ravi-Kumar, B. Lies, X. Zhang, H. Lyu, and H. Qin, "Laser ablation of polymers: a review," *Polym. Int.*, vol. 68, no. 8, pp. 1391–1401, 2019, doi: 10.1002/pi.5834.

[96] W. Z. and H. Z. Ruiqi Shen, Lizhi Wu, "Laser Ablation of Energetic Materials," in *Intech open*, vol. 2, 2017, p. 23.

[97] G. C. D'Couto and S. V. Babu, "Heat transfer and material removal in pulsed excimer-laser-induced ablation: Pulsewidth dependence," *J. Appl. Phys.*, vol. 76, no. 5, pp. 3052–3058, 1994, doi: 10.1063/1.357486.

[98] U. L. L. Thomas, "Photoablation of polymer materials," in *Photochemistry and Photophysics ofPolymer Materials*, N. S. Allen, Ed. John Wiley & Sons; Inc, 2010, pp. 541–568.

[99] G. Heise, M. Domke, J. Konrad, S. Sarrach, J. Sotrop, and H. P. Huber, "Laser lift-off initiated by direct induced ablation of different metal thin films with ultra-short laser pulses," *J. Phys. D. Appl. Phys.*, vol. 45, no. 31, 2012, doi: 10.1088/0022-3727/45/31/315303.

[100] S. S. Zakariyah, "Laser Ablation for Polymer Waveguide Fabrication."

[101] M. Hashida, a. F. Semerok, O. Gobert, G. Petite, Y. Izawa, and J. F. Wagner, "Ablation threshold dependence on pulse duration for copper," *Appl. Surf. Sci.*, vol. 197–198, pp. 862–867, 2002, doi: 10.1016/S0169-4332(02)00463-4.

[102] A. H. Hamad, "Effects of Different Laser Pulse Regimes (Nanosecond , Picosecond and Femtosecond) on the Ablation of Materials for Production of Nanoparticles in Liquid Solution," 2016.

[103] P. E. Dyer, S. M. Maswadi, C. D. Walton, M. Ersoz, P. D. I. Fletcher, and V. N. Paunov, "157-nm laser micromachining of N-BK7 glass and replication for microcontact printing," *Appl. Phys. A Mater. Sci. Process.*, vol. 77, no. 3–4, pp. 391–394, 2003, doi: 10.1007/s00339-002-1936-0.

[104] W. Wu, A. Katsnelson, O. G. Memis, and H. Mohseni, "A deep sub-wavelength process for the formation of highly uniform arrays of nanoholes and nanopillars," *Nanotechnology*, vol. 18, no. 48, 2007, doi: 10.1088/0957-4484/18/48/485302.

[105] D. Sumanth Kumar, B. Jai Kumar, and H. M. Mahesh, "Quantum Nanostructures (QDs): An Overview," in *Synthesis of Inorganic Nanomaterials*, Elsevier Ltd., 2018, pp. 59–88.

[106] S. Mitra, S. Chakraborty, R. Martinez-Duarte, and M. Madou, "SU-8

Photolithography and Its Impact on Microfluidics," in *Microfluidics and Nanofluidics Handbook*, no. 2006, 2012, pp. 231–268.

[107] X. Liu, X. Li, L. Li, W. Chen, and X. Luo, "Influence of sphere-surface distance and exposure dose on resolution of sphere-lens-array lithography," *Opt. Express*, vol. 23, no. 23, p. 30136, 2015, doi: 10.1364/oe.23.030136.

[108] J. B. Lee, K. H. Choi, and K. Yoo, "Innovative SU-8 lithography techniques and their applications," *Micromachines*, vol. 6, no. 1, pp. 1–18, 2015, doi: 10.3390/mi6010001.

[109] H. Ni *et al.*, "Large-scale high-numerical-aperture super-oscillatory lens fabricated by direct laser writing lithography," *RSC Adv.*, vol. 8, no. 36, pp. 20117–20123, 2018, doi: 10.1039/c8ra02644k.

[110] J.-H. Seo *et al.*, "Nanopatterning by Laser Interference Lithography: Applications to Optical Devices," *J. Nanosci. Nanotechnol.*, vol. 14, no. 2, pp. 1521–1532, 2014, doi: 10.1166/jnn.2014.9199.

[111] Y. Wen, F. Wang, H. Yu, Y. Wang, L. Liu, and W. J. Li, "Submicron processing using laser-induced photonic nanojet," *2017 IEEE 17th Int. Conf. Nanotechnology, NANO 2017*, vol. 2, no. c, pp. 940–941, 2017, doi: 10.1109/NANO.2017.8117311.

[112] C. A. Charitidis, P. Georgiou, M. A. Koklioti, A.-F. Trompeta, and V. Markakis, "Manufacturing nanomaterials: from research to industry," *Manuf. Rev.*, vol. 1, p. 11, 2014, doi: 10.1051/mfreview/2014009.

[113] S. Y. Chou, P. R. Krauss, and P. J. Renstrom, "Nanoimprint lithography.," *J. Vac. Sci. Technol. B*, vol. 14, no. 6, pp. 4129–4133, 1996, doi: 10.1116/1.588605.

[114] N. Kooy, K. Mohamed, L. T. Pin, and O. S. Guan, "A review of roll-to-roll nanoimprint lithography," *Nanoscale Res. Lett.*, vol. 9, no. 1, pp. 1–13, 2014, doi: 10.1186/1556-276X-9-320.

[115] Q. Wang *et al.*, "A Rapid and Simple Method for Fabricating Flexible , Wearable Nanophotonic Devices," no. August, 2018, doi: 10.1038/s41378-018-0031-4.This.

[116] W. Wu, D. Dey, O. G. Memis, A. Katsnelson, and H. Mohseni, "A deep sub-wavelength process for the formation of highly uniform arrays of nanoholes and nanopillars," *Nanoscale Res. Lett.*, vol. 3, no. 3, pp. 123–127, 2008, doi: 10.1007/s11671-008-9124-6.

[117] W. Wu, A. Katsnelson, O. G. Memis, and H. Mohseni, "A deep sub-wavelength process for the formation of highly uniform arrays of nanoholes and nanopillars,"

Nanotechnology, vol. 18, no. 48, 2007, doi: 10.1088/0957-4484/18/48/485302.

[118] X. Sedao, T. J. Y. Derrien, G. R. B. E. Romer, B. Pathiraj, and A. J. Huis In 'T Veld, "Large area laser surface micro/nanopatterning by contact microsphere lens arrays," *Appl. Phys. A Mater. Sci. Process.*, vol. 111, no. 3, pp. 701–709, 2013, doi: 10.1007/s00339-013-7651-1.

[119] H. S. Patel and S. K. Majumder, "Photonic nanojet: generation, manipulation and applications," vol. 31, no. 2, 2018.

[120] B. S. Luk'yanchuk, R. Paniagua-Domínguez, I. Minin, O. Minin, and Z. Wang, "Refractive index less than two: photonic nanojets yesterday, today and tomorrow [Invited]," *Opt. Mater. Express*, vol. 7, no. 6, p. 1820, 2017, doi: 10.1364/ome.7.001820.

[121] J. Zhu and L. L. Goddard, "All-dielectric concentration of electromagnetic fields at the nanoscale: the role of photonic nanojets," *Nanoscale Adv.*, pp. 4615–4643, 2019, doi: 10.1039/C9NA00430K.

[122] M. Mosbacher, H.-J. Münzer, J. Zimmermann, J. Solis, J. Boneberg, and P. Leiderer, "Optical field enhancement effects in laser-assisted particle removal," *Appl. Phys. A Mater. Sci. Process.*, vol. 72, no. 1, pp. 41–44, 2001, doi: 10.1007/s003390000715.

[123] A. Afanasiev *et al.*, "Two-color beam improvement of the colloidal particle lens array assisted surface nanostructuring," *Appl. Phys. Lett.*, vol. 106, no. 18, 2015, doi: 10.1063/1.4919898.

[124] Z. B. Wang *et al.*, "Laser micro/nano fabrication in glass with tunable-focus particle lens array," *Opt. Express*, vol. 16, no. 24, p. 19706, 2008, doi: 10.1364/OE.16.019706.

[125] R. Karstens, A. Gödecke, A. Prießner, and J. Ihlemann, "Fabrication of 250-nm-hole arrays in glass and fused silica by UV laser ablation," *Opt. Laser Technol.*, vol. 83, pp. 16–20, 2016, doi: 10.1016/j.optlastec.2016.03.020.

[126] I. Martín-Fabiani, J. Siegel, S. Riedel, J. Boneberg, T. A. Ezquerra, and A. Nogales, "Nanostructuring thin polymer films with optical near fields," *ACS Appl. Mater. Interfaces*, vol. 5, no. 21, pp. 11402–11408, 2013, doi: 10.1021/am4036543.

[127] W. Wu, D. Dey, O. G. Memis, A. Katsnelson, and H. Mohseni, "A novel self-aligned and maskless process for formation of highly uniform arrays of nanoholes and nanopillars," *Nanoscale Res. Lett.*, vol. 3, no. 3, pp. 123–127, 2008, doi: 10.1007/s11671-008-9124-6.

[128] A. Pena, Z. Wang, D. Whitehead, and L. Li, “Direct writing of micro/nano-scale patterns by means of particle lens arrays scanned by a focused diode pumped Nd:YVO4 laser,” *Appl. Phys. A Mater. Sci. Process.*, vol. 101, no. 2, pp. 287–295, 2010, doi: 10.1007/s00339-010-5819-5.

[129] D. Brodoceanu, H. Z. Alhmoud, R. Elnathan, B. Delalat, N. H. Voelcker, and T. Kraus, “Fabrication of silicon nanowire arrays by near-field laser ablation and metal-assisted chemical etching,” *Nanotechnology*, vol. 27, no. 7, p. 75301, 2016, doi: 10.1088/0957-4484/27/7/075301.

[130] R. Denk, K. Piglmayer, and C. Bäuerle, “Laser-induced nano-patterning by means of interference subpatterns generated by microspheres,” *Appl. Phys. A Mater. Sci. Process.*, vol. 76, no. 1, pp. 1–3, 2003, doi: 10.1007/s003390201413.

[131] L. P. Li, Y. F. Lu, D. W. Doerr, D. R. Alexander, and X. Y. Chen, “Parametric investigation of laser nanoimprinting of hemispherical cavity arrays,” *J. Appl. Phys.*, vol. 96, no. 9, pp. 5144–5151, 2004, doi: 10.1063/1.1796515.

[132] H. Nojiri, W. S. Pambudi, and M. Okoshi, “Formation of periodic microswelling structures on silicone rubber surface using ArF excimer laser to realize superhydrophobic property,” *Jpn. J. Appl. Phys.*, vol. 56, no. 7, 2017, doi: 10.7567/JJAP.56.072002.

[133] K. L. N. Deepak *et al.*, “Long range nanostructuring of silicon surfaces by photonic nanojets from microsphere Langmuir films,” no. April, p. 02003, 2013, doi: 10.1051/uvx/201302003.

[134] Y. Cao, Z. Liu, O. Minin, and I. Minin, “Deep Subwavelength-Scale Light Focusing and Confinement in Nanohole-Structured Mesoscale Dielectric Spheres,” *Nanomaterials*, vol. 9, no. 2, p. 186, 2019, doi: 10.3390/nano9020186.

[135] W. Wu, D. Dey, O. G. Memis, A. Katsnelson, and H. Mohseni, “A deep sub-wavelength process for the formation of highly uniform arrays of nanoholes and nanopillars,” *Nanoscale Res. Lett.*, vol. 3, no. 3, pp. 123–127, 2007, doi: 10.1007/s11671-008-9124-6.

[136] H. J. Münzer, M. Mosbacher, M. Bertsch, J. Zimmermann, P. Leiderer, and J. Boneberg, “Local field enhancement effects for nanostructuring of surfaces,” *J. Microsc.*, vol. 202, no. 1, pp. 129–135, 2001, doi: 10.1046/j.1365-2818.2001.00876.x.

[137] S. M. Huang, Z. Sun, and Y. F. Lu, “Nanofabrication by laser irradiation of polystyrene particle layers on silicon,” *Nanotechnology*, vol. 18, no. 2, 2007, doi: 10.1088/0957-4484/18/2/025302.

[138] M. Okoshi, “Fabrication of Superhydrophobic Silicone Rubber with Periodic Micro/Nano-Suction Cup Structure by ArF Excimer Laser-Induced Photodissociation,” *Nanomaterials*, vol. 9, no. 6, p. 870, 2019, doi: 10.3390/nano9060870.

[139] Q. A. Al-Jarwany *et al.*, “Realisation of a sub-wavelength dimple using a 193 nm wavelength photonic nano jet,” *Chem. Phys. Lett.*, vol. 750, no. March, p. 137400, 2020, doi: 10.1016/j.cplett.2020.137400.

[140] R. S. Kappes, “Laser Heating of Polymers,” 2012.

[141] Y.-H. Hung, H.-L. Chien, and Y.-C. Lee, “Excimer Laser Three-Dimensional Micromachining Based on Image Projection and the Optical Diffraction Effect,” *Appl. Sci.*, vol. 8, no. 9, p. 1690, 2018, doi: 10.3390/app8091690.

[142] O. O. Versolato, “Physics of laser-driven tin plasma sources of EUV radiation for nanolithography,” *Plasma Sources Sci. Technol.*, vol. 28, no. 8, 2019, doi: 10.1088/1361-6595/ab3302.

[143] B. Wu and A. Kumar, “Extreme ultraviolet lithography: A review,” *J. Vac. Sci. Technol. B Microelectron. Nanom. Struct.*, vol. 25, no. 6, pp. 1743–1761, 2007, doi: 10.1116/1.2794048.

[144] S. Bowyer, J. J. Drake, and S. Vennes, *Extreme Ultraviolet Astronomy*, vol. 409, no. 1. 2003.

[145] Laser Optics Corporation, “changing the technology, one fiber at at a time,” 2019. .

[146] V. A. Soifer, *Diffractive Nanophotonics*. Boca Raton London New York: CRC Press Taylor & Francis Group, 2014.

[147] G. Y. Chen, D. G. Lancaster, and T. M. Monro, “Optical microfiber technology for current, temperature, acceleration, acoustic, humidity and ultraviolet light sensing,” *Sensors (Switzerland)*, vol. 18, no. 1, 2018, doi: 10.3390/s18010072.

[148] Z. A. Aljawary, M. A. Alrwas, and M. K. Rashad, “Possible Lensing Schemes for Fiber-Optic Coupling,” vol. 96, no. 09, pp. 2458–2467, 2018.

[149] G. Son, S. Han, J. Park, K. Kwon, and K. Yu, “High-efficiency broadband light coupling between optical fibers and photonic integrated circuits,” *Nanophotonics*, vol. 7, no. 12, pp. 1845–1864, 2018, doi: 10.1515/nanoph-2018-0075.

[150] R. Kasztelanic *et al.*, “Integrating Free-Form Nanostructured GRIN Microlenses with Single-Mode Fibers for Optofluidic Systems,” *Sci. Rep.*, vol. 8, no. 1, pp. 1–12, 2018, doi: 10.1038/s41598-018-23464-6.

[151] M.-S. Kim *et al.*, “Refraction limit of miniaturized optical systems: a ball-lens

example," *Opt. Express*, vol. 24, no. 7, p. 6996, 2016, doi: 10.1364/OE.24.006996.

[152] K. S. Lee and F. S. Barnes, "Microlenses on the end of single-mode optical fibers for laser applications," *Appl. Opt.*, vol. 24, no. 19, pp. 3134–3139, 1985, doi: 10.1364/AO.24.003134.

[153] K. Boyd, "Techniques for the CO 2 Laser Fabrication of Soft Glass Optical Fibre Devices and Measurement of their Optical and Physical Properties," 2013.

[154] J. Powell, *CO2 Laser Cutting*. 1998.

[155] W. Zheng, "Optic lenses manufactured on fiber ends," *2015 Optoelectron. Glob. Conf. OGC 2015*, 2015, doi: 10.1109/OGC.2015.7336855.

[156] J. Huang, J. Wiener, D. Křemenáková, J. Militký, and M. Kašparová, "Micro-lensed polymeric optical fiber by CO_2 laser cutting," *J. Laser Appl.*, vol. 30, no. 3, p. 032014, 2018, doi: 10.2351/1.5023073.

[157] M. Thual, P. Rochard, P. Chanclou, and L. Quetel, "Contribution to research on micro-lensed fibers for modes coupling," *Fiber Integr. Opt.*, vol. 27, no. 6, pp. 532–541, 2008, doi: 10.1080/01468030802272450.

[158] L. G. Cohen and M. V Schneider, "Microlenses for coupling junction lasers to optical fibers.," *Appl. Opt.*, vol. 13, no. 1, pp. 89–94, 1974, doi: 10.1364/AO.13.000089.

[159] U. C. Paek and A. L. Weaver, "Formation of a Spherical Lens at Optical Fiber Ends with a CO2 Laser," *Appl. Opt.*, vol. 14, no. 2, p. 294, 1975, doi: 10.1364/AO.14.000294.

[160] A. J. C. Grellier, N. K. Zayer, and C. N. Pannell, "Heat transfer modelling in CO2laser processing of optical fibres," *Opt. Commun.*, vol. 152, no. 4–6, pp. 324–328, 1998, doi: 10.1016/S0030-4018(98)00164-3.

[161] M. Ferreira, A. Gomes, D. Kowal, G. Statkiewicz-Barabach, P. Mergo, and O. Frazão, "The Fiber Connection Method Using a Tapered Silica Fiber Tip for Microstructured Polymer Optical Fibers," *Fibers*, vol. 6, no. 1, p. 4, 2018, doi: 10.3390/fib6010004.

[162] S. M. Chandani, "Optical fiber-based liquid level sensor," *Opt. Eng.*, vol. 46, no. 11, p. 114401, 2007, doi: 10.1117/1.2801506.

[163] K. Q. Kieu and M. Mansuripur, "Biconical fiber taper sensors," *IEEE Photonics Technol. Lett.*, vol. 18, no. 21, pp. 2239–2241, 2006, doi: 10.1109/LPT.2006.884742.

[164] A. Shabaneh *et al.*, "Dynamic response of tapered optical multimode fiber coated

with carbon nanotubes for ethanol sensing application," *Sensors (Switzerland)*, vol. 15, no. 5, pp. 10452–10464, 2015, doi: 10.3390/s150510452.

[165] A. Malki, R. Bachelot, and F. Van Lauwe, "Two-step process for micro-lens-fibre fabrication using a continuous CO2 laser source," *J. Opt. A Pure Appl. Opt.*, vol. 3, no. 4, pp. 291–295, 2001, doi: 10.1088/1464-4258/3/4/310.

[166] H. Choi, D. Yoo, I. Sohn, Y. Noh, and J. Sung, "CO 2 Laser Assisted Fabrication of Micro-lensed Single-mode Optical Fiber," vol. 19, no. 4, pp. 327–333, 2015.

[167] Bartu Simsek, "CO2 laser glass processing for high power fiber laser applications," bilkent university, 2016.

[168] U. C. Paek and A. L. Weaver, "Formation of a Spherical Lens at Optical Fiber Ends with a CO_2 Laser," *Appl. Opt.*, vol. 14, no. 2, p. 294, 1975, doi: 10.1364/AO.14.000294.

[169] K. Mullaney, R. Correia, S. E. Staines, S. W. James, and R. P. Tatam, "Monitoring techniques for the manufacture of tapered optical fibers," *Appl. Opt.*, vol. 54, no. 28, p. 8531, 2015, doi: 10.1364/AO.54.008531.

[170] N. E. Demagh, A. Guessoum, R. Zegari, and T. Gharbi, "Self-centring technique for fibre optic microlens mounting using a concave cone-etched fibre," *Meas. Sci. Technol.*, vol. 22, no. 11, 2011, doi: 10.1088/0957-0233/22/11/115302.

[171] S. Calixto and F. J. Sanchez-Marin, "Spherical fused silica microlenses fabricated by the melting method," *Rev. Mex. Fis.*, vol. 49, no. 5, pp. 421–424, 2003.

[172] S. Y. Ryu, H. Y. Choi, J. Na, W. J. Choi, and B. H. Lee, "All-fiber probe for optical coherence tomography," *Coherence Domain Opt. Methods Opt. Coherence Tomogr. Biomed. XII*, vol. 6847, no. 68472, p. 68472L, 2008, doi: 10.1117/12.766316.

[173] N. Ma, "Tailoring Optical Fibers for Cell Transfection," University of St. Andrews, 2012.

[174] G. Kong *et al.*, "Lensed photonic crystal fiber obtained by use of an arc discharge," vol. 31, no. 7, pp. 894–896, 2006.

[175] T. Grosjean *et al.*, "Fiber microaxicons fabricated by a polishing technique for the generation of Bessel-like beams," 2007.

[176] M. Tao, Y. Jin, N. Gu, and L. Huang, "A method to control the fabrication of etched optical fiber probes with nanometric tips," *J. Opt. A Pure Appl. Opt.*, vol. 12, no. 1, 2010, doi: 10.1088/2040-8978/12/1/015503.

[177] S. Cabrini *et al.*, "Axicon lens on optical fiber forming optical tweezers, made by

focused ion beam milling," *Microelectron. Eng.*, vol. 83, no. 4-9 SPEC. ISS., pp. 804–807, 2006, doi: 10.1016/j.mee.2006.01.247.

[178] J. Sun *et al.*, "Fabrication of a side aligned optical fibre interferometer by focused ion beam machining," *J. Micromechanics Microengineering*, vol. 23, no. 10, 2013, doi: 10.1088/0960-1317/23/10/105005.

[179] J. M. P. Coelho, M. Nespereira, C. Silva, D. Pereira, and J. Rebordo, "Advances in Optical Fiber Laser Micromachining for Sensors Development," in *Current Developments in Optical Fiber Technology*, 2013, p. 28.

[180] H. M. Presby, A. F. Benner, and C. A. Edwards, "Laser micromachining of efficient fiber microlenses," *Appl. Opt.*, vol. 29, no. 18, p. 2692, 1990, doi: 10.1364/AO.29.002692.

[181] Y. Matsuura, "Optical fibers for medical applications," *Lasers Med. Appl. Diagnostics, Ther. Surg.*, pp. 110–124, 2013, doi: 10.1533/9780857097545.1.110.

[182] A. M. ´ NDEZ and T. F. MORSE, *Specialty Optical Fibers Handbook*. 2007.

[183] B. V. Hunter, K. H. Leong, C. B. Miller, J. F. Golden, R. D. Glesias, and P. J. Laverty, "Selecting a high-power fiber-optic laser beam delivery system," vol. 173, pp. E173–E182, 2018, doi: 10.2351/1.5059077.

[184] M. Richard P. Tumminelli, Ashland, "Method of making an optcal fibre or preform having a reduced hydrgen contact,"vol. 1,no. 19, 2003.

[185] H. M. Presby, A. F. Benner, and C. A. Edwards, "Laser micromachining of efficient fiber microlenses," *Appl. Opt.*, vol. 29, no. 18, p. 2692, 1990, doi: 10.1364/AO.29.002692.

[186] M. A. Jebali, " Temperature control of CO 2 laser glass melting for fiber processing technology ," *Laser Appl. Microelectron. Optoelectron. Manuf. XXII*, vol. 10091, p. 1009119, 2017, doi: 10.1117/12.2253621.

[187] P. Shukla, D. G. Waugh, J. Lawrence, and R. Vilar, *Laser surface structuring of ceramics, metals and polymers for biomedical applications: A review*. Elsevier Ltd, 2016.

[188] X. Zhao, N. Zhao, Y. Shi, H. Xin, and B. Li, "Optical Fiber Tweezers: A Versatile Tool for Optical Trapping and Manipulation," *Micromachines*, vol. 11, no. 2, p. 114, 2020, doi: 10.3390/mi11020114.

[189] H. Xin and B. Li, "Fiber-based optical trapping and manipulation," *Front. Optoelectron.*, vol. 12, no. 1, pp. 97–110, 2019, doi: 10.1007/s12200-017-0755-z.

[190] M. A. Farooq *et al.*, "Recent progress in nanotechnology-based novel drug

delivery systems in designing of cisplatin for cancer therapy: an overview," *Artif. Cells, Nanomedicine Biotechnol.*, vol. 47, no. 1, pp. 1674–1692, 2019, doi: 10.1080/21691401.2019.1604535.

[191] O. Trédan, C. M. Galmarini, K. Patel, and I. F. Tannock, "Drug resistance and the solid tumor microenvironment," *J. Natl. Cancer Inst.*, vol. 99, no. 19, pp. 1441–1454, 2007, doi: 10.1093/jnci/djm135.

[192] Q. Hu, L. Zhang, and R. P. Joshi, "Numerical evaluations of membrane poration by shockwave induced multiple nanobubble collapse in presence of electric fields for transport through cells," *AIP Adv.*, vol. 9, no. 4, 2019, doi: 10.1063/1.5085677.

[193] L. Diodes, S. Fibers, S. Yeh, S. Huang, W. Cheng, and S. Member, "A New Scheme of Conical-Wedge-Shaped Fiber Endface for Coupling Between High-Power," vol. 23, no. 4, pp. 1781–1786, 2005.

[194] Y. Li *et al.*, "Direct Approach toward Label-Free DNA Detection by Surface-Enhanced Raman Spectroscopy: Discrimination of a Single-Base Mutation in 50 Base-Paired Double Helixes," *Anal. Chem.*, vol. 91, no. 13, pp. 7980–7984, 2019, doi: 10.1021/acs.analchem.9b01887.

[195] S. Korposh, S. W. James, S. W. Lee, and R. P. Tatam, "Tapered Optical Fibre Sensors: Current Trends and Future Perspectives," *Sensors (Basel).*, vol. 19, no. 10, 2019, doi: 10.3390/s19102294.

[196] K. Mullaney, "The fabrication of micro-tapered optical fibres for sensing applications Kevin Mullaney The fabrication of micro-tapered optical fibres for sensing applications Centre for Engineering Photonics , School of Aerospace , Transport and Manufacturing . PhD The," 2017.

[197] H. Latifi, M. I. Zibaii, S. M. Hosseini, and P. Jorge, "Photonic Sensors Nonadiabatic Tapered Optical Fiber for Biosensor Applications," no. July 2014, 2012, doi: 10.1007/s13320-012-0086-z.

[198] D. G. Waugh and J. Lawrence, "Laser Surface Processing of Polymers for Biomedical Applications," vol. 161, 2013.

[199] A. Gortler and C. Strowitzki, "Excimer Lasers The powerful light source in the UV and VUV," *Laser Tech. J.*, vol. 2, no. 2, pp. 46–50, 2005.

[200] R. F. Delmdahl and B. Nikolaus, "Solid state pulsed high-repetition-rate excimer lasers," *Phot. Process. Microelectron. Photonics III*, vol. 5339, no. July 2004, p. 284, 2004, doi: 10.1117/12.525458.

[201] M. Tomczykowa and M. E. Plonska-Brzezinska, "Conducting polymers,

hydrogels and their composites: Preparation, properties and bioapplications," *Polymers (Basel).*, vol. 11, no. 2, pp. 1–36, 2019, doi: 10.3390/polym11020350.

[202] L. S. Alarcón, E. D. Martínez, L. M. Rodríguez, and H. Pastoriza, "Topographical and Physicochemical Contrast in Photopatterned SU-8 Films for Microfabrication of Multilayer Structures," *Adv. Mater. Sci. Eng.*, vol. 2016, pp. 1–7, 2016, doi: 10.1155/2016/5278102.

[203] B. Gale *et al.*, "A Review of Current Methods in Microfluidic Device Fabrication and Future Commercialization Prospects," *Inventions*, vol. 3, no. 3, p. 60, 2018, doi: 10.3390/inventions3030060.

[204] D. J. Carbaugh, J. T. Wright, R. Parthiban, and F. Rahman, "Photolithography with polymethyl methacrylate (PMMA)," *Semicond. Sci. Technol.*, vol. 31, no. 2, 2015, doi: 10.1088/0268-1242/31/2/025010.

[205] T. Mitsuoka, A. Torikai, and K. Fueki, "Wavelength sensitivity of the photodegradation of poly(methyl methacrylate)," *J. Appl. Polym. Sci.*, vol. 47, no. 6, pp. 1027–1032, 1993, doi: 10.1002/app.1993.070470609.

[206] H. Y. Tan, W. K. Loke, and N. T. Nguyen, "A reliable method for bonding polydimethylsiloxane (PDMS) to polymethylmethacrylate (PMMA) and its application in micropumps," *Sensors Actuators, B Chem.*, vol. 151, no. 1, pp. 133–139, 2010, doi: 10.1016/j.snb.2010.09.035.

[207] V. N. Rai, C. Mukherjee, and B. Jain, "UV-Vis and FTIR spectroscopy of gamma irradiated polymethyl methacrylate," *Indian J. Pure Appl. Phys.*, vol. 55, no. 11, pp. 775–785, 2017.

[208] F. Träger, *Handbook of Lasers and Optics*, Second Edi. Berlin, Germany: Springer Dordrecht Heidelberg London New York, 2012.

[209] A. Kausar, "A review of filled and pristine polycarbonate blends and their applications," *J. Plast. Film Sheeting*, vol. 34, no. 1, pp. 60–97, 2018, doi: 10.1177/8756087917691088.

[210] H. T. H. Nguyen, P. Qi, M. Rostagno, A. Feteha, and S. A. Miller, "The quest for high glass transition temperature bioplastics," *J. Mater. Chem. A*, vol. 6, no. 20, pp. 9298–9331, 2018, doi: 10.1039/c8ta00377g.

[211] C. Larosa, E. Stura, R. Eggenhöffner, and C. Nicolini, "Optimization of optical properties of polycarbonate film with thiol gold-nanoparticles," *Materials (Basel).*, vol. 2, no. 3, pp. 1193–1204, 2009, doi: 10.3390/ma2031193.

[212] H. Yaghoubi and N. Taghavinia, "Surface chemistry of atmospheric plasma modified polycarbonate substrates," *Appl. Surf. Sci.*, vol. 257, no. 23, pp. 9836–

9839, 2011, doi: 10.1016/j.apsusc.2011.06.034.

[213] A. L. O. K. G. Hanekar, M. A. R. Icci, Y. A. T. Ian, O. Tto, G. Regory, and Y. I. Z. Heng, “Dynamic optical response of SU-8 upon UV treatment,” vol. 8, no. 7, pp. 157–165, 2018.

[214] R. Feng and R. J. Farris, “Charecterization of optical properties of SU-8 and fabrication of optical components,” *J. Micromechanics Microengineering*, vol. 13, no. 1, pp. 80–88, 2003, doi: 10.1088/0960-1317/13/1/312.

[215] D. Lu and C. P. Wong, *Materials for advanced packaging, second edition*. 2016.

[216] A. Bertsch and P. Renaud, “Special issue: 15 years of SU8 as MEMS material,” *Micromachines*, vol. 6, no. 6, pp. 790–792, 2015, doi: 10.3390/mi6060790.

[217] T. Sabel, “Volume hologram formation in SU-8 photoresist,” *Polymers (Basel).*, vol. 9, no. 6, 2017, doi: 10.3390/polym9060198.

[218] Kangde Yao • Junjie Li Fanglian Yao • Yuji Yin, *Chitosan-Based Hydrogels Functions and Applications*. Boca Raton: Taylor & Francis Group, LLC, 2012.

[219] M. Rinaudo, “Chitin and chitosan: Properties and applications,” *Prog. Polym. Sci.*, vol. 31, no. 7, pp. 603–632, 2006, doi: 10.1016/j.progpolymsci.2006.06.001.

[220] I. Aranaz *et al.*, “Functional Characterization of Chitin and Chitosan,” *Curr. Chem. Biol.*, vol. 3, pp. 203–230, 2009, doi: 10.2174/187231309788166415.

[221] R. Czechowska-biskup, D. Jarosińska, B. Rokita, P. Ulański, and J. M. Rosiak, “Determination of Degree of Deacetylation of Chitosan - Comparaison of Methods,” *Prog. Chem. Appl. chitin its Deriv.*, vol. XVII, pp. 5–20, 2012.

[222] E. S. De Alvarenga, “Characterization and Properties of Chitosan,” *Biotechnol. Biopolym.*, pp. 91–108, 2011.

[223] A. A. Aesa and C. D. Walton, “193 nm ArF laser ablation and patterning of chitosan thin films,” *Appl. Phys. A Mater. Sci. Process.*, vol. 124, no. 6, p. 0, 2018, doi: 10.1007/s00339-018-1859-z.

[224] P. K. Dutta, J. Duta, and V. S. Tripathi, “Chitin and Chitosan: Chemistry, properties and applications,” *J. Sci. Ind. Res. (India).*, vol. 63, no. 1, pp. 20–31, 2004, doi: 10.1002/chin.200727270.

[225] a. Sionkowska, H. Kaczmarek, M. Wisniewski, J. Skopinska, S. Lazare, and V. Tokarev, “The influence of UV irradiation on the surface of chitosan films,” *Surf. Sci.*, vol. 600, no. 18, pp. 3775–3779, 2006, doi: 10.1016/j.susc.2006.01.090.

[226] F. Group, *CHITOSAN-BASED HYDROGELS*. 2012.

[227] M. Singh and K. Weidner, “Types and performance of high performing multi-mode polymer waveguides for optical interconnects,” in *Optical Interconnects*

for Data Centers, Elsevier Ltd, 2016, pp. 157–170.

[228] S. T. Koev *et al.*, “Chitosan: An integrative biomaterial for lab-on-a-chip devices,” *Lab Chip*, vol. 10, no. 22, pp. 3026–3042, 2010, doi: 10.1039/c0lc00047g.

[229] S. S. Voznesenskiy, A. Nepomnyaschiy, and Y. N. Kulchin, “Study of Biopolymer Chitosan as Resist for Submicron Electronic Lithography,” *Solid State Phenom.*, vol. 213, pp. 180–185, 2014, doi: 10.4028/www.scientific.net/ssp.213.180.

[230] J. F. Bille, S. W. Hell, and R. N. Weinreb, *High Resolution Imaging in Microscopy and Ophthalmology*. 2019.

[231] Z. Liu, X. Wang, and K. Hang, “Enhancement of trapping efficiency by utilizing a hollow sinh-Gaussian beam,” *Sci. Rep.*, vol. 9, no. 1, pp. 1–8, 2019, doi: 10.1038/s41598-019-46716-5.

[232] I. A. Favre-Bulle, A. B. Stilgoe, E. K. Scott, and H. Rubinsztein-Dunlop, “Optical trapping in vivo: Theory, practice, and applications,” *Nanophotonics*, vol. 8, no. 6, pp. 1023–1040, 2019, doi: 10.1515/nanoph-2019-0055.

[233] D. Choudhary, A. Mossa, M. Jadhav, and C. Cecconi, “Bio-molecular applications of recent developments in optical tweezers,” *Biomolecules*, vol. 9, no. 1, pp. 1–19, 2019, doi: 10.3390/biom9010023.

[234] P. J. P. Chausse, E. D. Le Boulbar, S. D. Lis, and P. A. Shields, “Understanding resolution limit of displacement Talbot lithography,” *Opt. Express*, vol. 27, no. 5, p. 5918, 2019, doi: 10.1364/oe.27.005918.

[235] H. Guo *et al.*, “Near-field focusing of the dielectric microsphere with wavelength scale radius,” vol. 21, no. 2, pp. 526–533, 2013.

[236] M.-S. Kim *et al.*, “Refraction limit of miniaturized optical systems: a ball-lens example,” *Opt. Express*, vol. 24, no. 7, p. 6996, 2016, doi: 10.1364/OE.24.006996.

[237] C. A. Mack, “Understanding focus effects in submicron optical lithography: Part 3--methods for depth-of-focus improvement,” *Opt. Microlithogr. V*, vol. 1674, no. 1992, p. 272, 1992, doi: 10.1117/12.130327.

[238] M. Riedl, *Optical Design: Applying the Fundamentals*. Washington: SPIE, 2009.

[239] Y. Ben-Aryeh, “Increase of resolution by use of microspheres related to complex Snell’s law,” *J. Opt. Soc. Am. A*, vol. 33, no. 12, pp. 2284–2288, 2016, doi: 10.1364/JOSAA.33.002284.

[240] Y. Wen *et al.*, “Photonic Nanojet Sub-Diffraction Nano-Fabrication With in situ

Super-Resolution Imaging," *IEEE Trans. Nanotechnol.*, vol. 18, pp. 226–233, 2019, doi: 10.1109/TNANO.2019.2896220.

[241] J. Zhu and L. L. Goddard, "Nanoscale Advances All-dielectric concentration of electromagnetic fi elds at the nanoscale : the role of photonic nanojets," 2019, doi: 10.1039/c9na00430k.

[242] B. S. Luk'yanchuk, N. Arnold, S. M. Huang, Z. B. Wang, and M. H. Hong, "Three-dimensional effects in dry laser cleaning," *Appl. Phys. A*, vol. 77, no. 2, pp. 209–215, 2003, doi: 10.1007/s00339-003-2139-z.

[243] A. C. Tam, W. P. Leung, W. Zapka, and W. Ziemlich, "Laser-cleaning techniques for removal of surface particulates," *J. Appl. Phys.*, vol. 71, no. 7, pp. 3515–3523, 1992, doi: 10.1063/1.350906.

[244] Y. F. Lu, W. D. Song, Y. Zhang, M. H. Hong, and T. C. Chong, "Laser removal of particles from solid surfaces," *RIKEN Rev. Focus. Laser Precis. Microfabr.*, vol. 32, no. 32, pp. 64–70, 2001.

[245] K. Hein, T. Hucke, M. Stintz, and S. Ripperger, "Analysis of Adhesion Forces Between Particles and Wall Based on the Vibration Method," vol. 19, pp. 269–276, 2002.

[246] L. Chen, Y. Zhou, Y. Li, and M. Hong, "Microsphere enhanced optical imaging and patterning: From physics to applications," *Appl. Phys. Rev.*, vol. 6, no. 2, 2019, doi: 10.1063/1.5082215.

[247] B. Bellich, I. D'Agostino, S. Semeraro, A. Gamini, and A. Cesàro, *"The good, the bad and the ugly" of chitosans*, vol. 14, no. 5. 2016.

[248] T. Grosges, A. Vial, and D. Barchiesi, "Models of near-field spectroscopic studies: comparison between Finite-Element and Finite-Difference methods," *Opt. Express*, vol. 13, no. 21, p. 8483, 2005, doi: 10.1364/OPEX.13.008483.

[249] S.-C. Chen, P. P. R. Baets, and S. P. C. Wuytens, "Optimization of gold-nanodome patterned chips towards a performant Surface Enhanced Raman Spectroscopy (SERS) platform," 2016.

[250] J. H. L. Iv and J. H. L. V, *A Heat Transfer Textbook*. Cambridge: J.H. Lienhard V, 2001.

[251] D. P. D. Theodore L. Bergman, Adrienne S. LavineFrank P. Incropera, *Introduction to Heat Transfer*, vol. 136, no. 1. Jefferson: John Wiley & Sons, Inc., 2011.

[252] S. N. Kazi, *Heat Transfer Phenomena and Applications*. 2012.

[253] R. V. M. and A. B. Mihai Oane, "A Parallel between Laser Irradiation and

Relativistic Electrons Irradiation of Solids," 2016.

[254] M. Kaltenbacher, *Numerical Simulation of Mechatronic Sensors and Actuators Finite Elements for Computational Multiphysics*, 3rd ed. Vienna: Springer Heidelberg New York Dordrecht London, 2015.

[255] S. M. K. Raiyan, "Finite Element Time Domain Method with a Unique Coupled Mesh System for Electromagnatics and Photonics," 2015.

[256] J. C. H. Pepper, Darrell W., *The Finite Element Method*. 2006.

[257] R. Fakir, N. Barka, and J. Brousseau, "Case study of laser hardening process applied to 4340 steel cylindrical specimens using simulation and experimental validation," *Case Stud. Therm. Eng.*, vol. 11, pp. 15–25, 2018, doi: 10.1016/j.csite.2017.12.002.

[258] F. P. Incropera, D. P. DeWitt, T. L. Bergman, and A. S. Lavine, "Introduction to Conduction," *Fundamentals of Heat and Mass Transfer*. p. 997, 2007, doi: 10.1016/j.applthermaleng.2011.03.022.

[259] A. O. Euan McLeod, "Nanofabrication using near-field optical probes," *Hydrobiologia*, vol. 116–117, no. 1, pp. 243–245, 2012, doi: 10.1177/2211068212450289.

[260] Z. Ye, L. Wei, L. Xiao, and J. Wang, "Laser illumination-induced dramatic catalytic activity change on Au nanospheres," *Chem. Sci.*, vol. 10, no. 22, pp. 5793–5800, 2019, doi: 10.1039/c9sc01666j.

[261] İ. R. Çapoğlu, A. Taflove, and V. Backman, "Computation of tightly-focused laser beams in the FDTD method," *Opt. Express*, vol. 21, no. 1, p. 87, 2013, doi: 10.1364/OE.21.000087.

[262] Z. L. Yang *et al.*, "FDTD for plasmonics: Applications in enhanced Raman spectroscopy," *Chinese Sci. Bull.*, vol. 55, no. 24, pp. 2635–2642, 2010, doi: 10.1007/s11434-010-4044-0.

[263] T. Grosges, A. Vial, and D. Barchiesi, "Models of near-field spectroscopic studies: comparison between Finite-Element and Finite-Difference methods," *Opt. Express*, vol. 13, no. 21, p. 8483, 2005, doi: 10.1364/OPEX.13.008483.

[264] F. I. B. And and A. Belkhir, "Finite Difference Time Domain Method for Grating Structures," in *Theory and Numeric Applications*, 7 Marseille Cedex: Institut Fresnel, Université d'Aix-Marseille, CNRS, 2013, p. 41.

[265] M. Benton, M. R. Hossan, P. R. Konari, and S. Gamagedara, "Effect of process parameters and material properties on laser micromachining of microchannels," *Micromachines*, vol. 10, no. 2, 2019, doi: 10.3390/mi10020123.

[266] T. E. L. Fred M. Dickey, *Laser Beam Shaping Applications*. 2017.

[267] R. M. Verdaasdonk, C. F. P. Van Swol, and P. Med, “Laser light delivery systems for medical applications,” 1997.

[268] S. Eilzer and B. Wedel, “Hollow core optical fibers for industrial ultra short pulse laser beam delivery applications,” *Fibers*, vol. 6, no. 4, 2018, doi: 10.3390/fib6040080.

[269] A. Kratky, D. Schuöcker, and G. Liedl, “Processing with kW fibre lasers: advantages and limits,” *XVII Int. Symp. Gas Flow, Chem. Lasers, High-Power Lasers*, vol. 7131, p. 71311X, 2008, doi: 10.1117/12.816655.

[270] L. Tong, “Micro/nanofibre optical sensors: Challenges and prospects,” *Sensors (Switzerland)*, vol. 18, no. 3, 2018, doi: 10.3390/s18030903.

[271] I. Alexeev *et al.*, “Optical trap assisted sub diffraction limited laser structuring,” in *Optically Induced Nanostructures: Biomedical and Technical Applications*, 2015, pp. 283–302.

[272] Ignac Capek, “Nanotechnology and nanomaterials,” in *Nanocomposite Structures and Dispersions*, 2006, pp. 1–93.

[273] Y. Cao, X. Zeng, Z. Cai, and J. Duan, “Laser micro/nano-fabrication techniques and their applications in electronics 1 1,” *Adv. Laser Mater. Process. Technol. Res. Appl.*, no. 863, pp. 629–670, 2010, doi: 10.1533/9781845699819.7.629.

[274] Y. Xu, P. Lu, L. Chen, and X. Bao, “Recent Developments in Micro-Structured Fiber Optic Sensors,” *Fibers*, vol. 5, no. 1, p. 3, 2017, doi: 10.3390/fib5010003.

[275] R. B. Hetnarski, *Encyclopedia of Thermal Stresses*. Rochester, Naples: Springer Dordrecht Heidelberg New York London, 2014.

[276] M. Udrea, “Laser polishing of optical fiber end surface,” *Opt. Eng.*, vol. 40, no. 9, p. 2026, 2002, doi: 10.1117/1.1390517.

[277] N. Healy *et al.*, “ CO 2 Laser-Induced Directional Recrystallization to Produce Single Crystal Silicon-Core Optical Fibers with Low Loss ,” *Adv. Opt. Mater.*, vol. 4, no. 7, pp. 1004–1008, 2016, doi: 10.1002/adom.201500784.

[278] S. Song *et al.*, “Laser restructuring and photoluminescence of glass-clad GaSb/Si-core optical fibres,” *Nat. Commun.*, vol. 10, no. 1, pp. 1–7, 2019, doi: 10.1038/s41467-019-09835-1.

[279] P. Actis, A. C. Mak, and N. Pourmand, “Functionalized nanopipettes : toward label-free , single cell biosensors,” pp. 177–185, 2010, doi: 10.1007/s12566-010-0013-y.

[280] D. C. Dumitras, *CO2 Laser – Optimisation and Application*. Croatia, 2012.

[281] S. C. Singh, H. Zeng, C. Guo, and W. Cai, “Lasers: Fundamentals, Types, and Operations,” in *Nanomaterials: Processing and Characterization with Lasers*, 2012, pp. 1–34.

[282] T. Doualle, L. Gallais, P. Cormont, D. Hébert, P. Combis, and J. L. Rullier, “Thermo-mechanical simulations of CO2laser-fused silica interactions,” *J. Appl. Phys.*, vol. 119, no. 11, pp. 1–10, 2016, doi: 10.1063/1.4944435.

[283] P. Holmberg, “Laser processing of Silica based glass,” KTH – Royal Institute of Technology, 2015.

[284] R. B. Hetnarski, *Encyclopedia of Thermal Stresses*. 2014.

[285] K. Borzycki and K. Schuster, “Arc fusion splicing of photonic crystal fibers,” *Photonic Cryst. - Introd. Appl. Theory*, 2012, doi: 10.5772/35252.

[286] J. M. P. Coelho, M. Nespereira, C. Silva, D. Pereira, and J. Rebordo, “Advances in Optical Fiber Laser Micromachining for Sensors Development,” 2013.

[287] Z. Liu, Z. F. Zhang, H. Tam, and X. Tao, “Multifunctional Smart Optical Fibers : Materials , Fabrication , and Sensing Applications,” pp. 1–24, 2019.

[288] T. Doualle, L. Gallais, P. Cormont, D. Hébert, P. Combis, and J. L. Rullier, “Thermo-mechanical simulations of CO2 laser-fused silica interactions,” *J. Appl. Phys.*, vol. 119, no. 11, 2016, doi: 10.1063/1.4944435.

[289] P. Holmberg, “Laser processing of Silica based glass,” 2015.

[290] T. V. D. Simon Ramo, John R. Whinne, *Fields and waves in communication electronics*, 3rd ed. Canada: Jhon Wiley & Sons, Inc., 1994.

[291] M. Polyanskiy, “RefractiveIndex.INFO website: © 2008-2020,” 2020. .

[292] A. B. Socorro-Leránoz, D. Santano, I. Del Villar, and I. R. Matias, “Trends in the design of wavelength-based optical fibre biosensors (2008–2018),” *Biosens. Bioelectron. X*, vol. 1, no. February, p. 100015, 2019, doi: 10.1016/j.biosx.2019.100015.

[293] G. Keiser, F. Xiong, Y. Cui, and P. P. Shum, “Review of diverse optical fibers used in biomedical research and clinical practice,” *J. Biomed. Opt.*, vol. 19, no. 8, p. 080902, 2014, doi: 10.1117/1.jbo.19.8.080902.

[294] K. Krupa *et al.*, “Multimode nonlinear fiber optics, a spatiotemporal avenue,” *APL Photonics*, vol. 4, no. 11, p. 110901, 2019, doi: 10.1063/1.5119434.

[295] S. Addanki, I. S. Amiri, and P. Yupapin, “Review of optical fibers-introduction and applications in fiber lasers,” *Results Phys.*, vol. 10, no. June, pp. 743–750, 2018, doi: 10.1016/j.rinp.2018.07.028.

[296] K. Bescherer, D. Munzke, O. Reich, and H.-P. Loock, “Fabrication and modeling

of multimode fiber lenses," *Appl. Opt.*, vol. 52, no. 4, p. B40, 2013, doi: 10.1364/ao.52.000b40.

[297] B. J. Skutnik, B. Foley, and K. B. Moran, "High-numerical-aperture silica core fibers," *Opt. Fibers Sensors Med. Appl. IV*, vol. 5317, p. 39, 2004, doi: 10.1117/12.529467.

[298] E. Mendez, K. M. Nowak, H. J. Baker, F. J. Villarreal, and D. R. Hall, "Localized CO2 laser damage repair of fused silica optics," *Appl. Opt.*, vol. 45, no. 21, pp. 5358–5367, 2006, doi: 10.1364/AO.45.005358.

[299] S. Fujino, "Surface tension of PbO-B 2 O 3 and Bi 2 O 3 -B 2 O 3 glass melts," vol. 0, pp. 2207–2212, 2005.

[300] K. Boyd, H. Ebendorff-Heidepriem, T. M. Monro, and J. Munch, "Surface tension and viscosity measurement of optical glasses using a scanning CO_2 laser," *Opt. Mater. Express*, vol. 2, no. 8, p. 1101, 2012, doi: 10.1364/ome.2.001101.

[301] T. F. M. Alexis Mendez, *Specialty Optical Fibers Handbook*, 1st ed. San Diego, London: Elsevier Inc, 2007.

[302] D. Grojo, A. Cros, P. Delaporte, and M. Sentis, "Experimental investigation of ablation mechanisms involved in dry laser cleaning," *Appl. Surf. Sci.*, vol. 253, no. 19, pp. 8309–8315, 2007, doi: 10.1016/j.apsusc.2007.02.117.

[303] J.-H. Kang, C. Lee, J.-Y. Joo, and S.-K. Lee, "Phase-locked loop based on machine surface topography measurement using lensed fibers," *Appl. Opt.*, vol. 50, no. 4, p. 460, 2011, doi: 10.1364/ao.50.000460.

[304] G. Böttger, H. Schröder, and R. Jordan, "Active or passive fiber-chip-alignment: approaches to efficient solutions," *Optoelectron. Interconnects XIII*, vol. 8630, p. 863006, 2013, doi: 10.1117/12.2014176.

[305] N. Ma, "Tailoring Optical Fibers for Cell Transfection," 2012.

[306] T. Dobrev, D. T. Pham, and S. S. Dimov, "Laser polishing," *4M 2006 - Second Int. Conf. Multi-Material Micro Manuf.*, no. February 2012, pp. 273–276, 2008, doi: 10.1016/b978-008045263-0/50061-1.

[307] W. J. Thomes, Jr., M. N. Ott, R. F. Chuska, R. C. Switzer, and D. E. Blair, "Fiber optic cables for transmission of high-power laser pulses," *Nanophotonics Macrophotonics Sp. Environ. V*, vol. 8164, no. October 2010, p. 81640F, 2011, doi: 10.1117/12.895964.

[308] K. Boyd *et al.*, "High precision 96 μm CO2 laser end-face processing of optical fibres," *Opt. Express*, vol. 23, no. 11, p. 15065, 2015, doi: 10.1364/oe.23.015065.

[309] H. K. Choi *et al.*, “CO2 laser assisted fabrication of micro-lensed single-mode optical fiber,” *J. Opt. Soc. Korea*, vol. 19, no. 4, pp. 327–333, 2015, doi: 10.3807/JOSK.2015.19.4.327.

[310] S. Boehme, E. Beckert, R. Eberhardt, and A. Tuennermann, “Laser splicing of end caps: process requirements in high power laser applications,” *Laser-based Micro- Nanopackaging Assem. III*, vol. 7202, no. cm, p. 11, 2009, doi: 10.1117/12.808161.

[311] A. Gomes, C. Monteiro, B. Silveira, and O. Frazão, “A Brief Review of New Fiber Microsphere Geometries,” *Fibers*, vol. 6, no. 3, p. 48, 2018, doi: 10.3390/fib6030048.

[312] K. Egashira and M. Kobayashi, “Analysis of thermal conditions in CO_2 laser splicing of optical fibers,” *Appl. Opt.*, vol. 16, no. 10, p. 2743, 1977, doi: 10.1364/AO.16.002743.